ESCOLA DE DOUTORAMENTO
INTERNACIONAL DA USC

Mads
Fromreide

Tese de doutoramento

Electromagnetic modelling of three-phase AC furnaces. Applications in metallurgical processes

Santiago de Compostela, 2023

Programa de Doutoramento en Métodos Matemáticos e Simulación Numérica en Enxeñaría e Ciencias Aplicadas

USC
UNIVERSIDADE
DE SANTIAGO
DE COMPOSTELA

TESE DE DOUTORAMENTO

ELECTROMAGNETIC MODELLING OF THREE-PHASE AC FURNACES. APPLICATIONS IN METALLURGICAL PROCESSES

Mads Fromreide

ESCOLA DE DOUTORAMENTO INTERNACIONAL DA UNIVERSIDADE DE SANTIAGO DE COMPOSTELA

PROGRAMA DE DOUTORAMENTO EN MÉTODOS MATEMÁTICOS E SIMULACIÓN NUMÉRICA EN ENXEÑERÍA E CIENCIAS APLICADAS

SANTIAGO DE COMPOSTELA

2023

USC
UNIVERSIDADE
DE SANTIAGO
DE COMPOSTELA

AUTORIZACIÓN DAS CODIRECTORAS DA TESE

Electromagnetic modelling of three-phase AC furnaces.
Applications in metallurgical processes

Dna. Mª Dolores Gómez Pedreira
Dna. Mª del Pilar Salgado Rodríguez

INFORMAN:

Que a presente tese, correspóndese co traballo realizado por D. Mads Fromreide, baixo a súa dirección, e autorizan á súa presentación, considerando que reúnen os requisitos esixidos no Regulamento de Estudos de Doutoramento da USC, e que como directoras desta non incorre nas causas de abstención establecidas na Lei 40/2015.

De acordo co indicado no Regulamento de Estudos de Doutoramento, declaran tamén que a presente tese de doutoramento é idónea para ser defendida en base á modalidade de Monográfica con reproducción de publicacións, nos que a participación do doutorando foi decisiva para a súa elaboración e as publicacións se axustan ao Plan de Investigación.

En Santiago de Compostela, 23 de maio de 2023

Asdo. Dolores Gómez Asdo. Pilar Salgado

USC
UNIVERSIDADE
DE SANTIAGO
DE COMPOSTELA

AUTHORIZATION FROM THE DIRECTOR OF THE THESIS

Electromagnetic modelling of three-phase AC furnaces.
Applications in metallurgical processes

Mr. Svenn Anton Halvorsen

REPORT:

that this thesis corresponds to the work carried out by Mr. Mads Fromreide, under his direction, and authorizes its presentation, considering that it meets the requirements that appear in the USC Regulations for Doctoral Studies, and that as director do not incur the causes of abstention established in Law 40/2015.

In accordance with what is indicated in the Regulations for Doctoral Studies, he also declares that the present doctoral thesis is suitable to be defended based on the Monograph modality with reproduction of publications, in which the participation of the doctoral student was decisive for its preparation and which publications adapt to the Research Plan.

En Santiago de Compostela, 23rd May 2023

Svenn A. Halvorsen

USC
UNIVERSIDADE
DE SANTIAGO
DE COMPOSTELA

DECLARACIÓN DO AUTOR/A DA TESE

D. Mads Fromreide

Título da tese: **Electromagnetic modelling of three-phase AC furnaces. Applications in metallurgical processes**

Presento a miña tese, seguindo o procedemento axeitado ao Regulamento, e declaro que:

1) A tese abarca os resultados da elaboración do meu traballo.
2) De ser o caso, na tese faise referencia ás colaboracións que tivo este traballo.
3) Confirmo que a tese non incorre en ningún tipo de plaxio doutros autores nin de traballos presentados por min para a obtención doutros títulos.
4) A tese é a versión definitiva presentada para a súa defensa e coincide a versión impresa coa presentada en formato electrónico

E comprométome a presentar o Compromiso Documental de Supervisión no caso de que o orixinal non estea na Escola.

Title of the thesis: **Electromagnetic modelling of three-phase AC furnaces. Applications in metallurgical processes.**

I present my thesis, following the appropriate Regulations, and declare that:

1) The thesis covers the results of my work.
2) There will be reference to the collaborations that this work had when applicable.
3) I confirm that the thesis does not involve any type of plagiarism from other authors or works presented by me to obtain other degrees.
4) The thesis is the final version presented for its defence and the printed version matches the one presented in electronic format.

I also pledge to present the Documentary Commitment of Supervision in the event that the original is not at the school.

In Grimstad, 23rd May 2023.

Mads Fromreide

USC
UNIVERSIDADE
DE SANTIAGO
DE COMPOSTELA

Acknowledgements

I want to start by thanking my academic supervisors at USC, Professor Pilar Salgado and Professor Dolores Gómez. Your support and guidance throughout my studies have been excellent. You both went above and beyond your duty, in welcoming and supporting me and my family in the lovely city of Santiago de Compostela during our stay. Your guidance through the writing of scientific papers and not least this thesis has undoubtedly helped and taught me a lot and shaped me as a researcher.

Further, I want to thank my supervisor, former leader, and colleague Svenn Anton Halvorsen, without whom this PhD project would never have been possible. Your experience within both mathematics and the metallurgical industry has been vital for the project from start to finish. I thank you for giving me this opportunity and guiding me over all these years. Without your ideas and intuition for interesting industrial problems this thesis would not be what it is.

I also want to thank the steering committee of the ElMet project, both from the industrial partners Elkem and Eramet, and NTNU. It has always been interesting to meet for technical workshops and to learn more about the industry and real-life challenges and needs.

I want to thank Adriana Castro at CITMaga for assisting me with translations of Spanish forms and with all administrative tasks related to my studies. I would also like to thank Carlos Grela for always fixing my IT issues, remotely or local.

I would also like to thank my former college Egil V. Herland, who played an important part during the first years of my PhD work. I have greatly benefited from your expertise in modelling and the use of COMSOL. Also, thanks to my college Manuel Sparta for the possibility to forward my work into the SAFECI project.

Further, I would like to thank my wife Margarita, for always supporting me and believing in me. Without you, I would never have been where I am today.

Finally, I would like to dedicate my work to my children, Matheo and Thimea Rose. You are the reason I do everything!

This thesis is published as part of the project Electrical Conditions and their Process Interactions in High Temperature Metallurgical Reactors (ElMet), with financial support from The Research Council of Norway (Pr.No. 247791) and the companies Elkem and Eramet Norway.

USC
UNIVERSIDADE DE SANTIAGO DE COMPOSTELA

USC
UNIVERSIDADE
DE SANTIAGO
DE COMPOSTELA

Contents

List of Figures xv

List of Tables xvii

Preface xix

Introduction 1
1. Motivation, objectives and methodology 1
2. List of publications 3

1 Industrial problem 7
1.1 Introduction 7
1.2 Three-phase furnaces for ferromanganese production 8
1.2.1 Production process of ferromanganese 9
1.2.2 Furnace operation in the production of other ferroalloys . . . 14

2 State of the art in the modelling of submerged arc furnaces 17
2.1 Modelling of the whole furnace 17
2.1.1 DC Models 18
2.1.2 AC Models 19
2.2 Models focused on electrodes, proximity effect and surroundings . . 21
2.3 Experimental results and model data 22
2.4 Novel insights: key contributions to the existing literature 25

3 Mathematical models: 3D and reduced dimension solutions 29
3.1 The time harmonic Maxwell's equations 30
3.2 A 3D eddy current model in a bounded domain with electric ports . 32
3.3 Formulation in magnetic vector potential and electric scalar potential 35
3.3.1 3D Modelling of the steel shell 38
3.4 2D model with in-plane currents 39
3.5 2D model with out-of-plane currents 41
3.5.1 A modified magnetic vector potential formulation 43
3.6 A direct current model 45
3.7 Non-dimensional tools. Analysis of the 2D electric field equation . . 47

USC UNIVERSIDADE DE SANTIAGO DE COMPOSTELA

4 Numerical simulation of FeMn furnaces **51**
4.1 Furnace description: a simplified 3D geometry . . . 52
4.2 Inductive effects in the furnace hearth . . . 57
4.2.1 2D model with in-plane currents . . . 58
4.2.2 Non-dimensional analysis . . . 60
4.2.3 Comparing AC models with DC models . . . 67
4.2.4 Conclusions . . . 71
4.3 2D in-plane versus 3D models in the furnace hearth . . . 72
4.3.1 3D Numerical results . . . 72
4.3.2 2D numerical results . . . 73
4.3.3 Conclusions . . . 77
4.4 Induced currents in the lining and steel shell . . . 78
4.4.1 Mathematical modeling: 2D and 3D approaches . . . 79
4.4.2 Structural modifications in the furnace . . . 80
4.4.3 2D simulation results . . . 84
4.4.4 3D simulation results . . . 86
4.4.5 Discussion . . . 91
4.4.6 Conclusions . . . 92
4.5 Exploring a new tool for the AC model approximation . . . 93

5 1D Analytical mathematical models **99**
5.1 Electric field distribution in one-dimensional conductors . . . 99
5.1.1 Simple examples for a single conductor . . . 100
5.2 Adjacent conducting layers and proximity effects . . . 102
5.3 Solution of a general 1D model with three or more layers . . . 106
5.3.1 Formulation with known electric field at the surface . . . 107
5.3.2 Alternative formulation with known total current . . . 109
5.3.3 Example case with N=5 layers . . . 110
5.4 Comparison of one-dimensional AC and DC simulations . . . 113
5.4.1 Single material layer . . . 113
5.4.2 Two adjacent material layers . . . 114
5.5 Approximating power generated in a conductor adjacent to a highly conductive material . . . 117
5.5.1 Derivation of the model . . . 117
5.5.2 Validation of the approximate model . . . 118
5.5.3 Distribution of current in the approximate solution . . . 120
5.5.4 Power generated for the approximate solution . . . 122
5.5.5 Discussion . . . 124
5.6 1D model applied to the hearth of a furnace . . . 125
5.7 1D model applied to the linings and casing of SAFs . . . 128
5.8 Discussion . . . 132
5.9 Conclusions . . . 134

USC UNIVERSIDADE DE SANTIAGO DE COMPOSTELA

Conclusions and further work **137**

Resumo **150**

Bibliography **150**

Nomenclature **161**

USC
UNIVERSIDADE DE SANTIAGO DE COMPOSTELA

USC
UNIVERSIDADE
DE SANTIAGO
DE COMPOSTELA

List of Figures

1.1 Illustration of a submerged arc furnace for FeMn production. Reproduced with permission of M. Tangstad. 9
1.2 The structure of a Søderberg electrode. 1. Carbon paste cylinders 2. Liquid carbon paste 3. Baking zone 4. Solid/baked electrode 5. Steel fins 6. Hydraulic cylinders for slipping 7. Current supply 8. Contact clamps. The red arrows indicate current flow, the blue arrows indicate the slipping mechanism. The figure has been adapted from Hannesson (2016). 10
1.3 Schematic representation of three phase furnace geometry with typical furnace features indicated: 1. Steel shell/casing 2. Ceramic lining 3. Carbon lining 4. Charge material 5. Electrode(s). Left: view from top (xy-plane). Right: yz-plane as indicated in left plot. 10
1.4 Schematic representation of the reduction steps of Mn in terms of temperature regions. Based on Figure 7.4 in Olsen et al. (2007). . . . 11
1.5 Schematic representation of zones in the FeMn furnace. The most important chemical reactions are given (red: exothermic, black: endothermic). Based on Figure 7.25 in Olsen et al. (2007). 13
3.1 Sketch of the 3D computational domain with electric ports on the top of the electrodes. 33
3.2 Computational domain of the 2D model with in-plane currents (left); 2D plane relative to the 3D model (right). 40
3.3 2D model with out-of-plane currents. Computational domain. 42
3.4 Rectangular conductor with thickness T, width W and electrical conductivity σ. 48
4.1 Furnace elements around the electrodes near the contact clamps. Reproduced with permission from Kadkhodabeigi et al. (2015). . . . 53
4.2 Simplified 3D geometry for modelling FeMn furnaces. 53
4.3 Geometric parameters of the 3D FeMn furnace model. 54
4.4 3D sketch of a FeMn furnace model with numbered material regions: 1. Electrodes 2. Charge 400 °C 3. Charge 800 °C 4. Charge 1200 °C 5. Coke beds 6. Alloy 7. Carbon lining 8. Oxide lining 9. Steel shell. . . 56
4.5 Sketch of Plane 1 and Plane 2 in a horizontal cross section of the 3D domain. 57
4.6 Simplified 3D furnace geometry with flat coke beds; carbon lining and steel shell are not included. 58

USC UNIVERSIDADE DE SANTIAGO DE COMPOSTELA

4.7 2D model with in-plane currents and flat coke beds. Material regions: 1. Air 2. Electrodes 3. Charge 4. Coke bed 5. Alloy. The colours indicate the material skin depth at $f = 50$ Hz, limited to $\delta < 10$ m. . . . 59
4.8 Sketch of the 2D model with geometric parameters (blue) and skin depths (red). . . . 60
4.9 Rectangular sub-regions defined within the simple 2D model. . . . 62
4.10 Mesh for the reference case around the right electrode. The background colours indicate the different materials. . . . 63
4.11 Current density distribution for the 2D reference case. . . . 64
4.12 Power density distribution for the 2D reference case. . . . 64
4.13 Power density distribution for the 2D model with $\sigma_{Co} = 1$ S/m. The color range is limited to 500 MW/m^3. . . . 66
4.14 Power density distribution for the 2D model with $\sigma_{Co} = 5000$ S/m. The colour range is limited to 3 MW/m^3. . . . 66
4.15 Current density norm in the coke bed center ($y = 0$ m) for different values of coke bed conductivity. The limits $z = 0$ m and $z = 2$ m correspond to the coke bed layer top and bottom, respectively. . . . 66
4.16 Power density for the 2D model with separated ellipsoidal shape coke beds (case 1): AC solution (top) and DC solution (bottom). The colour scale has been limited to 2 MW/m^3. . . . 69
4.17 Power density for the 2D models with flat coke bed: Case 2 (top), Case 3 (middle) Case 4 (bottom): AC solutions (left) and DC solutions (right). The colour scale has been limited to 2 MW/m^3. . . . 70
4.18 Current density norm in the 3D domain: Plane 1 (top) an Plane 2 (bottom). The color range is limited to 250 kA/m^2. . . . 73
4.19 Current density norm in the electrodes in the xy-plane placed at $z = 4$m. The surrounding materials are neglected. The color scale is limited to 200 kA/m^2. . . . 74
4.20 Active power density p in the 3D model: Plane 1(top) and Plane 2 (bottom). The color range is limited to 2 MW/m^3. . . . 74
4.21 Current density norm in the 2D model. The color scale is limited to 1 MA/m^2. . . . 75
4.22 Active power distribution in the 2D model. The color scale is limited to 10 MW/m^3. . . . 76
4.23 Geometry and materials in the 2D out-of-plane model, including: (1) air, (2) electrodes, (8) carbon lining, (9) oxide lining and (10) steel shell. The colour indicates skin depth of the material at $f = 50$Hz, with the scale restricted to 10 m. . . . 80
4.24 Mesh for a part of the domain surrounding an electrode. . . . 81
4.25 Rectangular elements near the lining-shell interface (lining yellow, shell red) and on the electrode surface. . . . 81

USC UNIVERSIDADE DE SANTIAGO DE COMPOSTELA

4.26 Positions of insulated gaps (in red) in the steel shell (in blue) for the 2D model. Left: 6 gaps symmetric, middle: 12 gaps symmetric, right: 12 gaps centred. 82
4.27 Positions of vertical and horizontal insulating gaps in the steel shell. Three of the six vertical gaps are centred on the electrodes. 83
4.28 Magnetic induction norm: left, when the carbon lining is neglected (Case 1); right, when the carbon lining is included (Case 2). The colour range is limited to 15 mT to resolve the outer parts. 85
4.29 Current density norm on the inner circumference of the steel shell with and without carbon lining present (Cases 2 and 1, respectively). The vertical lines indicate the position of each electrode. 85
4.30 Current density norm on the *inside* of the steel shell with 0, 6 and 12 insulated sections. Cases 2 and 3 are included in both plots; Case 4 (12 symmetrical gaps) in the top and Case 5 (12 centred gaps) in the bottom. 86
4.31 Current on the *inside* of the steel shell for the 3D reference case (Case 6) (top), extended height of carbon lining (Case 7) (bottom). The colour range is limited to 0-10 kA/m and shows the surface current density norm. The black arrows indicate the pattern of the shell current at a given time. The red arrows indicate the direction of the electrode currents. 88
4.32 Current on the *inside* of the steel shell when both vertical and horizontal insulation gaps are included. The vertical insulation gaps are placed symmetrically (Case 10) around the electrodes (top) and centred (Case 11) behind the electrodes (bottom). The color range is restricted to 0-10 kA/m and shows the surface current density norm. The red arrows indicate the direction of the electrode currents. 89
4.33 Current patterns on the *inside* of the steel shell for a section of the furnace for Case 11. The black arrows show the direction of the current at a given time. The colour represents the current norm as in Figure 4.32. 90
4.34 Procedure for obtaining the solution of Problem B from solution of Problem A. 94
4.35 Real part of the current density in a horizontal cross section of the electrode: (a) Single-phase case A, (b) Single-phase case B, (c) Linear combination of single-phase cases A and B with phase shift. 95
4.36 Symmetry plane of the furnace for solving Problem A. 95
4.37 Current density norm in a horizontal cross section through the electrodes: (a) Single-phase case A, (b) Single-phase case B, (c) Linear combination of single-phase cases A and B and (d) Full three-phase model. The colour range is limited to a maximum of 210 kA/m^2 in each plot. 96

USC UNIVERSIDADE DE SANTIAGO DE COMPOSTELA

4.38 Power density in Plane 2 through the two active electrodes in single-phase case A. 97
5.1 Electric field distribution in a thick conductor. 101
5.2 Electric field distribution in a symmetric conductor with thickness T for different values of electric conductivity. The values are normalized by the surface value $|E_0| = |E(0)|$. 102
5.3 Electric field density distribution in a two-layered conductor with three different conductivities for the second material layer. The base case $\sigma_1 = \sigma_2$ is the same in both (a) and (b). The thick vertical line represents the surface of medium 1, while the interface between both media is indicated by a dotted vertical line. 105
5.4 Schematic representation of a 1D domain with N layers. 106
5.5 Modulus of the electric field, density distribution and power density in a five-layered material example. On the left, the results correspond to $\mu_4 = 100\mu_0$ assuming either E_0 or I_{tot} are known; on the right, a comparison between cases $\mu_4 = 100\mu_0$ and $\mu_4 = \mu_0$ is shown with data E_0. 112
5.6 Comparison of AC and DC models as function of δ_1. Cases: $\delta_1/T = 10$ (left), $\delta_1/T = 1$ (middle) and $\delta_1/T = 1/2$ (right). The dotted line indicates the skin-depth of the second layer and the dashed line represents the interface between the two layers. 116
5.7 Electric field distribution in two layers with $\sigma_2 = 10^7$ S/m and $T = 2$ m for different values of σ_1. The solid lines represent the analytical solutions, while the dashed lines correspond to the approximate solutions. On the right, a zoom at the material interface is shown. The vertical dotted line at $z = 2.0225$ m represents the skin depth of the second material. 119
5.8 Difference between the full and approximate solutions (Δ_1) as a function of σ_1 for different values of σ_2. 120
5.9 Real part (top), imaginary part (middle) and norm (bottom) of the total current in layer 1 and total current at the interface $z = T$ in the limit $\delta_2 \to 0$ as a function of δ_1/T. 121
5.10 Real part (top), imaginary part (middle) and norm (bottom) of the total current in layer 1 and total current at the interface $z = T$ in the limit $\delta_2 \to 0$ (solid lines) and in layer 1 and layer 2 for the full two layer solution (dashed lines) for $\sigma_2 = 6 \cdot 10^8$ S/m and $T = 2$ m as a function of δ_1/T. 123
5.11 Non-dimensional power for the approximate solution as a function of δ_1/T. The vertical line indicates the maximum of the function. 124
5.12 Power density in the left side of coke bed of a *long and thin* furnace. The contour lines indicate levels of constant power with a difference of 0.5 MW/m^3. 126

USC UNIVERSIDADE DE SANTIAGO DE COMPOSTELA

5.13 Power density at furnace center for the reference case. The range is from the coke bed top ($z = 0$) to the metal bottom ($z = 2.5$). 127
5.14 Log-log plot of the deviation of 1D estimate for different parameter settings. $2\,(L_E/\delta)^2$ is changed by either changing f, σ or L_E, while keeping the other two parameters constant. 128
5.15 Geometry of 2D model including an enlarged detail of the linings and steel shell. 129
5.16 Radial electric field distribution as calculated by the numerical 2D simulation (solid) and the analytical 1D model (dashed) for two cases with magnetic and non-magnetic steel. 130
5.17 Normalized total power dissipated in the carbon lining as a function of δ_C/T_C 131

USC UNIVERSIDADE DE SANTIAGO DE COMPOSTELA

USC
UNIVERSIDADE
DE SANTIAGO
DE COMPOSTELA

List of Tables

2.1 Bulk resistivities of coke bed from pilot study, dry coke bed and material resistivity of Corus coke Eidem (2008). 24
2.2 Electrical resistivity and conductivity of FeMn ore in different temperature zones Dhainaut (2004). 24
2.3 Electrical resistivity and conductivity of the materials included in a FeMn furnace provided in Herland et al. (2018). 25
3.1 Electromagnetism notation and units. 31
4.1 Geometric parameters of the 3D FeMn furnace model. 55
4.2 Material properties of the FeMn furnace and skin depth at 50Hz. . . . 56
4.3 Geometric parameters for the model with flat coke beds. 59
4.4 Material parameters for the simple furnace geometry 59
4.5 Non-dimensional numbers based on parameters given in Table 4.3 and Table 4.4. W: Width, H: Height. 62
4.6 Simulation cases comparing AC versus DC models. 68
4.7 Dissipated power (2D) [MW/m], for both AC and DC current sources, in the different parts of the furnace for Cases 1-4. 71
4.8 3D model. Active power P in each material region. 75
4.9 2D model. Active power P in each material region. 76
4.10 Horizontal currents through material layers. 76
4.11 Cases considered in the 2D (from 1 to 5) and 3D (from 6 to 11) simulations. The reference case for the 3D simulations is number 6. . 83
4.12 Power in MW/m in the steel shell, carbon lining, electrodes and in total for a 2D model with twelve gaps of varying widths in the steel shell, with and without carbon lining. 84
4.13 Total heat loss density (in MW) in steel shell (surface), carbon lining, electrodes and interior for the 3D simulations. 90
5.1 Parameters of 1D model example with $N = 5$ and $f = 50$Hz. 111
5.2 1D model example with $N = 5$. Dissipated power. 111
5.3 Comparison of power ratios as a function of δ_1/T in the two-layer example. 115
5.4 Difference between the full and approximate solutions in material 1 for different values of σ_1 and σ_2 119
5.5 Material properties (from Herland et al. (2019)) and layer thickness for the furnace casing model; the skin depth is computed for $f = 50$ Hz. 131

USC UNIVERSIDADE DE SANTIAGO DE COMPOSTELA

USC
UNIVERSIDADE
DE SANTIAGO
DE COMPOSTELA

Preface

This PhD project has been developed within the framework of the competence knowledge building project *Electrical Conditions and their Process Interactions in High Temperature Metallurgical Reactors* (ElMet), developed for the period 2015-2020. Funded with 1.3 M€ from the Research Council of Norway, the project was led by the Modelling & Simulation research group in Teknova AS (Kristiansand/Grimstad, Norway). In 2018, Teknova merged with other institutes into NORCE Norwegian Research Centre AS. NORCE is an independent research institute headquartered in Bergen with a strong collaborative relationship with Norwegian industry. ElMet involved close collaboration between both academic and industrial partners. From the academic part, the University of Santiago de Compostela through the Technological Institute for Industrial Mathematics (now integrated in CITMAga), the University of Oxford and the Norwegian University of Science and Technology (NTNU); as industrial agents, the companies Elkem AS and Eramet Norway AS, which provided the 20% of the funding.

The main objective of the ElMet project was to better understand the electrical conditions and electromagnetic behaviour of large three-phase submerged arc furnaces (SAFs) for the production of ferroalloys. The first contact with the problem took place during the *122nd European Study Group with Industry*, held in Santiago de Compostela in 2016, when some of the challenges were presented. Since their inception in Oxford in 1968, these Study Groups have provided a forum for collaboration between industrial scientists and academic mathematicians on real-world problems of direct industrial relevance, and have gained international recognition for successfully facilitating technology and knowledge transfer between academia and industry. In the same spirit, the ElMet project has combined expertise in mathematical modelling and metallurgy with industrial experience and process knowledge to develop mathematical models and numerical simulations for SAFs, including some material data and model verification studies. The project focused on physics-based models, ranging from simple models to understand basic phenomena to finite element based numerical models for more realistic case studies. The research presented in this thesis is embedded in this specific context.

This thesis has been recognised by the International Doctoral School of the University of Santiago de Compostela (EDIUS) with the mention of *Industrial Doctorate*, an honorary mention awarded for original work that responds to an industrial problem or deals with innovative projects related to industry.

USC UNIVERSIDADE DE SANTIAGO DE COMPOSTELA

USC
UNIVERSIDADE
DE SANTIAGO
DE COMPOSTELA

Introduction

Submerged Arc Furnaces (SAF) are large-scale electric arc furnaces used primarily in the production of ferromanganese (FeMn) and other ferroalloys, as well as other materials. In the production of FeMn, manganese (Mn) ores are converted into Mn alloy by a chemical reduction process. This reduction requires large amounts of energy (heat) at high temperatures, which is supplied by ohmic heating using large electric currents. The currents supplied are of the order of 100 kiloamperes (kA) and the energy consumption of a single industrial furnace typically exceeds 40 megawatts (MW) Olsen et al. (2007).

This high energy consumption contributes to the overall production costs. The production method dates back more than a century. However, there are still many unknowns in this complex process. It is important to accurately describe and understand the operating conditions in order to optimize an energy-intensive process. Given the high current and power requirements, it is clear that even a small improvement can have a significant impact on the production costs. Better control of the process can also lead to better utilization of raw materials and a reduction in unwanted emissions, thus minimizing the environmental impact Kero et al. (2019).

Motivation, objectives and methodology

The temperature of the internal parts of the furnace is very high, making accurate measurements and direct observation of furnace conditions very difficult or impossible. Physics-based mathematical modelling and numerical simulation offer an alternative way of gaining indirect knowledge of the process. Both are fundamental tools for predicting the furnace behaviour, the evaluation of its performance and the optimisation of its design and operating parameters.

Although the complexity of the process often requires the development of simplified models, even in these cases the industry can benefit significantly from the use of mathematical tools. This approach eliminates the need for unnecessary prototyping, resulting in cost savings in the design, construction and operation phases. As a part of the Elmet project, this is one of the aims of this thesis.

Previous efforts found in literature to model the multiphysics behaviour of electrical furnaces cover aspects of heat transfer, electromagnetics, chemical reactions and

USC UNIVERSIDADE DE SANTIAGO DE COMPOSTELA

fluid dynamics. However, an identified gap is the accurate understanding of the effects of three-phase alternating current, including how the associated power distribution governs the chemical reactions and temperature distribution. An efficient method for computing three-phase current paths and power distribution is required.

The main objective of this thesis is to close this knowledge gap improving the understanding of the nature of three-phase AC and its inductive effects in the FeMn furnaces. Although the ferromanganese production process involves a variety of physical phenomena, the thesis focuses on the study of electromagnetic models. Several three-dimensional and two-dimensional mathematical models derived from Maxwell's equations have been considered. These models have been solved numerically using the Finite Element Method (FEM) through the commercial software package COMSOL Multiphysics®, and in particular the AC/DC module AC/DC Module User's Guide (2022). The models have been developed based on SAFs for the production of FeMn, but can also be applied to SAFs used in the production of other materials. The material properties used in the models have been collected from the published literature and are mainly based on the data presented in Herland et al. (2019) (and references therein). This work, also published as part of the ElMet project, provides data considered appropriate by the industrial partners in the project.

Apart from numerical simulations, non-dimensional analysis has been used to gain a qualitative understanding of the electromagnetic behaviour. This analysis has also been used to identify which parameters dictate the behaviour of the model and has provided the basis for an analytical one-dimensional model, which represents a simpler tool compared to similar work published previously. The model has been implemented in Python 3 (v.3.8) Van Rossum & Drake (2009) in a general and dynamic way, ensuring fast and easy computation of different cases. The implementation does not require any special libraries other than the standard *numpy* library Harris et al. (2020). Python was also used to generate figures and plots using the *matplotlib* library Hunter (2007), incorporating results from both the analytical model and FEM simulations in COMSOL.

Throughout the project, results have been shared and extensively discussed with the industrial partners. This dynamic interaction has not only generated new ideas, but also raised questions that have been the starting point for some of the research that has been carried out.

The outline of the thesis is as follows. First, Chapter 1 describes the industrial problem that motivated the study. Chapter 2 presents a review of the literature related to the electrical behaviour of three-phase furnaces in order to know the state of the art in this field and to define the main contributions of the thesis to the existing work. Then, Chapter 3 describes the mathematical equations governing the electromagnetic fields in SAFs. Starting from Maxwell's equations, formulations

USC UNIVERSIDADE DE SANTIAGO DE COMPOSTELA

based on scalar and vector potentials are introduced, corresponding to the different options implemented in COMSOL Multiphysics®. The last part of the chapter deals with the dimensionless analysis of the equation governing the electric field distribution in a simple 2D conductor. Subsequently, Chapter 4 presents the numerical results obtained in the simulation of a FeMn furnace using 3D and 2D models and non-dimensional analysis. Several 2D models are used to study specific features in localised parts of the furnace, while a more complicated 3D model allows to analyse its limitations and to perform a more realistic study of the whole furnace. Numerical results complete the non-dimensional analysis carried out to explain the inductive effects between different regions inside the furnace. Furthermore, some additional tools are studied to reduce the computational effort of the 3D numerical simulations. The aim of Chapter 5 is the construction and use of a 1D analytical model. The analytical solutions are used for several purposes: to analyse inductive effects in adjacent conductors, to calculate current distribution through multiple layers, and to compare AC and DC models. In particular, the tool is useful for calculating currents in two parts of FeMn furnaces: the outer part (steel shell and linings) and the region between two electrodes. Lastly, a summary of the main findings of the research, along with reflections and ideas for future work is included.

List of publications

As part of this PhD project, contributions have been made to a number of publications. The following two papers have been published in JCR ranked journals:

- M. Fromreide[*,o], D. Gómez[*,†], S.A. Halvorsen[o], E. Herland[+], P. Salgado[*,†]. (2021). *Reduced 2D/1D mathematical models for analysing inductive effects in submerged arc furnaces*. Applied Mathematical Modelling, vol. 98, pp. 59-70. ISSN: 0307-904X. doi:10.1016/j.apm.2021.04.034

  Journal rankings: Impact Factor (JCR): 5.336 (2021) Quartile (JCR): Q1, 7/108 (Mathematics, Interdisciplinary Applications).

  Author's contribution: Developing of the mathematical model, implementation of numerical simulations and writing of the article.

  Permissions: The article is published as open access under a CC BY-NC-ND 4.0 License. The publisher, Elsevier, grants authors the right to include as part of doctoral dissertations without express authorisation, provided that it is not commercially published (see https://www.elsevier.com/about/policies/copyright).

- M. Fromreide[*,o], D. Gómez[*,†], S.A. Halvorsen[o], E. Herland[+], P. Salgado[*,†]. (2023) *Induced currents in the lining and steel shell of submerged arc furnaces*. Journal of

USC UNIVERSIDADE DE SANTIAGO DE COMPOSTELA

Sustainable Metallurgy. Vol. 9. pp. 375-385. doi:10.1007/s40831-022-00625-6

Journal rankings: Impact Factor (JCR): 3.068 (2023) Quartile (JCR): Q2, 21/79 (Metallurgy & Metallurgical Engineering).

Author's contribution: Developing of the mathematical model, implementation of numerical simulations and writing of the article.

Permissions: The article is published as open access under a CC BY-NC-ND 4.0 License. The publisher, Springer Nature, grants authors the right to include as part of doctoral dissertations without express authorisation, provided that it is not commercially published.

At the time of submitting this thesis, a third paper is in preparation:

- M. Fromreide[*,o], D. Gómez[*,†], S.A. Halvorsen[o], P. Salgado[*,†]. *An analytical 1D model for computing low-frequency electromagnetic fields in conducting layers. Application to metallurgical furnaces*.

  Author's contribution: Developing of the mathematical model, implementation of numerical simulations and writing of the article.

The following publications have been included in peer-reviewed conference proceedings:

- S.A. Halvorsen[o], H.A.H. Olsen[‡] and M. Fromreide[*,o], (2016) *An Efficient Simulation Method for Current and Power distribution in 3-Phase Electrical Smelting Furnaces*. 17th IFAC Symposium on Control, Optimization and Automation in Mining, Mineral and Metal Processing MMM 2016: Vienna, Austria, 31 August—2 September 2016. In: IFAC-PapersOnLine 49.20 (2016), pp. 167–172. 10.1016/j.ifacol.2016.10.115

  Author's contribution: Contributed to parts of the presented mathematical analysis and writing of the paper.

- M. Fromreide[*,o], S.A. Halvorsen[o], M. Sparta[o], V.K. Risinggård[o], P. Salgado[*,†], D. Gómez[*,†] and E.V. Herland[+], (2021) *Effects of Alternating Currents in the Hearth of Submerged Arc Furnaces*. Proceedings of the 16th International Ferro-Alloys Congress (INFACON XVI) 2021, 10.2139/ssrn.3926716

  Author's contribution: Developing of the mathematical model, implementation of numerical simulations and main author of the article.

- S.A. Halvorsen[o], M. Sparta[o], V.K. Risinggård[o] and M. Fromreide[*,o], (2021) *Electrical Conditions in 3-phase Submerged Arc Furnaces: Learning from the ElMet Project*. Proceedings of the 16th International Ferro-Alloys Congress (INFACON XVI) 2021, 10.2139/ssrn.3926712

USC UNIVERSIDADE DE SANTIAGO DE COMPOSTELA

Author's contribution: Contributed to parts of the presented models and numerical results and writing of the paper.

- S.A. Halvorsen[o], M. Fromreide[*,o], M. Sparta[o], V.K. Risinggård[o] (2022). *Mathematical Models for Electromagnetic Conditions in Submerged Arc Furnaces.* In: Ehrhardt, M., Günther, M. (eds) Progress in Industrial Mathematics at ECMI 2021. ECMI 2021. Mathematics in Industry, vol 39. Springer, Cham. 10.1007/978-3-031-11818-0_51

  Author's contribution: Contributed to parts of the presented models and numerical results and writing of the paper.

In addition, during the course of this PhD project, two European Study Groups with Industry (ESGI) were attended, contributing to the resolution of the problems presented by the ElMet project and also contributing to the published group reports:

- Allwright, D., Correia, J.M.C., Fromreide, M.[*,o], Zefreh, M.G., Kavallaris, N., Manoylov, A., Please, C., Rooney, C., Roper, S., Sakradja, P., Sloman, B., Zyskin, M. (2016) *Improved model of an electric calciner for carbon materials*. Report for the Problem presented by Teknova at the 116th European Study Group with Industry, 11st-15th April 2016, Department of Mathematical Sciences, Durham University, Durham, England.
- Fromreide, M.[*,o], Gómez, D.[*,†], Halvorsen, S.A.[o], Herland, E.[+] and Salgado,P.[*,†], *Efficient simulation method for current and power distribution in electrical furnaces*. Report for the Problem presented by Teknova at the 122nd European Study Group with Industry, 19th-23rd September 2016, University of Santiago de Compostela, Santiago de Compostela, Spain.

[*] Department of Applied Mathematics, Universidade de Santiago de Compostela, E-15782 Santiago de Compostela, Spain.
[†] Galician Center for Mathematical Research and Technology (CITMAga) Campus Vida, E-15782, Santiago de Compostela, Spain.
[o] NORCE Norwegian Research Centre AS, Universitetsveien 19, NO-4630 Kristiansand, Norway
[+] Elkem ASA Technology, Fiskåveien 100, NO-4621 Kristiansand, Norway.
[‡] Norwegian University of Science and Technology, NO-7491,Trondheim, Norway.

USC UNIVERSIDADE DE SANTIAGO DE COMPOSTELA

USC
UNIVERSIDADE
DE SANTIAGO
DE COMPOSTELA

Chapter 1

Industrial problem

1.1 Introduction

The production of many metals heavily relies on electric energy to provide the power required for the production process. In particular, the modern production of ferroalloys takes place in large-scale electric smelting furnaces. Electric current is supplied through electrodes into the hearth of the furnace where the chemical reduction of ores takes place. An accurate understanding of the current distribution in the furnace is important for optimization and process control. The operation and control of smelting furnaces are still to a large degree empirically based and many important features of the process are not well understood and are difficult to measure. Mathematical modelling is therefore an important tool not only to improve understanding of the inner workings of furnaces, but also to contribute to the development of more efficient production processes.

Ferroalloys is the general name for iron-alloys with a significant proportion of one or more other elements. These alloys are usually grouped in two categories: bulk or major ferroalloys, which are produced in large quantities, and minor ferroalloys which are produced in smaller quantities FerroAlloys (2013). Examples of major ferroalloys are ferromanganese (FeMn), ferrosilicon (FeSi), silicon-manganese and ferrochrome. The types of minor ferroalloys are much more varied and include, for example, ferronickel (FeNi) and ferrocobalt (FeCo). The work presented in this thesis is mainly focused on the production of FeMn.

The commercial production of ferroalloys dates back to the nineteenth century. The production process took place in large blast furnaces where the burning of coke provided the process energy. The first commercial production of FeMn in an electric furnace began in the 1890s. However, during the first half of the twentieth century, almost all FeMn was produced in blast furnaces. Coke consumption is about 4 times higher in a blast furnace than in an electric arc furnace, which means that the blast furnace is generally a much more expensive method of production. This, of course, depends on the cost of coke relative to the electric energy and the way in which the electric energy is produced Coetsee (2020). Today, the electric furnace is the most

USC UNIVERSIDADE DE SANTIAGO DE COMPOSTELA

widely used, but there are still some blast furnaces in operation Olsen et al. (2007); Madias (2011). Furthermore, the electric furnace is more flexible than the blast furnace as it can produce different grades of Mn alloys with a higher Mn yield.

Depending on the given process, different furnace designs are used. Alternating current (AC) furnaces, with three or more electrodes submerged in a circular or rectangular furnace are most widely used. In circular furnaces, a three phase AC is supplied to each electrode with a 120° phase shift, so that the three currents meet at a star point in the furnace interior. Direct current (DC) is also used in some processes, where the furnaces have one electrode at the top and the casing acts as a second (bottom) electrode. Single-phase AC can also be used in smaller pilot furnaces with one top and one bottom electrode.

1.2 Three-phase furnaces for ferromanganese production

The work presented in this thesis has been carried out as part of an industrial cooperation project with the companies Elkem AS and Eramet Norway AS. Both partners operate multiple plants in Norway producing silicon and manganese alloys, respectively. The thesis focuses mainly on models of large three-phase circular furnaces for the production of FeMn.

The FeMn furnace consists of three electrodes arranged in an equilateral triangle configuration and submerged in the charge within a cylindrical furnace. Figure 1.1 provides an illustration of this furnace set up. The electrodes are of Søderberg type and are continuously consumed and renewed during the process. They are made from a carbon paste (consisting of carbon particles mixed with a tar-pitch binder), which is baked by the heat generated by the electrode currents. The electrode paste is loaded from the top as a solid material, it then melts before being baked, to form a highly conducting solid material.

Each electrode is surrounded by a steel casing containing steel fins that partially penetrate the electrode. These fins serve several purposes, including improving electrical conduction in the baking zone and ensuring strong mechanical contact between the casing and the baked electrode.

The steel casing and fins are partially melted below the baking zone and end up as part of the iron in the ferroalloy. Electric power is supplied to the FeMn furnace through contact clamps located on the outer surface of the steel cylinder. Figure 1.2 shows a sketch of a Søderberg electrode, providing a detailed view of the various material zones and structural elements involved.

The charge materials are surrounded by a lining and a steel shell. The lining is subject to thermal, chemical and mechanical wear. The inner lining of FeMn furnaces

USC UNIVERSIDADE DE SANTIAGO DE COMPOSTELA

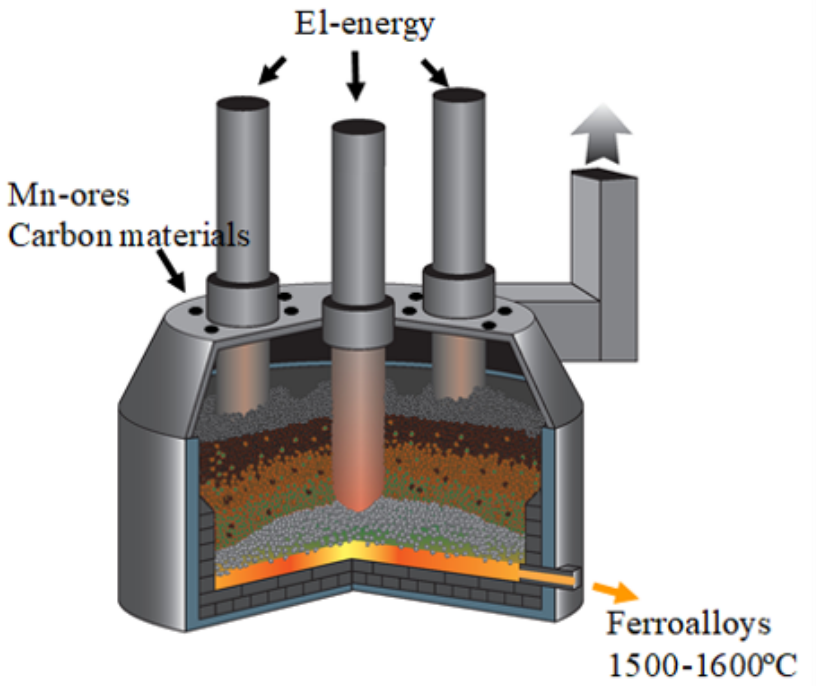

Figure 1.1. Illustration of a submerged arc furnace for FeMn production. Reproduced with permission of M. Tangstad.

consists of carbon/graphite and is used both in the bottom and along the sides to a level above the normal slag level. Between the carbon lining and the steel shell, a ceramic brickwork is used for the entire steel shell surface. A sketch of the geometry of a circular three phase furnace is shown in Figure 1.3.

1.2.1 Production process of ferromanganese

FeMn is produced by the carbothermic reduction of manganese ores. The primary manganese compound in these ores is typically MnO_2, although other reduced forms such as MnO, Mn_2O_3 and Mn_3O_4 may be present. MnO_2 is reduced to liquid manganese in four consecutive steps, each requiring increasing temperatures. Figure 1.4 provides a summary of the process. The diagram illustrates three main temperature zones where different reactions take place: the preheating zone (low temperature), the pre-reduction zone (medium temperature) and the reduction zone (high temperature, corresponding to the coke bed). Slag is formed in the coke bed and the final reduction (melting) of MnO to Mn occurs at temperatures of around 1250°C. The heat required for the process is generated by ohmic heating.

In addition to the manganese ores, other materials are required for the process.

USC UNIVERSIDADE DE SANTIAGO DE COMPOSTELA

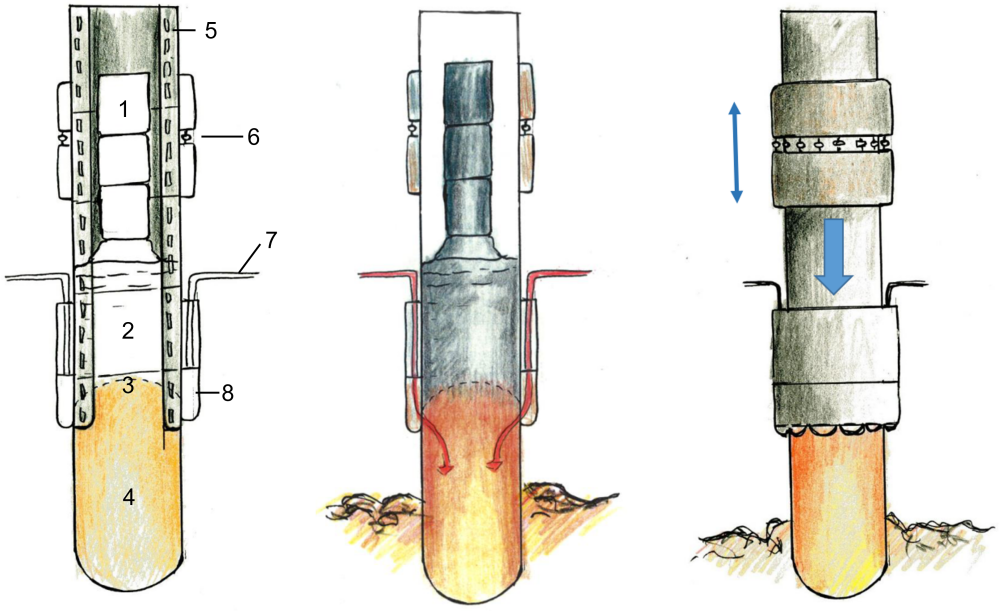

Figure 1.2. The structure of a Søderberg electrode. 1. Carbon paste cylinders 2. Liquid carbon paste 3. Baking zone 4. Solid/baked electrode 5. Steel fins 6. Hydraulic cylinders for slipping 7. Current supply 8. Contact clamps. The red arrows indicate current flow, the blue arrows indicate the slipping mechanism. The figure has been adapted from Hannesson (2016).

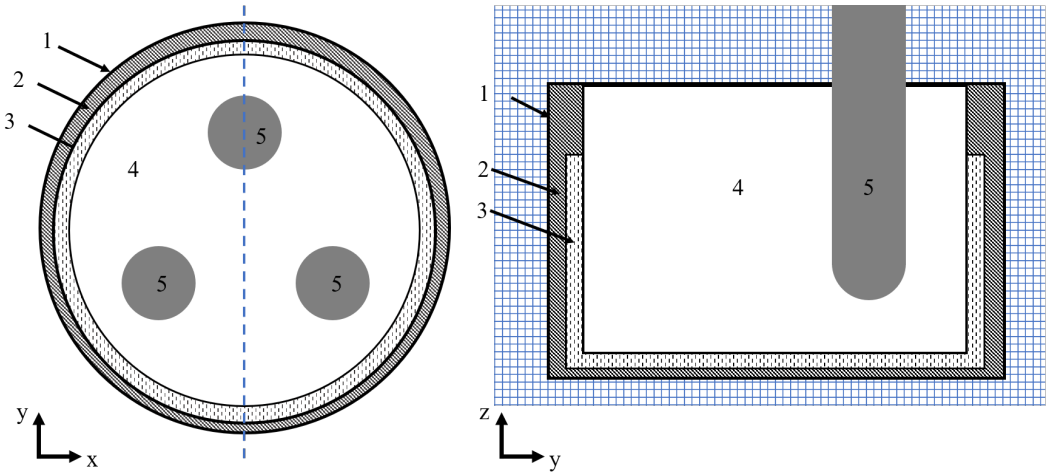

Figure 1.3. Schematic representation of three phase furnace geometry with typical furnace features indicated: 1. Steel shell/casing 2. Ceramic lining 3. Carbon lining 4. Charge material 5. Electrode(s). Left: view from top (xy-plane). Right: yz-plane as indicated in left plot.

USC UNIVERSIDADE DE SANTIAGO DE COMPOSTELA

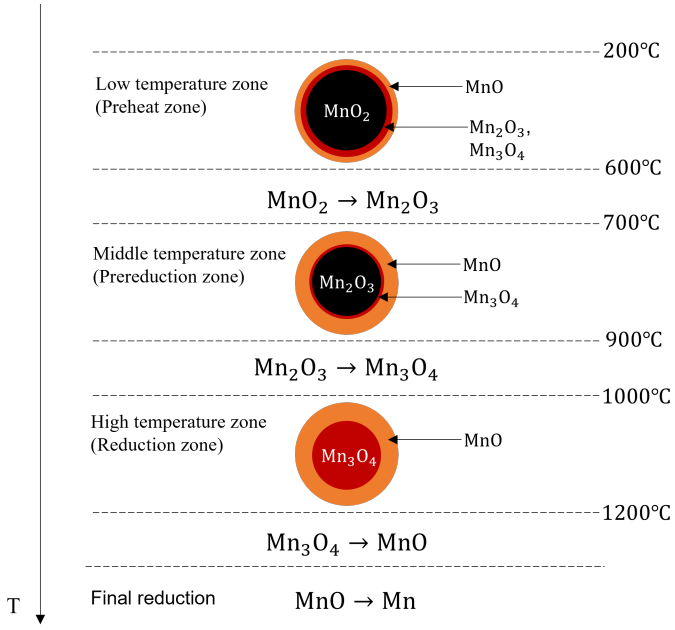

Figure 1.4. Schematic representation of the reduction steps of Mn in terms of temperature regions. Based on Figure 7.4 in Olsen et al. (2007).

Coke is added as the main source of carbon, acting both as a reducing agent and an electrical conductor. Good control of carbon supply and consumption is key to maintaining good furnace operation. Typically, there will be some difference between the supply and consumption of carbon. If the amount of coke particles is insufficient, the furnace is said to be under-coked. Similarly, if too much coke has been added, the furnace is said to be over-coked. Either condition should be corrected to maintain good production efficiency. Other materials called fluxes, such as limestone and dolomite, are added to give the slag desirable chemical and physical properties.

The raw materials are loaded at the top of the furnace and move down into the hearth. In the preheating zone, the materials are heated and dried by the ascending hot CO gas from the higher temperature zones, before moving on to the pre-reduction zone. The first three steps in the reduction of manganese are caused by reaction with the uprising CO through the following reactions Olsen et al. (2007)

$$2\,MnO_2 + CO_{(g)} \longrightarrow Mn_2O_3 + CO_{2(g)}, \quad \text{(I)}$$

$$3\,Mn_2O_3 + CO_{(g)} \longrightarrow 2\,Mn_3O_4 + CO_{2(g)}, \quad \text{(II)}$$

$$Mn_3O_4 + CO_{(g)} \longrightarrow 3\,MnO + CO_{2(g)}. \quad \text{(III)}$$

The material then enters the high temperature reduction zone, which is a coke-enriched region surrounding the electrode tips. This region is called the coke bed

USC UNIVERSIDADE DE SANTIAGO DE COMPOSTELA

and is an important characteristic of the FeMn furnace. In the coke bed, the ores and fluxes are melted, resulting in the formation of slag, and the final reduction steps take place. During the final reduction, MnO reacts with the solid coke particles in the coke bed according to the reaction

$$\mathrm{MnO} + \mathrm{C_{(s)}} \longrightarrow \mathrm{Mn} + \mathrm{CO_{(g)}}. \tag{IV}$$

The CO gas required for the reduction steps is produced by the Boudouard reaction

$$\mathrm{CO_{2(g)}} + \mathrm{C_{(s)}} \longleftrightarrow 2\,\mathrm{CO_{(g)}}, \tag{V}$$

which converts the CO_2 from the reduction process and the added coke particles into CO gas. The Boudouard reaction V is important in the pre-reduction zone, to maintain the CO-level

The FeMn production process operates continuously and the lifespan of the furnaces is generally between 10 and 12 years. Raw materials are introduced either in batches or continuously from the top of the furnace, while slag and alloy are tapped approximately every two hours. The furnaces are equipped with the necessary installations to minimize the emission of hazardous gases, greenhouse gases and airborne particulate matter, thereby reducing their environmental impact. Kero et al. (2019)

The process control of the FeMn furnace can be divided into four main areas each focusing on specific aspects of optimization and management: metallurgical control, furnace power control, electrode position control and electrode slipping control. These activities are briefly described in the sequel.

Metallurgical control involves the monitoring and modification of raw materials. The alloys and other materials may have different compositions and impurities. Figure 1.4 shows the different steps in the reduction of manganese ores. However, several other chemical reactions take place in the furnace. These reactions are also important for the operation of the furnace as they affect the energy balance. Figure 1.5 shows the main chemical reactions and mass flows that contribute to the energy balance of the FeMn furnace. Exothermic reactions (in red) will reduce the electrical power consumption of the furnace, while endothermic reactions (in black) will increase it. Effective metallurgical control ensures the desired chemical composition, proper slag formation and management, and efficient monitoring of the reduction reactions, all of which are vital for achieving optimal metallurgical results.

The aim of the furnace power control system is to provide an optimum load (power) to maximize production. The electric current supplied to the production plant is generally small but of high voltage. The internal resistance of the furnace is relatively low, so a high intensity current is required to achieve the required process power. Transformers enable the conversion from low to high intensity current and typically consist of two magnetically coupled coils. These coils have varying

USC UNIVERSIDADE DE SANTIAGO DE COMPOSTELA

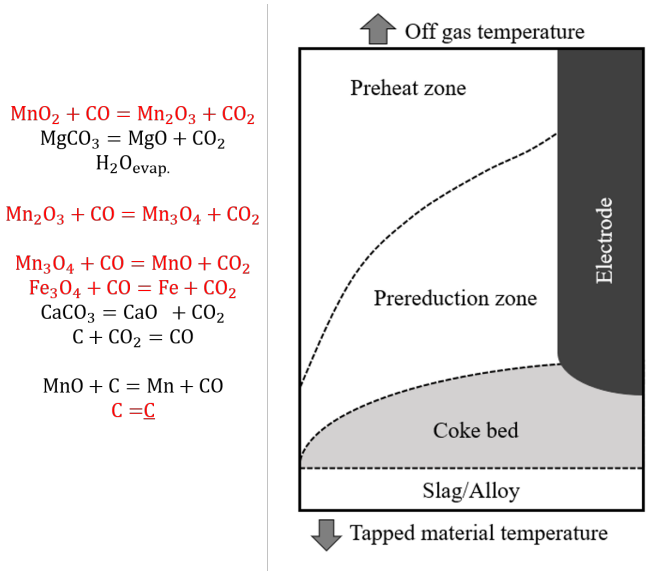

Figure 1.5. Schematic representation of zones in the FeMn furnace. The most important chemical reactions are given (red: exothermic, black: endothermic). Based on Figure 7.25 in Olsen et al. (2007).

numbers of turns, allowing the voltage/current transition. By adjusting the number of turns in the transformer coils, the desired set point load can be modified. As a measure of effective furnace operation, Westly's C3 formula Westly (1974), which correlates furnace power with electrode current, is often used as a reference. The formula has been validated using empirical data from furnaces of various sizes and power outputs. However, there are a number of practical limitations that must be considered in the electrical control of a furnace Olsen et al. (2007).

Electrode position control consists of fixing the position of the electrode tip, as each of the three electrodes of the three-phase furnace can be moved vertically. The current will flow mainly vertically through the coke bed and horizontally through the alloy between the electrodes. The coke bed beneath the electrodes is much less conductive than both the electrodes and the liquid alloy. Therefore, the electrical resistance of the coke bed will determine the total resistance of the furnace. This also means that the distance between the electrode tip and the alloy will directly control the electrical resistance of the furnace. The control system is based on measuring either the resistance or the electrode current and calculating the deviation from a given set point. Adjusting the position of one electrode will only affect the resistance under that particular electrode, while the resistance under the other two will remain constant. This is not the case with current control as the currents through the electrodes are coupled. Current control may be adequate for small furnaces, while resistance control is generally preferred for larger furnaces. The resistance control method relies on knowing the electrode voltage, which is difficult to measure as the zero point is inside the furnace. The standard method of voltage measurement

USC UNIVERSIDADE DE SANTIAGO DE COMPOSTELA

was developed by Bøchmann in the 1960s Bøckmann (1971) and is still widely used today, although some alternatives based on mathematical models have been developed more recently Mintek (n.d.). The electrode current method is simple from a measurement point of view. However, a disadvantage of this method is that the current in each of the electrodes is coupled, which means that when one electrode is changed, there is feedback from the other two. This results in more electrode movement and a longer time before stable operation is achieved.

As mentioned in the previous section, the electrodes are continuously baked by adding carbon paste to the top. The electrodes are consumed by the high temperatures in the furnace hearth. Therefore, in order to keep the electrode tip(s) in a favourable position, the electrodes must be slipped downwards. The rate at which the electrodes are slipped is an important process parameter that is subject to several constraints. For example, the rate at which the electrode is baked must be taken into account in order to obtain optimum electrode properties and to avoid cracking and breakage of the electrodes Olsen et al. (2007).

The mathematical models in this thesis are devoted to study the electromagnetic fields and power distribution within submerged arc furnaces. The models include different materials with given bulk properties, which are assumed to be known. Thus, from a metallurgical control point of view, the materials and settings remain constant and given for each model case. The studies include the demonstration of the control of the electrode position and its effect on the total energy consumption of the furnace. The work does not include dynamic considerations of material flow, variations in applied electric energy, slipping of electrodes or tapping of liquid alloy.

1.2.2 Furnace operation in the production of other ferroalloys

As mentioned before, this thesis focuses on submerged arc furnaces used in the production of FeMn. However, due to the broad applicability of the models considered, the findings and insights gained can be extended to three-phase furnaces employed for various other purposes. Submerged arc furnaces have applications in the production of steel, calcium carbide as well as other ferroalloys and silicon Lupi (2017). With this in mind, this section provides a brief overview of the characteristics of different ferroalloys, highlighting potential variations in furnace operation.

Ferrosilicon

The main difference between the high silicon FeSi ($> 75\%$ Si) process and the FeMn process is the coke bed zone. In the FeSi process there is a cavity below the electrode tip where an arc exists FerroAlloys (2013). The furnace is cylindrical and has three electrodes operating on three-phase AC, similar to FeMn furnaces. The charge

USC UNIVERSIDADE DE SANTIAGO DE COMPOSTELA

material in the upper part of the furnace has a low conductivity and the current will flow to a small extent directly between the electrodes in the upper part. Around the electrode tip, a crust of solid carbide material will form over the cavity below and the current can flow through the sides. The major part of the current will flow directly to the alloy through electric arcs consisting of thermal plasma with temperatures in the range of 10000 K to 25000 K. The reduction reactions for silicon require a temperature of >1900 °C, which is 50 % higher than for Mn reduction. The energy required for this reaction is mainly supplied by the electric arc FerroAlloys (2013); Tesfahunegn et al. (2020), which is the main difference to the FeMn furnaces.

Siliconmanganese

Mn and Si alloys can also be produced by a single process in which both ores are added to the process. The furnaces used commercially are similar to those used to produce FeMn only, but the energy required is greater as the reduction of silicon requires a higher temperature FerroAlloys (2013); Sparta, Risinggård, et al. (2021).

Ferrochrome

Similar to FeMn production, FeCr is produced by carbothermic reduction in SAFs. These furnaces are also characterized by a coke-enriched region (coke bed) under the electrodes, consisting mainly of solid coke particles and a liquid slag mixture of coke, molten chromium ore, fluxes and liquid FeCr alloy FerroAlloys (2013); Rauf Hurman (2014).

Ferronickel

FeNi is commercially produced in large cylindrical or rectangular furnaces with three or six electrodes, respectively FerroAlloys (2013). The reduction process begins with calcined nickel oxide. The electrode tips are immersed in a liquid slag. The electrical conductivity of the slag is low (0.5-3 S/m) FerroAlloys (2013); Sheng et al. (1998); K. T. Karalis et al. (2016) and a lot of power is lost through ohmic resistance. In addition, there can be small arcs under the electrode resulting in CO generated on the surface of the electrodes.

USC UNIVERSIDADE DE SANTIAGO DE COMPOSTELA

USC
UNIVERSIDADE
DE SANTIAGO
DE COMPOSTELA

Chapter 2

State of the art in the modelling of submerged arc furnaces

This chapter presents a review of the literature relevant to the electrical behaviour of three-phase furnaces. The references are grouped according to the objective of the models. Thus, Section 2.1 includes those devoted to the study of the complete furnace, while Section 2.2 focuses on the electrodes and surrounding parts. The publications considered most relevant to this thesis are presented with some additional details. Section 2.3 contains the references related to the experimental results and material data used in the models studied in the thesis. Finally, Section 2.4 summarises the main contributions of this thesis to the existing literature.

2.1 Modelling of the whole furnace

The behaviour of submerged arc furnaces is very complex and their accurate modelling would require a multiphysics approach involving heat transfer, fluid dynamics, chemical reactions, electromagnetic and structural problems. Most of these processes often require strong coupling and the tasks of modelling and numerical simulation can be very complicated. Thus, although there are efforts in the literature to develop multiphysics models, some of the problems are too complex to be treated separately. This is the case for the electromagnetic problem. Understanding the current distribution and power dissipation within the various components of the furnace is essential for optimising its operation. However, direct measurements inside the furnace are extremely limited. Therefore, numerical simulation tools offer a valuable alternative that can help to better understand the inductive effects in the furnace hearth and introduce innovative solutions from the point of view of operation, design or material properties.

The electromagnetic model can be derived from Maxwell's equations and is introduced in detail in Chapter 3.6. Since the electrical source is alternating, the so-called *eddy current model* or *quasi-static approximation* will be suitable for calculating

USC
UNIVERSIDADE DE SANTIAGO DE COMPOSTELA

the electromagnetic fields in this type of furnace. However, different approaches can be found in the literature, which differ in the way they treat the time-dependent terms present in Maxwell's equations: time-dependent eddy current models, time-harmonic eddy current approximations and steady-state models. The first two are referred to as AC models, while the latter is known as a DC model. The literature review presented below will be divided into these two groups.

2.1.1 DC Models

The DC approximation consists of including static sources in the problem and calculating static electric fields that are effectively decoupled from the magnetic fields (see Section 3.6). This model has been used to study AC furnaces because its computational cost and complexity in dealing with FEM methods is greatly reduced compared to an eddy current model; these features have been exploited particularly in multiphysics studies. However, the DC model neglects inductive effects. The main references based on DC models for submerged electric furnaces are summarised below.

The references Dilawari & Szekely (1977, 1978); Choudhary & Szekely (1980) use DC models to simulate the electroslag remelting process for steel remelting and refining. The same approach is applied in a 3D model of a six-electrode SAF for smelting nickel calcine in Sheng et al. (1998).

A 3D model for the study of a circular three-phase SAF representing a simple version of a FeMn furnace can be found in Dhainaut (2004). The model includes the different temperature regions of a FeMn process; each region is represented by a cylindrical disc of uniform conductivity. The study also includes calculations of the amount of current through each region at different electrode set points. In particular, it is shown that if the electrode set point is too high, the current between the electrodes is short-circuited, which is an undesirable effect.

On the other hand, in Tesfahunegn, Magnusson, et al. (2018b) the authors apply a 3D DC model to study the electrical current distribution in a FeSi furnace. The model includes the possible current paths from the electrode tip to the alloy, through a main (vertical) arc, side arcs and the solid crater wall. Different simulations are presented with and without the main arc, varying the number of side arcs and also the charge conductivity.

As mentioned earlier, the DC approximation is particularly advantageous in multiphysics simulations, not only because of the computational cost, but also due to the different time-scales involved in different problems. In this context, Darmana et al. (2012) used a DC approximation in the study of a transient multiphysics model of a three-phase submerged arc furnace for FeSi production. The model is applied to a one-electrode pilot furnace considered in an axisymmetric setting and to a full

USC UNIVERSIDADE DE SANTIAGO DE COMPOSTELA

3D three-electrode furnace. This work addresses the ability to model the complex system of a large melting furnace where the different sub-processes require widely varying time scales. The input data for reaction kinetics and changing material properties are addressed as a key challenge for an accurate model. Also in the field of multiphysics modelling, we can cite the work of K. T. Karalis et al. (2016); K. Karalis et al. (2017), which deals with a 2D multiphysics model of a FeNi furnace. In particular, the authors attempt to couple fluid flow, electromagnetic phenomena, melting and discrete phase phenomena, such as the interaction of CO bubbles with the bath, as a rational step towards a pragmatic description. The work is extended to a 3D furnace model in K. T. Karalis et al. (2021). More recent works dealing with the DC approximation in multiphysics modelling of three-phase AC furnaces are Cui et al. (2023) and Bezuidenhout et al. (2009) to study furnaces for titanium slag production and Platinum Group Metal (PGM) smelting, respectively.

Finally, some authors have attempted to modify the true DC model to approximate in some way the characteristics of three-phase furnaces. For example, in Halvorsen et al. (2016) the authors have proposed a technique based on combining the solution of three DC models to obtain a complex potential that takes into account a phase shift between the electrodes. Furthermore, in the case of a fully symmetric furnace, the solution can be found by solving only a DC problem for half of the furnace. The full solution is then obtained by mirror symmetry, rotation and time shifts. This procedure gives a more accurate estimate of the AC problem, but without considering induction effects.

2.1.2 AC Models

With advances in technology and increasing computing power, numerical finite element software can solve transient eddy current models efficiently and accurately, even on conventional workstations. However, simulations are usually performed using time-harmonic approximations because the computations are still complex and time-consuming, and the time scale of the AC current is much smaller than the furnace operating cycle. Therefore, most of the references cited below are time-harmonic and only a limited number of transient proposals are found in the context of submerged furnaces.

In McDougall (2007), a 3D eddy current model is solved in two types of furnaces: a rectangular six-electrode SAF for copper-nickel smelting and a circular three-electrode SAF for FeCr production. Similar to the geometry defined in Dhainaut (2004), the different temperature regions are modelled as horizontal layers characterised by constant electrical conductivities.

The inductive effects within large three-phase SAFs are studied in Herland et al. (2018). The focus of this work is on the skin and proximity effect of the electrodes as well as the other regions of the furnace. In particular, as a novelty with respect

USC UNIVERSIDADE DE SANTIAGO DE COMPOSTELA

to previous studies, the furnace lining and the steel casing are included in the analysis. Both a FeMn and a FeSi furnace are modelled with realistic geometries and material regions. The coke bed zones are modelled as half-ellipsoids. The internal geometry of the FeMn furnace model is based on that of Dhainaut (2004) and Eidem (2008). The arc present in the cavity under the electrode tip in the FeSi furnace is simplified and represented by a uniform material with fixed electrical conductivity. The inclusion of the steel shell allows the authors to conclude that large currents are induced in the steel casing and lid. It is also shown how the current distribution inside the furnace is modified by induction and the presence of the casing. The FeMn furnace model in Herland et al. (2018) has been adapted and further developed in Sparta, Stråbø, et al. (2021); Sparta, Varagnolo, et al. (2021); in these recent publications a *metamodel* is built based on the FEM simulation. The idea of the work is to develop a computationally low cost tool to study the electromagnetic conditions of the furnace. The metamodel is a statistical model based on a large number of computationally intensive FEM simulations. It has been further adapted to a FeSi furnace model and implemented as a web-based tool Sparta et al. (2022).

It is important to highlight a series of publications Tesfahunegn, Saevarsdottir, et al. (2018); Tesfahunegn, Magnusson, et al. (2018c,a); Tesfahunegn et al. (2019, 2020) which also calculate the induced currents and power distributions inside submerged arc furnaces. In Tesfahunegn, Saevarsdottir, et al. (2018); Tesfahunegn, Magnusson, et al. (2018c,a), the geometry is very simple, with three conducting electrodes surrounded by a dielectric; the problem is solved in the time domain and the results focus on demonstrating the skin and proximity effect of the electrodes. In Tesfahunegn et al. (2019) and Tesfahunegn et al. (2020) a FeSi furnace is studied using a time-harmonic eddy current model. The focus of Tesfahunegn et al. (2019) is on the current distribution through the main arcs, side arcs and crater walls between the electrode tip and the alloy. Various simulations are carried out, varying the number of side arcs, the charge conductivity and whether or not a main arc is present. The test cases studied are analogous to those presented in Tesfahunegn, Magnusson, et al. (2018b), where a DC model was applied. The same simulations form the basis of the work presented in Tesfahunegn et al. (2020), where a comparison is made between AC and DC models. The analysis is carried out in terms of the current and power distributions within the furnace and the total furnace resistance. In particular, the net current and dissipated power in each material are compared.

With regard to the solution of eddy current problems in multiphysics approaches, the following works have been found: Zhaozhao et al. (2022) presents a 3D coupling model that integrates electromagnetic, heat transfer and flow fields to investigate the effect of introducing a steel rod between the electrodes on electrode material consumption; Yu, Li, Qi, et al. (2021) and Yu, Li, Yun, et al. (2021) deal with 3D models for SiMn and a FeCr production respectively, where the reduction reactions and associated magneto-hydrodynamic flow are considered. The computational domain excludes the electrodes and focuses solely on the inner furnace region.

USC UNIVERSIDADE DE SANTIAGO DE COMPOSTELA

2.2 Models focused on electrodes, proximity effect and surroundings

The electrodes play an important role in the operation of the furnace. In fact, as the electrodes are consumed in the hearth and continuously replaced by baking new electrode material/paste, electrode maintenance is an important and complex process in itself Glastonbury, R. I. and Beukes, J. P. and van Zyl, P. G. and Tangstad, M. and Ringdalen, E. and Dall, D. and Steenkamp, J. D. and Mushwana, M. (2021). When operating the electrodes, the most critical part is to control the baking zone and ensure that the electrode does not break. Several studies have been devoted to investigating the temperature distributions and mechanical properties of the electrode. Both through numerical studies Meyjes et al. (2010); B. Larsen et al. (2013); Roberts et al. (2017) and analytical models Van Gorder et al. (2021); Kamilova (2021)), as well as through experimental analysis of electrode paste material properties and temperature measurements Beukes et al. (2013); Skjeldestad et al. (2015); Skjeldestad (2019); White et al. (2020).

The distribution of electric current in the furnace is largely determined by what happens at the electrodes. The high intensity vertical currents give rise to large eddy currents and therefore alter the distribution of electric energy in different parts of the furnace. There are many papers in the literature that study the current distribution within the electrodes. Some publications focus on modelling a single electrode (neglecting the proximity effect), while others consider the three electrodes to capture the skin and proximity effects. A multiphysics approach is required to calculate temperatures, stresses and current distributions in the electrodes, which are usually treated with thermo-electromagnetic-mechanical models or with the thermo-electromagnetic models that are strongly non-linear; see for example Bermúdez et al. (2005); Bermúdez et al. (1998) and references therein. In particular, the thermo-electromagnetic model has been extensively studied to deal in detail with the baking of the paste and the slipping of the electrodes Bermúdez et al. (2003).

Single electrode models typically exploit cylindrical symmetry and consider a 2D axisymmetric approximation; see for example Bermúdez et al. (1998, 2003); Gunnewiek et al. (2004). Full 3D models have also been considered to simulate only one electrode, for example in McDougall et al. (2004); Bermúdez et al. (2005); Meyjes et al. (2010). All of these models are typically used to add more detail to the simulation, especially in the contact clamp area: to account for fins in Søderberg electrodes, to model the baking of paste in a critical zone, to account for cooling and power supply in the contact clamp, etc.

As mentioned above, single electrode models do not take into account the proximity effect between adjacent electrodes. Many publications have been devoted to the study of this effect. Some early works Dunski (1962); Böchmann & Olsen (1968);

USC UNIVERSIDADE DE SANTIAGO DE COMPOSTELA

Hot et al. (1980) have considered analytical solutions of a 2D approach modelling a horizontal cross section through the furnace. The model includes three electrodes arranged in an equilateral triangle, where the current has a phase difference of $2\pi/3$ radians. Several numerical simulations in both 2D and 3D have also been published. Examples of 2D simulations are Bullón et al. (1998); Bermúdez et al. (1999); H. L. Larsen (2006); Innvær et al. (1987). In 3D, some of the already cited works, McDougall (2007); Herland et al. (2018); Tesfahunegn, Saevarsdottir, et al. (2018); Tesfahunegn, Magnusson, et al. (2018c,a); Tesfahunegn et al. (2019, 2020), focus on the skin and the proximity effect of the electrodes.

On the other hand, the work by Herland et al. (2019) focuses on the skin effect and the proximity effect between the electrodes and between the electrodes and the steel shell. The authors consider both analytical and numerical 2D models, which are validated with full 3D models. The analysis shows that the inductive effects inside the furnace depend on some non-dimensional quantities. Firstly, the skin effect is controlled by the ratio of the electrode radius R and the skin depth δ of the material, R/δ. For large SAFs, where $R \gg \delta$, the skin effect is significant. The electrode-to-electrode proximity effect also depends on the ratio of electrode radius to electrode separation, R/d. The proximity effect increases with this value. Large currents can be induced in the highly conductive steel shell surrounding the furnace. The ability to induce currents is determined by the ratio of steel thickness to skin depth, t_{sh}/δ_{sh}. This number is highly dependent on the quality of the steel and whether it is magnetic or not. The strength of the induced currents is governed by the distance of the electrodes from the shell, described by the ratio of the 'electrode pitch circle radius' to the furnace radius, $d/(\sqrt{3}R_F)$. An important contribution of this work is the demonstration of the electrode-shell proximity effect, which competes with the previously known electrode-electrode proximity effect Herland et al. (2019).

Finally, induced steel shell currents have been studied analytically, both for submerged arc furnaces Ryff (1981) and for the equivalent and more general case of a 2D cross-section of a three-phase cable with a surrounding coating Emanuel & Doepken (1974); Kawasaki et al. (1981).

2.3 Experimental results and model data

As mentioned above, mathematical models and numerical simulations are essential for understanding furnace behaviour. However, validation of these models requires experimental results, which are often difficult or impractical to obtain directly. In recent years, the availability of data from various excavations of industrial furnaces has greatly increased the knowledge of the properties of the reacted and unreacted charge as a function of its location, allowing the accuracy and reliability of numerical simulations to be improved and made more realistic.

USC UNIVERSIDADE DE SANTIAGO DE COMPOSTELA

This section presents experimental results, SAF excavations and other publications that provide the material data used in this thesis. Knowledge of the furnace interior and its various material regions can be obtained through furnace *dig-outs*, which can be carried out when a SAF is closed down, typically after more than ten years of operation. In particular, the structure of the coke bed area is of great importance as this is the main reaction zone of the furnace.

The results of an excavation conducted on a large 75 Mega Volt Amps (MVA) FeMn furnace are detailed in Barcza et al. (1979). In addition, Yoneka et al. (1980) reports the results of the excavation of a smaller 4 MVA triangular FeMn pilot furnace which had been in operation for one year.

Several excavations of SiMn furnaces have also been carried out. Olsen & Tangstad (2004) describes the excavation of a 16 MVA SiMn furnace which revealed a wide and flat coke bed. In Davidsen (2010) the results of the excavation of a 30 MVA are shown. In this furnace the coke bed was found to be higher immediately below the electrodes. The same feature was seen in Ringdalen & Ksiazek (2018), where the coke bed was reported to be low or non-existent between the electrodes. In the excavation presented in Steenkamp et al. (2018), the coke bed was found to be more conical below and around the electrodes, with a connected flat layer at the bottom.

In Ringdalen & Eilertsen (2001) the results of the excavation of a 54 MVA FeCr furnace are presented. The coke beds were found to be cylindrical with a diameter equal to the electrode diameter.

The results of the excavations show that the coke bed consists of regions of different material composition. Typically, there is a region of 'dry coke' at the top and a region of coke mixed with slag ('wet coke') at the bottom. The results also show how the shape of the coke bed varies from small cylindrical coke beds to wider bell-shaped coke beds, and even flat coke beds that span the entire width of the furnace.

Due to the different material composition, the electrical conductivity of the coke bed will vary from region to region. In this thesis, the models will consider the coke bed as a uniform material where the conductivity is given by the average bulk properties of the material.

The resistivity of coke beds has been extensively studied, both experimentally and by modelling in Eidem et al. (2007, 2008, 2009, 2010) and in Eidem (2008) PhD thesis. It includes measurements of the resistivity of packed dry coke (dry coke bed) and coke beds in a pilot furnace study. A 150kVA single phase AC furnace was used to study both the FeMn and SiMn processes. The FeMn case was run twice with different sizes of coke addition. The current and potential drop across the furnace was recorded during operation. The structure of the coke bed was determined from the excavation and based on this an axisymmetric numerical model was considered. The electrical resistivity of the coke bed was determined from the model using the

USC UNIVERSIDADE DE SANTIAGO DE COMPOSTELA

Table 2.1. Bulk resistivities of coke bed from pilot study, dry coke bed and material resistivity of Corus coke Eidem (2008).

Classification	Resistivity $[\mathrm{m}\Omega \cdot \mathrm{m}]$
Coke bed - pilot, FeMn, Corus 5-10 mm	1.71-2.2
Coke bed - pilot, FeMn, Corus 15-20 mm	0.95-1.62
Coke bed - pilot, SiMn, Corus 5-20 mm	3.5-4.1
Dry coke bed, Corus 5-10 mm, 1500 °C	4.26 ± 0.51
Dry coke bed, Corus 15-20 mm, 1500 °C	3.83 ± 0.61
Material Resistivity, Corus coke, 1600 °C	0.127 ± 0.041

Table 2.2. Electrical resistivity and conductivity of FeMn ore in different temperature zones Dhainaut (2004).

Ore temperature [°C]	Resistivity $[\Omega\,\mathrm{m}]$	Conductivity $[\mathrm{S/m}]$
400	13.3	0.075
800	6.7	0.15
1200	$6.7 \cdot 10^{-2}$	15
1500	$6.7 \cdot 10^{-3}$	150

logged current and potential drop values as input. The results of these estimates are given in Table 2.1, together with measurements of the resistivity of Corus coke at a representative temperature. The values show that the resistivity is significantly higher for a dry coke bed and it decreases with increasing particle size. This suggests that the main contribution to the bulk resistivity comes from the contact resistance between the coke particles. In the case of a wet coke bed, the current can flow through the slag between the coke particles rather than just through the contact points.

The excavations also support the formation of temperature zones at the top of the FeMn furnace, which can be modelled as horizontal layers of increasing conductivity. This approach has been used in Dhainaut (2004) where the material properties are based on measurements of manganese ores presented in Miyauchi et al. (2001). In Dhainaut (2004) the coke bed region is assumed to have an electrical resistivity of $6.7 \cdot 10^{-3}\ \Omega\,\mathrm{m}$. Furthermore, this work divides the load into three layers corresponding to temperature zones of 400°C, 800°C and 1200°C. From the data given in Miyauchi et al. (2001), the resistivity for the 400°C, 800°C and 1200°C regions is approximately 2000, 1000 and 10 times more resistive higher, respectively, than the coke bed region. The electrical properties at different temperatures are given in Table 2.2.

In this thesis, the bulk conductivity of the coke bed is assumed to be about $500\ \mathrm{S/m}$, which corresponds to the measurements presented in Eidem (2008). The conductivity value given by Dhainaut (2004) is considered to be too low. The same

USC UNIVERSIDADE DE SANTIAGO DE COMPOSTELA

value of 500 S/m is used in the more recent work by Herland et al. (2018), where the material data used are considered to be the most accurate to date. This publication also gives values for conductivity in electrodes, alloys, furnace linings and casing. The alloy conductivity used in Herland et al. (2018) is the same as in Dhainaut (2004), while the electrode values are different. The electrical properties used in the FeMn furnace model in Herland et al. (2018) are listed in Table 2.3.

For completeness and to facilitate comparison with existing literature, values of conductivity and resistivity are given. In this thesis, the results and sensitivity analysis are presented in terms of conductivity. With regard to magnetic properties, the referenced source states that the steel used for the shell is magnetic with a relative magnetic permeability of 100. All other materials considered in this study are non-magnetic. These electrical and magnetic properties will be used as reference values for this work.

Table 2.3. Electrical resistivity and conductivity of the materials included in a FeMn furnace provided in Herland et al. (2018).

Material	Resistivity [Ω m]	Conductivity [S/m]
Electrode	$2 \cdot 10^{-5}$	$5 \cdot 10^{4}$
Charge, 400°C	13.3	0.075
Charge, 800°C	6.7	0.15
Charge, 1200°C	$6.7 \cdot 10^{-2}$	15
Coke bed	$2 \cdot 10^{-3}$	500
Alloy	$6.7 \cdot 10^{-6}$	$1.5 \cdot 10^{5}$
Carbon lining	$7.1 \cdot 10^{-5}$	$1.4 \cdot 10^{4}$
Oxide lining	$1 \cdot 10^{6}$	$1 \cdot 10^{-6}$
Steel shell	$3.3 \cdot 10^{-7}$	$3 \cdot 10^{6}$

The materials within an industrial SAF are generally not uniform with defined boundaries and smooth transitions. In fact, the opposite is often true. The furnace hearth consists of a variety of granular raw materials that undergo chemical transformation under extreme conditions, creating new solids, liquids, gases or plasmas that are mixed together. In recent years, some analytical mathematical models have been applied to better understand how the complex interior of submerged arc furnaces can be homogenised to form bulk properties from coupled multiphysical models, including the electrical problem Rooney (2019); Rooney et al. (2021) (calcination furnace) Luckins (2021); Luckins, Oliver, Please, Sloman, & Van Gorder (2022); Luckins, Oliver, Please, Sloman, Valderhaug, & Van Gorder (2022) (FeSi furnace).

USC UNIVERSIDADE DE SANTIAGO DE COMPOSTELA

2.4 Novel insights: key contributions to the existing literature

The work of this thesis aims to contribute to the understanding of the electromagnetic behaviour in SAFs through the development and application of 3D models and reduced 2D and 1D models. The utilization of 3D models enables detailed numerical simulations of the furnaces, facilitating the assessment of new designs and the validation of reduced-dimensional tools. Conversely, the implementation of reduced models provides cheaper tools that can provide qualitative insights into localized areas of the furnaces. In general terms, the work in the thesis can be divided into two categories, as described below, in each of which the main contributions to the existing literature are highlighted.

1. **Study of analytical tools for understanding inductive effects**. Dimensional analysis is used to determine non-dimensional groups that govern the electromagnetic behaviour of conductors carrying alternating current. The main objective is to select the main parameters to study the electromagnetic behaviour inside a submerged arc furnace using appropriate industrial dimensions and material properties. The idea is to find the parameters in a simple 2D geometry for later application to the study of a part of the furnace. This focus is, in a sense, a continuation of the results presented in Schlanbusch et al. (2014), published during the *Metallurgical Scale Up* project, a prelude to the ElMet project Halvorsen et al. (2021). The aim of the current work is to apply the non-dimensional tools to the analysis of a representative furnace geometry, which will be validated by numerical simulations. Furthermore, the analysis of the 2D system will be the basis for the development of 1D analytical models that can be used to describe the electromagnetic fields in layers of materials with different properties. In particular, the 1D approach can be exploited to study both horizontal currents in the furnace hearth and vertical currents in the linings and steel shell.

   In the literature, techniques of non-dimensional analysis have been applied to simplify multiphysics models of parts of SAFs (see, for example, Sloman et al. (2017); Van Gorder et al. (2021); Luckins (2021)); however, the aim in these references is far from obtaining an analytical electric field as in this work. The analytical 1D model is inspired by the analysis performed in Deng et al. (2009), but with the novelty of treating several types of boundary conditions and focusing on the low frequency case. Furthermore, to the best of the author's knowledge, the application of such techniques to the analysis of the inductive effects in metallurgical applications has not been addressed before.

2. **Numerical simulations of FeMn furnace models.** Several three-dimensional and two-dimensional mathematical models derived from Maxwell's equations are considered. These models are solved numerically by the Finite

USC UNIVERSIDADE DE SANTIAGO DE COMPOSTELA

Element Method (FEM) using the commercial software package COMSOL Multiphysics®. Reduced 2D models under different assumptions in the electric current (lying in a plane or transverse to a plane) are introduced to simulate certain parts of the furnaces and also to compare AC and DC approximations. The use of non-dimensional analysis compared with numerical simulations for the electric conditions in submerged arc furnaces has not been found in the published literature. On the other hand, as we have advanced above, a comparison of AC and DC models can be found in Tesfahunegn et al. (2020) for a FeSi furnace using numerical techniques; however, in the current work the focus is on FeMn furnaces, whose behaviour below the electrodes is quite different.

As previously outlined, only a limited number of publications have included the steel shell and lining in the numerical simulation; see, for example, Herland et al. (2019); Tesfahunegn et al. (2020); Sparta, Stråbø, et al. (2021). In particular, Herland et al. (2019, 2018) have discussed about the importance of the induced currents in the steel shell of SAFs. The numerical studies carried out in this thesis represent original additions to the current knowledge of induction in the steel shell, considering new and innovative designs for the surrounding parts of the furnace.

From a numerical point of view, a new method is presented to increase the computational efficiency of three-phase AC furnaces. It consists of taking advantage of the linearity of Maxwell's equations and computing the solution of a three-phase AC fed model by means of a combination of solutions obtained with a single-phase source. This opens up the possibility of creating less computationally demanding models by exploiting the symmetries of the furnaces. This idea is inspired by the research conducted in Halvorsen et al. (2016) for DC approaches.

USC UNIVERSIDADE DE SANTIAGO DE COMPOSTELA

USC
UNIVERSIDADE
DE SANTIAGO
DE COMPOSTELA

Chapter 3

Mathematical models: 3D and reduced dimension solutions

The aim of this chapter is to present the electromagnetic models used in Chapter 4 for the numerical simulation of submerged electric furnaces. These models are derived from Maxwell's equations and include three-dimensional (3D) and two-dimensional (2D) formulations. The specific problems addressed in this research are studied using these models.

One of the objectives of this thesis is to develop reduced dimensional models to analyse different sections of the furnaces under appropriate assumptions, thereby reducing the computational cost compared to more complex 3D simulations. Another objective is to use these reduced models in localised parts of the furnace to gain a better qualitative understanding of the inductive effects while saving computational effort. To achieve these objectives, appropriate assumptions will be made about the electromagnetic fields and current density. The formulations will include scalar and/or vector potentials and appropriate boundary conditions will be chosen for each specific case.

The models will be solved numerically using COMSOL Multiphysics®, where the formulations sometimes deviate from the classical solutions found in the literature for low frequency scenarios. Therefore, sections 3.1 to 3.6 are devoted to detailing the partial differential equations governing the corresponding electromagnetic models in terms of different vector and scalar potentials according to the chosen module in the software.

In addition, Section 3.7 will focus on introducing non-dimensional tools to characterise different electric current regimes in a rectangular conductor domain. These tools will be used later in Chapter 4 to discuss 2D results and in Chapter 5 to obtain 1D analytical solutions under appropriate simplifications.

usc
UNIVERSIDADE DE SANTIAGO DE COMPOSTELA

3.1 The time harmonic Maxwell's equations

The behaviour of electromagnetic fields in materials is governed by a system of four equations, commonly known as *Maxwell's equations* which, in their differential form, reads as follows:

$$\frac{\partial \boldsymbol{\mathcal{B}}}{\partial t} + \mathbf{curl}\boldsymbol{\mathcal{E}} = \mathbf{0}, \tag{3.1}$$

$$\frac{\partial \boldsymbol{\mathcal{D}}}{\partial t} - \mathbf{curl}\boldsymbol{\mathcal{H}} = -\boldsymbol{\mathcal{J}}, \tag{3.2}$$

$$\text{div}\, \boldsymbol{\mathcal{D}} = \rho_V, \tag{3.3}$$

$$\text{div}\, \boldsymbol{\mathcal{B}} = 0, \tag{3.4}$$

where $\boldsymbol{\mathcal{E}}$ represents the electric field, $\boldsymbol{\mathcal{B}}$ stands for the magnetic flux density, $\boldsymbol{\mathcal{H}}$ is the magnetic field, $\boldsymbol{\mathcal{D}}$ is the electric displacement, $\boldsymbol{\mathcal{J}}$ corresponds to the current density and ρ_V is the volumetric charge density. These equations are valid in the whole space $\mathbb{R}^3$. Throughout this thesis, vector fields and variables will be denoted using boldface letters. In particular, all the fields in the previous equations are vector fields varying with time $t > 0$, and position $\mathbf{x} \in \mathbb{R}^3$. The notation employed is standard and it has been summarized in Table 3.1, together with the corresponding units in the International System of Units (SI).

Each equation in the system is named after the person who originally discovered the underlying relationships. Hence (3.1) is known as Faraday's Law, (3.2) represents Ampère's Law as amended by Maxwell to include the displacement current term $\partial\boldsymbol{\mathcal{D}}/\partial t$ and (3.3) and (3.4) are referred to as Gauss' Law for electric charge and Gauss' Law for magnetism, respectively.

The behaviour of the electromagnetic fields depends on the material properties, namely, the *electric permittivity* ϵ, *magnetic permeability* μ and *electrical conductivity* σ. This dependence is established by means of some complementary equations to the Maxwell's system relating fundamental with auxiliary fields, that is, $\boldsymbol{\mathcal{E}}$ and $\boldsymbol{\mathcal{B}}$ with $\boldsymbol{\mathcal{D}}$ and $\boldsymbol{\mathcal{H}}$, respectively. Generally, the equations describing these relations are called *constitutive laws*. In this thesis, it is assumed that all materials are linear and isotropic and then the relations read

$$\boldsymbol{\mathcal{B}}(\mathbf{x}, t) = \mu(\mathbf{x})\boldsymbol{\mathcal{H}}(\mathbf{x}, t), \tag{3.5}$$

$$\boldsymbol{\mathcal{D}}(\mathbf{x}, t) = \varepsilon(\mathbf{x})\boldsymbol{\mathcal{E}}(\mathbf{x}, t), \tag{3.6}$$

where μ and ε are scalar functions that depend on the position and their values remain constant in all directions within each material.

The electric permittivity is defined as $\epsilon(\mathbf{x}) = \epsilon_r(\mathbf{x})\epsilon_0$, where $\epsilon_r(\mathbf{x})$ represents the so-called relative permittivity associated with the material and $\epsilon_0 \simeq 10^{-9}/36\pi$ F/m is the electric permittivity of vacuum. Similarly, the magnetic permeability is

USC UNIVERSIDADE DE SANTIAGO DE COMPOSTELA

Table 3.1. Electromagnetism notation and units.

Symbol	Definition	SI Unit	Abbreviation
$\boldsymbol{\mathcal{E}}$	Electric field	volt/meter	V/m
$\boldsymbol{\mathcal{D}}$	Electric displacement	coulomb/meter^2	C/m^2
$\boldsymbol{\mathcal{B}}$	Magnetic flux density	tesla	T
$\boldsymbol{\mathcal{H}}$	Magnetic field	ampere/meter	A/m
$\boldsymbol{\mathcal{J}}$	Current density	ampere/meter^2	A/m^2
ϵ	Electric permittivity	farad/meter	F/m
μ	Magnetic permeability	henry/meter	H/m
σ	Electric conductivity	siemens/ meter	S/m
ρ_V	Volumetric charge density	coulomb/meter^3	C/m^3

defined as $\mu(\mathbf{x}) = \mu_r(\mathbf{x})\mu_0$, with $\mu_r(\mathbf{x})$ being the relative permeability associated with the material and $\mu_0 = 4\pi 10^{-7}$ H/m is the magnetic permeability of vacuum. Both the relative electrical permittivity and magnetic permeability are dimensionless quantities. Consequently, the units of electric permeability and magnetic permeability are the same as the corresponding constants in free space.

Another relation is frequently added to Maxwell's equations, at the same level of the constitutive relations, linking the current density and the electric intensity field, which is known as *Ohm's law*. In the case of static media, this law reads

$$\boldsymbol{\mathcal{J}}(\mathbf{x}, t) = \sigma(\mathbf{x})\boldsymbol{\mathcal{E}}(\mathbf{x}, t). \tag{3.7}$$

In dielectrics, the electrical conductivity σ is zero, while in conductors it generally follows a nonlinear tensor relationship influenced by factors such as temperature. Since this thesis does not address heat-coupled models, the independence of σ with respect to temperature will be assumed, and the value for each material will be known. Furthermore, since all materials are treated as isotropic, σ will be a positive scalar field in conductors, i.e., $\sigma(\mathbf{x}) > 0$.

Three-phase submerged arc furnaces typically operate with alternating current, meaning that the current sources are time-harmonic. Since, in addition, materials are assumed to be electromagnetically linear, this involves that electromagnetic fields are time-harmonic and can therefore be written in the form

$$\boldsymbol{\mathcal{G}}(\mathbf{x}, t) = \mathrm{Re}\left[e^{i\omega t}\mathbf{G}(\mathbf{x})\right]. \tag{3.8}$$

Here, $\mathbf{G}(\mathbf{x})$ represents the complex amplitude or phasor of the vector field $\boldsymbol{\mathcal{G}}(\mathbf{x}, t)$, i denotes the imaginary unit and ω corresponds to the angular frequency derived from the AC frequency f as $\omega = 2\pi f$. By using (3.8) Maxwell's equations can be expressed in terms of the complex amplitudes of the fields, resulting in the *time-*

USC UNIVERSIDADE DE SANTIAGO DE COMPOSTELA

harmonic Maxwell's system

$$i\omega\mathbf{B} + \mathbf{curlE} = \mathbf{0}, \tag{3.9}$$
$$i\omega\mathbf{D} - \mathbf{curlH} = -\mathbf{J}, \tag{3.10}$$
$$\text{div}\ \mathbf{D} = \rho_V, \tag{3.11}$$
$$\text{div}\ \mathbf{B} = 0, \tag{3.12}$$

together with the constitutive laws

$$\mathbf{B} = \mu\mathbf{H}, \tag{3.13}$$
$$\mathbf{D} = \epsilon\mathbf{E}, \tag{3.14}$$
$$\mathbf{J} = \sigma\mathbf{E}. \tag{3.15}$$

In the low-frequency harmonic regime, the term involving the electric displacement in Ampère's law can be neglected. This is the so-called 'quasi-static' assumption which is reasonable when the frequency of the current is low enough. This is the case for the industrial furnaces studied in this thesis, which operate at frequencies around 50 - 60 Hz (for a discussion of parameter ranges in which this model is valid, see, for instance, Bossavit (1998)). When the displacement current is neglected from Ampère's law, Gauss' electric law becomes unnecessary for describing the field in conductors Alonso-Rodríguez & Valli (2010); Bermúdez et al. (2014). Consequently, the so-called *time-harmonic eddy current model* is usually reduced to

$$i\omega\mathbf{B} + \mathbf{curlE} = \mathbf{0}, \tag{3.16}$$
$$\mathbf{curlH} = \mathbf{J}, \tag{3.17}$$
$$\text{div}\ \mathbf{B} = 0, \tag{3.18}$$
$$\mathbf{B} = \mu\mathbf{H}, \tag{3.19}$$
$$\mathbf{J} = \sigma\mathbf{E}, \tag{3.20}$$

considering that the time derivative of a field can be replaced by the product of $i\omega$ and the complex amplitude corresponding to that field. This eddy current model is classically used in many industrial problems at low frequency; in particular, the reader is referred to Bermúdez et al. (2014); Touzani & Rappaz (2014); Alonso-Rodríguez & Valli (2010) and Bermúdez et al. (2005) for applications related to SAFs.

3.2 A 3D eddy current model in a bounded domain with electric ports

To solve the mathematical model described by (3.16)-(3.20) using the finite element method, the equations are constrained to a simply connected three dimensional

USC UNIVERSIDADE DE SANTIAGO DE COMPOSTELA

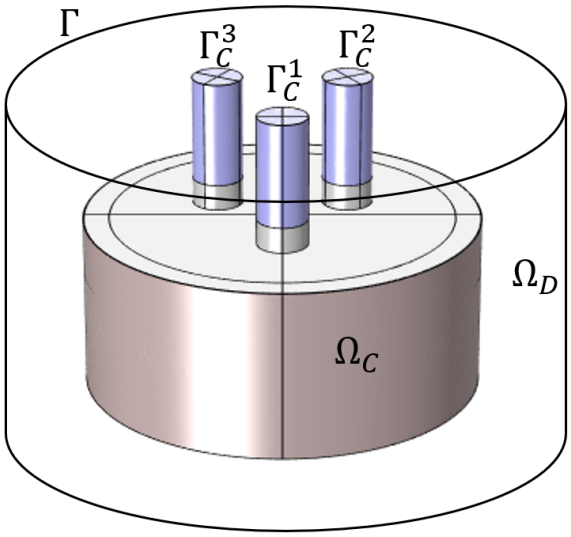

Figure 3.1. 3D computational domain with electric ports on the top of the electrodes.

domain Ω, by adding suitable boundary conditions that allow us to impose the sources in the model and define the behaviour of the fields at infinity. More precisely, the sources will be specified in terms of the currents entering the electrodes and/or the potential drop between two of them. The eddy current model with this boundary conditions on the conducting domain is commonly referred as *eddy curent model with electric ports*; see, for instance, Bermúdez et al. (2014).

This section introduces a three-dimensional mathematical framework suitable for the modelling of the industrial furnaces studied in this thesis.

The 3D model is formulated in Cartesian coordinates (x, y, z) with vector basis $(\mathbf{e}_x, \mathbf{e}_y, \mathbf{e}_z)$ and vector fields have the general form

$$\mathbf{G}(\mathbf{x}) = G_x(x, y, z)\mathbf{e}_x + G_y(x, y, z)\mathbf{e}_y + G_z(x, y, z)\mathbf{e}_z. \tag{3.21}$$

The computational domain Ω will be split in two parts: the conducting domain Ω_C and the dielectric domain Ω_D. The conducting domain Ω_C consists of the electrodes and the interior of the furnace, while Ω_D represents the dielectric (air) surrounding the conducting components. A schematic illustration of the computational domain is shown in Figure 3.1, where the conductive region is depicted using colors, while the surrounding dielectric material is represented in white. The inclusion of the dielectric material in the model serves to introduce approximate boundary conditions far from the areas of interests. These boundary conditions ensure the well-possedness of the problem. The computational domain Ω is assumed to have a Lipschitz-continuous boundary denoted by Γ. Further, let the open surface $\Gamma_C =$

USC UNIVERSIDADE DE SANTIAGO DE COMPOSTELA

$\partial\Omega_C \cap \Gamma$ be the outer boundary of Ω_C and the open surface $\Gamma_D = \partial\Omega_D \cap \Gamma$ be the outer boundary of Ω_D. The outer boundary of the conducting domain represents the points of entry and exit for the electric current and consists of three separate components denoted as Γ_C^n, with $n = 1, 2, 3$, corresponding to the top surfaces of the three electrodes.

By following Bermúdez et al. (2014), the boundary conditions to be considered are

$$\mathbf{E} \times \mathbf{n} = \mathbf{0} \quad \text{on } \Gamma_C^n \quad \text{for } n = 1, 2, 3, \tag{3.22}$$

$$\mu \mathbf{H} \cdot \mathbf{n} = 0 \quad \text{on } \Gamma, \tag{3.23}$$

where $\mathbf{n}$ denotes a unit outward vector to the given surface. The condition (3.22) states that the current enters and leaves Ω perpendicular to the surface, while (3.23) implies that the magnetic field is tangential to the boundary. Furthermore, as will be demonstrated below through formal calculations, (3.23) implies that the tangential component of the electric field is a gradient of a scalar potential. Combining (3.23) with (3.9) and (3.13), gives

$$\mathbf{curl}\mathbf{E} \cdot \mathbf{n} = 0. \tag{3.24}$$

Consider a closed surface S with boundary ∂S contained in Γ. The integral of $i\omega\mu\mathbf{H} \cdot \mathbf{n}$ over the surface S can be evaluated as

$$\int_S i\omega\mu\mathbf{H} \cdot \mathbf{n}\, dS = -\int_S \mathbf{curl}\mathbf{E} \cdot \mathbf{n}\, dS = 0. \tag{3.25}$$

By applying Stokes' theorem, it follows that

$$\int_{\partial S} \mathbf{E} \cdot \mathbf{t}\, dl = 0, \tag{3.26}$$

with $\mathbf{t}$ being a unit vector tangential to ∂S. This equation can be further expressed as

$$\int_{\partial S} \mathbf{n} \times \mathbf{E} \times \mathbf{n} \cdot \mathbf{t}\, dl = 0. \tag{3.27}$$

Since Γ is simply connected, from (3.27) one can assert that there exists a sufficiently smooth function V defined in Ω up to an arbitrary constant, such that $\mathrm{V}|_\Gamma$ is a surface potential of the tangential component of $\mathbf{E}$. That is, the electric scalar potential V can be defined as

$$\mathbf{E} \times \mathbf{n} = -\mathrm{grad}\,\mathrm{V} \times \mathbf{n} \quad \text{on } \Gamma. \tag{3.28}$$

On the other hand, the boundary condition (3.22) for the electric field implies that V must be constant on each connected component of Γ_C. The sources are introduced into the model either by imposing a fixed potential drop between two connected components of Γ_C or by applying a fixed current across a connected component. In the 3D furnace models studied in this thesis, the input current of the electrodes is

USC UNIVERSIDADE DE SANTIAGO DE COMPOSTELA

assumed to be known. However, it is still necessary to specify the potential at a particular point on the boundary Γ_C. This can be done, for instance, by setting $V = 0$ on Γ_C^1. The current is fixed at the remaining two disjoint connected components Γ_C^2 and Γ_C^3. Thus, the model is completed with the following boundary conditions:

$$V = 0 \quad \text{on } \Gamma_C^1, \tag{3.29}$$

$$\int_{\Gamma_C^n} \mathbf{J} \cdot \mathbf{n} dA = I_n \quad \text{for } n = 2, 3, \tag{3.30}$$

where I_n represents the known current traversing Γ_C^n.

Thus, the eddy current problem within the domain of interest can be summarized as follows:

$$i\omega \mathbf{B} + \mathbf{curl}\mathbf{E} = \mathbf{0} \qquad \text{in } \Omega, \tag{3.31}$$

$$\mathbf{curl}\mathbf{H} = \mathbf{J} \qquad \text{in } \Omega, \tag{3.32}$$

$$\text{div } \mathbf{B} = 0 \qquad \text{in } \Omega, \tag{3.33}$$

$$\mathbf{B} = \mu \mathbf{H} \qquad \text{in } \Omega, \tag{3.34}$$

$$\mathbf{J} = \sigma \mathbf{E} \qquad \text{in } \Omega_C, \tag{3.35}$$

$$\mathbf{J} = \mathbf{0} \qquad \text{in } \Omega_D, \tag{3.36}$$

$$\mathbf{E} \times \mathbf{n} = \mathbf{0} \qquad \text{on } \Gamma_C^n \quad \text{for } n = 1, 2, 3, \tag{3.37}$$

$$\mu \mathbf{H} \cdot \mathbf{n} = 0 \qquad \text{on } \Gamma, \tag{3.38}$$

$$V = 0 \qquad \text{on } \Gamma_C^1, \tag{3.39}$$

$$\int_{\Gamma_C^n} \mathbf{J} \cdot \mathbf{n} dA = I_n \qquad \text{for } n = 2, 3. \tag{3.40}$$

3.3 Formulation in magnetic vector potential and electric scalar potential

The numerical simulations presented in this thesis were performed in COMSOL Multiphysics®, which uses a formulation based on the magnetic vector potential, $\mathbf{A}$, and a scalar electric potential, V, the so-called $\mathbf{A}$/V formulation. In this section, these potentials and the corresponding model are introduced.

Equation (3.33) guarantees the existence of a vector field $\mathbf{A}$ such that

$$\mathbf{B} = \mathbf{curl}\mathbf{A} \quad \text{in } \Omega. \tag{3.41}$$

The vector field $\mathbf{A}$ is known as the magnetic vector potential. By substituting the expression for $\mathbf{B}$ from (3.41) into Faraday's law (3.31), the following equation is obtained

$$\mathbf{curl}\,(i\omega \mathbf{A} + \mathbf{E}) = \mathbf{0} \quad \text{in } \Omega. \tag{3.42}$$

USC UNIVERSIDADE DE SANTIAGO DE COMPOSTELA

Since Ω is simply connected, there exist an electric scalar potential V such that

$$i\omega\mathbf{A} + \mathbf{E} = -\text{grad V} \quad \text{in } \Omega. \tag{3.43}$$

Although the eddy current model is typically written by neglecting the electric displacement term in Ampère's law, this term can be easily included in the harmonic regime when using the $\mathbf{A}/\text{V}$ formulation. This is because, in that case, the electric displacement leads to a first order system, and hence the computational cost is not significantly increased. Consequently, COMSOL considers this term and formulates Ampère's law as follows

$$i\omega\epsilon\mathbf{E} - \mathbf{curl}\left(\frac{1}{\mu}\mathbf{curlA}\right) = -\sigma\mathbf{E}. \tag{3.44}$$

Taking into account (3.43), (3.44) can be reformulated in terms of the potentials as

$$\left(i\omega\sigma - \omega^2\epsilon\right)\mathbf{A} + \mathbf{curl}\left(\frac{1}{\mu}\mathbf{curlA}\right) + (\sigma + i\omega\epsilon)\,\text{grad V} = \mathbf{0}. \tag{3.45}$$

It should be noted that the equations (3.41) and (3.43) do not uniquely determine the $\mathbf{A}/\text{V}$ pair. Introducing the potentials

$$\tilde{\mathbf{A}} = \mathbf{A} + \text{grad}\,\phi, \tag{3.46}$$

$$\tilde{\text{V}} = \text{V} - i\omega\phi, \tag{3.47}$$

where ϕ is a scalar function, the same electric field and magnetic induction can be found. Indeed, $\tilde{\mathbf{A}}$ and $\tilde{\text{V}}$ also satisfy (3.43):

$$i\omega\tilde{\mathbf{A}} + \mathbf{E} = -\text{grad}\,\tilde{\text{V}}, \tag{3.48}$$

and $\tilde{\mathbf{A}}$ clearly satisfies (3.41). Therefore, additional conditions are needed for the potentials to guarantee the uniqueness of the solution. This can be done in several ways Alonso-Rodríguez & Valli (2010); Bermúdez et al. (2014); in this work, the *Coulomb gauge*

$$\text{div}\,\mathbf{A} = 0 \quad \text{in } \Omega, \tag{3.49}$$

with the boundary condition

$$\mathbf{A} \times \mathbf{n} = \mathbf{0} \quad \text{on } \Gamma, \tag{3.50}$$

is adopted. The existence and uniqueness of $\mathbf{A}$ are guaranteed by (Amrouche et al., 1998, Theorem 3.17).

In addition, it is necessary to take into account the following equation

$$\text{div}\left((i\omega\sigma - \omega^2\epsilon)\mathbf{A} + (\sigma + i\omega\epsilon)\text{grad V}\right) = 0, \tag{3.51}$$

USC UNIVERSIDADE DE SANTIAGO DE COMPOSTELA

which is obtained by applying the divergence operator to (3.45).

On the other hand, in the **A**/V formulation, where the electrical displacement is not neglected, the boundary conditions introduced to account for the input current sources in the classical eddy current model (3.31) - (3.40) are also used. Thus, in terms of **A** and V, the full model reads:

Problem 3.1. *Given the complex currents I_2 and I_3, find a vector field* **A** *and scalar field V such that*

$$\left(i\omega\sigma - \omega^2\epsilon\right)\mathbf{A} + \mathbf{curl}\left(\frac{1}{\mu}\mathbf{curlA}\right) + (\sigma + i\omega\epsilon)\,\text{grad V} = \mathbf{0} \quad \text{in } \Omega, \tag{3.52}$$

$$\text{div}\left(-i\omega\sigma\mathbf{A} + \omega^2\epsilon\mathbf{A} - \sigma\text{grad V} - i\omega\epsilon\text{grad V}\right) = 0 \quad \text{in } \Omega, \tag{3.53}$$

$$\text{div}\,\mathbf{A} = 0 \quad \text{in } \Omega, \tag{3.54}$$

$$\mathbf{A} \times \mathbf{n} = \mathbf{0} \quad \text{on } \Gamma, \tag{3.55}$$

$$\text{V} = 0 \quad \text{on } \Gamma_C^1, \tag{3.56}$$

$$\int_{\Gamma_C^n} \sigma\,(\text{grad V} + i\omega\mathbf{A}) \cdot \mathbf{n}\, dA = I_n \quad \text{for } n = 2, 3. \tag{3.57}$$

Remark 3.1. *It should be noted that in the official documentation provided by AC/DC Module User's Guide (2022) it is possible to find slight modifications in the presentation of the models in the time-harmonic regime. The main reason is that the displacement term in Ampère's law is not neglected and the current density is redefined as*

$$\mathbf{J} = (\sigma + i\omega\epsilon)\,\mathbf{E}, \tag{3.58}$$

that is, including the part of the Ohm's law and the displacement currents. Consequently, COMSOL explicitly enforces the insulation condition $\mathbf{J} \cdot \mathbf{n} = 0$ *on the boundary of the dielectric domain. In contrast, in the framework of the preceding model, this condition arises implicitly from the fact that* $\sigma = 0$ *within the dielectric.*

The furnaces studied in this work operate with three-phase current supplied through each electrode with a phase difference of $2\pi/3$ radians. Thus, the input currents in (3.57) are expressed as follows

$$I_2 = I_0 e^{i2\pi/3}, \tag{3.59}$$

$$I_3 = I_0 e^{-i2\pi/3}, \tag{3.60}$$

where I_0 represents the amplitude of the applied current intensity. By applying the principle of current conservation, it can be directly deduced that the current intensity on Γ_C^1 is $I_1 = I_0$.

The model given by equations (3.52)-(3.57) assumes that the conducting domain Ω_C is a volumetric domain comprising different regions that needs to be discretised to

USC UNIVERSIDADE DE SANTIAGO DE COMPOSTELA

compute the numerical solution for the problem. The presence of thin regions within the domain can significantly increase computational costs, particularly when dealing with highly conductive materials. This is due to the skin effect, which requires a large number of mesh elements to accurately capture the behaviour in these areas.

In the case of the industrial three-phase furnaces studied in this thesis, the steel shell surrounding the furnace presents such a computational challenge. This region is highly conductive, typically a few centimeters thick, and has a skin depth on the order of a few millimeters. Furthermore, the total surface area of the shell is substantial, as the furnaces have a diameter around 10 m.

To avoid the computational cost associated with constructing a suitable discretization, many studies in the literature exclude the steel shell from the computational domain. In this thesis this computational challenge is addressed in the 3D case by modelling the steel shell using an appropriate impedance boundary condition, which will be detailed in the next section. In subsequent 2D approximations of the problem, the discretization of the shell will be considered, as the associated cost is quite affordable.

3.3.1 3D Modelling of the steel shell

In the 3D model, the geometry of the steel shell is simplified to that of a straight cylindrical shell. Specifically, the physical volumetric shell is replaced by considering only its surface, where an impedance boundary condition is applied. Let Ω_S denote the part of Ω corresponding to the steel shell, and let Γ_S be its closed surface. Additionally, let Ω_I denote the part of Ω that excludes Ω_S, i.e., $\Omega_I = \Omega \setminus \bar{\Omega}_S$. Thus, the impedance boundary condition will be defined on Γ_S where the wave impedance Z_ω relates the tangential components of the magnetic and the electric fields according to the following expression Fawzi et al. (1985); Yuferev & Ida (2005); Meunier (2008)

$$\mathbf{n} \times \mathbf{E} = Z_\omega \mathbf{n} \times (\mathbf{n} \times \mathbf{H}) \quad \text{on } \Gamma_S. \tag{3.61}$$

The intrinsic wave impedance is determined by the material parameters (μ, ϵ, σ) of the shell and is given by Yuferev & Ida (2005)

$$Z_\omega = \sqrt{\frac{\mu}{\epsilon - i\sigma/\omega}}. \tag{3.62}$$

This methodology allows for the modelling of induced currents in the steel shell as surface currents and has been previously validated for the modelling of SAFs in Herland et al. (2019).

It is worth noticing that the impedance boundary condition in (3.61) can be expressed in terms of the vector potential $\mathbf{A}$ and the electric potential V as

USC UNIVERSIDADE DE SANTIAGO DE COMPOSTELA

follows:

$$\mathbf{n} \times (-\text{grad V} - i\omega\mathbf{A}) = \sqrt{\frac{\mu}{\epsilon - i\sigma/\omega}}\mathbf{n} \times \left(\mathbf{n} \times \frac{1}{\mu}\mathbf{curlA}\right) \quad \text{on } \Gamma_S. \tag{3.63}$$

Consequently, the 3D model in terms of $\mathbf{A}$ and V reads as follows:

Problem 3.2. *Given the complex currents I_2 and I_3, find a vector field $\mathbf{A}$ and scalar field V such that*

$$\left(i\omega\sigma - \omega^2\epsilon\right)\mathbf{A} + \mathbf{curl}\left(\frac{1}{\mu}\mathbf{curlA}\right) + (\sigma + i\omega\epsilon)\,\text{grad V} = \mathbf{0} \quad \text{in } \Omega_I, \tag{3.64}$$

$$\text{div}\left(-i\omega\sigma\mathbf{A} + \omega^2\epsilon\mathbf{A} - \sigma\text{grad V} - i\omega\epsilon\text{grad V}\right) = 0 \quad \text{in } \Omega_I, \tag{3.65}$$

$$\text{div}\,\mathbf{A} = 0 \quad \text{in } \Omega_I, \tag{3.66}$$

$$\mathbf{A} \times \mathbf{n} = \mathbf{0} \quad \text{on } \Gamma, \tag{3.67}$$

$$\text{V} = 0 \quad \text{on } \Gamma_C^1, \tag{3.68}$$

$$\int_{\Gamma_C^n} \sigma\,(\text{grad V} + i\omega\mathbf{A}) \cdot \mathbf{n}\, dA = I_n \quad \text{for } n = 2, 3. \tag{3.69}$$

$$\mathbf{n} \times (-\text{grad V} - i\omega\mathbf{A}) = \sqrt{\frac{\mu}{\epsilon - i\sigma/\omega}}\mathbf{n} \times \left(\mathbf{n} \times \frac{1}{\mu}\mathbf{curlA}\right) \quad \text{on } \Gamma_S. \tag{3.70}$$

3.4 2D model with in-plane currents

Reduced models in lower dimensions can be useful for analysing the qualitative behaviour of certain properties in the complex three-phase furnaces. In this section, a 2D model with in-plane currents is introduced, aiming to simulate a vertical cross section through two electrodes of the furnace. Such models have previously been employed to study SAFs; see, for instance, K. T. Karalis et al. (2016). In this formulation, the three-phase current is simplified to a single-phase, resulting in a more straightforward and intuitive distribution of the electromagnetic field.

Figure 3.2 shows the computational domain $\widehat{\Omega}$ and its boundary $\widehat{\Gamma}$. This figure also shows how the 2D geometry is related to the full 3D model discussed in Section 3.3. Notice that the sets and boundaries considered in this 2D case correspond to those introduced in 3D once intersected with a vertical plane, as shown in Figure 3.2. The notation 'hat' is used to denote the domains and boundaries obtained in 2D as a result of such intersection. Thus, $\widehat{\Omega}$ comprises a conducting part $\widehat{\Omega}_C$ and a dielectric part $\widehat{\Omega}_D$. The boundaries $\widehat{\Gamma}_C^1$ and $\widehat{\Gamma}_C^2$ represent the top surfaces of the two electrodes where the sources are specified, while $\widehat{\Gamma}_D = \widehat{\Gamma} \setminus (\widehat{\Gamma}_C^1 \cup \widehat{\Gamma}_C^2)$ denotes de boundary of $\widehat{\Omega}_D$.

USC UNIVERSIDADE DE SANTIAGO DE COMPOSTELA

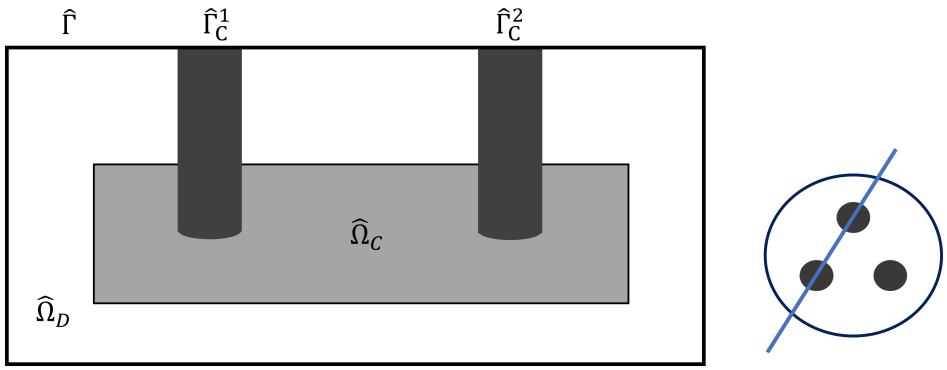

Figure 3.2. Computational domain of the 2D model with in-plane currents (left); 2D plane relative to the 3D model (right).

In the 2D model, the supplied current has a phase difference of π radians, which is equivalent to a single-phase transformer connecting the electrodes. The mathematical model defined by (3.52) - (3.57) still holds in the 2D case with some adjustments to the source entries. With two electrodes, the potential is still grounded on one electrode as given by (3.56), while (3.57) is rewritten as follows

$$\int_{\widehat{\Gamma}_C^2} \sigma \left(\text{grad V} + i\omega \mathbf{A}\right) \cdot \mathbf{n} dx = I_2 \quad \text{on } \widehat{\Gamma}_C^2, \tag{3.71}$$

where $I_2 = I_0 e^{i\pi} = -I_0$. According to current conservation, this leads to $I_1 = I_0$, where I_0 represents the amplitude of the AC current.

The model is formulated in the xy plane of a Cartesian coordinate system with basis vectors ($\mathbf{e}_x$,$\mathbf{e}_y$,$\mathbf{e}_z$) and the involved vector fields are assumed to have the following form:

$$\mathbf{J}(x,y) = J_x(x,y)\mathbf{e}_x + J_y(x,y)\mathbf{e}_y \quad \text{in } \widehat{\Omega}_C, \tag{3.72}$$
$$\mathbf{E}(x,y) = E_x(x,y)\mathbf{e}_x + E_y(x,y)\mathbf{e}_y \quad \text{in } \widehat{\Omega}, \tag{3.73}$$
$$\mathbf{H}(x,y) = H_z(x,y)\mathbf{e}_z \quad \text{in } \widehat{\Omega}. \tag{3.74}$$

Consequently, the magnetic vector potential takes the form

$$\mathbf{A}(x,y) = A_x(x,y)\mathbf{e}_x + A_y(x,y)\mathbf{e}_y, \tag{3.75}$$

and the model (3.52)-(3.56) is reduced to 2D, with equation (3.71) replacing (3.57). Thus, the full 2D model with in-plane currents reads:

USC UNIVERSIDADE DE SANTIAGO DE COMPOSTELA

Problem 3.3. *Given the complex current I_2, find a 2D vector field* **A** *and 2D scalar field V*

such that

$$\left(i\omega\sigma - \omega^2\epsilon\right)\mathbf{A} + \mathbf{curl}\left(\frac{1}{\mu}\mathbf{curlA}\right) + (\sigma + i\omega\epsilon)\,\mathrm{grad\ V} = \mathbf{0} \quad \text{in } \widehat{\Omega}, \tag{3.76}$$

$$\mathrm{div}\left(-i\omega\sigma\mathbf{A} + \omega^2\epsilon\mathbf{A} - \sigma\mathrm{grad\ V} - i\omega\epsilon\mathrm{grad\ V}\right) = 0 \quad \text{in } \widehat{\Omega}, \tag{3.77}$$

$$\mathbf{A}\times\mathbf{n} = \mathbf{0} \quad \text{on } \widehat{\Gamma}, \tag{3.78}$$

$$\mathrm{V} = 0 \quad \text{on } \widehat{\Gamma}_C^1, \tag{3.79}$$

$$\int_{\widehat{\Gamma}_C^2} \sigma\left(\mathrm{grad\ V} + i\omega\mathbf{A}\right)\cdot\mathbf{n}dx = I_2 \quad \text{on } \widehat{\Gamma}_C^2. \tag{3.80}$$

3.5 2D model with out-of-plane currents

To study the current distribution in the electrodes, lining, and steel shell of a three-phase SAF, a 2D model representing a horizontal cross section is often employed, specially to save computational effort. The use of a 2D model allows for the meshing of thin structures such as the shell and also enables the consideration of the proximity effect between the electrodes. Previous studies, including works by Bermúdez et al. (1999); Herland et al. (2019), have utilized this methodology.

The 2D model is an approximation of the 3D model under the assumptions that the computational domain Ω is very long in one spatial direction (typically the z-direction) and that the current primarily flows in this direction. Specifically, it is assumed that the geometry and parameters are invariant under translation in the z-direction and that the current density has only a non-null component in this direction which is independent of z. In particular, the current density vector is expressed as

$$\mathbf{J} = J_z(x,y)\mathbf{e}_z. \tag{3.81}$$

Consequently, the other vector fields involved can also be assumed to be independent of z.

Similar to the 2D models presented above, $\widehat{\Omega}$ represents the 2D computational domain, while $\widehat{\Omega}_C$ and $\widehat{\Omega}_D$ represent the conductive and dielectric subdomains, respectively, into which it is partitioned.

In the type of furnaces under study, the conducting sub-domain $\widehat{\Omega}_C$ is comprised of four disjoint connected components $\widehat{\Omega}_C^n$, $n = 1,\ldots,4$, each of them strictly contained in $\widehat{\Omega}$. In particular, $\widehat{\Omega}_C^1$, $\widehat{\Omega}_C^2$ and $\widehat{\Omega}_C^3$ will represent the cross-section of the electrodes, while $\widehat{\Omega}_C^4$ represent any conducting material in the furnace lining and steel casing. The dielectric region comprises both the interior region surrounding the electrodes and the outer region. A sketch depicting the geometry with the defined domains is illustrated in Figure 3.3. This geometry is considered in Section 4.4 to simulate the upper part of the furnace, where the model developed below is applicable.

USC UNIVERSIDADE DE SANTIAGO DE COMPOSTELA

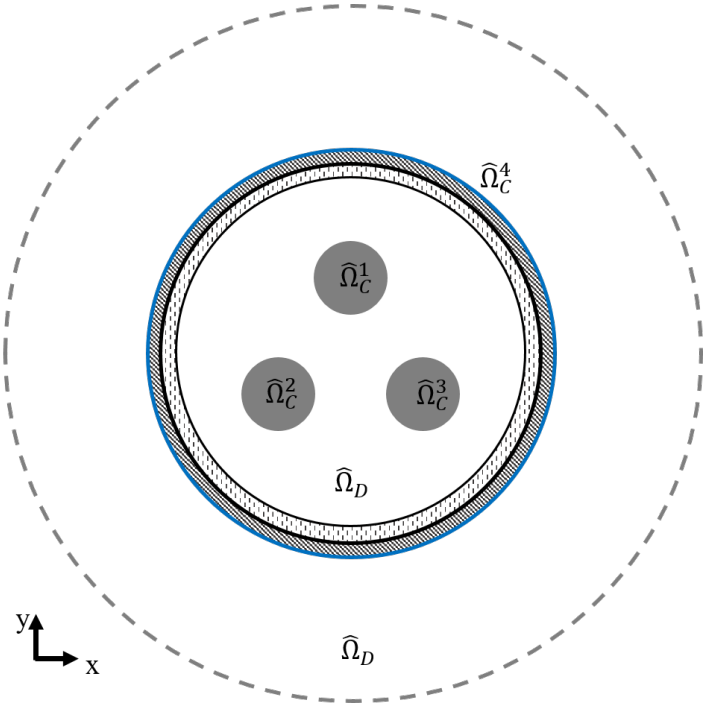

Figure 3.3. 2D model with out-of-plane currents. Computational domain.

Based on these assumptions, the magnetic field and the magnetic induction are of the form

$$\mathbf{H}(x,y) = H_x(x,y)\mathbf{e}_x + H_y(x,y)\mathbf{e}_y \quad \text{in } \widehat{\Omega}, \tag{3.82}$$

$$\mathbf{B}(x,y) = B_x(x,y)\mathbf{e}_x + B_y(x,y)\mathbf{e}_y \quad \text{in } \widehat{\Omega}. \tag{3.83}$$

From (3.41) it follows that the magnetic vector potential is independent of z and given by

$$\mathbf{A}(x,y) = A_z(x,y)\mathbf{e}_z \quad \text{in } \widehat{\Omega}. \tag{3.84}$$

The electric field must be considered more carefully. Based on Ohm's law (3.35), the electric field in the conducting domain must have the same form as the current density

$$\mathbf{E}(x,y) = E_z(x,y)\mathbf{e}_z \quad \text{in } \widehat{\Omega}_C. \tag{3.85}$$

However, in Bossavit (1999) it is argued that the electric field has a more general form in the dielectric region. This can be demonstrated by considering Faraday's law (3.31), which as stated in (3.43), gives raise to an electric scalar potential such that

$$i\omega\mathbf{A} + \mathbf{E} = -\text{grad V} \quad \text{in } \widehat{\Omega}. \tag{3.86}$$

USC UNIVERSIDADE DE SANTIAGO DE COMPOSTELA

Given the form of **A**, the electric field in $\widehat{\Omega}$ can be expressed as

$$E_x = -\frac{\partial \mathrm{V}}{\partial x}, \tag{3.87}$$

$$E_y = -\frac{\partial \mathrm{V}}{\partial y}, \tag{3.88}$$

$$i\omega A_z + E_z = -\frac{\partial \mathrm{V}}{\partial z}. \tag{3.89}$$

Thus, if E_x and E_y were null outside the conductors, it would imply that V must be independent of z, which contradicts the possibility of having different electric potentials in the conductors. Inside the conductors, as the left-hand side of (3.89) is independent of z, while the right hand side is independent of x and y, it follows that

$$\frac{\partial \mathrm{V}}{\partial z} = \widehat{\mathrm{V}}_n \in \mathbb{C}, \quad \text{in } \widehat{\Omega}_C^n, \quad n = 1, \ldots, 4, \tag{3.90}$$

where $\widehat{\mathrm{V}}_n$ represents the potential drop per unit length in the z-direction and is measured in volts per meter (V/m). Substituting this expression into (3.89) gives

$$i\omega A_z + E_z = -\widehat{\mathrm{V}}_n \quad \text{in } \widehat{\Omega}_C^n, \quad n = 1, \ldots, 4. \tag{3.91}$$

In these 2D models, it is assumed that either the current through a conducting component or the potential drop per unit length in the z direction is known. In the cross section of the furnaces, the total current crossing each electrode is assumed to be known. On the other hand, in the conducting section of the steel shell, the current is assumed to be zero. This is because the shell is modelled as an infinite conductor that does not close a circuit Bossavit (1999). To incorporate these types of sources, it is necessary to establish the relationships between the potential drops and the currents crossing a conducting cross-section. This will be the objective in the following lines.

By multiplying (3.91) by σ and integrating it over each $\widehat{\Omega}_C^n$ gives

$$i\omega \int_{\widehat{\Omega}_C^n} \sigma A_z dxdy + \int_{\widehat{\Omega}_C^n} \sigma E_z dxdy = -\widehat{\mathrm{V}}_n \int_{\widehat{\Omega}_C^n} \sigma dxdy. \tag{3.92}$$

By using the relationship $J_z = \sigma E_z$ and defining

$$I_n = \int_{\widehat{\Omega}_n} J_z dxdy = \int_{\widehat{\Omega}_n} \sigma E_z dxdy \tag{3.93}$$

as the current intensity going through $\widehat{\Omega}_C^n$, (3.92) can be rewritten as

$$i\omega \int_{\widehat{\Omega}_n} \sigma A_z dxdy + I_n = -\widehat{\mathrm{V}}_n \int_{\widehat{\Omega}_n} \sigma dxdy. \tag{3.94}$$

USC UNIVERSIDADE DE SANTIAGO DE COMPOSTELA

Thus, the relation which links these currents to the potential drops $\widehat{\mathrm{V}}_n, n = 1, \ldots, 4$ is given by

$$\int_{\widehat{\Omega}_C^n} \left(i\omega\sigma A_z + \sigma\widehat{\mathrm{V}}_n \right) dxdy = -I_n \quad \text{for } n = 1, \ldots, 4. \tag{3.95}$$

This relation must be incorporated somehow in the model if the data are given in terms of the currents crossing the connected conducting components.

3.5.1 A modified magnetic vector potential formulation

In the previous sections it has been shown that when dealing with domains in which the electric source is imposed by global variables such as voltages and/or currents in electric ports, an appropriate formulation relies on the use of the magnetic vector potential $\mathbf{A}$ and the electric scalar potential V Alonso-Rodríguez (2011); Bermúdez et al. (2014) . This option is also advantageous, for instance, for coupling distributed fields with electrical circuits De Gersem et al. (2004); Meunier (2008); Bermúdez et al. (2014); Scorretti (2021). However, in the specific 2D context addressed in this section, which involves out-of-plane currents and assumes known global quantities such as voltage and/or currents, but does not consider electrical circuits, a specific gauge can be used. This gauge allows the problem to be formulated in terms of a vector potential and the currents and/or potential drop, while eliminating the distributed scalar field V. This particular approach is the one adopted by COMSOL in its *Magnetic Field* interface, as it effectively reduces the number of unknowns involved. This procedure is detailed below, starting with the 3D case and using a particular choice of gauge.

As explained in the previous section, the magnetic vector potential and the electric potential are not uniquely defined. Introducing modified potentials $\tilde{\mathbf{A}}$ (3.46) and $\tilde{\mathrm{V}}$ (3.47) results in the same electric and magnetic fields as with the original ones, $\mathbf{A}$ and V. To ensure the uniqueness of the potentials in the 3D case, the classical Coulomb gauge, div $\mathbf{A} = 0$, was considered. An alternative approach, which allows us to eliminate the potential V, is to choose the scalar field ϕ as follows:

$$\phi = -\frac{i}{\omega}\mathrm{V}. \tag{3.96}$$

In this way, equations (3.46) and (3.47) leads to

$$\tilde{\mathbf{A}} = \mathbf{A} - \frac{i}{\omega}\text{grad V}, \tag{3.97}$$

$$\tilde{\mathrm{V}} = 0. \tag{3.98}$$

Thus the electric potential would not be necessary, and the only unknown in the problem would be $\tilde{\mathbf{A}}$, which is well known in engineering literature as the *modified*

USC UNIVERSIDADE DE SANTIAGO DE COMPOSTELA

magnetic vector potential. As an example, the reference work by Emson & Simkin (1983), which uses the modified magnetic vector potential in a 3D setting. In subsequent studies, the modified magnetic vector potential has been employed as a primary unknown and/or combined with other potentials in non-conducting domains Bossavit (1985); Kameari (1989, 1990); Bermúdez et al. (2013). Moreover, in transient problems, this unknown is associated with the time-primitive of the electric field Bermúdez et al. (2013). It is important to note that in this case the fields **B** and **E** can be defined as follows:

$$\mathbf{B} = \mathbf{curl}\tilde{\mathbf{A}} \tag{3.99}$$

and

$$\mathbf{E} = -i\omega\tilde{\mathbf{A}}. \tag{3.100}$$

To impose known currents or potential drops in certain conducting components, COMSOL utilizes a complementary tool based on the introduction of a *coil* and the application of an external current density in the direction of the desired current flow. This external current density $\mathbf{J}^e$ is defined as:

$$\mathbf{J}^e = \frac{\sigma\widehat{\mathrm{U}}_n}{L}\mathbf{e}_z. \tag{3.101}$$

Here, $\widehat{\mathrm{U}}_n$ represents an unknown applied potential drop, and L denotes the physics length over which this potential drop occurs. The value of $\widehat{\mathrm{U}}_n$ is determined by incorporating additional algebraic equations, which enforce the constraint that the total integrated current is equal to a specified value given by the use of the *coil* tool. In fact, considering that $\mathbf{J}$ is defined in this case as the sum of two terms, $\mathbf{J} = \sigma\mathbf{E} + \mathbf{J}^e$, both with only non-$z$ components, the additional constraints are be expressed as:

$$\int_{\widehat{\Omega}_C^n} (\sigma E_z + J_z^e)dxdy = I_n \quad \text{for } n = 1, \ldots, 4. \tag{3.102}$$

On the other hand, to take account of the external current, the Ampère's law is written in the form:

$$i\omega\epsilon\mathbf{E} - \mathbf{curlH} = -\sigma\mathbf{E} - \mathbf{J}^e, \tag{3.103}$$

which together with the equations (3.99) and (3.100) gives

$$\left(i\omega\sigma - \omega^2\epsilon\right)\tilde{\mathbf{A}} + \mathbf{curl}\left(\frac{1}{\mu}\mathbf{curl}\tilde{\mathbf{A}}\right) = \mathbf{J}^e \quad \text{in } \widehat{\Omega}. \tag{3.104}$$

Thus, using the expression for the external current density (3.101) in each conducting component $\widehat{\Omega}_C^n$ gives the following problem:

USC UNIVERSIDADE DE SANTIAGO DE COMPOSTELA

Problem 3.4. *Given input currents I_n, $n = 1, \dots, 4$, find $\tilde{A}_z$ and the unknown constants $\widehat{U}_n$ $(n = 1, \dots, 4)$ such that*

$$\left(i\omega\sigma - \omega^2\epsilon\right)\tilde{A}_z\mathbf{e}_z + \mathbf{curl}\left(\frac{1}{\mu}\mathbf{curl}\tilde{A}_z\mathbf{e}_z\right) = \sigma\frac{\widehat{U}_n}{L}\mathbf{e}_z \qquad \text{in } \widehat{\Omega}_C^n, n = 1, \dots, 4, \tag{3.105}$$

$$\left(-\omega^2\epsilon\right)\tilde{A}_z\mathbf{e}_z + \mathbf{curl}\left(\frac{1}{\mu}\mathbf{curl}\tilde{A}_z\mathbf{e}_z\right) = \mathbf{0} \qquad \text{in } \widehat{\Omega}_D, \tag{3.106}$$

$$\int_{\widehat{\Omega}_C^n}\left(-i\omega\sigma\tilde{A}_z + \sigma\frac{\widehat{U}_n}{L}\right)dxdy = I_n \qquad \text{for } n = 1, \dots, 4. \tag{3.107}$$

$$\tilde{A}_z = 0 \qquad \text{on } \widehat{\Gamma}. \tag{3.108}$$

Remark 3.2. *Note that (3.107) is equivalent to (3.95), which is derived from the classical formulation using the magnetic vector potential* **A** *and the electric scalar potential* V *to establish the link between currents and voltages. The only difference lies in the sign of the potential drop, which has been adjusted to match with the framework used by COMSOL when working with the modified magnetic vector potential in conjunction with the additional coil tool.*

3.6 A direct current model

Simulations involving direct current (DC) are also considered as part of this thesis. DC models have often been used in the context of three-phase furnaces to reduce computational costs or to simplify models involving coupled physics Darmana et al. (2012); Dhainaut (2004); Tesfahunegn, Magnusson, et al. (2018b); Halvorsen et al. (2016). However, DC models can also be applied to study the effects of induction by comparing them with AC models. In a DC scenario, the current source is independent of time, resulting in electromagnetic vector fields that are also independent of time. Consequently, Maxwell's equations can be expressed as:

$$\mathbf{curlE} = \mathbf{0}, \tag{3.109}$$

$$\mathbf{curlH} = \mathbf{J}, \tag{3.110}$$

$$\text{div } \mathbf{B} = 0, \tag{3.111}$$

$$\text{div } \mathbf{D} = \rho_V, \tag{3.112}$$

where the vector fields are related through the same constitutional laws (3.13) - (3.15) described in previous sections. Note that the time-independent vector fields in this section are denoted by the same symbols as the time-harmonic fields discussed earlier.

By taking the divergence in (3.110), the following equation is obtained

$$\text{div } \mathbf{J} = 0. \tag{3.113}$$

USC UNIVERSIDADE DE SANTIAGO DE COMPOSTELA

This equation is commonly referred to as the continuity equation for static electric current. The system of equations presented above demonstrates the decoupling of the electric and magnetic field equations in the static regime. This fact allows the electric field and current density to be calculated first by using the equations (3.109) and (3.113). Then the magnetic field can be determined from **E** and **J** using the equations (3.110) to (3.111). Next, the equations used to calculate the current density under the DC assumption are outlined.

Incorporating Ohm's law into (3.113) gives

$$\operatorname{div}(\sigma \mathbf{E}) = 0. \tag{3.114}$$

Note that this equation is only valid in the conducting domain Ω_C, since the conductivity σ is zero in the dielectrics. Moreover, (3.109) implies the existence of a scalar electric potential V, such that $\mathbf{E} = -\operatorname{grad} \mathrm{V}$. Substituting this expression into (3.114) gives

$$-\operatorname{div}(\sigma \operatorname{grad} \mathrm{V}) = 0 \quad \text{in } \Omega_C. \tag{3.115}$$

The model must be completed with appropriate boundary conditions, which can be specified in terms of the scalar potential or the current intensity crossing a part of the boundary. Let Γ be the boundary of Ω_C; let us consider $\Gamma = \Gamma_0 \cup \ldots \cup \Gamma_C^N$,where Γ_C^n, $n = 1, \ldots, N$ denote the connected parts of Γ where the current enters/leaves the domain and Γ_0 is the remaining part where the current flux is zero. Thus, the boundary conditions are as follows:

$$\mathbf{J} \cdot \mathbf{n} = 0 \quad \text{on } \Gamma_0 \tag{3.116}$$

$$\mathrm{V} = 0 \quad \text{on } \Gamma_C^1 \tag{3.117}$$

$$\int_{\Gamma_C^n} \mathbf{J} \cdot \mathbf{n} dA = I_n \quad \text{on } \Gamma_C^n, n = 2, \ldots, N, \tag{3.118}$$

where N denotes the number of electrodes and I_n is the current intensity going through Γ_C^n. Note that the integration over the boundary Γ_C^n is a surface integral for a 3D model and a line integral for a 2D model. The boundary condition in (3.118) can be written in terms of the unknown potential V as

$$\int_{\Gamma_C^n} \mathbf{J} \cdot \mathbf{n} dA = -\int_{\Gamma_C^n} \sigma \frac{\partial \mathrm{V}}{\partial \mathbf{n}} dA = I_n \quad \text{on } \Gamma_C^n, n = 2, \ldots, N. \tag{3.119}$$

In this way, and taking into account the above considerations, the resulting problem can be formulated as follows:

USC UNIVERSIDADE DE SANTIAGO DE COMPOSTELA

Problem 3.5. *Given the currents $I_n, n = 2, \ldots, N$, find the scalar potential* V *in Ω_C, such*

that

$$-\text{div}\,(\sigma \text{grad}\,\text{V}) = 0 \quad \text{in } \Omega_C \tag{3.120}$$

$$\sigma \frac{\partial \text{V}}{\partial \mathbf{n}} = 0 \quad \text{on } \Gamma_0 \tag{3.121}$$

$$\text{V} = 0 \quad \text{on } \Gamma_C^1 \tag{3.122}$$

$$-\int_{\Gamma_C^n} \sigma \frac{\partial \text{V}}{\partial \mathbf{n}} dA = I_n \quad \text{on } \Gamma_C^n, n = 2, \ldots, N. \tag{3.123}$$

This model will be used in the following chapters, considering both 2D and 3D cases with $N = 2$ and $N = 3$, respectively.

3.7 Non-dimensional tools. Analysis of the 2D electric field equation

Let us consider a 2D rectangular conductor with thickness T and width W as the one represented in Figure 3.4, with electromagnetic material properties defined by $(\sigma, \mu, \varepsilon)$.

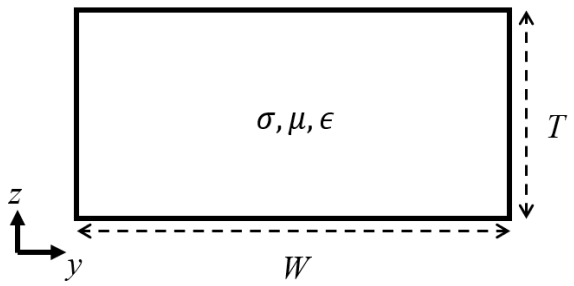

Figure 3.4. Rectangular conductor with thickness T, width W and electrical conductivity σ.

The conductor lies in the Cartesian yz-plane, with unit vector basis $\mathbf{e}_y$ and $\mathbf{e}_z$, and it carries an alternating current with frequency f flowing in this plane. Thus, the electric field in the conductor takes the form

$$\mathbf{E}(y, z) = E_y(y, z)\mathbf{e}_y + E_z(y, z)\mathbf{e}_z. \tag{3.124}$$

From the time-harmonic Maxwell's equations presented in Section 3.1, it is straightforward to obtain the expression governing the distribution of the electric field in the conductor. By taking the **curl** operator of Faraday's law (3.9), combining

USC UNIVERSIDADE DE SANTIAGO DE COMPOSTELA

it with Ampères's law (3.10), and taking into account the constitutive relations between the fields, it results

$$\mathbf{curl}(\mathbf{curl}\mathbf{E}) - w^2\epsilon\mu\mathbf{E} + iw\mu\sigma\mathbf{E} = \mathbf{0}, \tag{3.125}$$

equation that can be rewritten using the definition of the vector Laplacian operator as

$$\Delta\mathbf{E} + \left(\frac{2\pi}{\lambda}\right)^2\mathbf{E} - \frac{2i}{\delta^2}\mathbf{E} = \mathbf{0}. \tag{3.126}$$

In this expression, λ represents the electromagnetic wavelength defined as $\lambda = 2\pi c/\omega$, where $c = 1/\sqrt{\mu\epsilon}$ is the speed of light. Additionally, δ denotes the skin depth defined as $\delta = 1/\sqrt{\pi f\sigma\mu}$.

By explicitly writing the Laplace operator, (3.126) reads

$$\frac{\partial^2}{\partial y^2}\mathbf{E}(y,z) + \frac{\partial^2}{\partial z^2}\mathbf{E}(y,z) + \left(\frac{2\pi}{\lambda}\right)^2\mathbf{E}(y,z) - \frac{2i}{\delta^2}\mathbf{E}(y,z) = \mathbf{0}. \tag{3.127}$$

The main interest in this section is to perform a non-dimensional analysis to characterize different regimes for the electric current. Let us introduce the non-dimensional variables indicated by a tilde as:

$$y = W\tilde{y}, \quad z = T\tilde{z}, \quad \mathbf{E} = E_0\tilde{\mathbf{E}},$$

where E_0 is a characteristic field value such as, for instance, the maximum field strength at the conductor surface. Thus, the wave equation (3.127) can be written in terms of non-dimensional variables as follows

$$\frac{1}{W^2}\frac{\partial^2}{\partial\tilde{y}^2}\tilde{\mathbf{E}}(\tilde{y},\tilde{z}) + \frac{1}{T^2}\frac{\partial^2}{\partial\tilde{z}^2}\tilde{\mathbf{E}}(\tilde{y},\tilde{z}) + \left(\frac{2\pi}{\lambda}\right)^2\tilde{\mathbf{E}}(\tilde{y},\tilde{z}) - \frac{2i}{\delta^2}\tilde{\mathbf{E}}(\tilde{y},\tilde{z}) = \mathbf{0}. \tag{3.128}$$

Note that, in (3.128), the function $\tilde{\mathbf{E}}(\tilde{y},\tilde{z})$ is non-dimensional, while the coefficient in each term has units of $1/\mathrm{m}^2$. Furthermore, the intensity E_0 has disappeared from the equation as it is a common factor in all terms. This indicates that this intensity is a scaling factor, that determines the absolute value for the solution, while the qualitative behaviour is dictated by the remaining parameters.

The equation is written in non-dimensional form by multiplying it by a quantity with the unit m^2. All four coefficients in (3.128) can be used for this purpose. Depending on the particular problem, it will be natural to consider multiplication by W^2 and T^2.

The first step is to determine whether electromagnetic waves or electric currents are present. By multiplying the equation by the square of the characteristic length of the problem, i.e., $(\max(T,W))^2$, the resulting equation allows us to determine

USC UNIVERSIDADE DE SANTIAGO DE COMPOSTELA

the wave behaviour through the non-dimensional factor of the third term. This factor, $(2\pi \max(T,W)/\lambda)^2$, relates the characteristic length scale of the system to the electromagnetic wavelength. Depending on this ratio, three regimes of electromagnetic behaviour can be defined:

$$\left(\frac{2\pi \max(T,W)}{\lambda}\right)^2 \begin{cases} \gg 1 & \text{electromagnetic waves,} \\ \sim 1 & \text{electromagnetic waves and electric currents,} \\ \ll 1 & \text{electric currents.} \end{cases}$$

For low-frequency submerged arc furnaces, this ratio will always be significantly lower than 1. Therefore, in the applications considered in this thesis, it is assumed that the system operates in the *electric currents regime*, where electric currents are the dominant behaviour and the wave term can be neglected. Note that this approximation is a particular case of the eddy current assumption allowing to neglect the displacement current term in the Amperès's law (3.17).

In this regime, by neglecting the third term in (3.128) and multiplying the equation by T^2, it yields

$$\left(\frac{T}{W}\right)^2 \frac{\partial^2}{\partial \tilde{y}^2}\tilde{\mathbf{E}}(\tilde{y},\tilde{z}) + \frac{\partial^2}{\partial \tilde{z}^2}\tilde{\mathbf{E}}(\tilde{y},\tilde{z}) - 2i\left(\frac{T}{\delta}\right)^2 \tilde{\mathbf{E}}(\tilde{y},\tilde{z}) = \mathbf{0}. \tag{3.129}$$

The behaviour of this non-dimensional equation is governed by two non-dimensional factors, $(T/W)^2$ and $2(T/\delta)^2$. The first factor determines the aspect ratio or shape of the geometry, while the second one quantifies the strength of the electromagnetic induction, or skin effect. Based on the value of $(T/W)^2$, three different geometric configurations can be distinguished:

$$(T/W)^2 \begin{cases} \gg 1 & \text{thin and high,} \\ \sim 1 & \text{thick,} \\ \ll 1 & \text{long and thin,} \end{cases}$$

where 'high' describes a stretch in the vertical direction and 'long' describes a stretch in the horizontal direction. These regimes provide insights into the dominant geometric properties of the system, allowing a more focused analysis of the behaviour of the non-dimensional equation.

Similarly, different regimes for the electric current can be identified based on the value of the non-dimensional number $2(T/\delta)^2$. These regimes correspond to varying levels of skin effect, which can be categorized as follows:

$$2\,(T/\delta)^2 \begin{cases} \gg 1 & \text{high skin effect,} \\ \sim 1 & \text{low/moderate skin effect,} \\ \ll 1 & \text{negligible skin effect (DC approximation).} \end{cases}$$

USC UNIVERSIDADE DE SANTIAGO DE COMPOSTELA

It is worth noting that these regimes are sometimes described in terms of frequency, such as high frequency AC, low/moderate frequency AC and very low frequency AC. However, as the analysis shows, it is the skin depth which is important. Since the skin depth depends on several parameters, it is possible to be in a 'high skin effect' regime at a low frequency and vice versa, depending on the other parameters involved.

Our primary interest lies in the low/moderate skin effect regimes and the tendency towards the the DC approximation regime, which will be addressed in several parts of the thesis. On the other hand, the non-dimensional analysis will be also exploited in Chapter 5 to obtain an analytical 1D solution under suitable geometric assumptions.

USC
UNIVERSIDADE DE SANTIAGO DE COMPOSTELA

USC
UNIVERSIDADE
DE SANTIAGO
DE COMPOSTELA

Chapter 4

Numerical simulation of FeMn furnaces

The aim of this chapter is to exploit the mathematical models presented in the previous sections for the simulation of FeMn furnaces. Several 2D models will be applied to analyse specific features in localised parts of the furnace; in addition, a more complex 3D model will be used to evaluate the limitations of the previous models and to reproduce a more realistic behaviour of the whole furnace. The chapter is structured as follows. Section 4.1 is dedicated to the description of the furnace geometry and the main parts considered in the analysis. Section 4.2 deals with the numerical modelling of the interior of submerged furnaces using reduced 2D models to explain the inductive effects between the different regions. In Section 4.3, these reduced 2D approaches are compared with a genuine 3D model; Section 4.4 focuses on the calculation of induced currents in the surrounding parts of the furnace (lining and steel shell) and the analysis of the impact of structural changes in achieving energy savings. Finally, Section 4.5 presents some tools to simplify the 3D simulation.

This chapter reproduces contents from the following articles:

- M. Fromreide, D. Gómez, S. A. Halvorsen, E.V. Herland and P. Salgado (2021) *Reduced 2D/1D mathematical models for analyzing inductive effects in submerged arc furnaces*, Applied Mathematical Modelling, 98, 59–70. doi:10.1016/j.apm.2021.04.034

- M. Fromreide, D. Gómez, S.A. Halvorsen and P. Salgado (2023) *Induced currents in the lining and steel shell of submerged arc furnaces*. Journal of Sustainable Metallurgy, 9, 375-385. doi:10.1007/s40831-022-00625-6

- M. Fromreide, S.A. Halvorsen, M. Sparta, V.K. Risinggård, P. Salgado, D. Gómez and E.V. Herland (2021) *Effects of alternating currents in the hearth of submerged arc furnaces*. In Proceedings of the 16th International Ferro-Alloys Congress (INFACON XVI). doi:10.2139/ssrn.3926716

USC UNIVERSIDADE DE SANTIAGO DE COMPOSTELA

4.1 Furnace description: a simplified 3D geometry

This section presents a 3D model designed to analyse the electromagnetic characteristics of FeMn furnaces, with particular emphasis on the lower part of the electrodes. The model includes a simplified representation of the furnace, following principles similar to those proposed in the work of Herland et al. (2018).

As mentioned in the introduction, the whole furnace has a complex structure. However, in the modelling task, certain parts are often simplified based on the research interest. For example, studies concentrating on the baking of the electrode paste typically focus on a single electrode, assume axisymmetric conditions and use thermo-electrical models. These models include the contact clamps zone to better model the phase change, as well as factors such as contact clamps, cooling water and electrical current supply (see, e.g., Bermúdez et al. (1998, 2003)).

Similarly, works that address the eventual electrode breakage through thermo-mechanical studies also consider a single electrode and adopt an axisymmetric model (see Innvaer et al. (1985); Ingason & Jonsson (1996) and the references therein). In addition, a few studies take into account a 3D section of a single electrode to consider aspects such as the casing fins and contact clamps Innvær et al. (1987); Bermúdez et al. (2005).

In our specific case, the main focus is in the lower part of the electrode and the proximity effects between different components. Consequently, the modelling of the baking zone, electrode casing, contact clamps, busbar and flexibles will be omitted. Figure 4.1 shows an example of the complex configuration at the contact clamp level, highlighting the need for a fine mesh to capture the details of zones such as the casing or busbars. Alternatively, a combination of distributed and lumped models could be used to achieve a reasonable approximation. On the other hand, it should be noted that modelling the baking zone would require a coupling with a thermal model to accurately simulate the associated processes.

Therefore, in this study, the electrical supply to the furnace will be simplified by assuming that the current is applied through the tops of the electrodes at a given height. Consequently, a cylindrical 3D geometry will be considered, including the internal conductive materials described below, as well as the surrounding air (see Figure 4.2). The system is analysed using the mathematical model described in Section 3.2.

The interior of the furnace can be divided into several distinct areas, the main ones being the inner layers, coke beds, linings and the surrounding steel shell. These zones are shown in Figure 4.4. The function of the steel shell (zone 9) is to support the weight of the furnace, and is typically constructed of structural steel. It is worth noting that both the steel shell and the oxide lining (zone 8) extend the full height of the furnace, whereas the carbon lining (zone 7) does not extend as far.

USC UNIVERSIDADE DE SANTIAGO DE COMPOSTELA

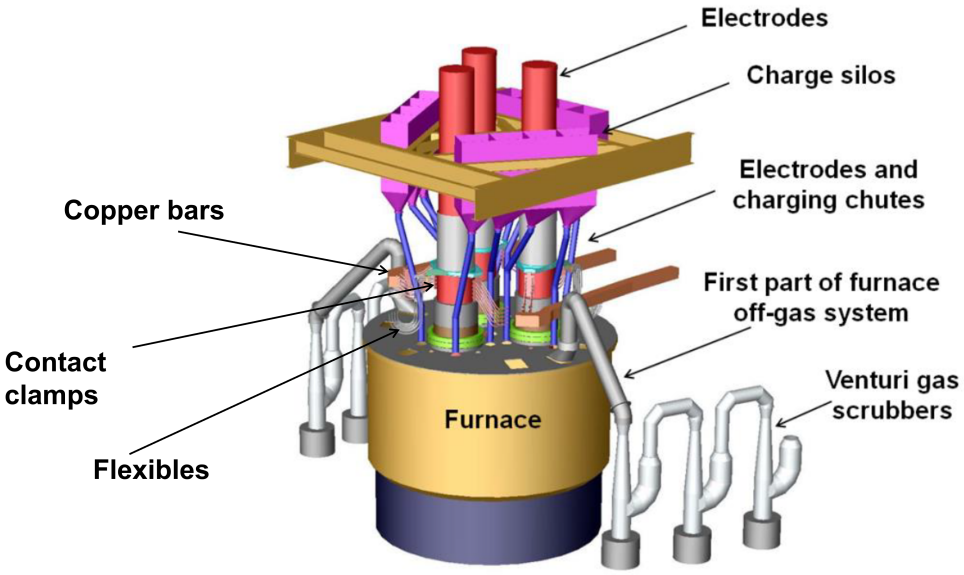

Figure 4.1. Furnace elements around the electrodes near the contact clamps. Reproduced with permission from Kadkhodabeigi et al. (2015).

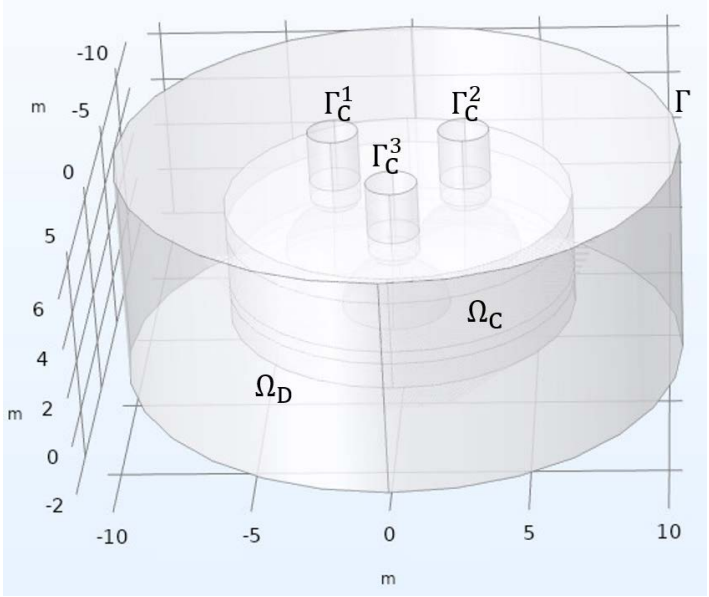

Figure 4.2. Simplified 3D geometry for modelling FeMn furnaces.

USC
UNIVERSIDADE
DE SANTIAGO
DE COMPOSTELA

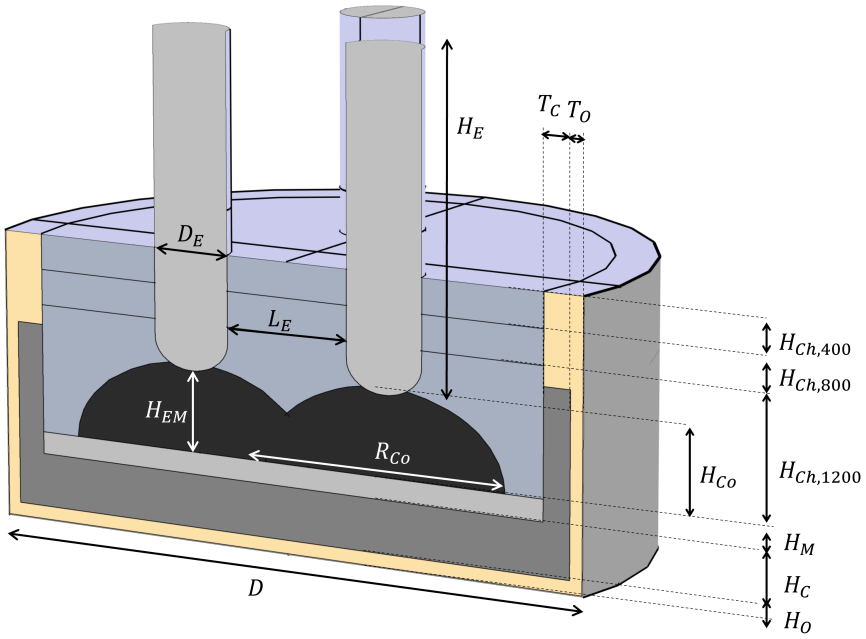

Figure 4.3. Geometric parameters of the 3D FeMn furnace model.

Moving inside the furnace, a first section can be observed consisting of the charge components (mixture) at different temperatures (zones 2, 3 and 4). This section includes the buried electrodes (zone 1), the coke bed (zone 5) and, at the bottom, a layer containing the resulting alloy. The term 'coke bed' refers to the enriched region between the electrode tip and the molten metal bath (zone 6) where the oxides are in a liquid state. The coke beds are modelled as half-ellipsoids that are connected/overlapping at the centre of the furnace.

The steel roof of the furnace is ignored in this study as it is not relevant to the specific investigation being undertaken. For detailed information on induced currents in the steel roof, reference is made to the work of Herland et al. (2018).

This study also assumes that the steel shell and carbon lining of the furnace are continuous and isotropic. Furthermore, any transition zones such as welds in the steel shell or cracks in the lining are not considered. These simplifications permit a simpler analysis.

With regard to internal raw materials, it should be noted that they are typically granular in nature. However, for simplicity, they are treated as uniform by using reasonable average bulk properties. This approach is commonly used in large-scale furnace models. Nevertheless, some research has been carried out to determine the electrical and thermal conductivity of granular materials using homogenised models in a metallurgical context Eidem (2008); Rooney (2019).

USC UNIVERSIDADE DE SANTIAGO DE COMPOSTELA

Table 4.1. Geometric parameters of the 3D FeMn furnace model.

Parameter	Value [m]	Description
D_F	14	Furnace diameter
D_E	1.9	Electrode diameter
H_E	4	Electrode height
d	4.9	Electrode distance (center-center)
H_{EM}	1.815	Electrode tip to metal distance
H_M	0.5	Metal alloy Thickness
$H_{Ch,400}$	0.8	Charge, 400 °C thickness
$H_{Ch,800}$	0.8	Charge, 800 °C thickness
$H_{Ch,1200}$	2.9	Charge, 1200 °C thickness
H_{Co}	2.0	Coke bed height
R_{Co}	3.0	Coke bed radius
H_C	1.2	Carbon lining bottom thickness
T_C	0.67	Carbon lining side thickness
H_O	0.3	Oxide lining bottom thickness
T_O	0.3	Oxide lining side thickness
T_{st}	0.025	Steel shell thickness

The 3D geometry of the furnace is defined by the set of geometric parameters outlined in Table 4.1. The dielectric (air) surrounding the conducting region is modelled as a cylinder with dimensions (R,H) chosen to be sufficiently large to not affect the solution within the conductors.

As mentioned above, the coke beds are modelled as half-ellipsoids with the horizontal section being circular. This implies that the horizontal semi-axes x and y, denoted as the coke bed radius (R_{Co}) in Table 4.1, are equal, while the vertical semi-axis z, denoted as the coke bed height (H_{Co}), can vary. In the specific case, the electrode distance (centre to centre) is set to 4.9 m and the coke bed radius is set to 3 m. Consequently, the three coke beds will overlap at the centre, effectively forming a single coke bed.

Table 4.2 shows the electrical conductivity, relative magnetic permeability and skin depth at 50 Hz of the different materials. The charge material is divided into three layers to account for the temperature dependent conductivity, following the layer division introduced in Dhainaut (2004) based on three temperature ranges (400 °C, 800 °C and 1200 °C). The steel shell, although typically a ferromagnetic material, is simplified for the purposes of this study as a linear magnetic material with a constant magnetic permeability.

Regarding the operating conditions, an alternating current source with a frequency of $f = 50$ Hz and an amplitude in the range of $100 - 190$ kA is applied. The phase shift between the electrodes is 120 degrees in an anti-clockwise rotation. Thus, the

UNIVERSIDADE DE SANTIAGO DE COMPOSTELA

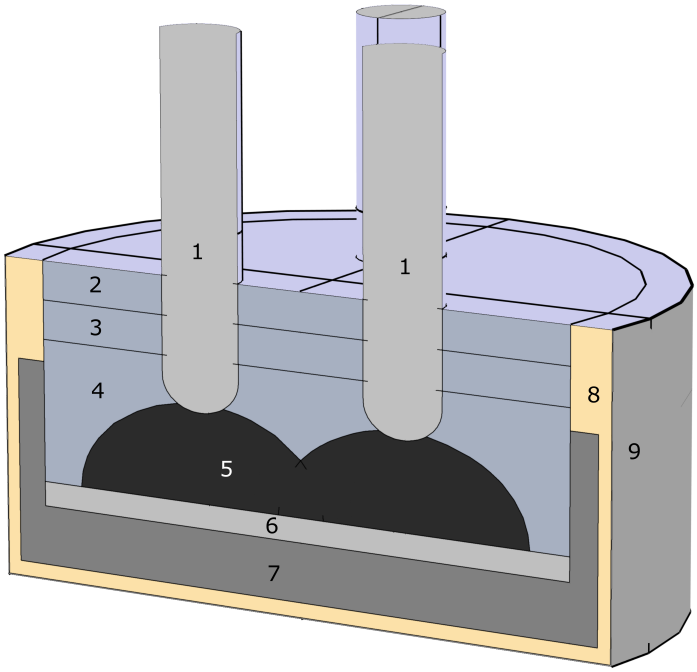

Figure 4.4. 3D sketch of a FeMn furnace model with numbered material regions: 1. Electrodes 2. Charge 400 °C 3. Charge 800 °C 4. Charge 1200 °C 5. Coke beds 6. Alloy 7. Carbon lining 8. Oxide lining 9. Steel shell.

Table 4.2. Material properties of the FeMn furnace and skin depth at 50Hz.

Material	σ[S/m]	μ_r[−]	δ[m]
Air	0	1	−
Electrode	$5 \cdot 10^4$	1	0.32
Charge 400 °C	0.075	1	260
Charge 800 °C	0.15	1	180
Charge 1200 °C	15	1	18
Coke bed	500	1	3.2
Alloy	$1.5 \cdot 10^5$	1	0.18
Carbon lining	$1.4 \cdot 10^4$	1	0.60
Oxide lining	$1 \cdot 10^{-6}$	1	$7.1 \cdot 10^4$
Steel shell	$3 \cdot 10^6$	100	0.0041

USC UNIVERSIDADE DE SANTIAGO DE COMPOSTELA

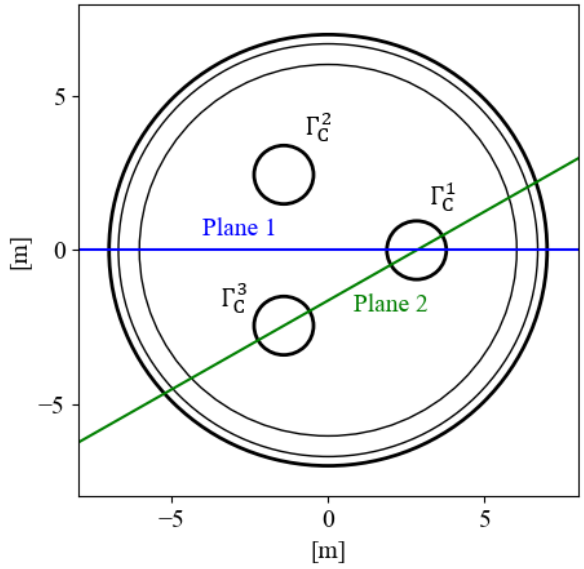

Figure 4.5. Sketch of Plane 1 and Plane 2 in a horizontal cross section of the 3D domain.

mathematical model used for the simulation is the one described in Section 3.2, which considers the tops of the three electrodes as electric ports.

To postprocess the results, two 2D planes are introduced, as shown in Figure 4.5. These planes cover the full width and height of the 3D domain. Plane 1 divides the furnace in two, intersecting the furnace centre and the centre of electrode 1, while Plane 2 intersects the centre of electrode 1 and electrode 3.

4.2 Inductive effects in the furnace hearth

In this section, the focus is on the study of the inductive effects of low frequency AC sources within submerged arc furnaces, where highly conducting materials (metal, electrodes) are combined with moderate conductors (slag, coke bed) and very low conducting materials (charge, insulating lining). To analyse the influence of geometry and materials and understand the inductive effects between these different regions, a reduced 2D model will be used. The study will include non-dimensional analysis and numerical simulations. In addition, 2D models will also be employed to compare the use of true AC models with DC approximations. This comparison will be made by considering different approximations for the coke bed region.

USC UNIVERSIDADE DE SANTIAGO DE COMPOSTELA

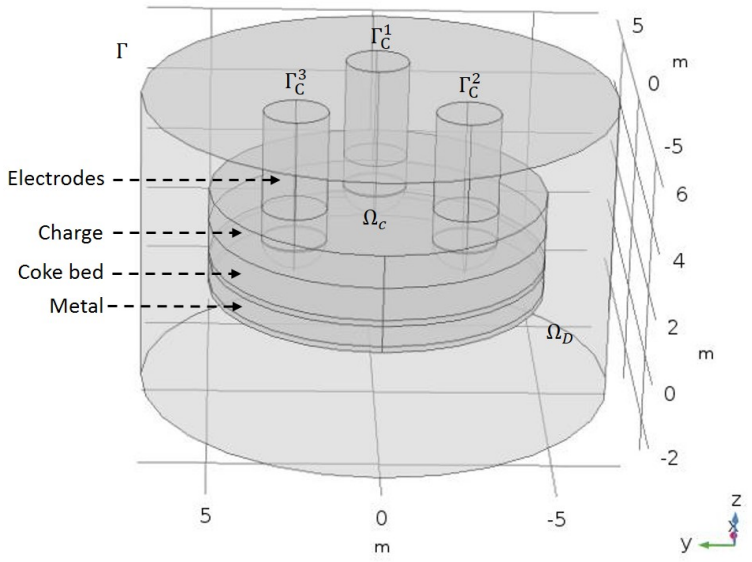

Figure 4.6. Simplified 3D furnace geometry with flat coke beds; carbon lining and steel shell are not included.

4.2.1 2D model with in-plane currents

To study 2D models, the geometry of the furnace was simplified by considering a flat coke bed and a single layer of charge; furthermore, the surrounding linings and the steel shell are neglected, resulting in the geometry shown in Figure 4.6. Based on this simplified 3D geometry, a 2D model with in-plane currents is defined. This model considers two rectangular electrodes submerged inside the furnace, which is divided into three material layers: charge material, coke bed and metal alloy as shown Figure 4.7. The geometric parameters characterising this simple 2D case are given in Table 4.3, where the diameter D is interpreted as the width of the 2D furnace. The current is assumed flowing in this plane, so $\mathbf{J} = J_y(y,z)\mathbf{e}_y + J_z(y,z)\mathbf{e}_z$. Accordingly, the mathematical equations used are those presented in Section 3.4.

In this simple model, all materials are assumed to be non-magnetic ($\mu_r = 1$) and their electrical conductivity is used to characterise them. The conductivity assigned to each material can be found in Table 4.4, along with its corresponding skin depth. The conductivity value assigned to the charge layer corresponds to the Charge 800 °C given in Table 4.2.

Figure 4.7 illustrates the different material regions by plotting the material skin depth evaluated at a 50 Hz AC source. Note that the electrode tips have been rounded to mitigate strong corner effects in the numerical simulations. However, this minor adjustment is not reflected in Figure 4.8, Figure 4.9 or the non-dimensional analysis.

USC UNIVERSIDADE DE SANTIAGO DE COMPOSTELA

Table 4.3. Geometric parameters for the model with flat coke beds.

Parameter	Value [m]	Description
D	13	Furnace diameter
D_E	1.9	Electrode diameter
L_E	4.0	Electrode-electrode distance
H_M	0.5	Metal layer thickness
H_{Co}	2.0	Coke bed layer thickness
H_{Ch}	1.0	Charge layer thickness
H_E	6.3	Total electrode height
H_{EM}	1.7	Electrode-metal distance
H_A	5.0	Distance (z-direction) from conducting parts to the outer boundary
L_A	5.0	Distance (y-direction) from conducting parts to the outer boundary

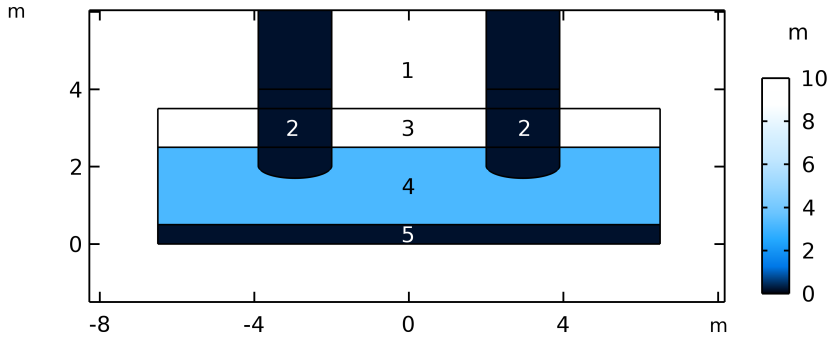

Figure 4.7. 2D model with in-plane currents and flat coke beds. Material regions: 1. Air 2. Electrodes 3. Charge 4. Coke bed 5. Alloy. The colours indicate the material skin depth at $f = 50$ Hz, limited to $\delta < 10$ m.

Table 4.4. Conductivity and skin depth at $f = 50$Hz; $\mu = \mu_0$.

Material	σ [S/m]	δ [m]
Charge	0.15	184
Coke bed	500	3.18
Metal	$1.5 \cdot 10^5$	0.18
Electrodes	$1.5 \cdot 10^5$	0.18

USC UNIVERSIDADE DE SANTIAGO DE COMPOSTELA

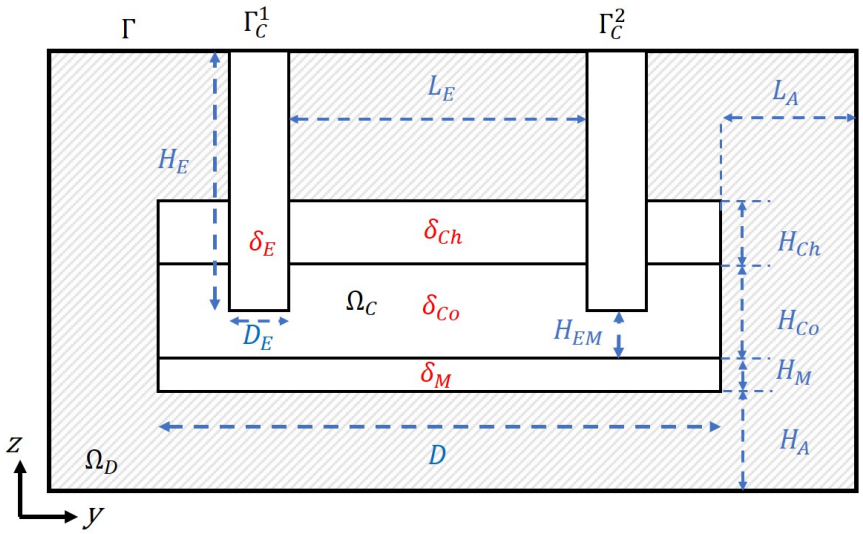

Figure 4.8. Sketch of the 2D model with geometric parameters (blue) and skin depths (red).

4.2.2 Non-dimensional analysis

The dimensional analysis performed in Section 3.7 showed the occurrence of different regimes of electrical behaviour in conductors. In particular, for SAFs it was concluded that the wave behaviour can be neglected and that the electromagnetic fields are mainly governed by the non-dimensional parameters $(T/W)^2$ and $2\,(T/\delta)^2$. In this section, this analysis will be applied to the simple 2D model of a SAF.

The simplified 2D furnace setting in Figure 4.7 is defined by its geometry, the material properties and the applied current. Considering the material properties in terms of skin depth, the model can be characterised by 14 unit length parameters in addition to the applied current. The current acts as a scaling factor, while the qualitative behaviour is determined by the non-dimensional parameters introduced in Section 3.7.

Figure 4.8 shows the geometry of the simple 2D furnace model and highlights the defining parameters. The symbol notation used for these parameters follows the conventions introduced in Table 4.1. As can be seen in the figure, the charge is treated as a single layer and the coke bed is also represented as a layer spanning the entire width of the furnace.

Selection of the parameters to be studied

Although all fourteen parameters shown in Figure 4.8 are necessary to determine the geometry, not all of them have a significant effect on the behaviour of the

USC UNIVERSIDADE DE SANTIAGO DE COMPOSTELA

electromagnetic fields inside the furnace. By making reasonable assumptions, the number of important parameters can be reduced.

The electrodes themselves are not of interest as the focus is on the furnace interior. Therefore, the material properties and scales of the electrodes (δ_E and H_E) can be neglected, although their high conductivity remains important.

The air surrounding the furnace is included in the model to ensure proper boundary conditions for the magnetic vector potential. The distance from the conducting parts to the outer boundary must be sufficiently large, so that the numerical solution in the interior is not affected. These parameters are assigned reasonable values to ensure accurate numerical solutions. However, the qualitative results will still hold even if some numerical precision is lost, and then the parameters H_A and L_A can be ignored in the analysis.

As the low conductivity layer is traversed by the high conductivity electrodes, the current will flow mainly from the electrodes to the coke bed. Therefore the parameters associated with the charge layer (δ_{Ch} and H_{Ch}) can be neglected. Further, it is assumed that most of the current flows in the space between the electrodes, rather than on the outside, thus the electrode distance L_E can be assumed to be more important than the furnace diameter D. When the current leaves the electrodes it may distribute itself, both between the electrodes and down into the metal alloy. Considering the high conductivity of liquid manganese, the skin depth in the metal layer is assumed to be much smaller than the layer thickness. As will be shown later, the proximity effect between a good conductor and its surroundings can be important. With this in mind, the parameters defining the current distribution in the metal alloy, H_M and δ_A, must be considered.

In an industrial furnace, the coke bed is typically a mixture of solid coke particles and liquid slag and metal, resulting in a wide range of electrical conductivity within a small region Eidem (2008). However, for simplicity, a uniform layer is considered and a reasonable assumption is made regarding the average effective conductivity. The value is given in Table 4.2, which provides a skin depth of the same order as the dimensions of the coke bed. This suggests that variations in the composition and geometry of the coke bed play a significant role in the operation of the furnace.

The current flowing from the electrode tip into the metal tends to be confined in the area determined by the electrode diameter, D_E, and the electrode-to-metal distance (or set point), H_{EM}. Thus, these two parameters are also important. Taking these considerations into account, the initial fourteen parameters can be reduced to seven, namely D_E, L_E, H_{Co}, H_M, H_{EM}, δ_M and δ_{Co}.

As discussed in Section 3.7, the parameters must be considered in terms of non-dimensional quantities such as $(T/W)^2$ and $2\,(T/\delta)^2$. Figure 4.9 illustrates the 2D model with five rectangular regions of interest defined. These regions represent the main current paths within the furnace. It has already been established that the

USC UNIVERSIDADE DE SANTIAGO DE COMPOSTELA

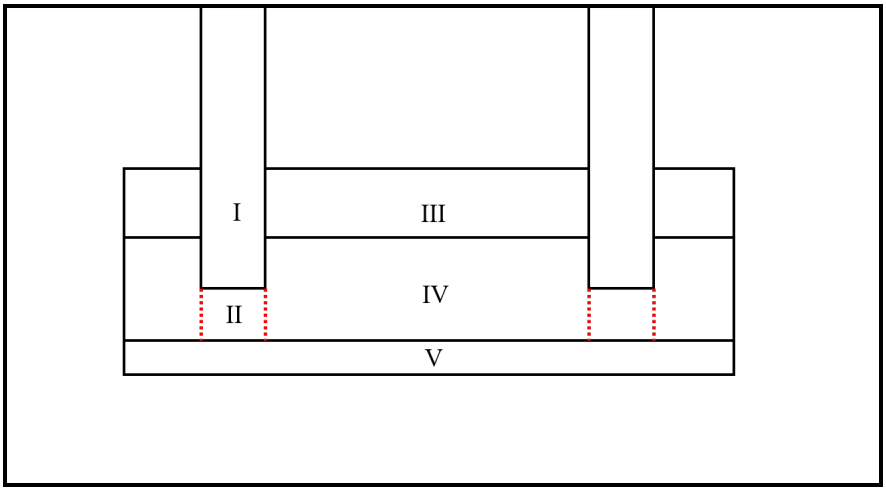

Figure 4.9. Rectangular sub-regions defined within the simple 2D model.

charge and electrodes do not have a significant effect and this fact will be emphasised in the following discussion.

By considering each of these sub-regions individually, the non-dimensional analysis in Section 3.7 can be applied to describe the behaviour of the electric fields. The dimensions of each of the five rectangles are defined so that the main current flow is parallel to the length. For example, in the case of the electrodes (I) and the region below the electrode tip (II), the vertical component represents the width, while the electrode diameter represents the thickness. In the remaining regions, the horizontal component represents the width and the layer thickness corresponds to the height. It is important to note that the non-dimensional numbers associated with the electrodes are included only to illustrate the skin effect and the 1D behaviour within these regions.

Table 4.5 gives the values of the non-dimensional numbers $(T/W)^2$ and $2\,(T/\delta)^2$ for each of the sub-regions defined in Figure 4.9. In the given geometry, and with the specified material properties, it is evident that the alloy and electrode regions fall into the long and thin regime ($(T/W)^2 \ll 1$).

Table 4.5. Non-dimensional numbers based on parameters given in Table 4.3 and Table 4.4. W: Width, H: Height.

Region	W	T	$(T/W)^2$	$2(T/\delta)^2$
I	H_E	D_E	0.09	223
II	H_{EM}	D_E	1.25	0.71
III	L_E	H_{Ch}	0.06	6E-5
IV	L_E	H_{Co}	0.25	0.79
V	L_E	H_M	0.015	15

USC UNIVERSIDADE DE SANTIAGO DE COMPOSTELA

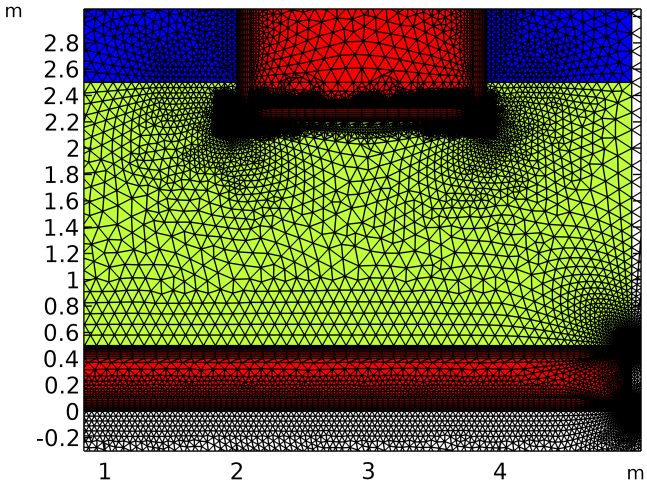

Figure 4.10. Mesh for the reference case around the right electrode. The background colours indicate the different materials.

Furthermore, the values of $2\,(T/\delta)^2$ indicate that the electric field will behave differently in different parts of the furnace. The electrodes and alloy are in the high skin effect regime, indicating significant attenuation of the electric field. In contrast, the coke bed is in the low to moderate skin effect regime. The charge layer falls into the DC approximation regime. In addition, due to its relatively low conductivity and the fact that the electrodes are immersed in the coke bed, the current flow through the charge layer is expected to be negligible.

Numerical simulations

The 2D model was implemented in COMSOL Multiphysics® using the *Magnetic and Electric fields Interface*. To ensure a well-defined mesh for each parameter setting, the element size was determined based on the skin depth in the most conductive materials, such as electrodes and metal. Specifically, a boundary layer of rectangular elements was defined on the surface of these materials. This approach allowed increased resolution in the direction normal to the surface without significantly increasing the overall mesh size. In addition, the mesh was refined around the electrode tips and at the corners. Figure 4.10 shows a detailed representation of the mesh created for the reference case following these guidelines. The different materials are indicated by their respective background colours.

The problem has been solved for three different cases, which take into account variations in the conductivity of the coke bed. First, a reference case is considered using the parameters listed in Table 4.3 and Table 4.4.

Numerical results are presented in terms of the distributions of the current density $\mathbf{J}$, the active power density and the dissipated power in each region. It is important

USC UNIVERSIDADE DE SANTIAGO DE COMPOSTELA

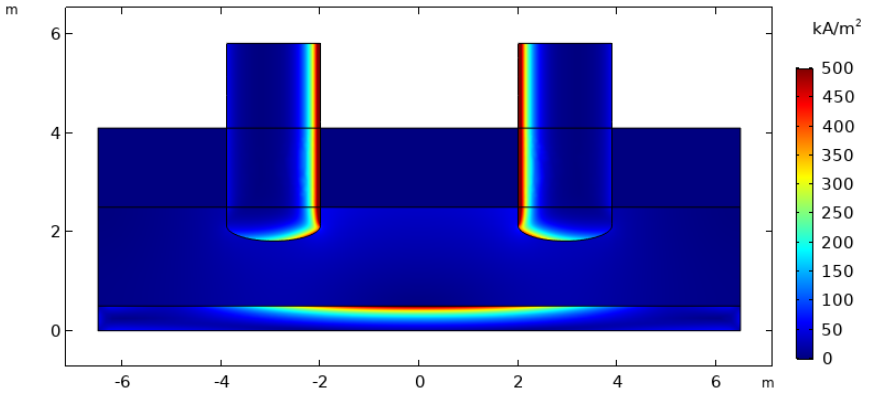

Figure 4.11. Current density distribution for the 2D reference case.

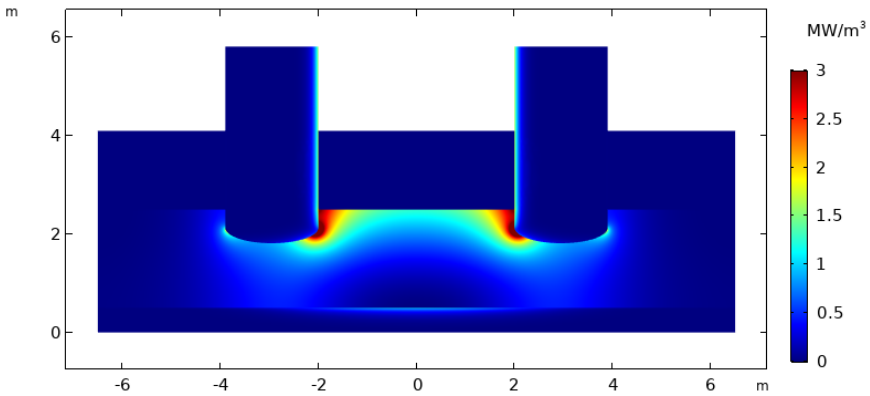

Figure 4.12. Power density distribution for the 2D reference case.

to note that the active power density (in $\mathrm{W/m^3}$) at each point in the furnace is given by

$$p(x,y) = \frac{|\mathbf{J}(x,y)|^2}{2\sigma}. \tag{4.1}$$

On the other hand, the dissipated power P in a given region R (measured in $\mathrm{W/m}$) can be calculated by integrating p over this region, that is,

$$P = \int_R p(x,y)\, dA. \tag{4.2}$$

The current density and power density distributions for the reference case are given in Figure 4.11 and Figure 4.12, respectively. In these figures, the skin effect is observed to be significant in both the electrodes and the metal alloy. Moreover, due to the proximity effect of the two electrodes, the current tends to concentrate near the inner walls. However, in the coke bed layer the current distribution appears to be more uniform. It is worth noting that some of the current flows directly between the electrodes in the upper part, while some flows down into the metal. It can also be seen that only a negligible amount of current flows through the charge layer.

USC UNIVERSIDADE DE SANTIAGO DE COMPOSTELA

The power density distribution shows that most of the power is generated in the coke bed region. However, there is some concentration of power in the surface layers of the metal and electrodes. The figures agree well with the interpretation of the non-dimensional numbers given in Table 4.5.

The interest is in how the electrical distribution behaves with the parameters. The values in Table 4.5 suggest that the distribution is most sensitive to changes in the coke bed, as the non-dimensional numbers are of $\mathcal{O}(1)$. As the power density distribution in Figure 4.12 shows, most of the power is generated in the coke bed. This emphasises the crucial role of the coke bed region in determining the overall electrical conditions within the furnace.

In addition to the model defined by Table 4.3 and Table 4.4, two additional cases have been simulated. One case with a very low conductivity for the coke bed ($\sigma_{Co} = 1\ \mathrm{S/m}$), and the other case with a higher conductivity ($\sigma_{Co} = 5000\ \mathrm{S/m}$). The other parameters are kept constant and the input current is fixed at 115 kA. The power density distributions for these two cases are shown in Figure 4.13 and Figure 4.14, for $\sigma_{Co} = 1\ \mathrm{S/m}$ and $\sigma_{Co} = 5000\ \mathrm{S/m}$, respectively.

In the case of high coke bed conductivity, it can be observed that the electric field distribution is approximately one-dimensional. This behaviour is further discussed in Chapter 5.1, where a 1D model for the electric field distribution is described. It is important to note that this behaviour is found when the aspect ratio $(T/W)^2$ is kept constant. Since the enhanced skin effect causes the majority of the current to flow in a thin layer near the top of the coke bed, the effective thickness is closer to δ_{Co} than to T_{Co}, placing the coke bed in the 'long and thin' regime.

In particular, it is interesting to study how the current flows through the coke bed. Another way of describing the distribution is to consider the horizontal currents through the furnace centre. This shows how deep the current flows in the furnace, and to what extent it flows through the metal. Figure 4.15 shows the current density across the vertical section at the centre of the coke bed for the three cases of different conductivity. It can be seen that the changes in coke bed conductivity change both the total amount of horizontal current passing through it and the internal distribution of the current.

The non-dimensional analysis revealed that the field behaviour is most sensitive to changes in the coke bed. With natural first assumptions, the effective conductivity, effective height and width of the coke bed were identified as important parameters affecting the electromagnetic behaviour. The numerical simulations further confirmed that the coke bed is the region where most of the electrical power is dissipated, which is consistent with prior knowledge and other published models Herland et al. (2019). The hearth of the furnace is also one of the least accessible zones for measurements and detailed knowledge of its structure and material properties is often limited. Large variations in the coke bed structure have been

USC UNIVERSIDADE DE SANTIAGO DE COMPOSTELA

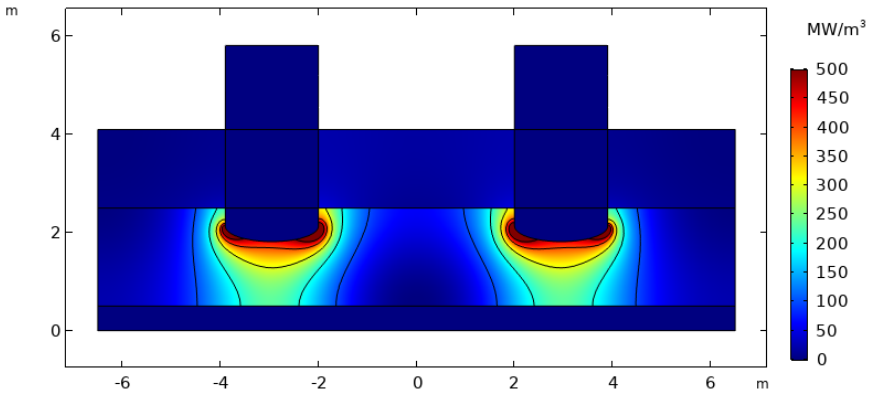

Figure 4.13. Power density distribution for the 2D model with $\sigma_{Co} = 1$ S/m. The color range is limited to 500 MW/m^3.

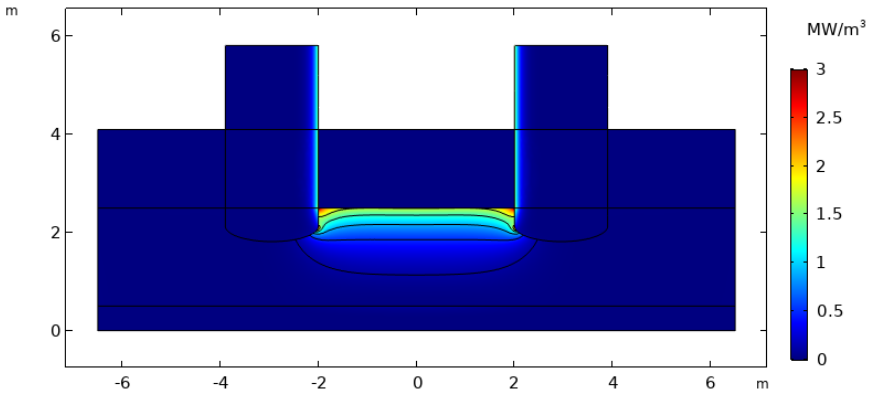

Figure 4.14. Power density distribution for the 2D model with $\sigma_{Co} = 5000$ S/m. The colour range is limited to 3 MW/m^3.

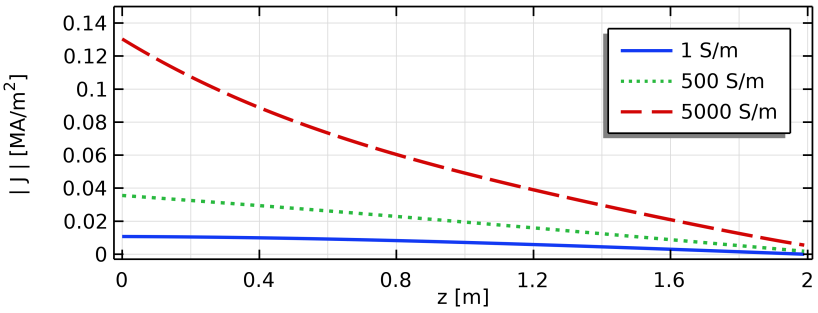

Figure 4.15. Current density norm in the coke bed center ($y = 0$ m) for different values of coke bed conductivity. The limits $z = 0$ m and $z = 2$ m correspond to the coke bed layer top and bottom, respectively.

USC UNIVERSIDADE DE SANTIAGO DE COMPOSTELA

reported by dig-outs of industrial furnaces as discussed in Section 2.3. Consequently, it is reasonable to expect significant variations in material properties and geometry within the furnace hearth.

The greatest concentration of power generation is in the coke bed, just beneath the electrode tips. Hence, the shape of the electrode tip and the effective contact region with the coke bed can have a significant effect on overall furnace operation. For example, a 'pencil' shaped electrode tip would likely provide a significantly different contact area than a broad cylindrical shaped tip. This aspect was not considered in this study and further investigation is recommended.

4.2.3 Comparing AC models with DC models

In this section, numerical results based on 2D in-plane models are presented in order to compare the DC approach with the AC approach. The aim is to analyse whether the simplified DC models, used in certain proposals in the literature and very valuable in multiphysics solutions, can provide accurate estimates for real industrial furnaces.

In the DC model, the current is allowed to flow only within a surface layer of thickness δ in the electrodes and metal to mimic the skin effect. Given the strong proximity effect observed in Figure 4.11, only the inward parts of the electrodes are included in the model.

Two different geometries have been considered in this section, with variations in the shape of the coke beds, the charge composition and the presence or not of carbon lining and steel shell:

- Rectangular coke bed without lining and steel shell, considering only one layer in the charge (as in the previous section);
- Separated coke beds with an ellipsoidal shape under each electrode, including lining and steel shell in the geometry and differentiating three layers in the charge.

For each geometric case, both the DC and AC models have been used. In each of the AC simulations, the same current is applied with an amplitude of 100 kA, while the root mean square (RMS) value $100/\sqrt{2}$ kA is applied for the DC simulations. In the case of flat coke beds, different values of electrical conductivity have been used. Table 4.6 gives a summary of the simulation cases. For the AC case with ellipsoidal coke beds, a reference value for the electrode tip position was set at $H_{EM} = 1.215$ m (see Figure 4.3). Through an iterative procedure, the electrode tip positions for the other AC cases were adjusted to obtain the same total electrical power as in the ellipsoidal case. The values obtained from the simulations are also included in Table 4.6; these values were used in each case for the DC approximation.

The power distributions for the AC and DC cases are shown in Figure 4.16. In the DC

Table 4.6. Simulation cases comparing AC versus DC models.

Simulation	Case 1		Case 2		Case 3		Case 4	
Coke bed shape	ellipsoidal		flat		flat		flat	
Coke bed conductivity σ_{Co} [S/m]	500		100		500		1500	
Distance H_{EM} [m]	1.215		0.143		1		2.39	
Current source	AC	DC	AC	DC	AC	DC	AC	DC
Current data [kA]	100	$100/\sqrt{2}$	100	$100/\sqrt{2}$	100	$100/\sqrt{2}$	100	$100/\sqrt{2}$
Total Power [MW/m]	11.15	9.92	11.15	10.03	11.15	7.04	11.15	5.82

solution, the white areas of the electrode and alloy represent the regions excluded from the computational domain. In general, the distributions look quite similar, with most of the power being generated in the coke bed. The distribution within the modelled part of the electrode is uniform and the current continues through the coke bed, into the alloy and towards the right electrode. On the other hand, in the AC case, skin and proximity effects are clearly visible in both the electrode and the alloy. In addition, inductive effects are observed in the coke bed, resulting in a distribution that is more skewed towards the other electrode compared to the DC case.

Figure 4.17 shows the power distributions for the cases of flat coke beds with different conductivity values, using both the AC and DC approaches. For the lowest conductivity (and lowest electrodes), the current predominantly flows downwards into the alloy, where it then moves horizontally between the electrodes. For the moderately conducting coke bed, the current exhibits a dual flow pattern. It flows both directly between the electrodes within the coke bed and downwards into the alloy. Finally, for the highest conductivity, the current flows mainly at the top of the coke bed.

When comparing these results with those obtained from the DC simulations, an increasing difference is observed as the coke bed conductivity increases. In the case of a low conducting coke bed, the AC and DC two solutions appear very similar. When the conductivity is increased, a different scenario arises. In the moderate conducting case, ($\sigma_{Co} = 500$ S/m), most of the DC power is generated below the electrode tips, and very little between the electrodes. This effect is further enhanced in the latter case, where the DC model shows a more uniform power density around and below the electrodes, compared to the large horizontal current concentrations in the AC solutions. It is also noticeable how the total power decreases significantly in the DC cases.

For each of the simulation cases, the integrals of the 2D power density for each material region are shown in Table 4.7.

When comparing the AC and DC models, the lower conductivity results in an AC model that can be adequately approximated, at least quantitatively, by the DC model. In the case of DC current, it tends to be distributed uniformly over the entire section. On the other hand, AC current accumulates due to skin and proximity effects.

USC UNIVERSIDADE DE SANTIAGO DE COMPOSTELA

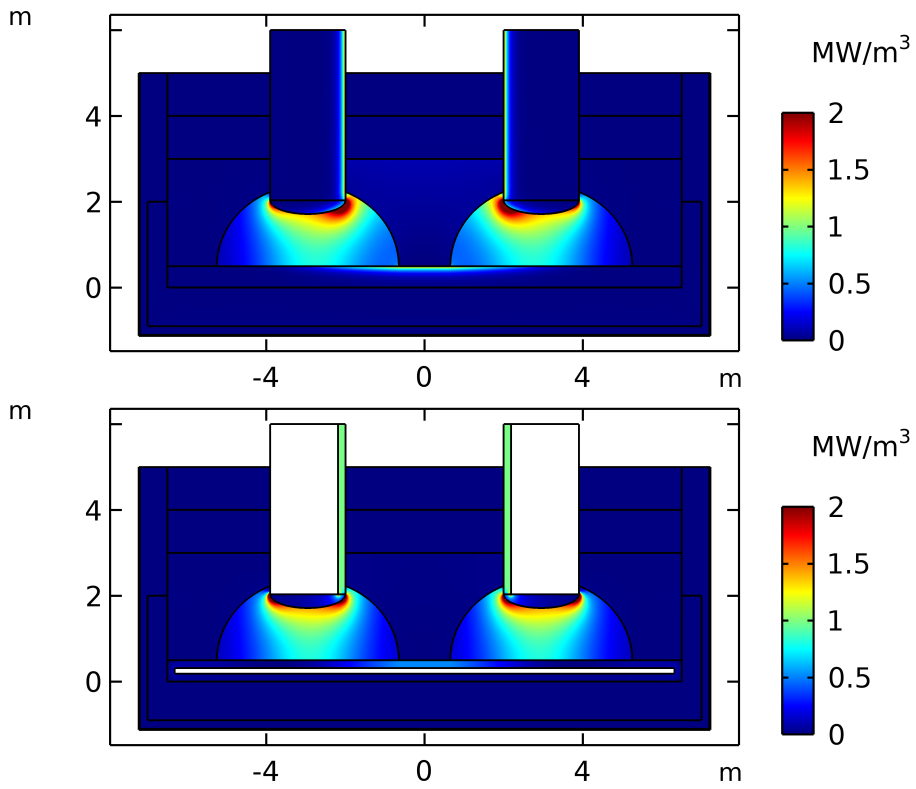

Figure 4.16. Power density for the 2D model with separated ellipsoidal shape coke beds (case 1): AC solution (top) and DC solution (bottom). The colour scale has been limited to 2 MW/m^3.

USC UNIVERSIDADE DE SANTIAGO DE COMPOSTELA

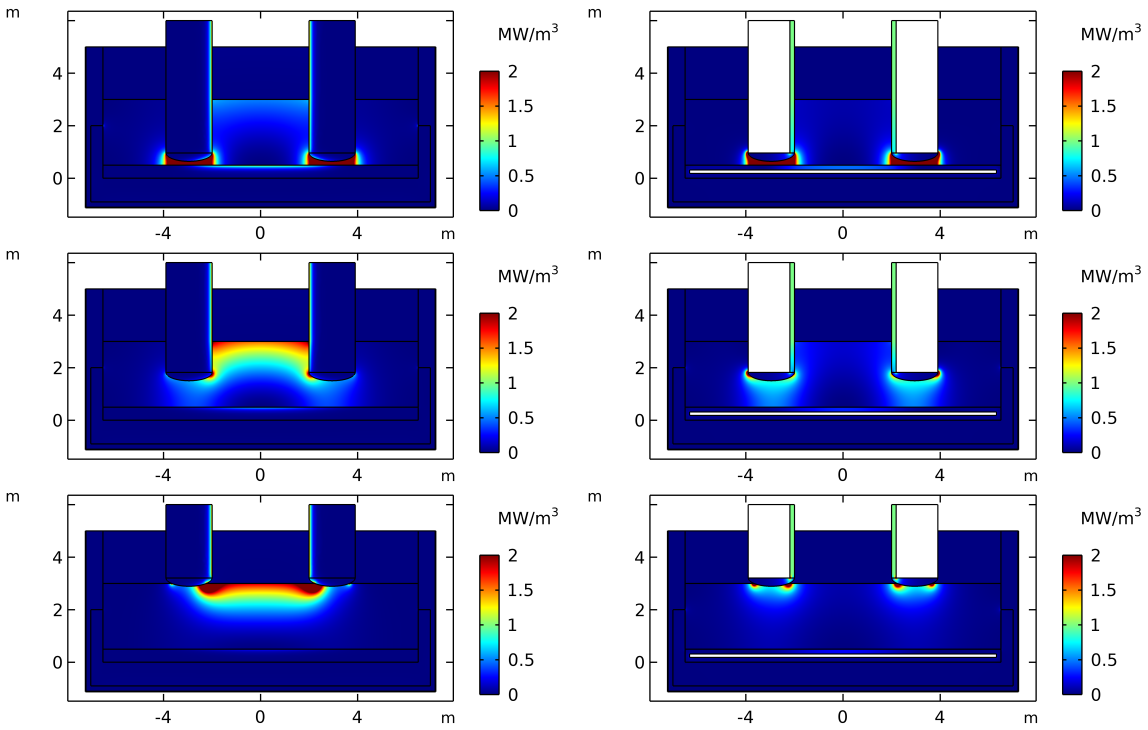

Figure 4.17. Power density for the 2D models with flat coke bed: Case 2 (top), Case 3 (middle) Case 4 (bottom): AC solutions (left) and DC solutions (right). The colour scale has been limited to 2 MW/m^3.

USC UNIVERSIDADE DE SANTIAGO DE COMPOSTELA

Table 4.7. Dissipated power (2D) [MW/m], for both AC and DC current sources, in the different parts of the furnace for Cases 1-4.

Simulation	Case 1		Case 2		Case 3		Case 4	
Coke bed shape	ellipsoidal		flat		flat		flat	
σ_{Co} [S/m]	500		100		500		1500	
H_{EM} [m]	1.215		0.143		1		2.39	
Power density	Fig. 4.16		Fig. 4.17 (top)		Fig. 4.17 (middle)		Fig. 4.17 (bottom)	
Current source	AC	DC	AC	DC	AC	DC	AC	DC
Electrodes	1.350	1.573	1.618	1.876	1.262	1.526	1.008	1.180
Charge, 400 °C	0.008	0.001	-	-	-	-	-	-
Charge, 800 °C	0.052	0.007	0.120	0.013	0.082	0.006	0.064	0.007
Charge, 1200 °C	0.403	0.105	-	-	-	-	-	-
Coke bed(s)	8.517	7.714	8.594	7.619	9.308	5.180	9.786	4.329
Alloy	0.622	0.486	0.630	0.497	0.317	0.298	0.123	0.258
Carbon lining	0.055	0.034	0.053	0.000	0.053	0.000	0.051	0.000
Oxide lining	0.000	0.000	0.000	0.000	0.000	0.000	0.000	0.000
Steel shell	0.145	0.000	0.138	0.000	0.130	0.000	0.119	0.000
Total Power [MW/m]	11.15	9.92	11.15	10.03	11.15	7.04	11.15	5.82

In each of the four cases considered, the DC simulations underestimated the power dissipated in the whole furnace and in the hearth, but not in the electrodes, where the values were slightly higher than in the AC cases. In general, the DC solutions are closer to the AC solutions when horizontal currents can be neglected outside of the highly conducting alloy. Such currents are partly due to the shortest distance between the electrodes if the coke bed conductivity is large enough, but are also caused by induction due to the strong currents in the underlying alloy. The AC in the coke bed is pushed upwards by the adjacent current in the alloy. Note that in Case 1 and Case 2 the DC does not deviate much from the AC; the difference increases as the coke bed conductivity increases and the AC power can be twice the value of the DC power value in the coke bed. Moreover, the DC power decreases as the coke bed conductivity increases.

The AC distribution between the electrodes looks 1D. This has motivated the analytical 1D model which will be introduced in Section 5.1.

4.2.4 Conclusions

The analysis and case studies show that 2D models are valuable tools for gaining insight into the qualitative aspects of current paths in large metallurgical furnaces. The electric current distribution in the furnace is governed by two types of non-dimensional numbers, $(T/W)^2$ and $2\,(T/\delta)^2$, i.e., squared geometric aspect ratios and the squared ratio between a length/thickness and the corresponding skin depth.

USC UNIVERSIDADE DE SANTIAGO DE COMPOSTELA

Analysis of non-dimensional equations with natural assumptions for parameter values is sufficient to show that the coke bed properties (conductivity, effective height and width) are important for the electrical conditions of the furnace and therefore important for furnace operation.

When current flows between two good conductors through a less conductive material, the AC and DC solutions are similar. However, if there are parallel currents in adjacent materials of different conductivities, the AC will be reduced near the better conductor and enhanced further away. The DC, on the other hand, will be approximately uniform in the less conductive material. If there are significant currents in the less conductive material, the AC and DC models will deviate. The deviation will increase as the conductivity increases.

4.3 2D in-plane versus 3D models in the furnace hearth

To obtain more realistic quantitative results and to analyse the limitations of the simplified 2D approach presented earlier, current calculations were performed inside the furnace using a 3D model. The furnace geometry and physical parameters introduced in Section 4.1 were used to calculate the currents and active power in different parts of the furnace. The computational domain is shown in Figure 4.2 and the distribution of materials is indicated in Figure 4.4.

The model presented in Section 3.2 has been solved by applying a three-phase current with an amplitude of 190 kA to the top of the three electrodes. It is worth mentioning that in the 3D case the steel shell is simplified as a straight cylindrical surface where the impedance boundary condition (3.61) is considered, as described in Section 3.3.1.

4.3.1 3D Numerical results

Figure 4.18 shows the current density norm distribution in Plane 1 and Plane 2 defined in Figure 4.5. Note that the skin effect is visible in both the electrodes and the metal alloy as the current accumulates on the surface. In the electrodes, most of the current is concentrated on their surface due to the high skin effect and in the part facing the furnace interior due to the proximity effect. Both effects can also be seen in Figure 4.19, where the norm of the current density is plotted in a horizontal section placed at height $z = 4$ m, which corresponds to the 800 °C charge region. The materials around the electrodes are neglected.

The active power density p is shown in Figure 4.20 for both Plane 1 and Plane 2. Note that it is mainly generated in the coke bed and the distribution looks fairly symmetrical.

USC UNIVERSIDADE DE SANTIAGO DE COMPOSTELA

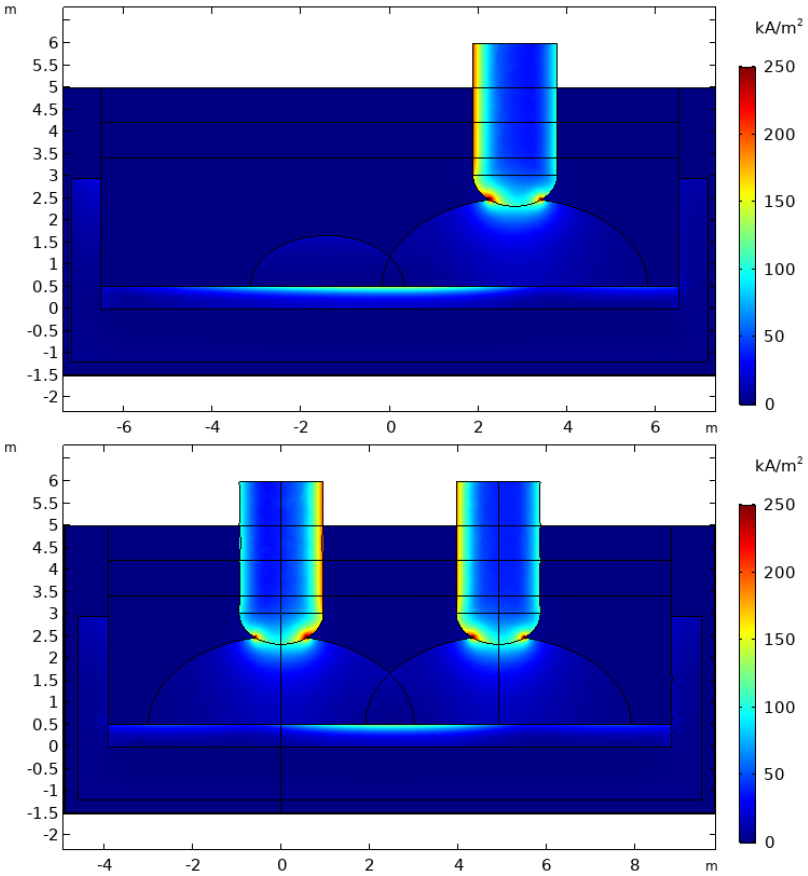

Figure 4.18. Current density norm in the 3D domain: Plane 1 (top) an Plane 2 (bottom). The color range is limited to 250 kA/m^2.

The total active power P (in W) is computed for each material region. In the 3D case, the calculation is performed as $P = \int_R p dV$, where p is the power density and R the 3D region. However, the notation of P is retained as in (4.2) because it is clear in each context. The resulting values are listed in Table 4.8. It should be noted that approximately 83% of the active power is generated in the coke bed. The power generated in the electrodes and in the charge layer at 1200 °C is of the same order of magnitude (7% and 8%, respectively). In addition, Figure 4.20 shows hot spots near the tip of the electrodes in the charge above the coke bed.

4.3.2 2D numerical results

In this section, the numerical results obtained by solving a 2D in-plane model (defined in Plane 2, as shown in Figure 4.5) are presented for comparison with the 3D results. The same current value is used as in the 3D model, $I = 190$ kA. It should be noted that the current in the 2D model is only a scaling factor and the absolute values of resistance and power in the furnace cannot be directly compared with those

USC UNIVERSIDADE DE SANTIAGO DE COMPOSTELA

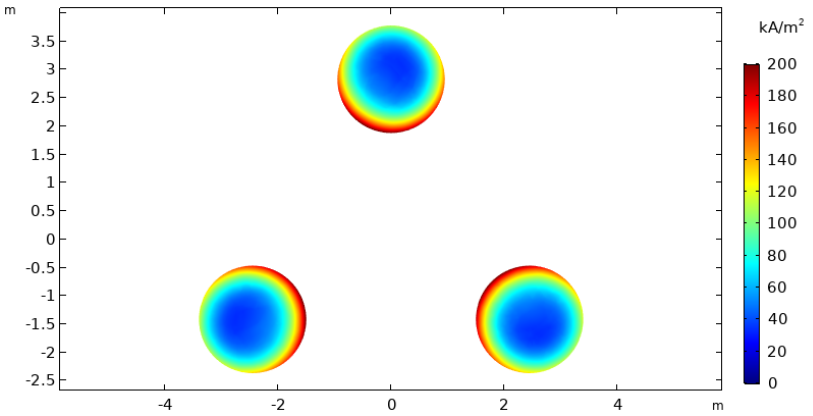

Figure 4.19. Current density norm in the electrodes in the xy-plane placed at $z = 4$m. The surrounding materials are neglected. The color scale is limited to 200 kA/m^2.

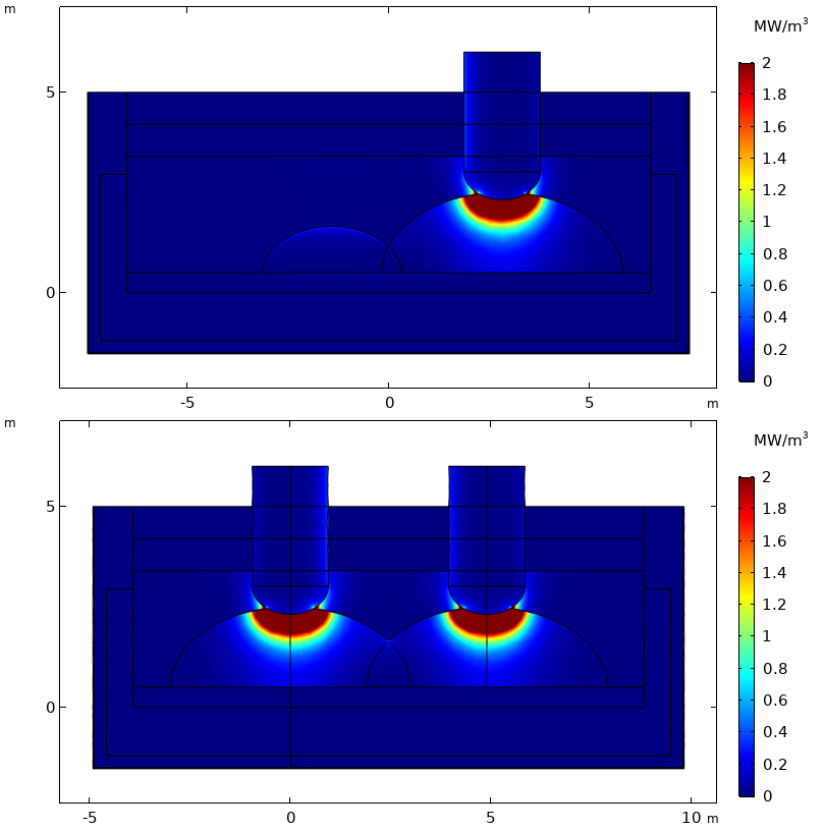

Figure 4.20. Active power density p in the 3D model: Plane 1(top) and Plane 2 (bottom). The color range is limited to 2 MW/m^3.

USC UNIVERSIDADE DE SANTIAGO DE COMPOSTELA

Table 4.8. 3D model. Active power P in each material region.

Region	P [MW]	Percentage of total [%]
Electrodes	2.69	6.66
Charge, 400 °C	0.01	0.025
Charge, 800 °C	0.02	0.05
Charge, 1200 °C	3.27	8.1
Coke bed	33.33	82.54
Alloy	0.18	0.45
Carbon lining	0.28	0.69
Oxide lining	0.00	0
Steel shell	0.58	1.44
Total	40.38	100

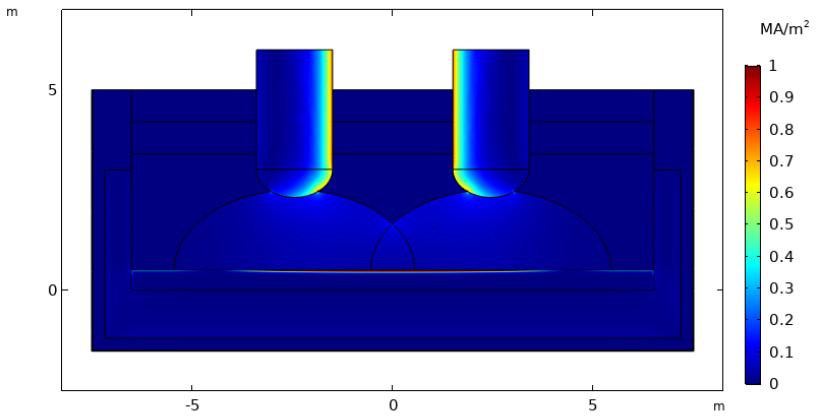

Figure 4.21. Current density norm in the 2D model. The color scale is limited to 1 $\mathrm{MA/m^2}$.

of a full 3D model.

The distribution of the current density norm is shown in Figure 4.21, where the colour scale is limited to 1 $\mathrm{MA/m^2}$. It can be seen that the current density is concentrated on the inward sides of the electrodes and on the surface of the alloy layer.

Figure 4.22 shows the distribution of active power within the furnace. The active power is primarily concentrated in the coke bed, particularly near the electrode tips. There is also a concentration of power in the centre of the furnace, possibly due to the narrow and sharp region where the elliptical regions intersect.

The results are summarised by considering the total power generated in each region of the furnace. The active power values obtained are presented in Table 4.9. It

USC UNIVERSIDADE DE SANTIAGO DE COMPOSTELA

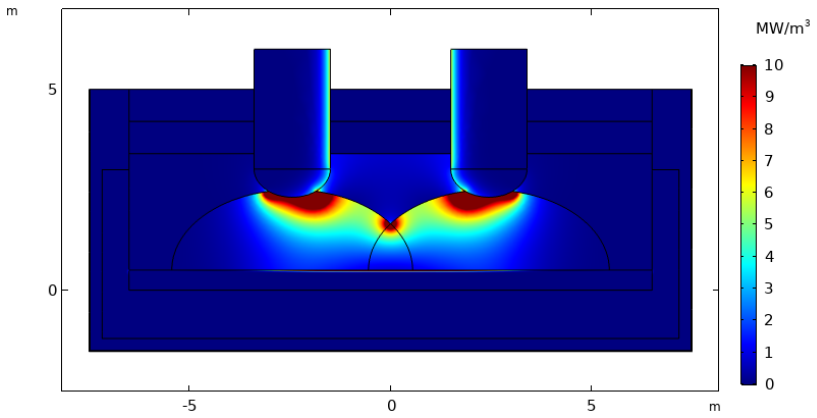

Figure 4.22. Active power distribution in the 2D model. The color scale is limited to 10 MW/m^3.

Table 4.9. 2D model. Active power P in each material region.

Region	P [MW/m]	Percentage of total [%]
Electrodes	7.42	9.65
Charge 400 °C	0.02	0.026
Charge 800 °C	0.03	0.039
Charge 1200 °C	3.38	4.4
Coke bed	56.96	74.11
Alloy	8.53	11.10
Carbon lining	0.17	0.22
Oxide lining	0.00	0.00
Steel shell	0.36	0.468
Total	76.86	100

Table 4.10. Horizontal currents through material layers.

Region	$\int_{\Gamma_m} J_x$ [kA/m]	Percentage of total [%]
Charge 400 °C	0.02	0.01
Charge 800 °C	0.04	0.02
Charge 1200 °C	7.71	3.68
Coke bed	75.2	35.88
Alloy	113.6	54.20
Carbon lining	12.9	6.15
Steel Shell	0.03	0.01
Total	209.6	100

USC UNIVERSIDADE DE SANTIAGO DE COMPOSTELA

is observed that 74% of the active power is generated in the coke bed region. In addition, 11% of the power is generated in the alloy and 10% in the electrodes. Only 4% of the power is generated in the 1200 °C charge region and below 1% in the steel shell. The active power in the remaining regions was found to be negligible.

The distribution of the current was also examined by considering the amount of current flowing horizontally through each layer of material. Due to symmetry, only the horizontal component of the current J_x is non-zero at the vertical centre of the furnace. By integrating this horizontal component through each layer of material and taking the norm of the complex result, a measure of the total amount is obtained. The results of these line integrations for all materials are summarised in Table 4.10, where, for simplicity, Γ_m denotes the line integration for all materials. These results provide a quantitative insight into how the current is distributed within the furnace hearth. It is observed that most of the horizontal currents passes through the alloy, with a significant part also flowing through the coke bed. Some horizontal currents are also present in the charge region just above the coke bed and in the conductive carbon lining at the bottom. The values agree well with the intuition from the plot of current density norm.

4.3.3 Conclusions

The 3D model presented in this section is inspired in that presented in Herland et al. (2019) by considering small simplifications in the geometry. The results obtained are in good agreement with this reference. It is noteworthy that the majority of the electrical energy is generated in the coke bed, which is consistent with both the expected result and the desired distribution for the operational requirements of the furnace. It was also shown that a significant amount of energy is produced in the charge layer above the coke bed, particularly in the vicinity of the electrode tip. It is likely that this result is highly dependent on the modelled shape and position of the electrode tip. These parameters are very difficult to fully understand and control in real furnaces. The exact shape and material properties within the coke bed are also difficult to determine, and the applied model is oversimplified with uniform and well-defined material regions.

In the 2D model, there is a well-defined shortest/lowest loss path between the two electrodes, which is not as straightforward in the 3D case. Moreover, in the 2D case, a greater proximity effect is observed than in the 3D model. The current in the electrodes tends only towards the inner sides of the two electrodes due to the opposite currents on both sides. That is, if the sum of the current is upward at the left electrode, it is downward at the right electrode, since the phase difference will always be 180° with two electrodes. In contrast, in the 3D case, the mutual induction between the electrodes is more distributed and not just directed between the pairs of electrodes.

UNIVERSIDADE DE SANTIAGO DE COMPOSTELA

The same effect is manifested in the power density distribution in the coke bed. In the 3D case, there is an almost a symmetrical (with respect to the electrode) region of high power under each electrode tip, whereas in 2D, the high power region is more skewed towards the other electrode. The 2D model seems to underestimate the relative amount of power dissipated in the coke bed and overestimate the amount in the alloy.

Therefore, 2D studies such as those presented in the previous section should not replace fully 3D simulations, which will be needed to determine more precisely the local behaviour in some parts of the furnace. However, the simplicity of 2D models can help to understand the sensitivity to different physical and geometrical parameters.

4.4 Induced currents in the lining and steel shell

In this section the study of induced currents in the lining and steel shell of FeMn furnaces is carried out using both 2D and 3D models. The AC currents supplied through the electrodes cause a significant amount of induced power in a conductive (carbon) lining and in the surrounding steel shell. Such currents generate heat where cooling is needed and potentially damaging hot spots can be found where the currents concentrate on the steel shell. In particular, the investigation will address an issue that has been raised in discussions with industry: Will the conditions improve if smaller current loops are enforced by subdividing the steel shell into sections?

As mentioned in Chapter 2, the steel shell surrounding the furnace is not included in the computational domain. As the steel shell is comparatively thin and has a large surface area, the computational cost of fully solving it will increase significantly. The main function of the steel shell is structural, i.e., to provide a suitable casing for the furnace. However, structural steel is both highly conductive and (usually) ferromagnetic. Thus, large eddy currents are induced Olsen et al. (2007); Herland et al. (2019, 2018).

The shell currents are mainly due to induction from the high intensity currents of the electrodes. This in turn causes a proximity effect between the electrode currents and the shell currents, which competes with the electrode-electrode proximity effect Herland et al. (2018, 2019) and thus affects the internal conditions. Between the steel shell and the inner part of the furnace there is a lining, typically consisting of both conductive (carbon) and non-conductive (ceramic) layers. There will be interactions between induced currents in the steel and currents in the conductive layers, depending on their material properties and geometry Fromreide, Gómez, et al. (2021); Fromreide, Halvorsen, et al. (2021).

USC UNIVERSIDADE DE SANTIAGO DE COMPOSTELA

The induced currents on the inside of the steel shell flow in three large loops, vertically behind each electrode and closing horizontally between the electrodes. At

the bottom, the current loops are wide, while they concentrate near the inner top of the steel shell Herland et al. (2018). This leads to significant heat dissipation at the shell (loss of power) and the subsequent need for active water cooling. If this situation persists over time, the steel may become thinner and deteriorate due to oxidative damage. In the worst scenario, the steel may crack or puncture, resulting in the risk of uncontrolled gas leakage, reduced process efficiency, unwanted production stops for repairs and potentially shorter furnace lifetime.

To improve the conditions, it was assumed that smaller current loops might reduce the induced currents and the accompanying heat generation.

Since the currents in the steel shell are mainly caused by the vertical electrode currents, 2D models with out-of-plane currents can quantitatively describe the mechanisms, especially in the upper part. But the 2D models will overestimate the intensity of the shell currents and 3D models are required for accurate solutions Herland et al. (2019). This section uses both 2D models with out-of-plane currents and full 3D models. The computational cost of 2D models is significantly lower than that of 3D models, making them valuable for gaining qualitative insight into the system. In many cases, simple 2D models can contribute to a better understanding of the governing mechanisms, compared to more complex 3D models. In particular, the mutual induction (proximity effect) between the shell currents and the electrode currents can be effectively studied using 2D models.

With a focus on induced currents in the steel shell and in the conductive lining of FeMn furnaces, the study aims to investigate the effects of modifying the lining and the potential impact of subdividing the steel shell. The main objective is to analyse whether such structural changes would lead to energy savings and less wear of materials, and therefore to a more sustainable production.

The dimensions and materials of the furnace are based on the description given in Section 4.1.

4.4.1 Mathematical modeling: 2D and 3D approaches

This section summarises the main features of the eddy current approaches used to calculate the currents in the steel shell and lining. The 3D model remains the same as that used in the previous section. Therefore, the focus is on the 2D approach.

The main assumption of the 2D model is that the current density only has a nonzero component in the z-direction, that is, it has the form $\mathbf{J} = J_z(x,y)\mathbf{e}_z$, which is applicable in the upper part of the furnace. This assumption is the one considered in the so-called 'out-of-plane model' in COMSOL and is used in the model introduced in Section 3.5 of Chapter 3. Note that in this case the electrical source must be imposed with some constraints. In particular, the total current through each electrode is given. On the other hand, in the conducting sections of the steel, it is

USC UNIVERSIDADE DE SANTIAGO DE COMPOSTELA

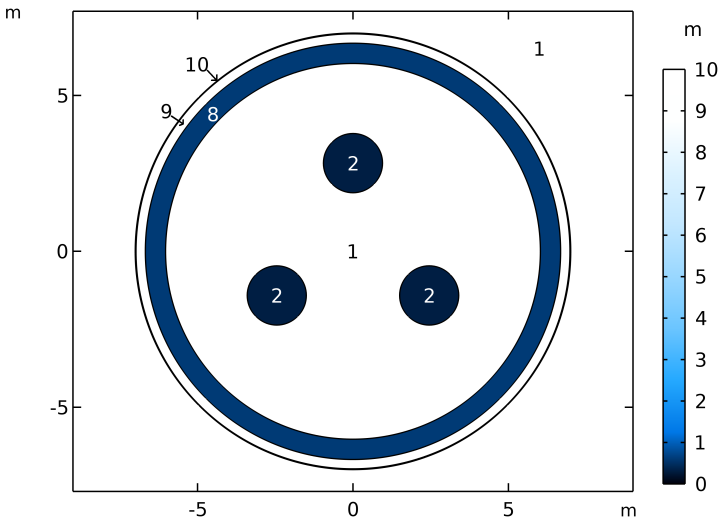

Figure 4.23. Geometry and materials in the 2D out-of-plane model, including: (1) air, (2) electrodes, (8) carbon lining, (9) oxide lining and (10) steel shell. The colour indicates skin depth of the material at $f = 50\text{Hz}$, with the scale restricted to 10 m.

also necessary to provide the current or the voltage. The total current through the steel shell is assumed to be zero due to the fact that the shell is modelled as an infinite conductor that does not close a circuit Bossavit (1999). In cases where the steel shell is divided into insulated sections (see Figure 4.26), the total current in each section is also zero.

The geometry of the 2D model is shown in Figure 4.23, where the numbering of the different material regions follows Table 4.2. Notice that this 2D geometry only refers to the upper part of the furnace where the current can be assumed to be vertical.

In the COMSOL implementation, the 2D model is mainly meshed with triangular elements, except for near the surfaces of the good conductors (electrodes, carbon lining and steel shell), where rectangular boundary layer elements are used. The rectangular elements allow a high resolution in the radial direction in order to account for the skin effect, without having to increase the resolution in the tangential direction. A part of the mesh is shown in Figure 4.24. The figure includes one electrode, interior, linings and steel casing. Due to the large size of the system ($D_F = 14$ m) compared to the thickness of the conductive shells, and the thickness of the thin boundary layers in the steel, carbon and electrodes, the mesh elements are not easily visible in the figure. However, the main idea of adding high resolution boundary layers in the good conducting regions is well represented.

USC UNIVERSIDADE DE SANTIAGO DE COMPOSTELA

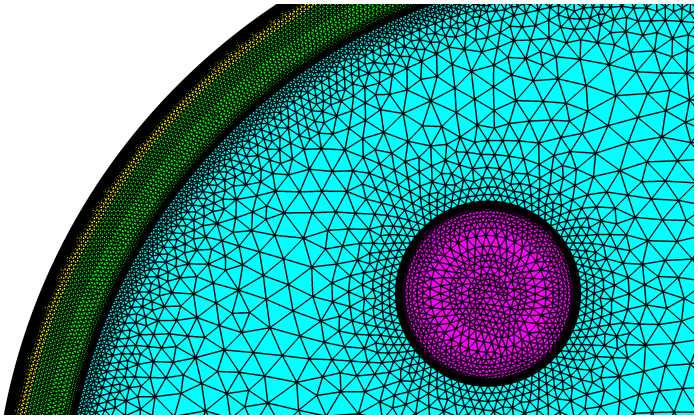

Figure 4.24. Mesh for a part of the domain surrounding an electrode.

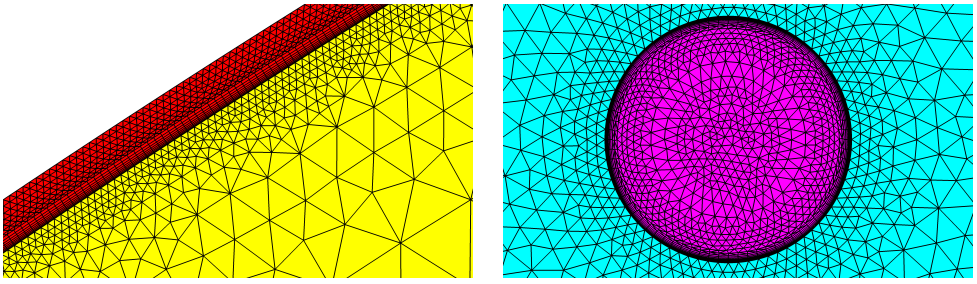

Figure 4.25. Rectangular elements near the lining-shell interface (lining yellow, shell red) and on the electrode surface.

USC UNIVERSIDADE DE SANTIAGO DE COMPOSTELA

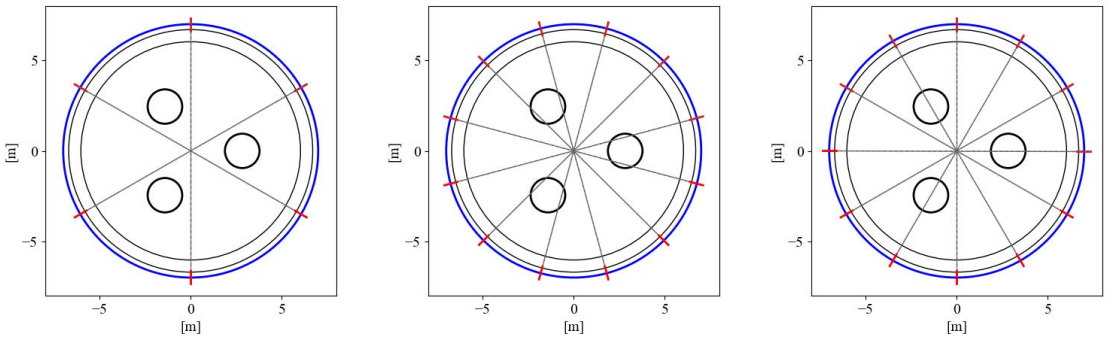

Figure 4.26. Positions of insulated gaps (in red) in the steel shell (in blue) for the 2D model. Left: 6 gaps symmetric, middle: 12 gaps symmetric, right: 12 gaps centred.

4.4.2 Structural modifications in the furnace

The material composing the steel shell is highly conductive, and strong eddy currents are induced in it which can also modify the currents of the electrodes. The objective is to analyse the influence of structural modifications in the furnace on the current distribution and power dissipation in both the steel shell and the carbon lining.

To attain this goal, various simulations have been performed involving modifications to either the steel shell, the carbon lining or both. Specifically, the simulations consist of five 2D cases and six 3D cases, which are summarised in Table 4.11. In the 2D simulations, two cases involve a solid steel shell with or without the presence of the conductive carbon lining. There is also one case with six gaps in the steel shell and two cases with twelve gaps in the shell. The two twelve gaps cases differ in the position of the gaps, which is either placed symmetrically around or centred behind the electrodes. In the six-gap case, the insulating gaps are symmetrically placed around the electrodes. The positions of the insulating gaps relative to the electrodes are shown in Figure 4.26.

In the 3D simulations, a reference case (Case 6) based on the geometry described in Section 4.1 was considered. In addition, three cases were examined where the carbon lining was extended vertically, so that it has the same height as the steel shell. In these three cases the thickness of the entire side wall of the carbon lining was varied. In the last two cases, the steel shell was subdivided by including six vertical insulating gaps and two horizontal gaps around the entire periphery of the steel shell. The vertical gaps are placed in the centre or symmetrically around the electrodes. In both cases, the horizontal insulating gaps are kept fixed, so that the upper one is placed slightly above the electrode tip, and the other is placed underneath the tip. This means that the upper section will experience most induction from the electrode current, the middle section will experience some induction from the electrodes, while the bottom section will not be subject to significant induction from the electrode currents. As an

USC UNIVERSIDADE DE SANTIAGO DE COMPOSTELA

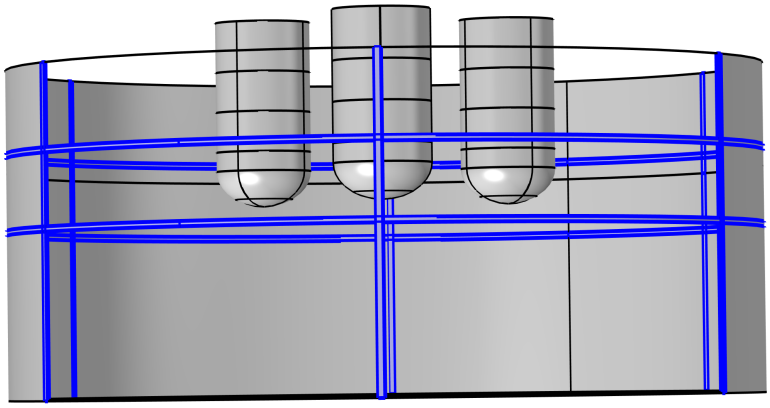

Figure 4.27. Positions of vertical and horizontal insulating gaps in the steel shell. Three of the six vertical gaps are centred on the electrodes.

example, Figure 4.27 shows the position of the gaps for the case where the vertical gaps are centred behind the electrodes.

The effect of the size of the insulating gaps was also investigated by analysing 2D simulations with different gap sizes. The gap size ranged from 0.1° to 1.5°, corresponding to approximately 1 cm to 15 cm, in a 2D model with twelve gaps in the steel shell. These gaps were positioned symmetrically around the electrodes (Case 4) and simulations were carried out both with and without the carbon lining.

4.4.3 2D simulation results

By analysing various 2D simulations, it has been found that the size of the insulating gaps has a negligible effect. The results of these simulations, considering different situations, are summarised in Table 4.12. The dissipated power (in MW/m) in the steel shell (P_S), the carbon lining (P_C), the electrodes (P_e) and the total dissipated power (P_{total}) are given. The change in the dissipated power is minimal across the different gap sizes, with the most significant variation localised in the steel shell. Consequently, this work focuses on a gap size of 1°, which corresponds to approximately 10 cm for the given furnace diameter. In the 3D model, the horizontal gaps were also set to 10 cm.

Figure 4.28 shows the norm of the magnetic induction $|\mathbf{B}|$ for the 2D model, illustrating the cases with and without the conducting carbon lining (Cases 1 and 2 respectively). The distributions exhibit similarities in the central region, but noticeable differences appear in the outer region. In particular, the field strength at the outer steel shell is stronger in the case without carbon lining (Case 1) than in the

USC UNIVERSIDADE DE SANTIAGO DE COMPOSTELA

Table 4.11. Cases considered in the 2D (from 1 to 5) and 3D (from 6 to 11) simulations. The reference case for the 3D simulations is number 6.

Case	no. shell divisions (vert.)	C-lining	C-lining thickness (m)	Gap positions
1	0	Not included	0.65	-
2	0	Included	0.65	-
3	6	Included	0.65	Symmetric
4	12	Included	0.65	Symmetric
5	12	Included	0.65	Centred
6	0	Included	0.65	-
7	0	Extended	0.65	-
8	0	Extended	0.30	-
9	0	Extended	0.10	-
10	6	Included	0.65	Symmetric
11	6	Included	0.65	Centred

Table 4.12. Power in MW/m in the steel shell, carbon lining, electrodes and in total for a 2D model with twelve gaps of varying widths in the steel shell, with and without carbon lining.

Gap width [°]	Carbon lining included	P_s	P_c	P_e	P_{total}
1.5	no	63.7	-	720	785
1.0	no	68.2	-	720	789
0.5	no	73.9	-	719	794
0.1	no	80.1	-	719	800
1.5	yes	0.95	120	684	804
1.0	yes	1.03	119	684	804
0.5	yes	1.13	119	684	804
0.1	yes	1.24	119	684	804

USC UNIVERSIDADE DE SANTIAGO DE COMPOSTELA

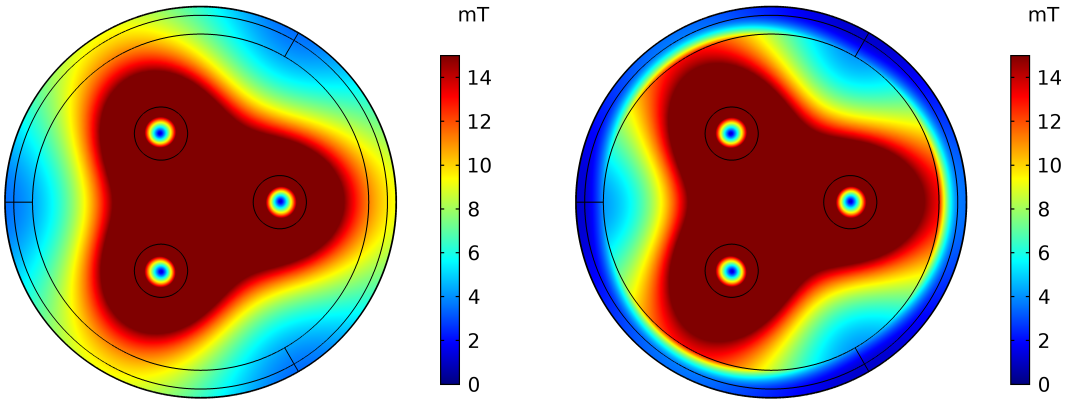

Figure 4.28. Magnetic induction norm: left, when the carbon lining is neglected (Case 1); right, when the carbon lining is included (Case 2). The colour range is limited to 15 mT to resolve the outer parts.

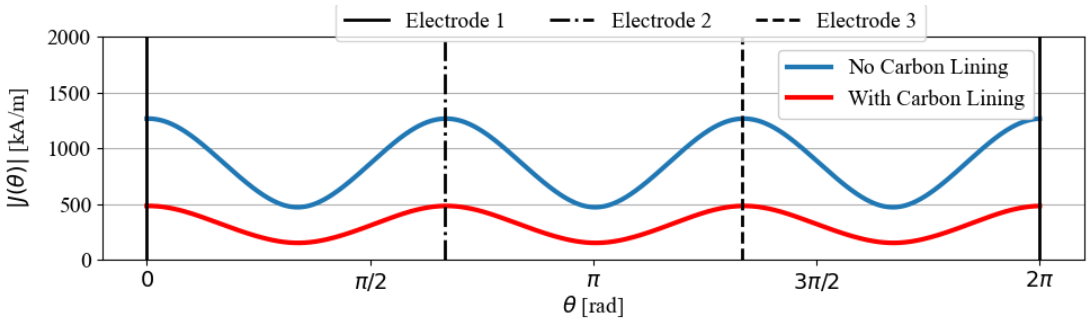

Figure 4.29. Current density norm on the inner circumference of the steel shell with and without carbon lining present (Cases 2 and 1, respectively). The vertical lines indicate the position of each electrode.

case with carbon lining (Case 2). However, the introduction of the conducting lining increases the field strength considerably near its inner boundary, thus increasing the concentration towards the center. The effect on the induced currents in the steel shell is visualised by considering the induced currents on the *inside* of the steel shell. Figure 4.29 shows the norm of the current density at the inner circumference of the shell for Cases 1 and 2. The curves demonstrate how the induced shell currents are attenuated by the carbon lining.

Figure 4.30 displays the norm of the current density on the *inside* of the steel shell illustrating different scenarios where the shell is divided into insulated sections (Cases 3, 4 and 5 as listed in in Table 4.11). Both plots include the curve for a solid steel shell (same as in Figure 4.29) with the carbon lining included (Case 2). The top plot corresponds to the twelve-gap case with the gaps symmetrical around the electrodes (Case 4), and the bottom plot to the twelve-gap case with the gaps centred

USC UNIVERSIDADE DE SANTIAGO DE COMPOSTELA

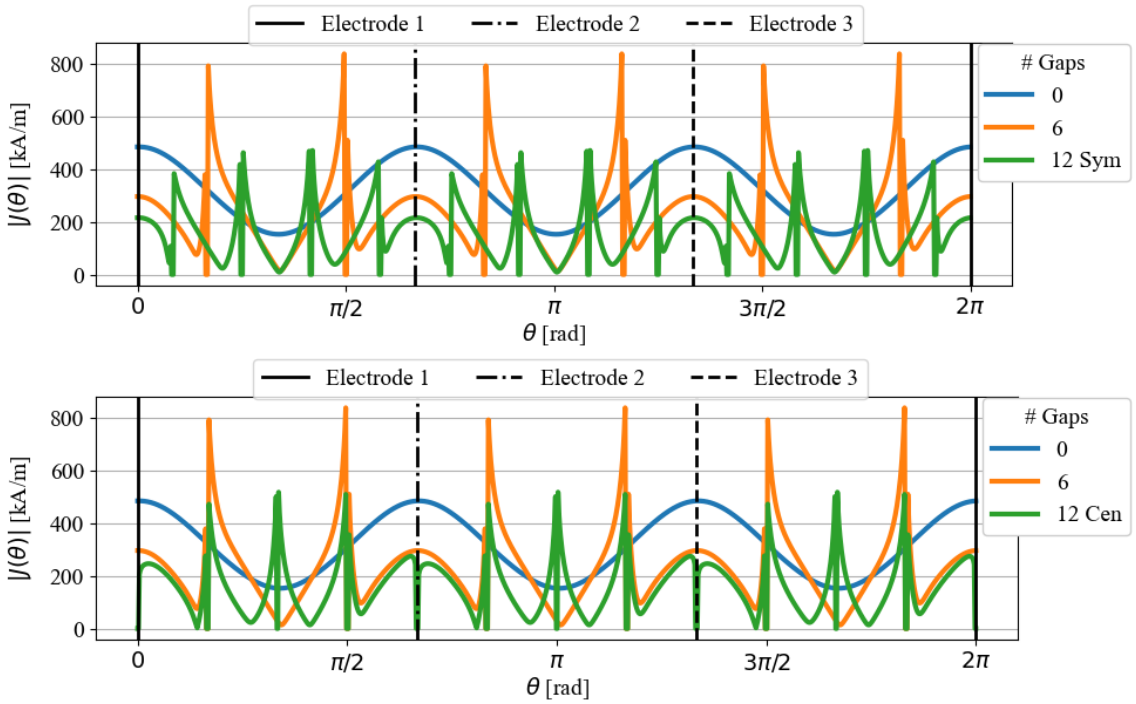

Figure 4.30. Current density norm on the *inside* of the steel shell with 0, 6 and 12 insulated sections. Cases 2 and 3 are included in both plots; Case 4 (12 symmetrical gaps) in the top and Case 5 (12 centred gaps) in the bottom.

on the electrodes (Case 5). The positions of the gaps in the six-gap case (Case 6) remain consistent in both plots. The figure shows how the insulated gaps create local peaks in the current norm on both sides of the insulating material.

4.4.4 3D simulation results

Figure 4.31 shows the induced current on the *inside* of the steel shell in the full 3D model (Cases 6 and 7). The colour indicates the norm of the current, while the black arrows indicate the direction of the current. The red arrows in each electrode represent the direction of the total current in each electrode. The length of the red arrows reflects the intensity in the electrodes. However, the red and black arrows are scaled individually. For each of the plots, the time-instant for the arrows is chosen so that there is a maximum current in the front electrode which distributes equally to the other two electrodes. The plot in the top shows the (reference) Case 6, i.e, neither shell divisions nor extended carbon lining are considered. The lower plot corresponds to the case where the carbon lining is extended vertically to the top of the steel shell (Case 7). In the reference case, it is observed that vertical currents are induced behind each electrode, flowing in the opposite direction relative to the

USC UNIVERSIDADE DE SANTIAGO DE COMPOSTELA

nearest electrode. The currents close in loops and move horizontally, at the top and bottom, between the electrodes. There is significant current accumulation at the top of the shell, between the electrodes with a risk of creating hot-spots. This distribution agrees well with the results found in Herland et al. (2018). In the case where the extended carbon lining is taken into account, the intensity of the current is significantly reduced and the accumulation at the top is less visible. The direction of the current distribution is similar in both cases.

The current distribution on the *inside* of the steel shell is plotted in Figure 4.32 for the two cases with subdivided steel shell (Cases 10 and 11). As in Figure 4.31, the colour range has been restricted to 10 kA/m for both cases. The 3D simulations show similar behaviour to the 2D case, with a large local increase in the current density norm near the insulated gaps. The hot spots are generated along both the vertical and horizontal gaps.

The different positioning of the insulating gaps gives rise to some changes in the current distributions. Compared to the reference case with a solid steel shell (Figure 4.31), the sub-sectioning cases give a significant increase in the total induced current.

As a measure of the impact of the different models on the steel shell and linings, the total electric power in different parts of the furnace and the total power for each 3D case were calculated. The power dissipated in the steel shell (P_s), carbon lining (P_c), electrodes (P_e), remaining interior (P_{interior}) and total power (P_{total}) were considered. For the steel shell, the value was determined based on the surface loss density on the steel shell surface, associated with the calculated surface currents. For the remaining parts, the electric power was calculated as the usual volumetric power, $P = |\mathbf{J}|^2/(2\sigma)$. The results are summarised in Table 4.13. From these results it can be observed that the total power is comparable for all cases, with an increase of about 1.6% from the reference case (Case 6) to the highest cases (Cases 10 and 11). This increase is mainly due to the induced power in the carbon lining. Furthermore, it is concluded that the extended carbon lining (in height) reduces the induced power in the steel shell, even when the thickness of the full sidewall is reduced to 0.10 m. At the same time, there is an increase in the power induced in the carbon lining. For the two cases where the steel shell is subdivided (Cases 10 and 11), there is an increase in the total power induced in the steel shell. However, the effect on the carbon lining is much more pronounced, as the total induced power is more than doubled. There is also a small increase in the electrodes and interior for these cases.

4.4.5 Discussion

Electromagnetic induction follows the general principle that nature resists changes; in this case: a change in the magnetic field in a conductor will induce a voltage (an E-field) to create a current that counteracts the change in the magnetic field.

USC UNIVERSIDADE DE SANTIAGO DE COMPOSTELA

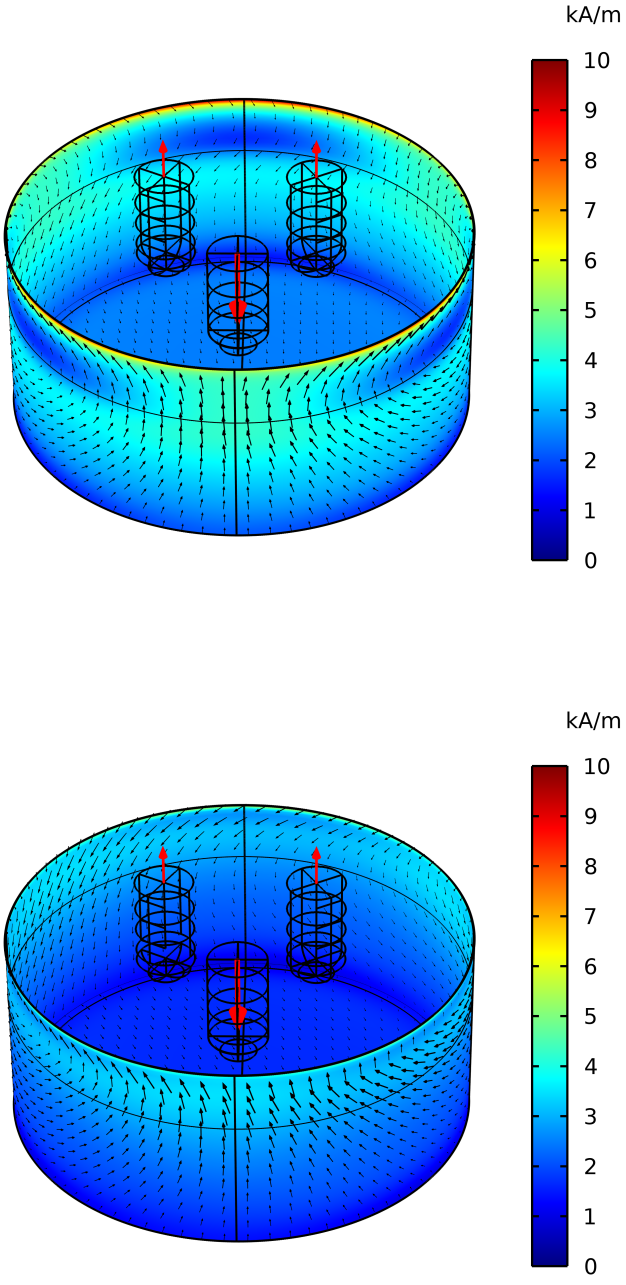

Figure 4.31. Current on the *inside* of the steel shell for the 3D reference case (Case 6) (top), extended height of carbon lining (Case 7) (bottom). The colour range is limited to 0-10 kA/m and shows the surface current density norm. The black arrows indicate the pattern of the shell current at a given time. The red arrows indicate the direction of the electrode currents.

USC UNIVERSIDADE DE SANTIAGO DE COMPOSTELA

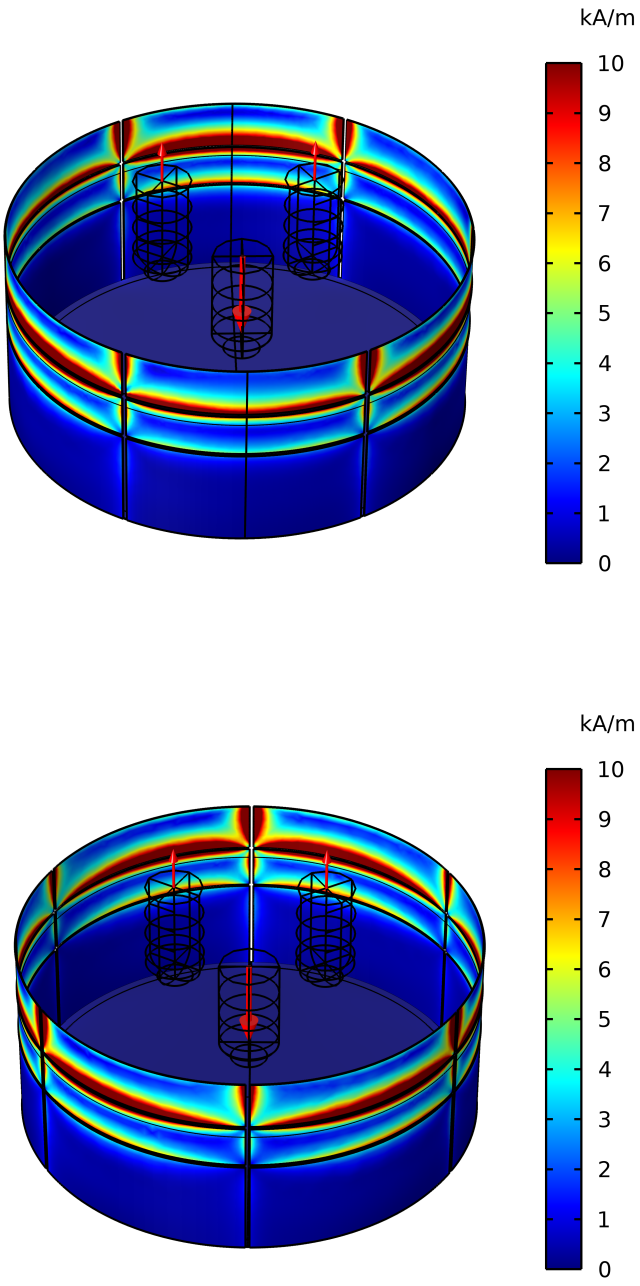

Figure 4.32. Current on the *inside* of the steel shell when both vertical and horizontal insulation gaps are included. The vertical insulation gaps are placed symmetrically (Case 10) around the electrodes (top) and centred (Case 11) behind the electrodes (bottom). The color range is restricted to 0-10 kA/m and shows the surface current density norm. The red arrows indicate the direction of the electrode currents.

USC UNIVERSIDADE DE SANTIAGO DE COMPOSTELA

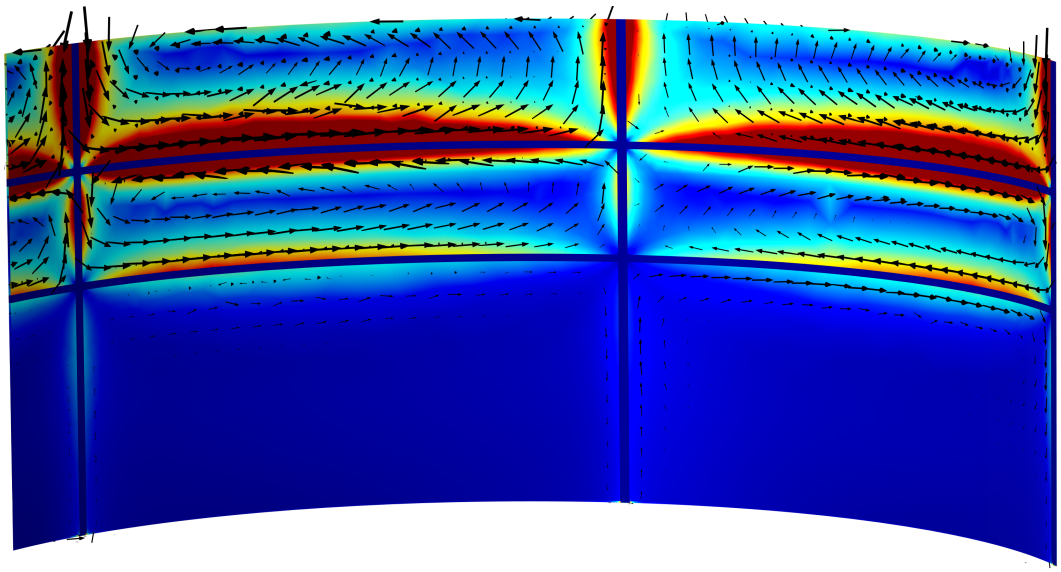

Figure 4.33. Current patterns on the *inside* of the steel shell for a section of the furnace for Case 11. The black arrows show the direction of the current at a given time. The colour represents the current norm as in Figure 4.32.

Table 4.13. Total heat loss density (in MW) in steel shell (surface), carbon lining, electrodes and interior for the 3D simulations.

Case	P_s	P_c	P_{s+c}	P_e	$P_{interior}$	P_{total}
6	0.29	0.33	0.62	2.63	36.59	39.84
7	0.10	0.53	0.63	2.61	36.55	39.79
8	0.15	0.53	0.68	2.62	36.59	39.89
9	0.22	0.39	0.61	2.63	36.63	39.87
10	0.32	0.69	1.01	2.74	36.75	40.50
11	0.31	0.69	1.00	2.74	36.75	40.49

USC UNIVERSIDADE DE SANTIAGO DE COMPOSTELA

In good conductors, the magnetic field is largely reduced in the interior and the current is concentrated at the boundaries. Generally, parallel currents in the same direction are 'pushed away' from each other Lupi (2017). By Ampère's law the alternating magnetic fields far away from the conductors are given by the total current. The cyclic changes in the magnetic field are best reduced by moving the currents away from each other.

Parallel currents in opposite directions are 'moved towards' each other Lupi (2017). The magnetic fields from opposing currents will counteract each other, and the cyclic changes in the magnetic field will be reduced when the opposing currents are close together.

It might be thought that reducing the size of the current loops would reduce the concentration of induced currents. However, the simulations show strong, opposing current loops with enhanced current concentrations. Therefore, in three-phase electric furnaces, insulating gaps would imply a higher risk of hot spots and increased heat loss due to the associated electric power from the eddy currents on the steel shell.

The effect of the gap size between the sections has been investigated by some 2D simulations. The general trend is more concentrated currents on each side of the gap when the gap is reduced. The power generated in the steel shell increases accordingly. Other effects are minor. Based on this result, it was decided that variation of the gap size was not necessary for the remaining cases. A relatively large gap size of 1°/10 cm was chosen. This avoids the need for very small elements in the gaps, which would have required more computation time.

The simulations show that the carbon lining has a shielding effect. Induced currents in the lining imply much less induction in the steel shell. There is a strong proximity effect between parallel currents in adjacent conductors. The electric current is generally 'pushed away' from the good conductor (here, steel) into the less conductive material (here, carbon) Fromreide, Gómez, et al. (2021). In our simulations, it is assumed that there is good electrical contact within the lining and between the lining and the steel shell. If not, the paths of the induced currents will be restricted with potentially unfavourable effects.

The simulations demonstrate a general learning that simple models (here, 2D models) are very valuable for studying the basic effects. The 2D models clearly show that there will be induced currents (in the lining and the steel shell) behind each electrode, where the induced currents will be opposite to the respective electrode currents. The shielding effect of a carbon lining, the unfavourable effect the steel shell sectioning and the influence of the gap size are also clearly seen. But some effects cannot be studied with the assumptions of the 2D model (strictly, vertical current). 3D models are, for instance, required to compute how the current loops close, and to include both vertical and horizontal insulating gaps. Full 3D models

USC UNIVERSIDADE DE SANTIAGO DE COMPOSTELA

are also required to get results that can be applied to study details of the furnace design, such as the thickness and height of a carbon lining.

The steel shell has been treated as a linear magnetic material with constant magnetic permeability. Some simple test calculations have shown that constant magnetic permeability works well and gives the same general results as a (more expensive) non-linear model that includes magnetic saturation. The results for a linear model can be improved by adjusting the relative magnetic permeability to the actual magnitude of the magnetic fields. This requires a separate study which is beyond the scope of this work.

Induction in the steel shell and a conductive lining cannot be avoided. However, it can be controlled to some extent by appropriate design modifications. It is advisable to perform electrical simulations specifically tailored to the actual furnace designs. Such calculations must include all relevant details. For example, there will be induced currents in a steel roof. Here, the effects of opposing currents due to the insulating 'gap' between the lid and the furnace casing can be seen (see Herland et al. (2018)).

The insulating gaps could also be considered as parts of the shell where the steel has been degraded. The results show how this leads to a vicious loop, where degraded steel gives rise to hot spots which will further degrade that part, making the problem worse.

4.4.6 Conclusions

Electromagnetic simulations have been successfully applied to study induced currents in the lining and steel shell of three-phase submerged arc furnaces. Strong vertical currents are induced behind each electrode. The induced currents form three large loops, with horizontal currents between the electrodes at the top of the steel shell and below the electrode tips. At the top, there are strong current concentrations with corresponding risk of (damaging) hot spots.

Limiting the size of the current loops has a detrimental effect. If the steel shell is sectioned with (electrically) insulating gaps, strong opposing currents will be formed on either side of the gaps, implying more heat loss and a higher risk of damaging hot spots.

The induced currents in the steel shell are modified by an electrically conductive lining. Such a lining has a shielding effect, reducing the currents in the steel shell.

Electromagnetic simulations are recommended as part of furnace design studies to investigate, for instance, the effect of variables such as the height and width of an electrically conductive lining. This can contribute to furnace designs with less

USC UNIVERSIDADE DE SANTIAGO DE COMPOSTELA

undesired power dissipation due to induction, heat losses and the need for water cooling. In addition, furnace life and uptime can be extended by incorporating advanced electromagnetic analysis at an early stage of design. All of this improves the economic and environmental sustainability of furnace processes.

4.5 Exploring a new tool for the AC model approximation

In this section, a new tool aimed at simplifying the 3D simulation of the metallurgical furnaces studied in this thesis is explored. The objective is to compute the solution of the electromagnetic model powered by a three-phase alternating current by using a combination of solutions obtained with a single-phase source. This tool can be valuable in reducing the computational time required to simulate furnaces with specific types of symmetry and linear magnetic materials.

It is important to note that all constitutive laws are assumed to be linear. Therefore, the three-phase electric currents applied to the furnaces can be treated as a superposition of single-phase models. This concept is inspired by the methodology used in Halvorsen et al. (2016), where solutions to DC problems were combined to approximate a three-phase current. However, the DC-based approach described in that paper does not account for inductive effects and prevents to obtain a solution to a three-phase eddy current problem.

Next, two time-harmonic eddy current problems with a single-phase source will be defined and their solutions will be used to determine the current density associated with a time-harmonic eddy current problem with a three-phase source. Recall that in the 3D problems discussed previously, a three-phase current was imposed on the top electrodes by fixing the current in two electrodes and the potential in the third one. Specifically, the conditions for electrodes 1, 2 and 3 are set as follows:

$$I_1 = I, \quad I_2 = Ie^{i\theta}, \quad V_3 = 0, \tag{4.3}$$

where I is the amplitude of the applied current and θ is the phase shift, which is equal to $2\pi/3$. Note that $I_3 = Ie^{-i\theta}$.

Now, to define the *single-phase* problems, a current with a phase difference of π is applied to the top of two electrodes, while the net current in the remaining electrode is set to zero. Specifically, the single-phase Problem A is defined with the following data

$$I_1 = I, \quad I_2 = 0, \quad V_3 = 0. \tag{4.4}$$

In a similar way, Problem B is defined with the data

$$I_1 = 0, \quad I_2 = I, \quad V_3 = 0. \tag{4.5}$$

USC UNIVERSIDADE DE SANTIAGO DE COMPOSTELA

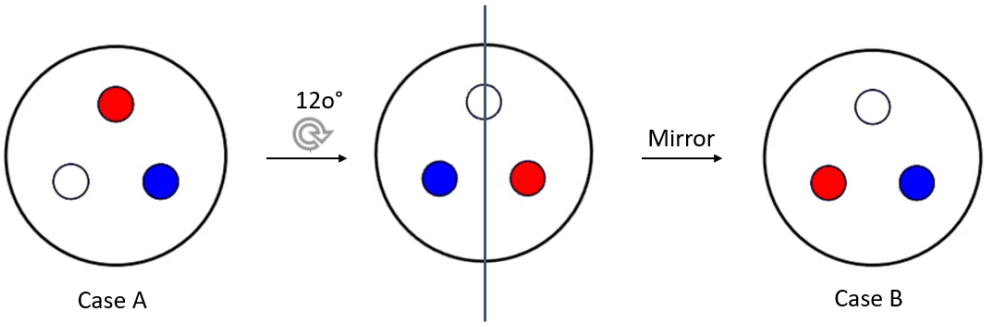

Figure 4.34. Procedure for obtaining the solution of Problem B from solution of Problem A.

For both cases A and B, the total current through electrode 3 is found to be $-I$, or $Ie^{i\pi}$ in terms of the amplitude I and the phase angle (π). It is worth noticing that the solution to problem B can be obtained from the solution to problem A by combining a rotation and a symmetry in an appropriate way. This procedure is sketched in Figure 4.34, and the the real part of the current density corresponding to Problems A and B can be visualized in Figure 4.35 (a) and (b), respectively.

Moreover, the combination of solutions A and B in the form $A + Be^{i\theta}$ gives the solution to the original three-phase problem with the data defined in equation (4.3). Consequently, only one of the single-phase problems needs to be solved. Moreover, for each single-phase problem, computational savings can be achieved by exploiting the symmetry, as shown in Figure 4.36. This theoretical approach can be easily implemented in an in-house code, for instance. However, when working with commercial software, there may be limitations in manipulating and combining individual solutions or files from independent projects. Indeed, there are certain limitations when using COMSOL.

Figure 4.37 shows the current density norm in a horizontal cross section of the electrodes. Notice that a strong proximity effect between the two active electrodes can be observed in the solution of Problems A and B (Figure 4.37 (a) and (b)). Figure 4.37 (c) shows the combined solutions which are very similar to the full three-phase solution in plot (d). To assess the accuracy of the combined approach, the total electric power was calculated for both the combined and the full three-phase models of the entire furnace. The relative difference between the two calculations was found to be 0.25%.

Finally, Figure 4.38 shows the power density distribution in Plane 2 for single-phase case A. For this case, the two active electrodes are those included in the 2D cut plane. However, as the plot shows, the power distribution is similar to the full three-phase case (Figure 4.20) with nearly symmetrical hot spots beneath the electrode tips.

USC UNIVERSIDADE DE SANTIAGO DE COMPOSTELA

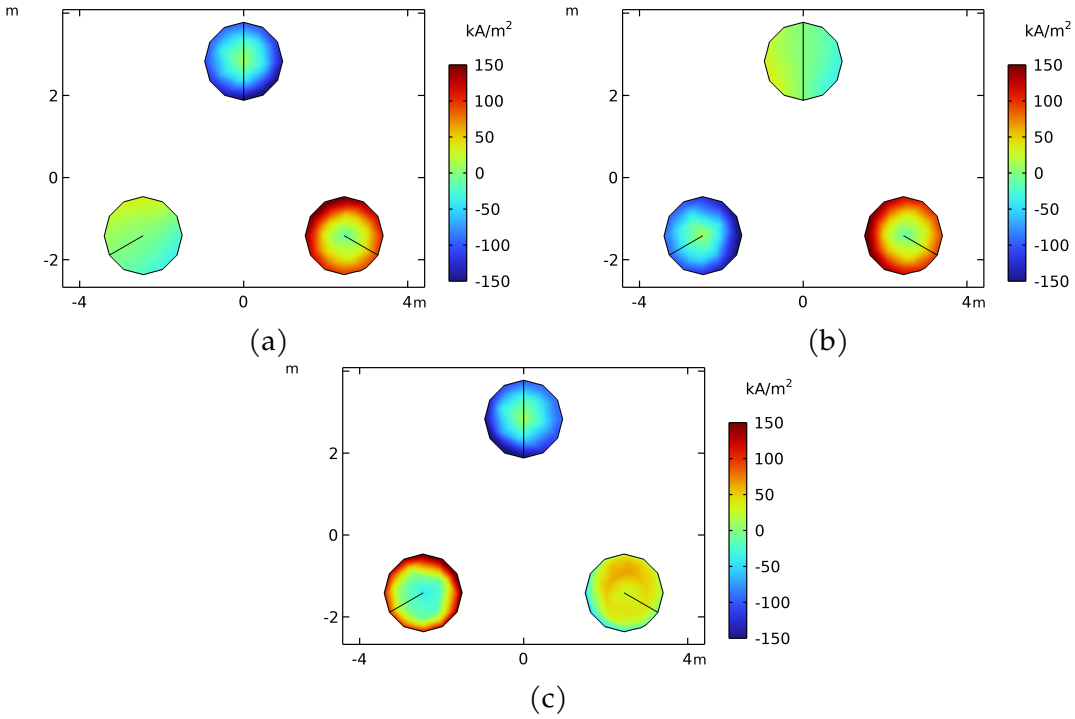

Figure 4.35. Real part of the current density in a horizontal cross section of the electrode: (a) Single-phase case A, (b) Single-phase case B, (c) Linear combination of single-phase cases A and B with phase shift.

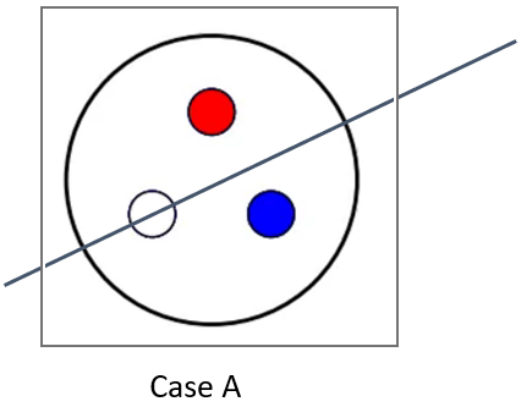

Figure 4.36. Symmetry plane of the furnace for solving Problem A.

USC UNIVERSIDADE DE SANTIAGO DE COMPOSTELA

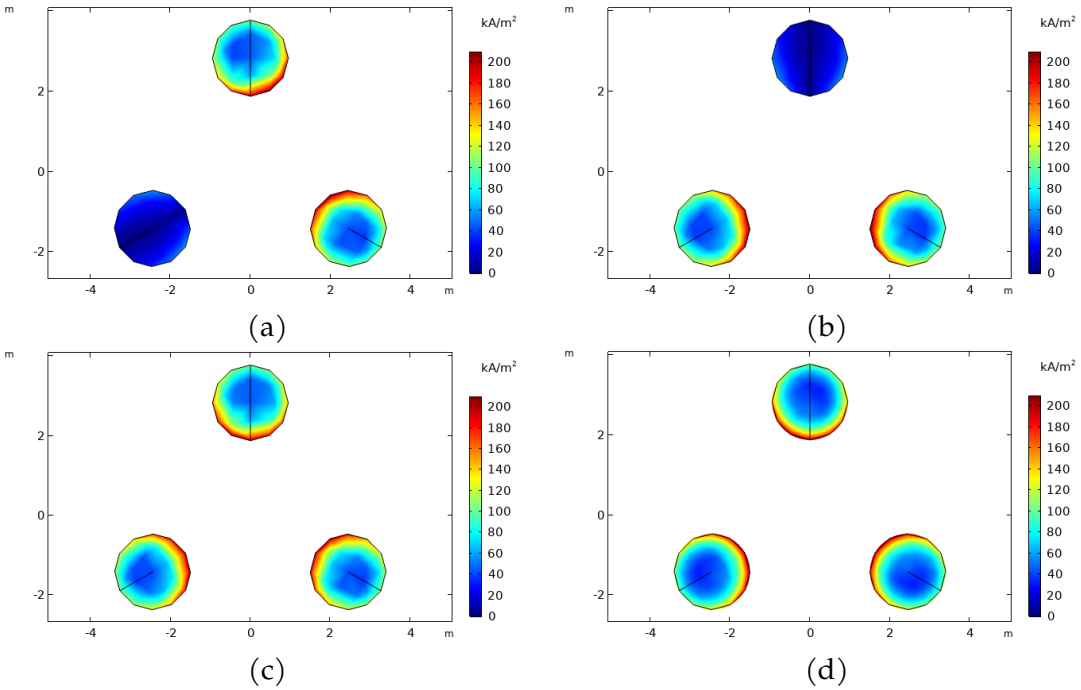

Figure 4.37. Current density norm in a horizontal cross section through the electrodes: (a) Single-phase case A, (b) Single-phase case B, (c) Linear combination of single-phase cases A and B and (d) Full three-phase model. The colour range is limited to a maximum of 210 kA/m^2 in each plot.

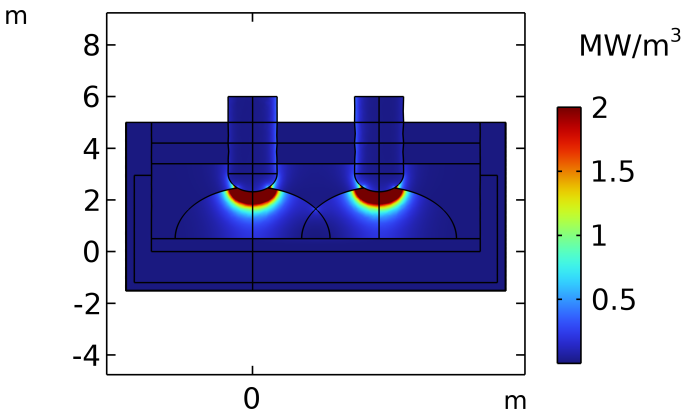

Figure 4.38. Power density in Plane 2 through the two active electrodes in single-phase case A.

USC
UNIVERSIDADE DE SANTIAGO DE COMPOSTELA

Chapter 5

1D Analytical mathematical models

This chapter presents a one-dimensional model for analysing the effects of alternating current in submerged arc furnaces. The model is derived through dimensional analysis of the electric field equation discussed in Chapter 3. In this chapter, it will be used to study inductive effects in adjacent conductors, compute current distribution through multiple layers, and compare AC and DC models. Additionally, the one-dimensional approach will be compared to 2D numerical simulations to investigate two different furnace zones. First, the furnace hearth is considered by analysing horizontal current within the region situated between the electrodes. Subsequently, the induction of current in the casing of a three-phase furnace is considered.

5.1 Electric field distribution in one-dimensional conductors

In Section 3.7, it was demonstrated that the electric field exhibits 1D behaviour under certain assumptions. Let us consider a scenario where the current density in the conductor primarily consists of horizontal current. Specifically, for the rectangular conductor depicted in Figure 3.4, let us assume that the current enters and exits the domain through the vertical edges. Furthermore, suppose that the horizontal edges are insulated. Then $\tilde{E}_z = 0$ due to symmetry and only the horizontal component $\tilde{E}_y$

This chapter reproduces some contents from the following articles:

- M. Fromreide, D. Gómez, S. A. Halvorsen, E. H. Vålandsmyr and P. Salgado (2021) *Reduced 2D/1D mathematical models for analyzing inductive effects in submerged arc furnaces*, Applied Mathematical Modelling, 98, 59–70. doi:10.1016/j.apm.2021.04.034
- M. Fromreide, D. Gómez, S.A. Halvorsen, P. Salgado. *An analytical 1D model for computing low-frequency electromagnetic fields in conducting layers. Application to metallurgical furnaces*, In Preparation.

USC UNIVERSIDADE DE SANTIAGO DE COMPOSTELA

needs to be considered (notice that the same analysis applies to $\tilde{E}_z$ in the opposite case where $\tilde{E}_y = 0$).

In particular, for 'long and thin' conductors where the ratio of thickness to width $(T/W)^2 \ll 1$, the first term in (3.129) can be neglected. In this case, by reintroducing the dimensional variable $z = T\tilde{z}$, the governing equation for the electric field is reduced to an analytically solvable differential equation that takes the form

$$\frac{d^2}{dz^2}E_y(z) - \frac{2i}{\delta^2}E_y(z) = 0. \tag{5.1}$$

Its general solution is given by

$$E_y(z) = Ae^{-\alpha z/\delta} + Be^{\alpha z/\delta}, \tag{5.2}$$

where $\alpha = 1 + i$ and A and B are unknown complex constants that must be determined from the boundary conditions. On the other hand, the one-dimensional form of the electric field, $\mathbf{E} = E_y(z)\mathbf{e}_y$, implies, from Faraday's law (3.1), that the magnetic field also takes a one-dimensional form. The only non-zero component is in the x-direction, $\mathbf{H} = H_x(z)\mathbf{e}_x$. That is, the magnetic field is out of plane relative to the 2D conductor.

This model can be solved for any number of material layers, which would represent the different layers in a smelting furnace, and be used to investigate the distribution of the electric field in conducting materials and how regions with different material properties affect each other. In the subsequent sections, several cases will be examined. But first, two simple examples will be presented.

5.1.1 Simple examples for a single conductor

Let us consider an infinitely thick conductor, where the thickness is much larger than the skin depth ($T \gg \delta$). For any position z, the electric field must be bounded which means that $B = 0$ in (5.2). As a result, the expression for the electric field distribution in this conductor is simplified to

$$E_y(z) = Ae^{-\alpha z/\delta}. \tag{5.3}$$

The coefficient A can be determined in two ways. If the electric field E_0 is known at a specific point such as the conductor surface ($z = 0$), the solution is simply given by

$$E_y(z) = E_0 e^{-\alpha z/\delta}. \tag{5.4}$$

Alternatively, if the total current across the conductor per unit length, I_{tot}, is known, A can be obtained by evaluating the integral

$$I_{tot} = \int_0^{+\infty} \sigma(z)E_y(z)dz, \tag{5.5}$$

USC UNIVERSIDADE DE SANTIAGO DE COMPOSTELA

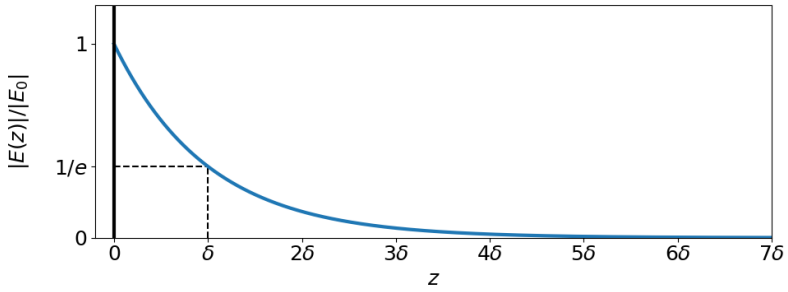

Figure 5.1. Electric field distribution in a thick conductor.

which provides $A = \alpha I_{tot}/(\sigma\delta)$. Consequently,

$$E_y(z) = \frac{\alpha}{\sigma\delta} I_{tot} e^{-\alpha z/\delta}. \tag{5.6}$$

Figure 5.1 shows the electric field norm distribution as a function of distance from the conductor surface. The values are normalized with respect to the surface value E_0. This curve is a well-known result and is often used to illustrate the concept of the skin depth Bermúdez et al. (2014); Griffiths (2017), which is defined as the distance from the surface where the field has dropped to the value E_0/e. As shown in the figure, the field strength has dropped to this value at $z = \delta$. Moreover, integration reveals that approximately 86% of the current is concentrated within the skin layer $(0 < z < \delta)$.

Another simple example to illustrate the use of the 1D model is the case of a symmetric, finitely thick conductor. Consider an infinitely long conductor with thickness T and uniform material properties, including conductivity σ and permeability μ, and a skin depth δ. Let us assume the conductor has identical dielectric $(\sigma = 0)$ conditions on both sides, resulting in symmetry along the line $z = T/2$. Consequently, the electric field must be symmetric along this line and A and B must be equal. Then,

$$E_y(z) = A\left(e^{-\alpha z/\delta} + e^{\alpha(z-T)/\delta}\right), \tag{5.7}$$

where A is a constant to be determined based on a single (boundary) condition. This condition can be, for instance, a non-zero field value at a specific position or the total current. When the total current I_{tot} is known, A can be determined by evaluating the integral:

$$I_{tot} = \sigma A \int_0^T \left(e^{-\alpha z/\delta} + e^{\alpha(z-T)/\delta}\right) dz, \tag{5.8}$$

which gives

$$A = \frac{\alpha}{2\sigma\delta} \frac{1}{1 - e^{-\alpha T/\delta}} I_{tot}. \tag{5.9}$$

USC UNIVERSIDADE DE SANTIAGO DE COMPOSTELA

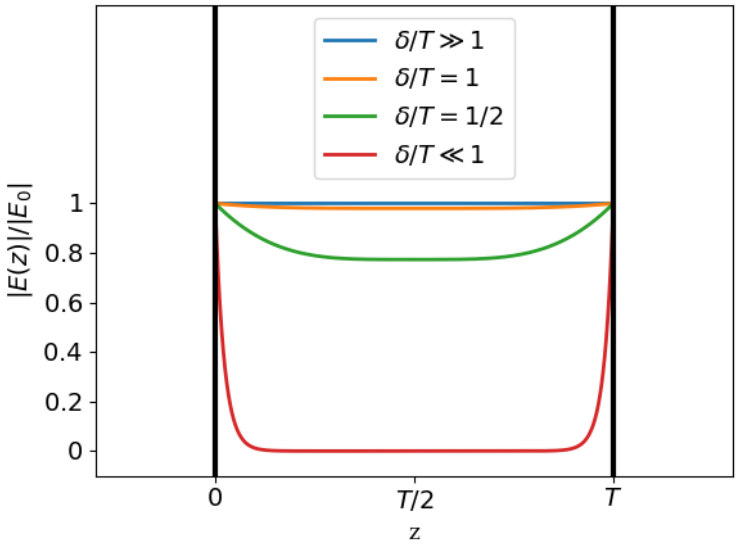

Figure 5.2. Electric field distribution in a symmetric conductor with thickness T for different values of electric conductivity. The values are normalized by the surface value $|E_0| = |E(0)|$.

Figure 5.2 shows the resulting electric field for different values of σ. Four cases are presented: two extreme cases where $\delta/T \ll 1$ and $\delta/T \gg 1$, and two cases where δ and T are of the same order.

The curves presented in Figure 5.9 show that when $\delta/T \gg 1$, the electric field distribution is uniform and resembles a DC solution. Even when $\delta = T$, the distribution remains almost uniform, until the skin effect begins to have an effect at smaller values of δ. In the case where $\delta \ll T$, the skin effect is highly influential, causing the field to decay rapidly to zero within a short distance from the surface.

5.2 Adjacent conducting layers and proximity effects

The one-dimensional model described in (5.1) can be applied to adjacent layers of materials to analyse how the electric field distribution is affected by varying material properties. One interesting application is to study the induced currents in low to moderate conductors caused by nearby good conductors. For the submerged arc furnaces this might be the raw materials adjacent to the electrode, the coke bed (or slag) above the alloy or the furnace lining inside the steel shell Fromreide, Gómez, et al. (2021).

USC UNIVERSIDADE DE SANTIAGO DE COMPOSTELA

Let us consider a medium with two adjacent conducting layers labelled as 1 and 2.

The interface between the layers is denoted as $\Gamma_{1,2}$. The material properties of each layer are characterized by σ_j (conductivity), μ_j (permeability), and ϵ_j (permittivity), with each layer having an associated skin depth, δ_j, where $j = 1, 2$.

As material properties are included in the equation, (5.1) must be solved individually for each layer, and the coefficients be obtained from the boundary conditions and a set of interface conditions.

The interface conditions shall enforce continuity and a smooth transition of electromagnetic fields from one material to the other. They are derived from Maxwell's equations and depend on the nature of the interface and the material properties of each layer. Assuming that no charge accumulation or surface currents are present on the interface, the typical interface conditions at $\Gamma_{1,2}$ are given by (see, for instance, Bermúdez et al. (2014); Griffiths (2017))

$$\mathbf{n} \times (\mathbf{E}_1 - \mathbf{E}_2) = 0, \tag{5.10}$$
$$\mathbf{n} \times (\mathbf{H}_1 - \mathbf{H}_2) = 0, \tag{5.11}$$
$$\mathbf{n} \cdot (\mathbf{D}_1 - \mathbf{D}_2) = 0, \tag{5.12}$$
$$\mathbf{n} \cdot (\mathbf{B}_1 - \mathbf{B}_2) = 0, \tag{5.13}$$

where $\mathbf{n}$ denotes the unit normal vector outside the interface $\Gamma_{1,2}$ pointing from medium 1 to medium 2. In 1D, (5.10) and (5.11) give

$$E_{y,1} = E_{y,2} \quad \text{at } \Gamma_{1,2}, \tag{5.14}$$
$$H_{x,1} = H_{x,2} \quad \text{at } \Gamma_{1,2}, \tag{5.15}$$

that is, the tangential components of the electric field $\mathbf{E}$ and magnetic field $\mathbf{H}$ remain continuous across the interface.

The field $\mathbf{E}$ has only one component in the y-direction. From Ampère's law (3.17) it then follows

$$\frac{d}{dz} E_y = -i\omega\mu H_x. \tag{5.16}$$

From this relation, based on the continuity of H_x at the interface, it can be deduced that the continuity of $(1/\mu) dE_y/dz$ is also required, i.e.,

$$\frac{1}{\mu_1} \frac{d}{dz} E_{y,1}(z) = \frac{1}{\mu_2} \frac{d}{dz} E_{y,2}(z) \quad \text{at } \Gamma_{1,2}. \tag{5.17}$$

Let us consider now that the conductor is infinitely long and that material 1 occupies the region $0 \leq z \leq T$, while material 2 occupies the region $z > T$. In the following discussion, to simplify notation, the subscript 'y' indicating field direction will be omitted.

USC UNIVERSIDADE DE SANTIAGO DE COMPOSTELA

From (5.2), the electric field can be expressed as

$$E_1(z) = A_1 e^{-\alpha z/\delta_1} + B_1 e^{\alpha z/\delta_1} \qquad \text{for } 0 \leq z \leq T, \tag{5.18}$$

$$E_2(z) = A_2 e^{-\alpha z/\delta_2} + B_2 e^{\alpha z/\delta_2} \qquad \text{for } z > T. \tag{5.19}$$

To determine the four unknown coefficients above, the model is completed with boundary conditions at $z = 0$ and at $\lim_{z\to\infty}$, as well as the two interface conditions given by (5.14) and (5.17). As in the single conductor case, the boundary condition at the surface can be replaced by the total cross-section current per unit length by evaluating the integral in (5.5). Since the electric field is bounded, it follows that $B_2 = 0$. Moreover, by applying the interface conditions to (5.18) and (5.19), it is not difficult to show that B_1 and A_2 can be written in terms of A_1 as $B_1 = A_1 B_1^*$ and $A_2 = A_1 A_2^*$, for suitable B_1^* and A_2^*. Indeed, from (5.14) and (5.17) it can be deduced that

$$A_1 e^{-\alpha z/\delta_1} + B_1 e^{\alpha z/\delta_1} = A_2 e^{-\alpha z/\delta_2}, \tag{5.20}$$

$$\frac{\delta_2 \mu_2}{\delta_1 \mu_1}\left(A_1 e^{-\alpha z/\delta_1} + B_1 e^{\alpha z/\delta_1}\right) = A_2 e^{-\alpha z/\delta_2}. \tag{5.21}$$

Consequently, the left hand side of (5.20) and (5.21) must be equal and then

$$A_1 e^{-\alpha z/\delta_1}\left(1 - \frac{\delta_2\mu_2}{\delta_1\mu_1}\right) = -B_1 e^{-\alpha z/\delta_1}\left(1 + \frac{\delta_2\mu_2}{\delta_1\mu_1}\right), \tag{5.22}$$

from where it follows that $B_1 = A_1 B_1^*$ with

$$B_1^* = \frac{\mu_2\delta_2 - \mu_1\delta_1}{\mu_2\delta_2 + \mu_1\delta_1} e^{-2\alpha T/\delta_1}. \tag{5.23}$$

Thus, the constant B_1 in (5.20) can be written in terms of A_1 from which, multiplying both terms by $e^{\alpha T/\delta_2}$ and rearranging the result yields $A_2 = A_1 A_2^*$ with

$$A_2^* = 2\frac{\mu_2\delta_2}{\mu_2\delta_2 + \mu_1\delta_1} e^{-\alpha T(1/\delta_1 - 1/\delta_2)}. \tag{5.24}$$

At this point, two expressions can be used to determine the coefficient A_1 depending on the information that is known. If the surface value E_0 is known, A_1 is given by

$$A_1 = \frac{E_0}{1 + B_1^*}. \tag{5.25}$$

Alternatively, if the total current per unit length I_{tot} is known, then (5.5) can be used to determine this coefficient, which gives

$$A_1 = \frac{\alpha I_{tot}}{\sigma_1\delta_1\left(B_1^*(e^{\alpha T/\delta_1} - 1) - e^{-\alpha T/\delta_1} + 1\right) + \sigma_2\delta_2 A_2^* e^{-\alpha T/\delta_2}}. \tag{5.26}$$

USC UNIVERSIDADE DE SANTIAGO DE COMPOSTELA

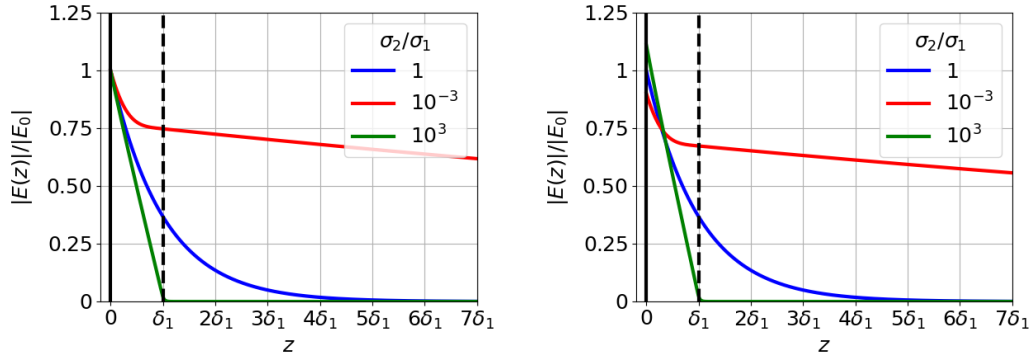

(**a**) Same value of E_0 for all cases.

(**b**) Same value of I_{tot} for all cases.

Figure 5.3. Electric field density distribution in a two-layered conductor with three different conductivities for the second material layer. The base case $\sigma_1 = \sigma_2$ is the same in both (a) and (b). The thick vertical line represents the surface of medium 1, while the interface between both media is indicated by a dotted vertical line.

Figures 5.3a and 5.3b, provide an example of the two-layer model with fixed surface value E_0 and total current I_{tot}, respectively. In both examples, the thickness of the first material layer $(0 \leq z \leq T)$ is set equal to its skin depth $(T = \delta_1)$. In order to analyze the proximity effects due to the second material layer, three cases are considered: one with the same conductivity in both layers, one with far less conductivity on the inside $(z \geq \delta_1)$ and one with much high conductivity. The remaining material properties are the same for both materials.

In Figure 5.3a, the electric field distribution curves are normalized by the fixed surface value E_0. This normalization facilitates the comparison of the electric field distribution for the three different conductivity values in the second material layer.

In Figure 5.3b, the three curves are normalized by the value of E_0 calculated for the case where the conductivities of both material layers are equal $(\sigma_1 = \sigma_2)$. This normalization ensures that the differences in the electric field distribution are solely due to the difference in conductivity in the second material layer, which for fixed total current results in different values for E_0.

Both figures illustrate how the properties of one layer strongly affect the electric field distribution in the other. In particular, when one of the layers is considerably more conductive than the other, the electric field is 'pushed' towards the surface of the less conductive material.

This effect can be viewed as a proximity effect, which, like the skin effect,

USC UNIVERSIDADE DE SANTIAGO DE COMPOSTELA

redistributes and reinforces the electric field in a conductor. The skin effect arises due to induction in a conductor, which causes the electric field to accumulate on the surface. The proximity effect, on the other hand, describes how mutual induction from nearby conductors (or, in this case, adjacent material layers) affects the electric field distribution Griffiths (2017).

5.3 Solution of a general 1D model with three or more layers

The analysis presented in the previous section can be extended to include more material layers, which is often more realistic in practical applications. In this section, the model is generalized to three or more layers, where the inner layer is a dielectric. This model will later be used to describe various situations in a smelting furnace.

Consider a medium with N layers, where $N \geq 3$. The materials are located in the infinite half-plane defined by $z \geq 0$, and an alternating current flows parallel with the layers in the y direction. It is assumed that the first $N-1$ layers are conductors, while the N-th layer is a dielectric with infinite thickness.

Each conducting layer $j = 1, \ldots, N-1$ is characterized by its electromagnetic properties: $\sigma_j > 0$, μ_j, and ϵ_j. In contrast, the N-th layer has $\sigma_N = 0$, $\mu_N = \mu_0$, and $\epsilon_N = \epsilon_0$. The interface between material j and $j+1$ is denoted by L_j, where material j occupies the space $L_{j-1} \leq z < L_j$ for $j = 1, \ldots, N-1$ (with $L_0 = 0$), while the N-th layer occupies the region $z \geq L_{N-1}$. The thickness of each conducting layer is given by $T_j = L_j - L_{j-1}$ for $j = 1, \ldots, N-1$. A schematic representation of this domain is shown Figure 5.4.

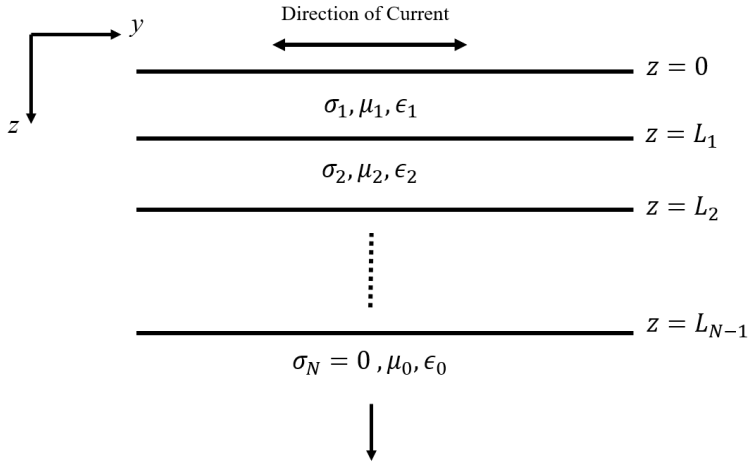

Figure 5.4. Schematic representation of a 1D domain with N layers.

USC UNIVERSIDADE DE SANTIAGO DE COMPOSTELA

The solution to (5.1) for each conducting layer $j = 1, \ldots, N-1$ is given by

$$E_j(z) = A_j e^{-\alpha z/\delta_j} + B_j e^{\alpha z/\delta_j} \quad \text{for } L_{j-1} \leq z < L_j. \tag{5.27}$$

For the dielectric layer ($j = N$), the governing equation reduces to

$$\frac{d^2}{dz^2} E_N(z) = 0, \tag{5.28}$$

which has the general solution

$$E_N(z) = A_N z + B_N. \tag{5.29}$$

Equations (5.27) and (5.29) form a set of N equations with $2N$ unknown coefficients. These coefficients can be determined using the same boundary and interface conditions as for the two-layer model discussed in the previous section. However, in this case, recursive expressions can be used to determine them

5.3.1 Formulation with known electric field at the surface

Let us first assume that the electric field at the surface, E_0, is known. In this case, the boundary and interface conditions can be summarized as follows

$$E(z) = E_0 \qquad \text{at } z = 0, \tag{5.30}$$

$$E_j(z) = E_{j+1}(z) \qquad \text{at } z = L_j, \tag{5.31}$$

$$\frac{1}{\mu_j}\frac{d}{dz} E_j(z) = \frac{1}{\mu_{j+1}}\frac{d}{dz} E_{j+1}(z) \qquad \text{at } z = L_j, \tag{5.32}$$

$$|E(z)| < C \qquad \forall z. \tag{5.33}$$

Here, $j = 1, \ldots, N-1$ and C is a positive constant. By applying these four conditions to the expressions (5.27) and (5.29), the coefficients $A_j, B_j, j = 1, \ldots, N$ can be determined. Since the electric field is bounded, then $A_N = 0$, which implies that the electric field within the dielectric layer is constant.

Recursive relationships can be used to determine the remaining coefficients,

USC UNIVERSIDADE DE SANTIAGO DE COMPOSTELA

yielding

$$A_1 = \frac{E_0}{1 + \frac{\beta_1/\gamma_1 - 1}{\beta_1/\gamma_1 + 1} e^{-2\alpha L_1/\delta_1}}, \tag{5.34}$$

$$A_j = A_{j-1} \frac{2}{\gamma_{j-1} + \beta_{j-1}} e^{-\alpha L_{j-1}/\delta_{j-1}} \qquad j = 2,\ldots,N-1, \tag{5.35}$$

$$A_N = 0 \tag{5.36}$$

$$B_j = A_j \frac{\beta_j/\gamma_j - 1}{\beta_j/\gamma_j + 1} e^{-2\alpha L_j/\delta_j} \qquad j = 1,\ldots,N-2, \tag{5.37}$$

$$B_{N-1} = A_{N-1} e^{-2\alpha L_{N-1}/\delta_{N-1}}, \tag{5.38}$$

$$B_N = 2A_{N-1} e^{-\alpha L_{N-1}/\delta_{N-1}}, \tag{5.39}$$

where, for $N > 3$, the constants β_j and γ_j ($j = 1,\ldots,N-2$) have been introduced. These constants are, in turn, determined recursively by

$$\beta_j = e^{-\alpha L_j/\delta_{j+1}} + \frac{\beta_{j+1}/\gamma_{j+1} - 1}{\beta_{j+1}/\gamma_{j+1} + 1} e^{\alpha(L_j - 2L_{j+1})/\delta_{j+1}}, \tag{5.40}$$

$$\gamma_j = \frac{\delta_j}{\delta_{j+1}} \frac{\mu_j}{\mu_{j+1}} \left(e^{-\alpha L_j/\delta_{j+1}} - \frac{\beta_{j+1}/\gamma_{j+1} - 1}{\beta_{j+1}/\gamma_{j+1} + 1} e^{\alpha(L_j - 2L_{j+1})/\delta_{j+1}} \right), \tag{5.41}$$

for $j = N-3,\ldots,1$, given that β_{N-2} and γ_{N-2} can be computed beforehand as

$$\beta_{N-2} = e^{-\alpha L_{N-2}/\delta_{N-1}} + e^{\alpha(L_{N-2} - 2L_{N-1})/\delta_{N-1}}, \tag{5.42}$$

$$\gamma_{N-2} = \frac{\delta_{N-2}}{\delta_{N-1}} \frac{\mu_{N-2}}{\mu_{N-1}} \left(e^{-\alpha L_{N-2}/\delta_{N-1}} - e^{\alpha(L_{N-2} - 2L_{N-1})/\delta_{N-1}} \right). \tag{5.43}$$

Once the electric field distribution has been determined, the current and power density can be calculated for each layer $j = 1,\ldots,N-1$. The current density is computed using Ohm's law:

$$J_j(z) = \sigma_j \left(A_j e^{-\alpha z/\delta_j} + B_j e^{\alpha z/\delta_j} \right). \tag{5.44}$$

The power density is calculated by taking the time average of the scalar product of the current density and electric field over one cycle of the AC current. In the harmonic regime, this integral yields $|\mathbf{J}|^2/(2\sigma)$. Then, for $j = 1,\ldots,N-1$, straightforward calculations provide

$$p_j(z) = \frac{\sigma_j}{2} \left[|A_j|^2 e^{-2z/\delta_j} + |B_j|^2 e^{2z/\delta_j} + 2\,\mathrm{Re}\left(A_j \bar{B}_j e^{-2iz/\delta_j} \right) \right], \tag{5.45}$$

USC UNIVERSIDADE DE SANTIAGO DE COMPOSTELA

with $L_{j-1} \leq z < L_j$. To obtain this expression, the relation $|A|^2 = A\bar{A}$ was used, where $\bar{A}$ is the complex conjugate of A. The total power generated in layer j can be found by evaluating the integral

$$P_j = \int_{L_{j-1}}^{L_j} p_j(z)dz, \tag{5.46}$$

which gives

$$P_j = \frac{\sigma_j \delta_j}{4}\Bigg[- |A_j|^2 \left(e^{-2L_j/\delta_j} - e^{-2L_{j-1}/\delta_j}\right) + |B_j|^2 \left(e^{2L_j/\delta_j} - e^{2L_{j-1}/\delta_j}\right) + 2\,\mathrm{Re}\left(iA_j\bar{B}_j\left(e^{-2iL_j/\delta_j} - e^{-2iL_{j-1}/\delta_j}\right)\right)\Bigg]. \tag{5.47}$$

5.3.2 Alternative formulation with known total current

The N-layer model studied in the previous section assumes knowledge of the electric field value E_0 at the surface of the first layer. An alternative approach involves using the total electric current per unit length, I_{tot}, through the conductor. This approach requires the expression (5.34) for A_1 to be rewritten as a function of I_{tot}. After this step, the same recursive expressions presented in Section 5.3 can be utilized to determine the remaining parameters.

The total current per unit length I_{tot} is related to the electric field distribution through an integral over the current density in the conducting domain. This integral can be expressed as the sum of integrals for each layer, which, taking into account the Ohm's law, gives

$$I_{tot} = \sum_{j=1}^{N-1} \int_{L_{j-1}}^{L_j} \sigma_j E_j(z)dz, \tag{5.48}$$

where, as previously defined, $L_0 = 0$. This expression replaces the boundary condition (5.30) used in the previous case, while conditions (5.31)-(5.33) remain unchanged. Taking into account the general solution for the electric field in each layer, (5.48) becomes

$$I_{tot} = \sum_{j=1}^{N-1} \sigma_j \int_{L_{j-1}}^{L_j} \left(A_j e^{-\alpha z/\delta_j} + B_j e^{\alpha z/\delta_j}\right) dz, \tag{5.49}$$

which leads to

$$I_{tot} = \sum_{j=1}^{N-1} \frac{\sigma_j \delta_j}{\alpha}\left(- A_j \left[e^{-\alpha L_j/\delta_j} - e^{-\alpha L_{j-1}/\delta_j}\right] + B_j \left[e^{\alpha L_j/\delta_j} - e^{\alpha L_{j-1}/\delta_j}\right]\right), \tag{5.50}$$

USC UNIVERSIDADE DE SANTIAGO DE COMPOSTELA

where the conductivity and thickness of each layer, as well as the coefficients A_j and B_j for the electric field in each layer, are involved.

The recursive relations (5.34)-(5.39) for finding the coefficients A_j and B_j, as given in previous section, are still valid. Moreover, for all j, equations (5.34)-(5.43) can be employed to write A_j and B_j as a product of A_1 as

$$A_j = A_1 \widehat{A}_j, \tag{5.51}$$

$$B_j = A_1 \widehat{B}_j, \tag{5.52}$$

with $\widehat{A}_1 = 1$. By substituting (5.51)-(5.52) in (5.50) yields

$$I_{tot} = A_1 \sum_{j=1}^{N-1} \frac{\sigma_j \delta_j}{\alpha} \left(- \widehat{A}_j \left[e^{-\alpha L_j/\delta_j} - e^{-\alpha L_{j-1}/\delta_j} \right] + \widehat{B}_j \left[e^{\alpha L_j/\delta_j} - e^{\alpha L_{j-1}/\delta_j} \right] \right)$$

and solving for A_1 results

$$A_1 = I_{tot} \left[\sum_{j=1}^{N-1} \frac{\sigma_j \delta_j}{\alpha} \left(- \widehat{A}_j \left[e^{-\alpha L_j/\delta_j} - e^{-\alpha L_{j-1}/\delta_j} \right] + \widehat{B}_j \left[e^{\alpha L_j/\delta_j} - e^{\alpha L_{j-1}/\delta_j} \right] \right) \right]^{-1}.$$

The expressions for $\widehat{A}_j$ and $\widehat{B}_j$ can be obtained using equations (5.35), (5.37), and (5.38). Specifically,

$$\widehat{A}_j = \prod_{k=1}^{j-1} \frac{2}{\gamma_k + \beta_k} e^{-\alpha L_k/\delta_k}, \quad \text{for } j = 2, \ldots, N-1, \tag{5.53}$$

$$\widehat{B}_j = \widehat{A}_j \frac{\beta_j/\gamma_j - 1}{\beta_j/\gamma_j + 1} e^{-2\alpha L_j/\delta_j}, \quad \text{for } j = 1, \ldots, N-2, \tag{5.54}$$

$$\widehat{B}_{N-1} = \widehat{A}_{N-1} e^{-2\alpha L_{N-1}/\delta_{N-1}}, \tag{5.55}$$

where β_j and γ_j are defined in (5.40)-(5.43) depending on the value of j. Finally, the coefficients A_N and B_N are also the same as in the case where E_0 is known, namely $A_N = 0$ and $B_N = 2A_{N-1}e^{-\alpha L_{N-1}/\delta_{N-1}}$ (see (5.36) and (5.39)).

5.3.3 Example case with N=5 layers

As an illustrative example of the general 1D model, let us consider a case with five layers that includes insulators, moderate and very good conductors. The layer properties and thicknesses are provided in Table 5.1. The selected values for the numerical example are representative of typical properties observed in a submerged arc furnace, including those of the coke bed, carbon lining, oxide lining, and steel

USC UNIVERSIDADE DE SANTIAGO DE COMPOSTELA

Table 5.1. Parameters of 1D model example with $N = 5$ and $f = 50\text{Hz}$.

Layer	$T[\text{m}]$	$\sigma[\text{S/m}]$	$\mu_r[-]$	$\epsilon_r[-]$	$\delta[\text{m}]$
1	0.5	$5 \cdot 10^2$	1	1	3.18
2	0.5	$1.4 \cdot 10^4$	1	1	0.60
3	0.2	$1 \cdot 10^{-6}$	1	1	$7.1 \cdot 10^4$
4	0.2	$1 \cdot 10^6$	100	1	$7.1 \cdot 10^{-3}$
5	'∞'	0	1	1	–

Table 5.2. 1D model example with $N = 5$. Dissipated power.

	$\mu_4 = \mu_0$		$\mu_4 = 100\mu_0$	
Layer	P_j [W]	P_j/P_{tot} [%]	P_j [W]	P_j/P_{tot} [%]
1	73.09	14	71.61	11
2	424.01	82	507.30	78
3	0	0	0	0
4	20.30	4	74.87	11
Total	517.40	100	653.78	100

shell. To demonstrate the effect of magnetic permeability on the field behaviour, one of the materials is assigned a relative magnetic permeability different from 1. The electric field is assumed to be known at the surface and set it to $E_0 = 1\text{V/m}$ with $f = 50\text{Hz}$.

Figure 5.5, left, shows the resulting distributions of the electric field, current density, and power density. The electric field exhibits a noticeable non-smooth transition on the surface of the magnetic material. In addition, due to the jumps in conductivity, both the current density and power density exhibit discontinuities at the boundaries of the different materials. Two cases are shown in each figure, assuming either E_0 or I_{tot} is known. For a given I_{tot}, the problem is solved and the corresponding E_0 at the surface is computed. This value is used as the starting point in the other simulation.

The total power dissipated in each layer is presented in Table 5.2. The conductive layers in the example case generate a total power output of approximately 654 W. The second layer is the most significant contributor to the total power output, accounting for 78% of the total power. To examine the impact of magnetic permeability on the results, the test was repeated while changing the value of the relative magnetic permeability in the fourth layer, here denoted by μ_4, from 1 to 100. As a result, the power dissipated in that layer increased considerably, as did the total dissipated power. The resulting distributions of the electric field, current density and power density are also shown in Figure 5.5, right.

USC UNIVERSIDADE DE SANTIAGO DE COMPOSTELA

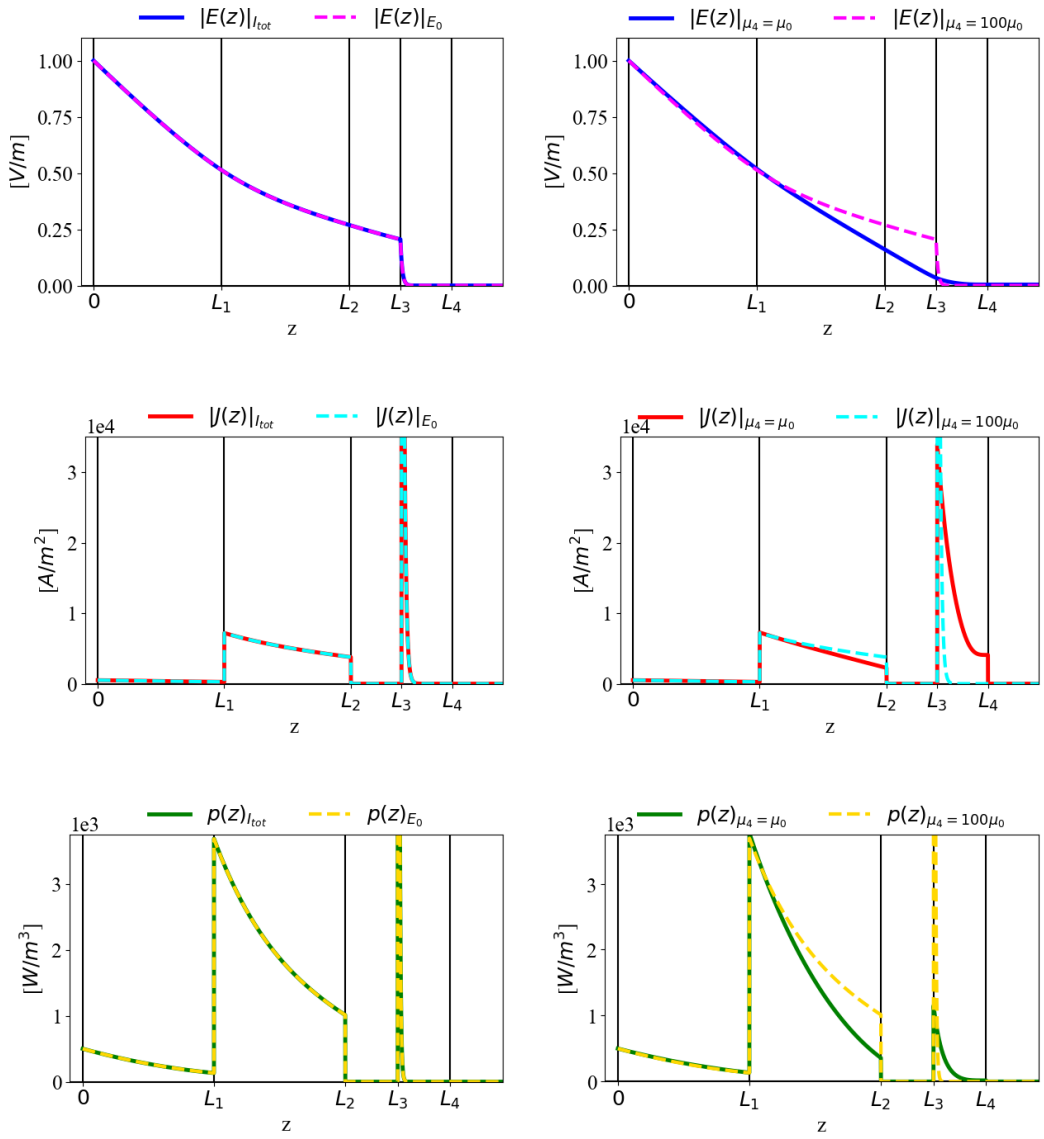

Figure 5.5. Modulus of the electric field, density distribution and power density in a five-layered material example. On the left, the results correspond to $\mu_4 = 100\mu_0$ assuming either E_0 or I_{tot} are known; on the right, a comparison between cases $\mu_4 = 100\mu_0$ and $\mu_4 = \mu_0$ is shown with data E_0.

USC UNIVERSIDADE DE SANTIAGO DE COMPOSTELA

5.4 Comparison of one-dimensional AC and DC simulations

A one-dimensional DC model for the electric field can be obtained by taking the limit as $\delta \to \infty$ ($f \to 0$) of equation (5.1). This results in a constant electric field that extends across multiple material layers. The DC model can be an effective approach for characterizing AC systems in certain cases, depending on the materials and AC frequency involved. However, it fails to consider inductive effects such as the skin effect and proximity effect. Consequently, although the disparity between AC and DC simulations is generally small for a single material with a large skin depth, introducing a second highly conducting layer adjacent to a low/moderate conducting layer will affect the electric field in the first material due to the proximity effect.

This section aims to compare the one-dimensional AC and DC models and analyse the circumstances in which the DC model can provide an accurate approximation of the AC model.

5.4.1 Single material layer

First, let us examine the scenario of a single highly conductive material carrying an alternating current, as introduced in Section 5.1.1. The conductor has a thickness T, conductivity σ, magnetic permeability μ_0, and skin depth δ. Let us also assume that $T \gg \delta$, i.e., the skin depth is significantly smaller than the thickness of the material and, as a result, it can be considered to be infinite.

From the expression (5.6) for the electric field distribution, it is immediate to obtain the total AC power in the conductor

$$P_{AC} = \int_0^{+\infty} \frac{\sigma}{2} E_y(z) \bar{E}_y(z) dz = \frac{1}{2\sigma\delta} I_{tot}^2. \tag{5.56}$$

Let us consider now a conductor with the same conductivity σ and thickness δ carrying DC. In this case, the electric field is constant and given by

$$E_{DC} = \frac{I_{DC}}{\sigma\delta}, \tag{5.57}$$

where I_{DC} denotes the DC current. Consequently, the total DC power is

$$P_{DC} = \frac{1}{\sigma\delta} I_{DC}^2. \tag{5.58}$$

From (5.56) and (5.58), it can be deduced that when the applied DC current is equal to the root mean square value of the AC amplitude, i.e., $I_{DC} = I_{AC}/\sqrt{2}$, then

USC UNIVERSIDADE DE SANTIAGO DE COMPOSTELA

$P_{AC} = P_{DC}$. In other words, for a single highly conducting material, using the one-dimensional DC model with a thickness of δ and an RMS current provides the same power as the one-dimensional AC model with thickness $T \gg \delta$. It is important to note that this comparison is relevant for assessing the total power dissipated in a conducting layer, but not for computing local heating effects due to local differences in power distribution.

Next, let us consider the scenario where the conductivity is low and the skin depth is much larger than the thickness ($\delta \gg T$). This corresponds to the 'DC approximation' regime established in Section 3. In this situation, the second term in equation (5.1) can be neglected, simplifying the problem to be described by equation (5.28) with a constant electric field as solution.

If the full AC model (5.1) were to be considered, the same solution would be obtained for large values of δ, indicating that the AC problem can be treated as a DC problem for an isolated long conductor with a sufficiently large skin depth. However, this holds true only for the material/conductor under consideration if it is not located near a highly conductive material. In such cases, the proximity effect induces additional current, leading to a deviation between AC and DC estimates, as illustrated in the following section.

5.4.2 Two adjacent material layers

In this example, a second conductor is introduced adjacent to the first low/moderate conductor. This configuration can represent, for instance, the presence of liquid metal in a smelting furnace positioned next to the coke bed. The focus lies in examining the effect of the highly conductive second conductor on the current distribution within the low/moderate conductor.

To compute the field distribution in the AC case, the one-dimensional two-layer model introduced in Section 5.2 is considered, with known input current I_{tot}, and material properties $\mu_j = \mu_0$, $\epsilon_j = \epsilon_0$, and σ_j for $j = 1, 2$ with $\sigma_2 \gg \sigma_1$. The first conducting layer occupies the region $0 < z < T$, while the second layer extends from $z \geq T$. Moreover, the conductivity of the second layer, σ_2, is held constant, ensuring that $\delta_2/T \ll 1$.

Based on the insight for a single material, a comparable DC model is considered by confining the second material layer to a thickness of δ_2 and applying a direct current of $I_{DC} = I_{tot}/\sqrt{2}$. For the analysis, three distinct cases are considered, where the electrical conductivity σ_1 of the first layer is varied from the lowest to the highest

USC UNIVERSIDADE DE SANTIAGO DE COMPOSTELA

Table 5.3. Comparison of power ratios as a function of δ_1/T in the two-layer example.

δ_1/T	P_{AC}/P_{DC}	$(P_1/P)_{AC}$	$(P_1/P)_{DC}$
100	1.006	0.004	0
10	1.39	0.28	0.0003
1	23.9	0.975	0.034
1/2	16.6	0.995	0.123
1/10	12.8	1	0.77

value. This results in the following ratios of skin depth to thickness:

$$\delta_1/T = 10,$$
$$\delta_1/T = 1,$$
$$\delta_1/T = 1/2.$$

The electric field obtained is depicted in Figure 5.6a, while Figure 5.6b illustrates the comparison of power density between the AC and DC models for various values of σ_1. The given examples are calculated with $T = 2$ m, $I_{tot} = 1$ A/m and $\sigma_2 = 1 \cdot 10^6$ S/m. The figure emphasizes how the disparity between the AC and DC models varies with the skin depth of the first layer. In the case of low conductivity ($\delta_1/T = 10$), the power in the first layer is small and the difference between AC and DC can be neglected as a first approximation. Significant values and deviations are observed in the other two cases. Notably, for the second material layer, the power density distributions exhibit substantial differences across all scenarios. The qualitative difference of the power distributions in layer 1 will be similar in all cases, but this does not matter when it is small.

Table 5.3 presents a comparison of the total power calculated by the AC (P_{AC}) and DC (P_{DC}) models. Additionally, the ratio of power dissipated in the first material layer relative to the total power (P_1/P) is provided. The table includes the three example cases depicted in Figure 5.6b, along with two additional cases featuring more 'extreme' conductivity values. The values demonstrate that the disparity between AC and DC power becomes more pronounced with increasing conductivity, consistent with the trends observed in Figure 5.6b.

Table 5.3 shows that there is a maximum value of the ratio P_{AC}/P_{DC}, beyond which the ratio gradually becomes smaller. For high values of the conductivity ($\delta_1 \ll T$), the electric field does not penetrate into the second layer, and the results can be interpreted using a single layer-model for the AC. In such cases, the total AC power is given by (5.56). This formula shows that $P_{AC} \sim |I_{tot}|^2/\sqrt{\sigma}$, which tends to zero as the conductivity increases. In this regime, the system can be represented by a DC current in layer one, within a boundary layer of thickness δ_1. Hence,

USC UNIVERSIDADE DE SANTIAGO DE COMPOSTELA

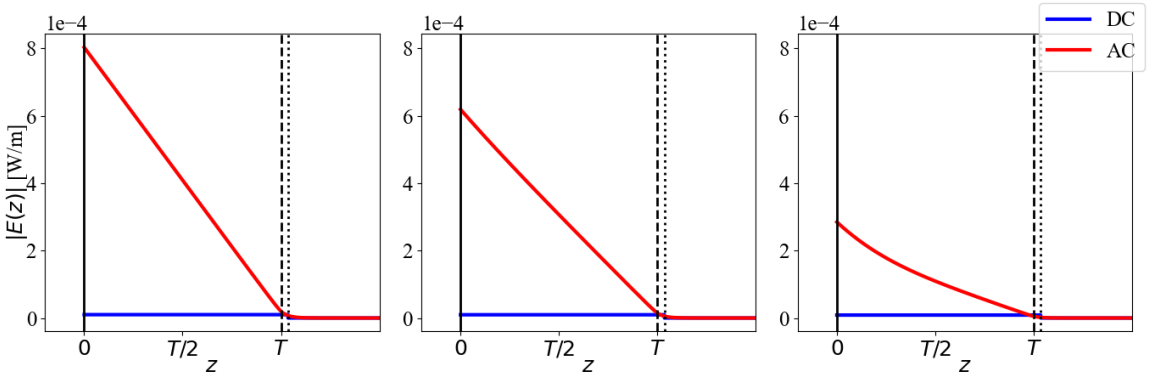

(**a**) E field distribution.

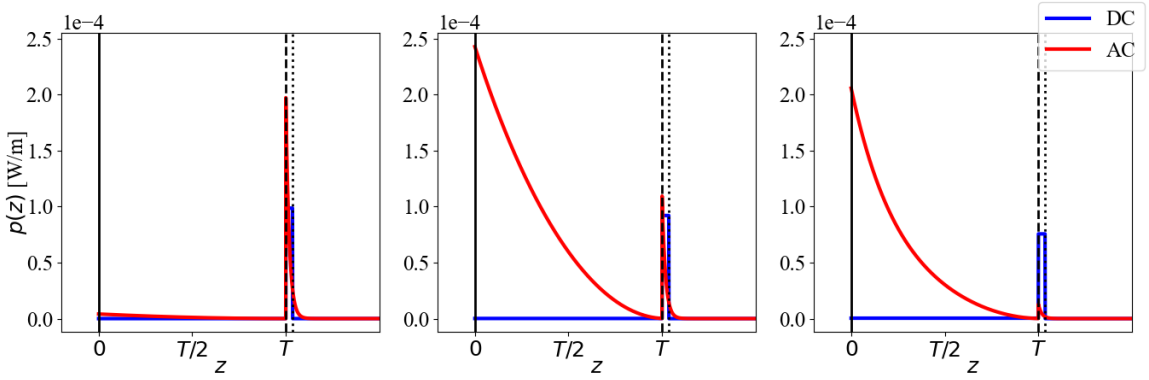

(**b**) Power density.

Figure 5.6. Comparison of AC and DC models as function of δ_1. Cases: $\delta_1/T = 10$ (left), $\delta_1/T = 1$ (middle) and $\delta_1/T = 1/2$ (right). The dotted line indicates the skin-depth of the second layer and the dashed line represents the interface between the two layers.

USC UNIVERSIDADE DE SANTIAGO DE COMPOSTELA

- For small values of δ_1, it is possible to apply a DC model for the first layer, ignoring the current in the second one.
- For high values of δ_1, with $\sigma_2 \gg \sigma_1$, both DC and AC power in layer 1 will be negligible and a DC approximation for layer 2 will be adequate.
- In between, a DC approximation will give significant deviation compared to the power for the AC solution, especially when δ_1/T is close to one.

5.5 An approximate solution for a conductor adjacent to a highly conductive material

This section presents an approximation for the two-layer 1D model discussed in Section 5.2, focusing on the case where the inner layer is a highly conductive material. The analysis considers the total current, I_{tot}, to be constant and examines the conditions when the conductivity of the inner layer approaches infinity. It turns out that the model then approaches a limit with

- Zero E-field at the boundary, $z = T$,
- I_{tot} distributed between the inner layer and a surface current at the boundary,
- Zero power associated with the boundary current.

5.5.1 Derivation of the model

As previously demonstrated, the electric field distribution can be expressed in terms of A_1, B_1^*, and A_2^* as

$$E_1(z) = A_1 e^{-\alpha z/\delta 1} + A_1 B_1^* e^{\alpha z/\delta_1} \qquad \text{for } 0 \le z \le T, \tag{5.59}$$

$$E_2(z) = A_1 A_2^* e^{-\alpha z/\delta_2} \qquad \text{for } z \ge T, \tag{5.60}$$

where B_1^*, A_2^* are defined in (5.23) and (5.24), when the total current I_{tot} is known, A_1 is given by (5.26). From these expressions for A_1, B_1^* and A_2^*, it follows that the electric field in each of the layers, and hence the total power, depend on each other through the skin depths δ_1 and δ_2.

The present analysis examines the behaviour of the two-layer system as the second layer becomes a good conductor with a very high electrical conductivity, σ_2, in the limit, $\sigma_2 \to \infty$ and thereby $\delta_2 \to 0$. For simplicity, the study assumes that the magnetic permeability of both materials is the same $\mu_1 = \mu_2 = \mu_0$.

USC UNIVERSIDADE DE SANTIAGO DE COMPOSTELA

Evaluating the limit for B_1^* and A_2^* gives

$$\lim_{\delta_2 \to 0} B_1^* = \lim_{\delta_2 \to 0} \left(\frac{\delta_2 - \delta_1}{\delta_2 + \delta_1} e^{-2\alpha T/\delta_1} \right) = -e^{-2\alpha T/\delta_1}, \tag{5.61}$$

$$\lim_{\delta_2 \to 0} A_2^* = \lim_{\delta_2 \to 0} \left(2\frac{\delta_2}{\delta_2 + \delta_1} e^{-\alpha T(1/\delta_1 - 1/\delta_2)} \right) = 0. \tag{5.62}$$

Computing the same limit for A_1 involves both the limits for B_1^* and A_2^*, which enter as products with other factors. In particular, A_2^* enters as a product with $e^{-\alpha T/\delta_2}$, and the terms T/δ_2 in the exponential cancel. Thus, it is straightforward to check that the limit for A_1 provides

$$\lim_{\delta_2 \to 0} A_1 = \pi f \mu_0 \alpha I_{tot} \frac{\delta_1}{e^{-2\alpha T/\delta_1} + 1}, \tag{5.63}$$

where it is taken into account that

$$\sigma_j \delta_j = \frac{1}{\pi f \mu_0} \frac{1}{\delta_j}, \quad j = 1, 2.$$

From (5.62) and (5.63) it can be deduced that when $\delta_2 \to 0$ the electric field in the second layer $E_2(z)$ tends to zero, while the expressions in (5.61) and (5.63) show that $E_1(z)$ is independent of δ_2. Thus, an approximate solution for the two-layer problem has been obtained, where $E_2(z)$ is zero and $E_1(z)$ depends only on the material properties of the first layer.

5.5.2 Validation of the approximate model

The approximate model is validated by comparing it with some results for the analytical 2-layer model.

In Figure 5.7 the approximate solution for the electric field distribution is shown together with the analytical solution for three different scenarios. In each case, the total cross-section current is 1 A/m, and the frequency is 50 Hz. The conductivity of the second layer is set to $\sigma_2 = 10^7$ S/m, which corresponds to a skin depth of $\delta_2 = 0.0225$ m assuming $\mu_2 = \mu_0$. The thickness of the first layer is fixed at $T = 2$ m, and three different conductivity values are considered for σ_1: 50, 500, and 5000 S/m. These conductivity values correspond to skin depths of $\delta_1 = 10.1$, 3.18, and 1.01 m, respectively. These values are representative of the materials commonly found in metallurgical furnaces. Note that in the first layer, the field is not fully damped due to the chosen conductivity values.

The approximate solution forces the electric field to be zero in the second region ($A_2^* = 0$), leading to a systematic error in the solution. This error will decrease

USC UNIVERSIDADE DE SANTIAGO DE COMPOSTELA

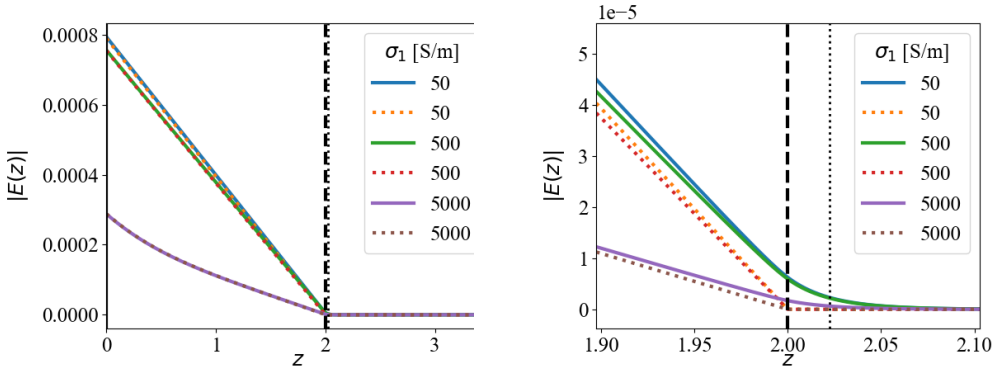

(**a**) $|E(z)|$ in two layers. (**b**) Zoom at the material interface.

Figure 5.7. Electric field distribution in two layers with $\sigma_2 = 10^7$ S/m and $T = 2$ m for different values of σ_1. The solid lines represent the analytical solutions, while the dashed lines correspond to the approximate solutions. On the right, a zoom at the material interface is shown. The vertical dotted line at $z = 2.0225$ m represents the skin depth of the second material.

with increasing conductivity (σ_1) since the field will tend towards zero in layer 1. This phenomenon is illustrated in Figure 5.7b, which displays the same curves as in Figure 5.7a, but only for a small region around the material interface.

The approximate solution $(E_{app}(z))$ is compared numerically with the analytical solution $(E(z))$ by evaluating the relative difference between the two solutions in the first layer, defined as

$$\Delta_1 = \frac{\int_0^T |E(z) - E_{app}(z)|dz}{\int_0^T |E(z)|dz}. \tag{5.64}$$

Table 5.4 shows the values of Δ_1 for each of the three cases presented in Figure 5.7, as well as for the same three values of σ_1 but with σ_2 increased by a factor of 10. As expected, the approximate solutions perform better for higher values of σ_2. Additionally, the solutions are more similar for higher values of σ_1, in agreement with the described difference at the interface.

Table 5.4. Difference between the full and approximate solutions in material 1 for different values of σ_1 and σ_2, calculated from (5.64).

σ_1[S/m]	$\sigma_2 = 1.e7$ [S/m]	$\sigma_2 = 1.e8$ [S/m]
50	0.0157	0.0050
500	0.0151	0.0048
5000	0.0064	0.0021

USC UNIVERSIDADE DE SANTIAGO DE COMPOSTELA

In addition to the values for σ_1 and σ_2 presented in Table 5.4, additional simulation

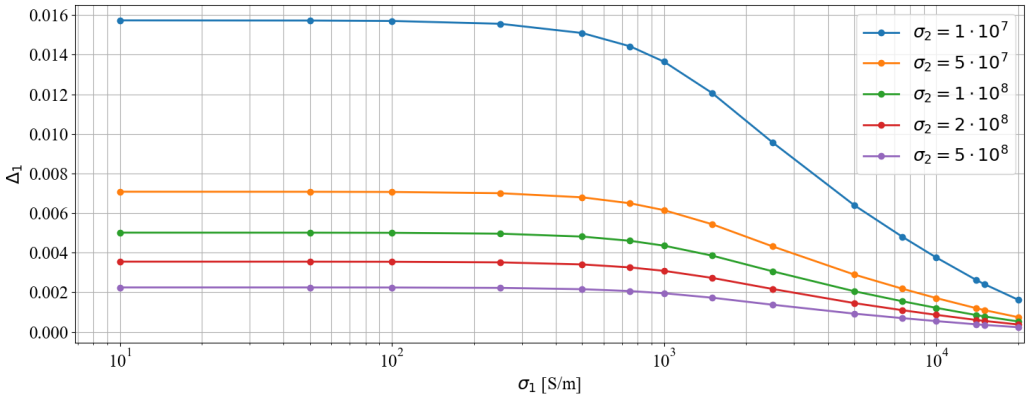

Figure 5.8. Difference between the full and approximate solutions (Δ_1) as a function of σ_1 for different values of σ_2.

cases are performed to observe the behaviour of the deviation of the approximate model. Figure 5.8 displays the values of Δ_1 for various values of σ_2 and σ_1. The plot reveals that the deviation is larger for lower values of σ_2, which corresponds to moving away from the condition for the approximation ($\delta_2 \to 0$). Additionally, the plot shows how the deviation decreases as σ_1 increases. This is due to the fact that the skin depth of the first layer is reduced, so that field is more damped before the interface where it is forced to zero by the approximate solution.

5.5.3 Distribution of current in the approximate solution

In the derivation of the approximate solution, the effective region for current in the second (inner) layer is diminished as δ_2 approaches zero. In the limit of $\delta_2 = 0$, the effective thickness of the outer layer is zero and a possible limit for the current should be interpreted as a surface current at $z = T$.

The total current in layer 1 can be computed. By applying the expressions in (5.61) and (5.63) for B_1^* and A_1, gives

$$I_1 = I_{tot} \frac{\left(e^{-\alpha T/\delta_1} - 1\right)^2}{e^{-2\alpha T/\delta_1} + 1}, \tag{5.65}$$

as the limit when $\delta_2 \to 0$.

Since the total current is given, the interface current at $z = T$, will be

$$I_T = I_{tot} - I_1 = I_{tot} \left(1 - \frac{\left(e^{-\alpha T/\delta_1} - 1\right)^2}{e^{-2\alpha T/\delta_1} + 1}\right). \tag{5.66}$$

USC UNIVERSIDADE DE SANTIAGO DE COMPOSTELA

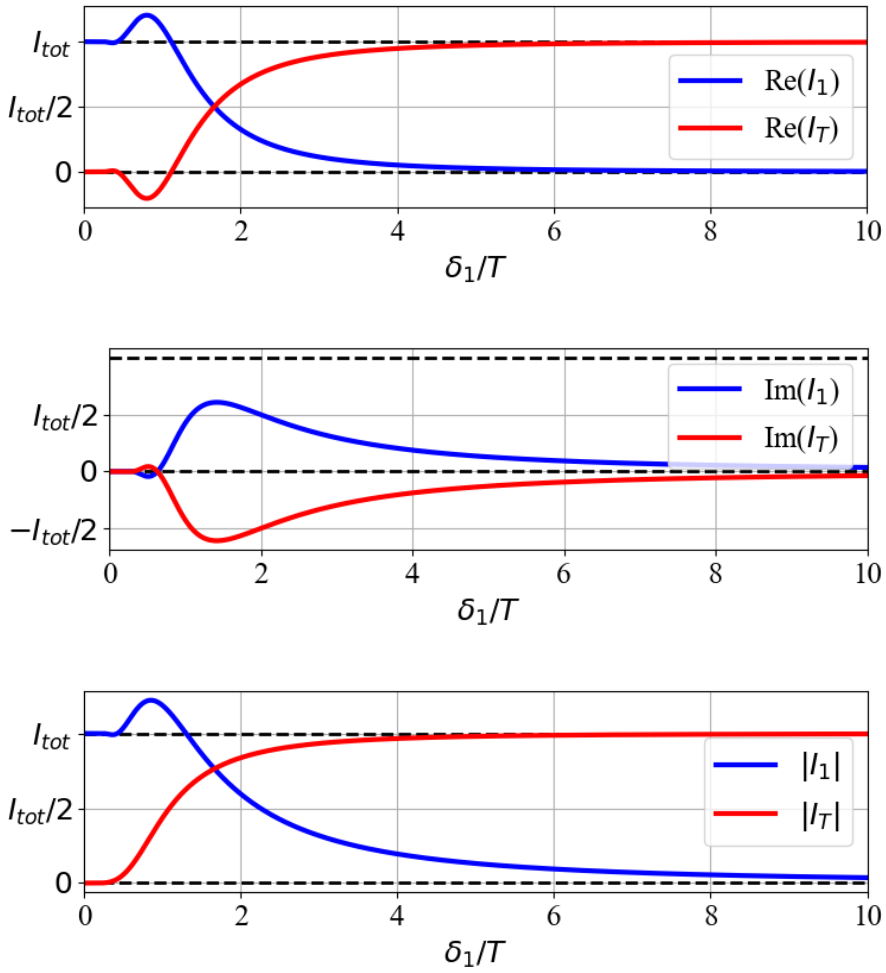

Figure 5.9. Real part (top), imaginary part (middle) and norm (bottom) of the total current in layer 1 and total current at the interface $z = T$ in the limit $\delta_2 \to 0$ as a function of δ_1/T.

In Figure 5.9, these two expressions, I_1 and I_T, are plotted as functions of δ_1/T. As expected, when δ_1/T is very low, i.e., layer 1 is a very good conductor, all of the current runs in this layer, with no field penetrating the cross section. Furthermore, in the opposite case, when δ_1/T is very large and the layer is a very poor conductor, all current is flowing in the surface of the very good conductor. In between these two extremes, an interesting behaviour occur. The total current in the first layer, I_1, exceeds the total current, I_{tot}, for a range of values of δ_1/T. The details are shown in Figure 5.9.

The observed qualitative behaviour is validated by comparing the results with an example calculated by the full model as given in Section 5.2. By fixing the conductivity of the second layer to $\sigma_2 = 6 \cdot 10^8$ S/m and the thickness of the first

layer to $T = 2$ m, the distribution of current has been calculated by varying the conductivity in the first layer. The total current in each case is fixed to $I_{tot} = 1$ A/m. The results are shown in Figure 5.10.

As the figure shows, the curves are similar with the same qualitative behaviour, but with some differences.

5.5.4 Power generated for the approximate solution

For the approximate solution, the E-field is zero at $z = T$ and the line current is limited, c.f. (5.66). Hence, the power associated with the surface current is zero, and all power is generated in the outer layer, $P_{tot} = P_1$, where P_{tot} is the total power and P_1 is the power generated in the outer layer.

New non-dimensional variables denoted by ˜ are introduced as follows

$$z = T\tilde{z}, \tag{5.67}$$

$$E(z) = \frac{I_{tot}}{\sigma_1 T}\tilde{E}(\tilde{z}), \tag{5.68}$$

$$\sigma(z) = \sigma_1\tilde{\sigma}(\tilde{z}). \tag{5.69}$$

We recall that T is the thickness of the first layer in meters, I_{tot} is the total current per unit length in SI units of amperes per meter, and σ_1 is the electrical conductivity of the first layer. Since I_{tot} is given, the E-field is non-dimensionalized by applying Ohm's law, $U = RI_{tot}$, to compute a reference potential (typical E-field). We have then chosen the resistance of layer one (per unit length and width) as the reference resistance, $R = 1/\sigma_1 T$.

By using these new variables and expression (5.59), the non-dimensional power density in the first layer is given by

$$\tilde{p}_1(\tilde{z}) = \frac{1}{2}\left(\frac{T\sigma_1}{I_0}\right)^2 |A_1|^2 \left[e^{-(2T/\delta_1)\tilde{z}} + |B_1^*|^2 e^{(2T/\delta_1)\tilde{z}} + 2\,\mathrm{Re}\left(\bar{B}_1^* e^{-(2iT/\delta_1)\tilde{z}}\right)\right]. \tag{5.70}$$

The total non-dimensional power in the first material is then obtained by evaluating the integral

$$\tilde{P}_1 = \int_0^1 \tilde{p}_1(\tilde{z})d\tilde{z}, \tag{5.71}$$

which gives

$$\tilde{P}_1 = \frac{1}{4}\frac{\delta_1}{T}\left(\frac{T\sigma_1}{I_0}\right)^2 |A_1|^2 \times \left(-\left(e^{-2T/\delta_1} - 1\right) + |B_1^*|^2\left(e^{2T/\delta_1} - 1\right) + 2Re\left[i\bar{B}_1^*\left(e^{-2iT/\delta_1} - 1\right)\right]\right). \tag{5.72}$$

USC UNIVERSIDADE DE SANTIAGO DE COMPOSTELA

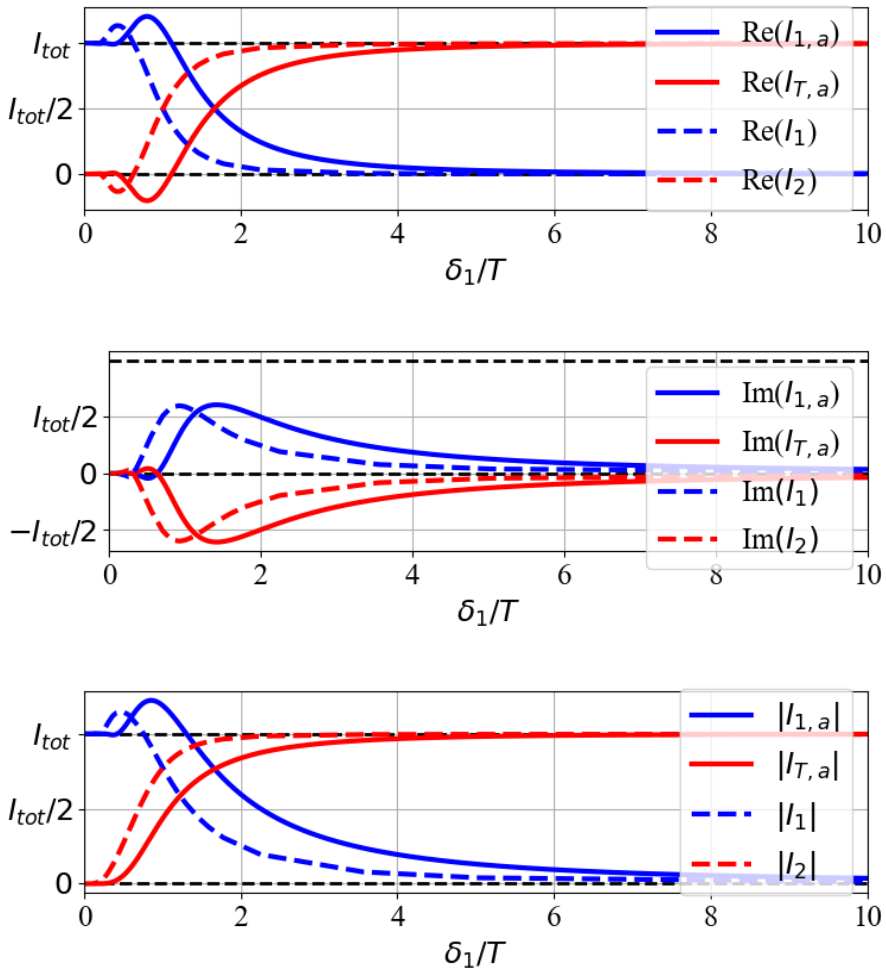

Figure 5.10. Real part (top), imaginary part (middle) and norm (bottom) of the total current in layer 1 and total current at the interface $z = T$ in the limit $\delta_2 \to 0$ (solid lines) and in layer 1 and layer 2 for the full two layer solution (dashed lines) for $\sigma_2 = 6 \cdot 10^8$ S/m and $T = 2$ m as a function of δ_1/T.

USC UNIVERSIDADE DE SANTIAGO DE COMPOSTELA

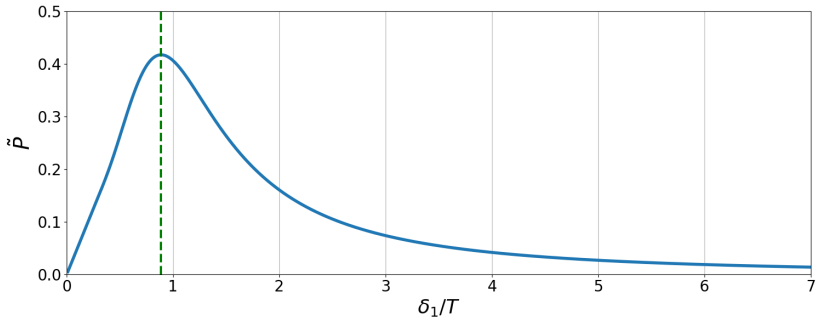

Figure 5.11. Non-dimensional power for the approximate solution as a function of δ_1/T. The vertical line indicates the maximum of the function.

Finally, taking into account the values for A_1 and B_1^* in the limit $\delta_2 \to 0$ obtained in (5.61) and (5.63), the total non-dimensional power results.

$$\lim_{\delta_2 \to 0} \tilde{P}_1 = \frac{1}{4}\frac{\delta_1}{T}\left|\frac{\alpha}{e^{-2\alpha T/\delta_1}+1}\right|^2 \left(-e^{-2T/\delta_1} + e^{-4T/\delta_1} + 2Re\left[ie^{2\bar{\alpha}T/\delta_1}\right]\right). \tag{5.73}$$

It is worth noticing that this expression is a function of the ratio between δ_1 and T, as these are the only physical quantities present in the expression. This dependence is illustrated by plotting the expression as a function of the ratio δ_1/T in Figure 5.11. The curve exhibits a well-defined maximum and decreases rapidly on both sides of the maximum. For small values of δ_1/T, the expression reduces to $\delta_1/2T$, which corresponds to the almost linear slope below the maximum point. This point is determined numerically to be $\delta_1/T = 0.887$.

In the Section 5.7, this 1D model will be applied to the linings and steel shell of a SAF and the results compared with that of a 2D model that includes out-of-plane currents.

5.5.5 Discussion

When I_{tot} is given, the total current will be distributed between the inner and outer layers. For the approximate model, there will be a surface current at $z = T$, representing the current in the inner layer.

The sum of the real values of the currents add up to I_{tot}, while any imaginary value of the outer current is counteracted by an opposite imaginary component, c.f. Figure 5.9.

The approximate model behaves as expected in the two extremes, c.f. Figure 5.9. When $\delta_1/T \ll 1$, the electromagnetic field will not penetrate to the outer layer and (almost) all current will run in layer 1. In the limit, $I_1 = I_{tot}$, $I_T = 0$ and the current distribution in layer 1 is like the distribution for the one-layer case. At high values

UNIVERSIDADE DE SANTIAGO DE COMPOSTELA

for δ_1, the field will penetrate the outer layer, and a substantial part of the current will be distributed to the surface current at $z = T$. In the limit when $\delta_1 \to \infty$, $I_1 = 0$ and $I_T = I_{tot}$.

At moderate levels for δ_1 / T, Figure 5.9 shows negative real values of the surface current and correspondingly increased current in layer 1, i.e., $I_1 > I_{tot}$. This is interpreted as a consequence of normal induction. When there is AC in layer one, layer 2 responds with an induced current in the opposite direction. This effect dominates for some values of δ_1 / T. For increasing values of δ_1 / T, the current will preferentially run with no resistance at the boundary, until all current is found here. Figure 5.9 also shows that induction is dominated by the imaginary component from $\delta_1 / T \sim 1$ and higher values.

Figure 5.10 shows the current distribution between the two layers for a finite value of σ_2 along with the values for the approximate solution. There is a competition between three effects:

- The current tries to run in the less resistive layer.
- The electromagnetic field must penetrate layer 1 to enable current in layer 2, and this effect will reduce the amount of current in layer 2.
- When there is current in one conductor (here layer 1), a nearby conductor (layer 2) will counteract by inducing a current in the opposite direction.

Figure 5.10 shows that the curves are shifted towards lower δ_1 / T values for a finite σ_2. In addition, the finite conductivity causes more rapid decay towards all current in the inner layer. This demonstrates that the effect of lowered resistance in the inner layer is effectively counteracted by less penetration of the electromagnetic fields when δ_2 approaches zero.

Since there is a maximum for the current in layer 1, we expect a corresponding maximum for the total power, as shown in Figure 5.11. The maximum point implies that there exists a value of the electrical conductivity for maximizing the generated power, given a certain thickness T, or vice versa.

5.6 1D model applied to the hearth of a furnace

In this section, the 1D model is applied to approximate the current density distribution in the region between the electrodes in a three phase furnace. The results will be compared with those provided by the 2D model with in-plane currents defined in Section 4.2.2, along the vertical centreline of the furnace.

The analysis in previous sections have shown that a 1D model of the electric field is valid for long and thin conductors. To validate the study, simulations were initially conducted using an unrealistic long furnace model. For this purpose, the

USC UNIVERSIDADE DE SANTIAGO DE COMPOSTELA

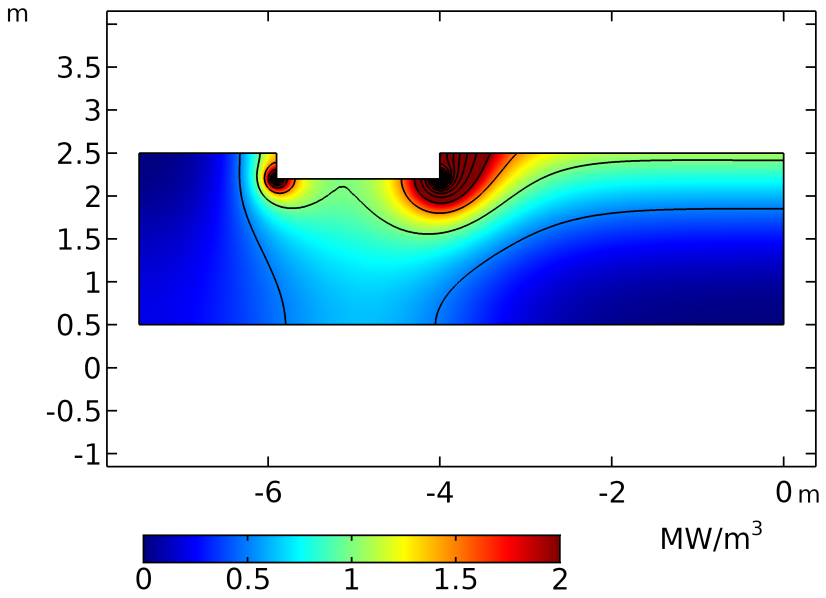

Figure 5.12. Power density in the left side of coke bed of a *long and thin* furnace. The contour lines indicate levels of constant power with a difference of 0.5 $\mathrm{MW/m^3}$.

distance between the electrodes is set to 8 m and the total furnace width is extended accordingly. This modification makes the coke bed region between the electrodes to become long and thin. The remaining parameters are kept equal to the simple furnace model in Section 4.2.1. This gives $(H_{Co}/L_E)^2 = 0.0625 \ll 1$, which is clearly in the long and thin regime.

In Figure 5.12 the power distribution on the left side of the coke bed is represented. The included contour lines show that the electric behaviour is 1D outside a boundary region around the electrode tip. This suggests that using a simplified 1D model would be sufficient to capture the essential behaviour of the system in this zone, where the current flow occurs horizontally, and the variations in power density occur primarily in the vertical direction. Thus, the numerical simulation agrees with the analysis.

Next, a comparison between the analytical 1D model and numerical 2D model is conducted for the reference case scenario; that is, the dimensions of the 2D model follow the reference case in Table 4.1. The relevant non-dimensional ratios defining the furnace are presented in Table 4.5. Even if in this case the region is not 'long and thin', the 1D model may provide insight. Figure 5.13 presents a plot of the power density across the vertical cross section at the furnace center. In the 1D model, the value E_0 was assigned as input at the top of the coke bed (defined at $z = 0$ m). For the purpose of this analysis, only the coke bed $(0 - 2$ m) and alloy $(2 - 2.5$ m) regions are considered, while the low conducting charge is neglected.

USC UNIVERSIDADE DE SANTIAGO DE COMPOSTELA

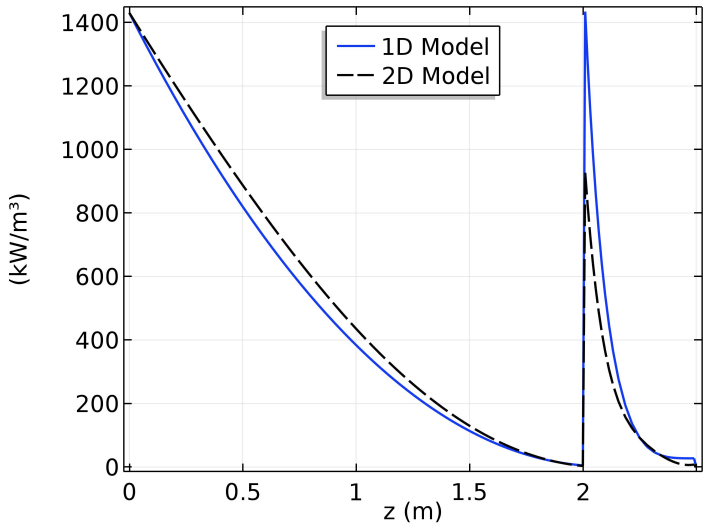

Figure 5.13. Power density at furnace center for the reference case. The range is from the coke bed top ($z = 0$) to the metal bottom ($z = 2.5$).

The comparison shows good agreement between the two models in the coke bed region. Even a larger deviation is observed in the top surface of the metal layer, the figure demonstrates that the 1D model adequately captures the overall behaviour of the power density distribution. To assess the sensitivity of the comparison depicted in Figure 5.13, a similar analysis was conducted for different values of coke bed conductivity σ_{CB}, AC frequency f, and electrode distance L_E. The deviation between the analytical 1D model and numerical 2D model was quantified using the following error measure

$$\kappa = \frac{\int |P_{1D}(z) - P_{2D}(z)| dz}{\int P_{2D}(z) dz}, \tag{5.74}$$

where the line integrals are evaluated from the coke bed top to the middle of the metal layer. As usual, the values of the power P_{1D} and P_{2D} are obtained from the formula $P = |\mathbf{J}|^2/2\sigma$ applied to the 1D and 2D model, respectively. In the 1D model, we only have a horizontal field so that $\mathbf{J} = J_y \mathbf{e}_y$. Due to the symmetry of the 2D model, the current density vector takes the same form as in the 1D model, as the vertical component must be zero. The 1D model is unable to describe the horizontal currents in the outer skin of the metal, as they are to a large extent caused by 2D effects. Therefore, in order to neglect a systematic error, the bottom half of the metal has been not considered.

From this numerical inspection it is found that the 1D estimate is most sensitive to variations in the relationship between the electrode distance and the coke bed skin depth. Figure 5.14 depicts the value of κ as a function of the non-dimensional number $2(L_E/\delta_{CB})^2$, which characterizes the electromagnetic behaviour in the region. The deviations for three different studies are shown where changes in the non-dimensional number $2(L_E/\delta)^2$ have been performed by either changing

USC UNIVERSIDADE DE SANTIAGO DE COMPOSTELA

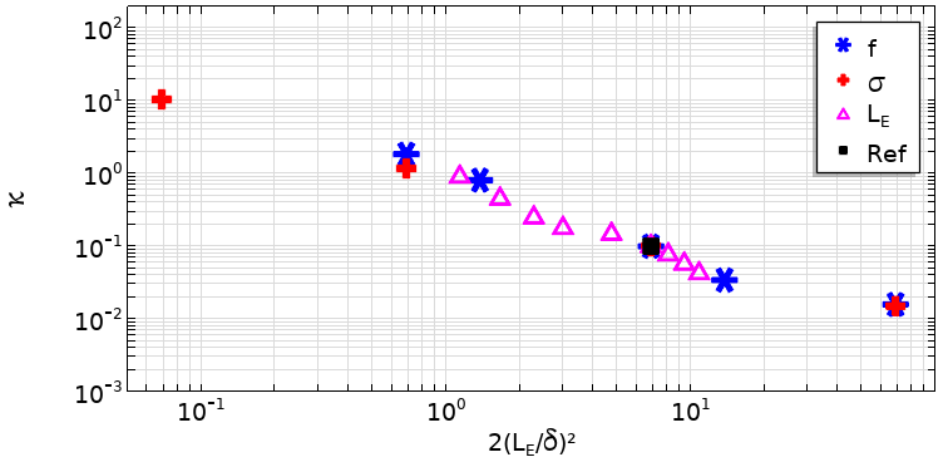

Figure 5.14. Log-log plot of the deviation of 1D estimate for different parameter settings. $2\,(L_E/\delta)^2$ is changed by either changing f, σ or L_E, while keeping the other two parameters constant.

the frequency f, the coke bed conductivity σ or the electrode distance L_e, while keeping the other two parameters constant. Each symbol/color represents a different parameter variation. The reference case, corresponding to the analysis displayed in Figure 5.13, is indicated by a black square. The deviation in this case is about 10%. The findings follow a roughly declining line in the log-log plot. The deviation of the 1D model compared with 2D decreases when either the electrode distance increases or the coke bed skin depth decreases. This result agrees well with the non-dimensional analysis

5.7 1D model applied to the linings and casing of SAFs

In this section, the general analytical 1D model is applied to describe the distribution of electromagnetic fields in the linings and steel shell casing surrounding a submerged arc furnace. Moreover, the 1D model results are compared to the numerical simulations obtained from the 2D model with out-of-plane currents presented in Section 4.4. Figure 5.15 illustrates the 2D model geometry, comprising all three electrodes, an inner (dielectric) charge material, different lining layers, the steel shell casing, and the surrounding air. This 2D geometry pertains solely to the upper part of the furnace, where the current can be assumed to be vertical.

A small portion of the linings and shell within the different material regions is highlighted. The 1D model applies to this area, which encompasses a conducting carbon lining, an insulating oxide lining, the steel shell, and the surrounding air, thus forming a four-layer system. The fourth layer, consisting of the surrounding air, acts as the infinite dielectric base layer of the general N-layer model. Due to the large

USC UNIVERSIDADE DE SANTIAGO DE COMPOSTELA

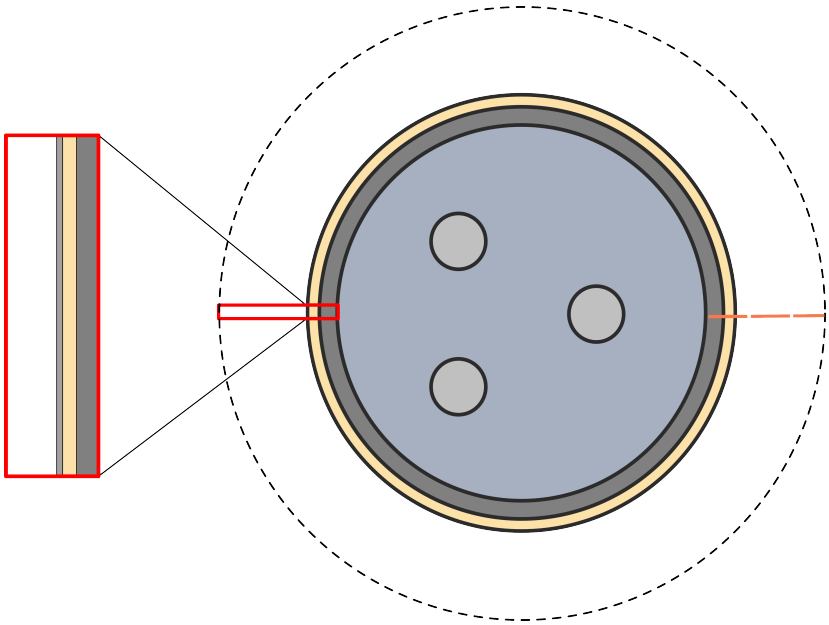

Figure 5.15. Geometry of 2D model including an enlarged detail of the linings and steel shell.

diameter of the furnace and the comparatively small thickness of the linings and steel shell, this region can be considered as a long one-dimensional conductor.

To compare the 1D and 2D models, the radial electric field distribution along the dashed line indicated in Figure 5.15 will be examined.

Figure 5.16 compares the results of numerical 2D simulations with those of the analytical 1D model for two different simulation cases. The two cases differ with respect to the properties of the steel shell, where one is magnetic with a relative magnetic permeability of $\mu_s = 100$ (as in the reference case), while the other is non-magnetic with $\mu_s = 1$. The electrical conductivity of the steel shell also varies between the two cases, with $\sigma_s = 3 \cdot 10^6$ for the magnetic case and $\sigma_s = 1 \cdot 10^6$ for the non-magnetic one. These values reflect the different types of steel casings found in practical applications and are consistent with those used in Herland et al. (2018). In both cases, all materials are considered magnetically linear.

The plot presents the radial distribution of the electric field from the inner surface of the carbon lining to the outer boundary of the steel shell. In both cases, the field value at the surface (E_0) is extracted from the numerical solution and used as input for the analytical 1D model. The results demonstrate that the 1D model effectively captures the behaviour of the electric field in the radial direction for both simulation cases.

It should be noticed that in the given example, the 1D model depends on the E_0 input data calculated by the 2D simulations for each case. This represents a limitation of

USC UNIVERSIDADE DE SANTIAGO DE COMPOSTELA

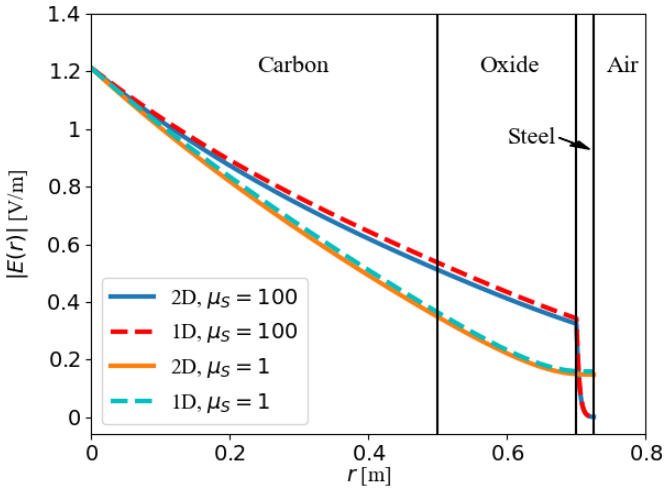

Figure 5.16. Radial electric field distribution as calculated by the numerical 2D simulation (solid) and the analytical 1D model (dashed) for two cases with magnetic and non-magnetic steel.

the model in terms of delivering precise numerical results. However, as the example illustrates, the E_0 value is nearly identical for the two cases.

The primary advantage of the 1D model lies in providing a qualitative understanding rather than quantitative results. As demonstrated in this example, it can be utilized to investigate the impact of modifying the properties of a specific layer, as the ratio of the two different distributions will be (approximately) independent of E_0.

Moreover, if the steel is assumed to be a 'very good' conductor and the combined carbon and oxide linings are regarded as a moderately conducting layer, this model can serve as an example of the approximate model derived in Section 5.5.

It is of interest to investigate whether the qualitative behaviour described by (5.73) and illustrated in Figure 5.11 can replicate the behaviour of the 2D model. To examine this, the 2D model was simulated with varied carbon lining conductivity, while keeping the remaining parameters constant according to Table 5.5, with non-magnetic steel in the shell. For each simulation, the total power generated in the carbon lining was computed through numerical integration in COMSOL. The integration was performed for both the full annulus representing the carbon lining and a small section with an angular width of 0.1° placed centered behind an electrode, as illustrated in Figure 5.15. The integration within a small section is adequate for comparing the 1D model with the 2D simulations. In principle, the same qualitative result for any section is expected. The integration of the whole annulus represents an average of all sections and is computed to check whether it behaves similar to a single section.

USC UNIVERSIDADE DE SANTIAGO DE COMPOSTELA

Table 5.5. Material properties (from Herland et al. (2019)) and layer thickness for the furnace casing model; the skin depth is computed for $f = 50$ Hz.

Material	σ [S/m]	μ_r [-]	δ [m]	T [m]
Carbon	$1.4 \cdot 10^4$	1	0.60	0.5
Oxide	$1 \cdot 10^{-6}$	1	$7.1 \cdot 10^4$	0.2
Magnetic Steel	$3 \cdot 10^6$	100	0.0041	0.025
Non-Magnetic Steel	$1 \cdot 10^6$	1	0.71	0.025
Air	0	1	–	–

Figure 5.17 displays the resulting distribution $P(\sigma_{carbon})$ along with the 1D approximated solution obtained in Section 5.5, with the distributions plotted as a function of the ratio of the skin depth to the thickness of the carbon lining (δ_C / T_C). To enable meaningful comparisons, all the curves were normalized by scaling them with the maximum value.

The values obtained from the numerical 2D integration display the same qualitative behaviour as the analytical 1D approximation, with a slight shift in the peak position. Some deviation from the 1D analytical model is expected due to the cylindrical geometry, distributed electrodes, and design of the lining. One would expect the results from the small section nearest to the electrode to be more similar to the analytical result, and they are. However, the discrepancy in peak position between the small section integral and the full integral is nearly insignificant.

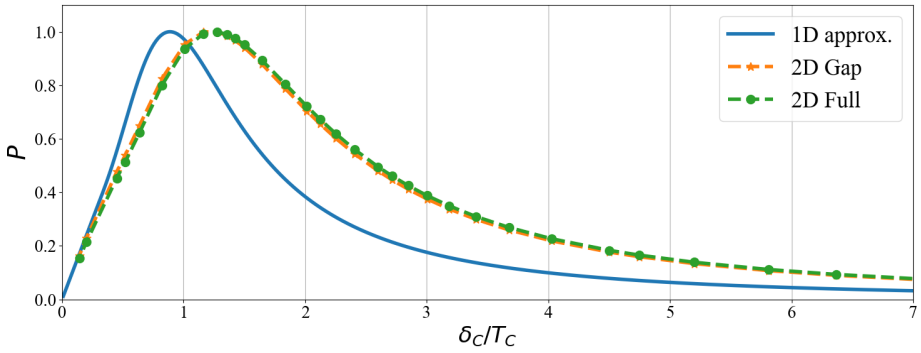

Figure 5.17. Normalized total power dissipated in the carbon lining as a function of δ_C / T_C calculated with varying conductivity by the analytical 1D model and by numerical 2D integrals over the full domain and a small section of the carbon lining.

USC UNIVERSIDADE DE SANTIAGO DE COMPOSTELA

5.8 Discussion

In this chapter, a general model for the electromagnetic field behaviour in a multilayer one-dimensional system has been presented. The model is similar to the 'multilayer coated conductor' model introduced in Deng et al. (2009), which defines a measure for the 'effective skin depth' in layers of well-conducting materials in a high-frequency regime that requires a full wave solution. The boundary conditions in Deng et al. (2009) are defined in terms of the field strength E_0 at the outer surface and by forcing the field to zero in a well-conducting N-th layer (base conductor), where the skin depth is very small compared to the thickness, ensuring that the field would decay to zero within it.

The motivation and derivation for the model presented in this thesis are different. Since this work considers electrical furnaces operating at low-frequency AC, only the low-frequency solution is of interest. Therefore, the term corresponding to electromagnetic waves has been neglected, simplifying the model and its corresponding solution. Furthermore, the boundary conditions can be given in two forms: either in terms of the electric field value at the surface (or any field value for a given position z along the 1D-axis) or the total current over the conducting cross-section.

The multilayer model is limited by the need for input data that might be difficult to obtain, at least in the case of metallurgical furnaces, where both the field value E_0 for a given surface within the furnace and the total current over a cross-section are, in principle, immeasurable. However, as has been demonstrated, the model can still serve as a tool to better understand the mechanisms at work and provide an initial estimate of the effect of changing materials or dimensions. If the value E_0 is approximately equal in two separate cases, the relative difference between them can be calculated by the 1D model, as the field value E_0 cancels on both sides of the equation. An example of this is given in Figure 5.16, which shows the results from two different simulations with varying steel shell properties. In general, the extracted E_0 value from the 2D simulations did not change significantly. This is understandable in situations like this, where the value E_0 is primarily governed by the applied electrode current and the distance to the conducting outer layers (carbon lining and steel shell) Herland et al. (2019). Furthermore, this demonstrates that the change in the electric field density and, consequently, the current and power distributions could have been estimated by the 1D model.

Both of the boundary conditions, E_0 and I_{tot}, are scaling factors for the resulting distribution. The shape of the distribution is independent of the applied electrical energy, which is why relative differences and quantities such as the effective skin depth (as in Deng et al. (2009)) can be calculated.

A possible use of the N-layer model is to study the electromagnetic fields in a material where the conductivity varies due to temperature changes. The model

USC UNIVERSIDADE DE SANTIAGO DE COMPOSTELA

could then provide a fast answer by subdividing a material into any number of layers with a given variation in conductivity.

Furthermore, a special case with two material layers was considered, and an approximate solution was derived. The approximation is based on having a moderately conducting layer adjacent to a very good conductor, an arrangement that can be related to several regions in a SAF, such as the steel shell surrounding the furnace lining and interior. In the approximate solution, the dependence on the highly conducting layer disappears for the distribution in the first layer. By considering the total generated power in the first layer on a non-dimensional form as a function of the ratio δ/T, an interesting behaviour occurs. For small values of δ/T, the power increases linearly as the ratio increases. Then, a maximum is found for a given value ($\delta/T = 0.887$) before the function decays and tends to zero as $\delta/T \to 0$. If the skin depth is much smaller than the thickness of the first layer, the field would tend to zero within it, and the solved model would be equivalent to solving only for one material layer, ignoring the second (good conducting) layer altogether. For the values presented in Table 4.2, which are considered reasonable for industrial furnaces, $\delta/T \approx 0.95$ for the carbon lining, and thus close to the maximum of the generated power function. By calculating the total power generated in the carbon lining using a 2D model for different electrical conductivities, the same-shaped function was obtained (Figure 5.17), showing that the behaviour is adequately explained by the analytical 1D model. There was a shift in the maximum point for the 2D simulations compared with the analytical 1D. Such a shift was expected, c.f. section 5.5.5 which focused on how the total current distributes between the two layers. Also notice that, the maximum point was approximately the same if the full carbon lining was considered in the integral or if only a small section around it was selected.

The two-layer model, with its approximation, illustrates very well how various types of models supplement each other: The approximate 1D model reveals the fundamental behaviour when a very good conductor is adjacent to a moderate one. Then the two-layer model will disclose how various values of the conductivities in both layers can affect the solution. Finally, the out-of-plane furnace model, verifies that the findings for the 1D model are relevant for the behaviour within the furnace lining and steel shell. When applying the results for an actual furnace design, the simulations should be supplemented with at least one 3D simulation. The induced currents have to close in loops, and 3D is required to include this effect.

The analytical 1D model and its deviation from the 2D numerical simulations for the conditions between two electrodes were evaluated as follows. The deviation was studied as a function of the non-dimensional ratio $2\,(L_E/\delta)^2$, which describes the ratio between the distance between the inside of the electrodes and the coke bed skin depth. A similar decay was found independent of which of the three parameters, L_E, f, or σ, was varied. From the underlying assumptions of the 1D model, it is

USC UNIVERSIDADE DE SANTIAGO DE COMPOSTELA

straightforward to expect that as the distance between the electrodes is increased, the aspect ratio L/T increases and the model becomes more 'long and thin', thus being more close to 1D. Both the AC frequency, f, and the electrical conductivity of the coke bed, σ, will change the skin depth in the coke bed. As the skin depth gets smaller, the effective region carrying current will be thinner, resulting in a 'long and thin' effective conductor. Thus, the similar behaviour of the 1D deviation from 2D is also found for variations in these parameters.

Since the 2D model with in-plane currents is symmetric about the central axis, the fields at this point will always vary only in the vertical direction. This is generally not true for 3D furnaces, either in symmetrical or non-symmetrical cases. The overall effect of the distribution and inductive effect will, however, translate to 3D, but the effects might be less clear due to the more complex geometry and spatial distribution of the fields.

For the two-layer 1D model we have focused on the condition where the total current is given. This is evidently appropriate when a given current enters and leaves a region, for instance for the 2D simulations of the furnace hearth. But it will also work well in many cases where the currents are induced. For example, consider an out-of-plane model for the upper part of the furnace. For the limiting case with line currents describing the electrodes, non-conducting charge and lining, and infinitely thin steel shell, the vertical induced currents in the steel shell can be described by an analytical model Herland et al. (2018). As the lining and steel shell are comparatively thin, these induced currents can still be applied as an approximation for a real furnace. Hence, the 1D model with the total current given can be used to study the behaviour of different materials and design variations. Based on the findings, the 1D models should be supplemented with some 2D and/or 3D simulations for a final verification of the simpler model.

5.9 Conclusions

An analytical low-frequency 1D model has been developed to describe the electric field in layered conductors, with a particular focus on metallurgical smelting furnaces. The model can determine the electric field distribution over a layered material by knowing a single field value or the total cross-section current per unit length.

The model provides insight into the mechanisms of inductive effects in adjacent conductors and how the material properties of one material impact other materials in its proximity. The distribution in a single material layer is governed by the ratio of the material skin depth to the layer thickness. Additionally, the surrounding materials have a significant impact, determined by the interface conditions for the electric and magnetic fields.

USC UNIVERSIDADE DE SANTIAGO DE COMPOSTELA

Comparison of the predicted electric field distribution by the 1D model with a numerically solved 2D model has shown that the 1D model provides a good estimate of the 2D solution, particularly when applied to various regions of SAFs. Thus, the physical mechanisms involved are adequately described by the 1D model.

When a (moderately) conducting layer is in proximity to a very good conductor, the current density will be 'pushed' outward, increasing the current in adjacent moderate conductors. Then, an approximation can be made that considers only the moderate conducting layer itself to determine the solution. This solution has an interesting property for the total generated power of the conductors. By introducing non-dimensional variables, a simple expression for the total dissipated power in terms of the ratio δ/T has been obtained, which has a distinct maximum. Thus, for any thickness T, there is a given conductivity σ that gives the maximum amount of dissipated power. The same behaviour has been observed in numerical 2D calculations of dissipated power in the carbon lining of submerged arc furnaces.

The 1D model has been employed to analyse the difference between DC and AC simulations. For a single infinite conductor, a DC model, applied with a thickness delta and an RMS current, yields the same power as the infinite conductor. In the case of a low-conducting (finite) conductor, AC and DC estimates will be similar when the thickness delta approaches infinity. However, this holds true solely for the particular material or conductor in question, provided it is not situated near a highly conductive material. The proximity effect, in such cases, induces additional current, leading to an even greater deviation between AC and DC estimates.

The 1D model can be used as a tool for better understanding inductive effects for distributions through multiple material layers. It is easy to implement and analyse and can work as an aid in the design of furnace linings or other applications where the current can be thought of as one-dimensional. Thus, the 1D model is a tool for qualitative analysis and insight into the mechanisms at work, but more precise full-scale models will still be needed for a detailed understanding of the system.

USC UNIVERSIDADE DE SANTIAGO DE COMPOSTELA

USC
UNIVERSIDADE
DE SANTIAGO
DE COMPOSTELA

Conclusions and future work

The aim of this thesis has been to gain a better understanding of the distribution of electromagnetic fields and inductive effects in submerged arc furnaces (SAFs). The work has been carried out within the framework of the ElMet project, which was conducted in close collaboration with two industrial partners, Elkem and Eramet Norway. The project was initiated to better understand the electrical conditions in SAFs, with the ultimate goal of developing mathematical models and tools for process understanding and control. Throughout the project, the results have been presented and discussed with the industrial partners, generating new ideas and questions to be answered. In this chapter, the main conclusions from the work are summarized and an outlook to future work is presented.

Conclusions

This work has been devoted to the study of reduced dimensional models using both analytical and numerical methods. However, more real furnace simulations have also been carried out for specific cases. Numerical simulations in 2D and 3D have been implemented using the AC/DC module in COMSOL Multiphysics®, which formulates Maxwell's equations in terms of a magnetic vector potential **A** and an electric scalar potential V and solves the model by the finite element method. Furthermore, a general analytical model for the electric field has been derived to study inductive effects and has been applied to several cases related to the SAFs.

The main conclusions of this study are summarised in the following sections.

1. **General experience**
   The models demonstrate a general experience with respect to modelling: Simple models in 1D and 2D are preferable to reveal/study the basic phenomena. On the other hand, more comprehensive 3D models, including all significant effects, are needed to clarify the conditions in real furnaces.

2. **Mathematical modelling and numerical simulation in 3D and different 2D frameworks**
   SAFs are supplied with low frequency alternating current. Therefore, the mathematical model can be formulated using the classical eddy current formulation where the displacement current can be neglected. The formulations

USC UNIVERSIDADE DE SANTIAGO DE COMPOSTELA

include scalar and/or vector potentials and appropriate boundary conditions chosen for each specific case. The numerical simulations have been implemented in COMSOL Multiphysics®, where the displacement term is included as it does not cause any additional computational cost. In this sense, an effort has been made to relate the classical formulations to those implemented in the software.

3. **Inductive effects in the furnace hearth by using 2D in-plane models**

   – By analysing the governing equation for the electric field for a 2D conductor, it is found that the electrical current distribution within the conductor is governed by two types of non-dimensional numbers, $(T/W)^2$ and $2(T/\delta)^2$, i.e., the squared geometric aspect ratios and the squared ratio between a length/thickness and the respective skin depth. This has been applied to a 2D furnace model and validated with numerical simulations.

   – The analysis of dimensionless equations with natural assumptions for parameter values, is sufficient to show that the coke bed properties (conductivity, effective height and width) are important for the electrical conditions of the furnace and therefore important for furnace operation.

   – When current flows between two good conductors through a less conductive material, the AC and DC solutions are similar. However, if there are parallel currents in adjacent materials of different conductivity, inductive effects will alter the AC distribution. If there is considerable current in the less conductive material, the AC and DC models differ strongly, and the difference increases with increasing conductivity.

4. **2D in-plane versus 3D models**

   – The results of the 3D simulations are in good agreement with previously published models. Most of the electrical energy is generated in the coke bed, which is both the expected and desired distribution for process operation. In particular, the power density is concentrated around the electrode tips. The conditions are likely to be highly dependent on the shape and position of the electrode tip, which are very difficult to measure and control in real furnaces. Similarly, the exact shape and material properties in the coke bed are very difficult to know, and the model applied is oversimplified with respect to these parameters.

   – In the 2D model, there is a well-defined shortest path/lowest loss path between the two electrodes, which is not so straightforward in the 3D case. The simulations confirm that the proximity effect is much greater in 2D than in 3D. In 2D, the current only tends towards the inner sides of the two electrodes. The 2D model also appears to underestimate the total power dissipated in the coke bed and overestimate the amount in the alloy. In addition, the power density in the coke bed is more inwardly skewed in 2D compared to the more

USC UNIVERSIDADE DE SANTIAGO DE COMPOSTELA

symmetrical (relative to the electrode) 3D distribution.

- 2D in-plane current models are not well suitable to replace full 3D simulations. However, their simplicity and qualitative behaviour can help to understand the sensitivity to different physical and geometrical parameters.

5. **Analysing the impact of alternative structural designs on energy savings and material wear in lining and steel shell**

   - The simulations confirm previous results showing that large vertical currents are induced in the steel shell behind each electrode. The induced currents form three large loops, with horizontal currents between the electrodes at the top of the steel shell and below the electrode tips. At the top, there are strong current concentrations with a corresponding risk of (damaging) hot spots. Further studies in this topic show that limiting the size of the current loops has a detrimental effect. If the steel shell is sectioned with (electrically) insulating gaps, strong opposing currents will form on either side of the gaps, resulting in more heat loss and a higher risk of damaging hot spots.

   - The induced currents in the steel shell are modified by an electrically conductive lining. Such a lining has a shielding effect that reduces the currents in the steel shell. Modifying the geometry of the conductive lining can therefore contribute to furnace designs with less unwanted power dissipation. This will reduce heat loss, the need for cooling water, the risk of damage to the structural steel and potentially increase the life of a furnace shell. As only the electromagnetic problem is solved, other process implications have not been fully explored. Further work is therefore advised on the topic.

6. **One-dimensional modelling of the electric field in layered conductors**

   - From the 2D analysis, a 1D model of the electromagnetic field distribution in conductors in the low frequency domain was developed. This model was further extended to a general model considering layers of different materials.

   - The distribution in a single material layer is governed by the ratio of the material skin depth to the layer thickness. In addition, the surrounding materials have a significant influence, determined by the interface conditions for the electric and magnetic fields.

   - Comparison of the predicted electric field distribution from the 1D model with a numerically solved 2D model has shown that the 1D model provides a good estimate of the 2D solution, particularly when applied to different regions of SAFs. Thus, the physical mechanisms involved are adequately described by the 1D model.

   - When a (moderately) conducting layer is close to a very good conductor, the current density is 'pushed' outwards, increasing the current in adjacent

USC UNIVERSIDADE DE SANTIAGO DE COMPOSTELA

moderate conductors. An approximation can then be made that considers only the moderately conducting layer itself to determine the solution. This solution has interesting properties for the case where the total current is given. For the extreme situations where δ/T is very small or very large, the model shows that almost all current will run in one of the layers, as expected. But when δ/T is around 0.85, there will be an *opposite* current induced in the high conductivity layer and the current in the moderate conductor will therefore be greater than the total current. Correspondingly, there will be a maximum amount of power dissipated. Thus, for any thickness T there is a given conductivity σ which gives the maximum amount of power dissipated. The same behaviour has been observed in 2D numerical calculations of the power dissipated in the carbon lining of submerged arc furnaces.

- The 1D model can be applied to analyse the difference between DC and AC simulations.
- The 1D model can be used as a tool to better understand inductive effects for distributions through multiple layers of materials. It is easy to implement and analyse and can be used as an aid in the design of furnace linings or other applications where the current can be thought of as one-dimensional. The 1D model is therefore a tool for qualitative analysis and insight into the mechanisms at work, but more accurate full scale models are still required for a detailed understanding of the system.

Future work

As a continuation of the ElMet project, a new collaborative project entitled *Electrical Conditions in Submerged Arc Furnaces - Identification and Improvement* (SAFECI) has been started. The SAFECI project involves several industrial partners. The results and findings of the ElMet project, including the models developed in this thesis, will be further investigated and used as valuable tools for the industry.

Further investigation of the inductive effects in FeMn and other furnaces, with more case studies of full 3D simulations, will be a natural continuation of the studies carried out with 2D simulations and analytical models. It will be interesting to observe whether the behaviour of the currents through the coke bed remain consistent in the 3D simulations, as demonstrated in the 2D simulations and derived analytically in the 1D analysis, depending on the properties of the coke bed. Such investigation will, among others, provide insight into the applicability of using DC models as approximations for comprehensive AC models.

The proposed method of exploiting the linearity and symmetry of the three-phase models should be further explored to provide a much faster 3D computational tool.

USC UNIVERSIDADE DE SANTIAGO DE COMPOSTELA

In addition, the analytical 1D model proposed in this work has potential for application in various processes where induced currents occur. It can, for instance, be extended beyond submerged arc furnaces (SAFs) to other furnace types and metallurgical processes, such as induction furnaces.

In the studies developed in the thesis, the steel was treated as a linear magnetic material with constant permeability. It would be interesting to go one step further and consider non-linear magnetic materials. This question could be particularly interesting in the analysis related to the induced currents in the steel shell.

This work has only considered the electromagnetic problem. Future research should investigate the coupling of these electromagnetic phenomena with other effects to gain a full understanding of their impact on the overall process. Not least for the work on induced currents in the lining and steel shell of SAFs. Heat generation, changes in steel quality and mechanical wear of the steel are all interesting and industrially relevant issues. The extension of the carbon lining has been shown to shield the steel shell from induction. At the same time, more heat is dissipated in the lining itself and the effects on the heat balance and the process within the furnace should be studied in more detail.

USC
UNIVERSIDADE DE SANTIAGO DE COMPOSTELA

USC
UNIVERSIDADE
DE SANTIAGO
DE COMPOSTELA

Resumo

Os fornos de arco somerxido, (SAF polas súas siglas en inglés), son fornos de arco eléctrico a gran escala empregados principalmente na produción de ferromanganeso (FeMn) e outras ferroaliaxes, así como outros materiais. Na produción de FeMn, os minerais de manganeso (Mn) convértense en aliaxe de Mn mediante un proceso de redución química. Esta redución require unha cantidade grande de enerxía, que se proporciona mediante quecemento resistivo empregando corrente eléctrica. As correntes eléctricas son da orde de 100 kiloamperios (kA) e o consumo enerxético dun forno industrial adoita superar os 40 megawatts (MW) Olsen et al. (2007). Este consumo elevado de enerxía contribúe aos custos globais de produción. Aínda que o método de produción se remonta a fai máis dun século, segue habendo moitas incógnitas neste proceso tan complexo. Describir e comprender con precisión as condicións de funcionamento é moi importante para optimizar un proceso que consome moita enerxía. Tendo en conta os requisitos de corrente e potencia tan elevados, unha pequena mellora pode ter un impacto significativo nos custos de produción. Así mesmo, un mellor control do proceso pode conducir a unha mellor utilización das materias primas e a unha redución das emisións non desexadas, minimizando o impacto ambiental Kero et al. (2019). Hai que ter en conta que a temperatura das partes internas do forno é moi alta, por iso obter medidas precisas así como conseguir unha observación directa das condicións do forno é realmente unha tarefa moi complexa ou incluso imposible. O modelado matemático e a simulación numérica ofrecen un xeito alternativo de conseguir coñecemento indirecto do proceso converténdose en ferramentas fundamentais para predicir o funcionamento do forno, avaliar o seu correcto funcionamento así como optimizar o deseño e as condicións de operación.

Neste contexto, esta tese de doutoramento desenvolveuse no marco dun proxecto competitivo titulado 'Electrical Conditions and their Process Interactions in High Temperature Metallurgical Reactors' (ElMet) (2015-2020), que tiña como obxectivo principal comprender mellor as condicións eléctricas e o comportamento electromagnético dos fornos trifásicos de arco somerxidos para a produción de ferroaliaxes. O proxecto foi subvencionado con 1.3 M€ polo Consello de Investigación de Noruega (Research Council of Norway) e liderado polo Centro de Investigación Noruego NORCE. Nel participaron tanto socios académicos, a Universidade de Santiago de Compostela, a Universidade de Oxford e a Universidad Noruega de Ciencia e Tecnoloxía (NTNU), como socios industriais, as industrias

USC UNIVERSIDADE DE SANTIAGO DE COMPOSTELA

noruegas Elkem e Eramet Norway, que proporcionaron o 20% da subvención. Deste xeito, o proxecto combinou coñecementos especializados en modelado matemático e metalurxia coa experiencia industrial e o coñecemento dos procesos, para desenvolver modelos matemáticos e simulacións numéricas para SAF; incluíu ademais estudos de verificación de datos materiais e modelos. O proxecto ElMet centrouse en modelos baseados na física: dende modelos sinxelos para comprender os fenómenos básicos ata modelos máis avanzados de elementos finitos para estudos de casos máis realistas. Abordáronse métodos numéricos 3D flexibles e adaptados tanto á produción de ferromanganeso como á de ferrosilicio.

Os esforzos previos atopados na literatura para modelar o comportamento multifísico de fornos eléctricos cobren aspectos de transferencia de calor, electromagnéticos e dinámica de fluídos. Con todo, aínda hai desafíos importantes na comprensión precisa dos efectos da corrente alterna trifásica, incluído o modo en que a distribución de potencia asociada goberna as reaccións químicas e o perfil da temperatura. Por iso, é crucial dispor dun método eficaz para calcular as traxectorias da corrente trifásica e a distribución da potencia. O principal obxectivo desta tese é pechar esta brecha de coñecemento mellorando a comprensión da natureza da corrente alterna trifásica e os seus efectos indutivos en fornos de produción de ferromanganeso. Aínda que o proceso de produción de ferromanganeso implica unha variedade de fenómenos físicos, a tese céntrase unicamente no estudo de modelos electromagnéticos tanto en 3D como en dimensións reducidas 2D/1D. Os modelos 3D permiten realizar simulacións numéricas detalladas do forno co obxectivo de avaliar novos deseños ou validar as ferramentas de orde reducida. Pola súa banda, os modelos reducidos permiten obter ferramentas de menos custe computacional que contribúen a conseguir un coñecemento cualitativo de partes localizadas do forno. Para resumir os desenvolvementos máis importantes en cada un destes eidos, é preciso describir de xeito breve as características máis relevantes dos fornos estudados nesta tese.

Os fornos trifásicos empregados na produción de ferromanganeso consisten nunha carcasa cilíndrica con tres electrodos cilíndricos somerxidos na carga. Unha corrente eléctrica trifásica introdúcese en cada un dos electrodos con un desfase de 120 graos entre eles. Os electrodos, que son moi bos conductores da electricidade, conducen a corrente ata o interior do forno onde se producen as principais reaccións químicas. En particular, a enerxía liberada emprégase para fundir o metal e reducir óxidos a metal. O interior do forno divídese en diferentes rexións, basicamente varias capas interiores, os leitos de coque, o revestimento e a carcasa de aceiro. Estas rexións pódense ver detalladas na Figura 2. Concretamente, podemos distinguir unha primeira parte con carga a diferentes temperaturas (zonas 2, 3 e 4), onde os electrodos (zona 1) están enterrados, o leito de coque (zona 5) e no fondo, unha capa coa aliaxe resultante (zona 6). O termo *leito de coque* fai referencia á área enriquecida entre a punta do electrodo e o metal, onde os óxidos son líquidos. Estes leitos de coque son modelados como medias elipsoides que se conectan no centro do forno.

USC UNIVERSIDADE DE SANTIAGO DE COMPOSTELA

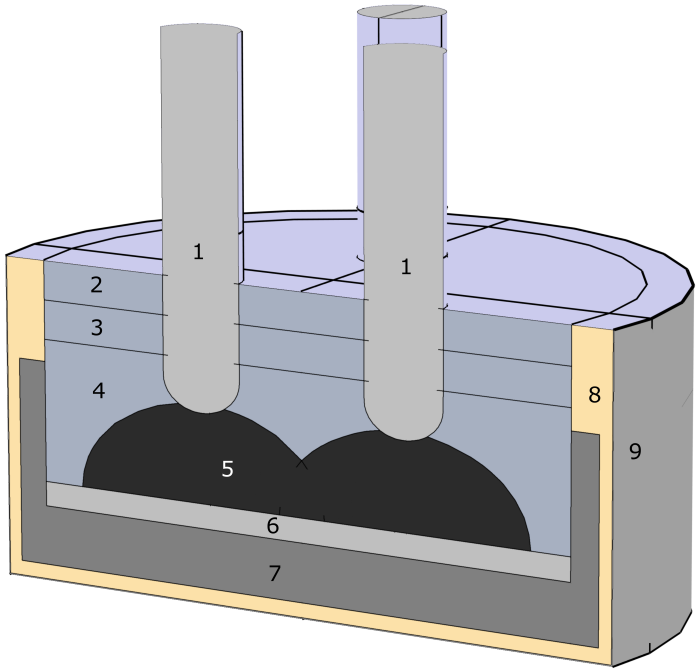

Figure 2. Esquema dun forno de produción de FeMn: 1. Electrodos 2. Carga 400 °C 3. Carga 800 °C 4. Carga 1200 °C 5. Leito de coque 6. Aliaxe 7. Revestimento de carbono 8. Revestimento de óxido 9. Carcasa de aceiro.

A maioría dos fornos industriais teñen unha carcasa de aceiro (zona 9) que ten a función de soportar o peso do forno.

Hai que sinalar que os fornos SAF teñen unha estrutura moito máis complexa, e frecuentemente, nas tarefas de modelado e simulación numérica é preciso simplificar o problema dependendo do interese da investigación. No noso caso, como o interese principal é no fogar do forno, consideráronse as zonas descritas previamente, sen ter en conta outros detalles como a virola que recubre o electrodo, os flexibles e cables de corrente, etc.

Para abordar o modelado electromagnético destes fornos, o traballo da tese pode dividirse, en termos xerais, en dúas categorías que se describen a continuación e onde se resumen algunhas contribucións da tese respecto á literatura existente neste ámbito.

1. **Estudo de ferramentas analíticas para entender os efectos indutivos**. Empregouse análise adimensional para determinar os grupos adimensionais que gobernan o comportamento electromagnético dos condutores que transportan a corrente alterna. O obxectivo principal é seleccionar os parámetros máis importantes para estudiar o comportamento electromagnético no fogar dun forno de arco somerxido empregando dimensións de fornos industriais e propiedades de materiais axeitadas. A idea é determinar os

USC UNIVERSIDADE DE SANTIAGO DE COMPOSTELA

parámetros nunha xeometría 2D sinxela para a súa aplicación posterior a unha parte do forno. Este enfoque, é dalgún xeito, unha continuación dos resultados presentados en Schlanbusch et al. (2014), e publicados durante o proxecto 'Metallurgical Scale Up', un proxecto predecesor do ElMet Halvorsen et al. (2021). O obxectivo nesta tese é aplicar as ferramentas adimensionais ao estudo dunha xeometría de forno representativa que é validada mediante simulacións numéricas. Por outra banda, a análise do sistema 2D constitúe a base para o desenvolvemento de modelos analíticos 1D que se poden empregar para describir o comportamento dos campos electromagnéticos en capas de materiais con distintas propiedades. Concretamente, o enfoque 1D pódese aproveitar para o estudo de correntes horizontais tanto no interior do forno como para estudo de correntes verticais nos revestimentos e na carcasa de aceiro.

Na literatura pódense atopar algunhas técnicas de análise non dimensional aplicadas á simplificación de modelos multifísicos en partes dos SAFs (ver, por exemplo, Sloman et al. (2017); Van Gorder et al. (2021); Luckins (2021)); porén, o obxectivo destas referencias está lonxe de obter unha expresión analítica do campo eléctrico, que si é un propósito neste traballo. O modelo analítico 1D que se estuda está inspirado nas ferramentas introducidas en Deng et al. (2009), pero coa novidade de tratar distintos tipos de condicións de contorno e centrándose no caso de baixa frecuencia. Ademais, non se coñece a aplicación destas técnicas ao estudo de procesos metalúrxicos.

2. **Simulación numérica de fornos de produción de FeMn.** Desenvolvéronse distintos modelos matemáticos 3D e 2D partir da ecuacións de Maxwell e resolvéronse numericamente mediante elementos finitos empregando o software comercial COMSOL Multiphysics®. Máis concretamente, introducíronse modelos reducidos 2D baixo hipóteses axeitadas na corrente eléctrica (corrente vivindo nun plano ou corrente perpendicular ao plano) para simular partes concretas do forno e para comparar modelos e corrente alterna (AC) con modelos aproximados de corrente continua (DC). A comparación da análise non dimensional con resultados obtidos da simulación numérica é novidoso respecto á literatura existente. Ademais, aínda que a comparación entre AC e DC se abordou nalgún traballo da literatura Tesfahunegn et al. (2020) fíxose para fornos de FeSi, e neste traballo o estudo céntrase en fornos de ferromagnaneso que presentan un comportamento bastante diferente.

   Por outra banda, a inclusión da carcasa de aceiro e dos revestimentos fíxose ata o momento nun número limitado de publicacións Herland et al. (2019); Tesfahunegn et al. (2020); Sparta, Stråbø, et al. (2021). Así, por exemplo, nos traballos Herland et al. (2019, 2018) discutiuse a importancia das correntes inducidas na carcasa de aceiro dos SAFs. Nesta tese abordáronse deseños innovadores da carcasa e do revestimento do forno, aportando novas

USC UNIVERSIDADE DE SANTIAGO DE COMPOSTELA

contribucións ao estado de arte neste campo.

Dende o punto de vista numérico, tamén se presentou un método novidoso que permite mellorar a eficiencia computacional de modelos de correntes inducidas en 3D. Máis concretamente, baixo a hipótese de materiais magnéticos lineais, proponse resolver un problema de corrente trifásica a partir da combinación linear dun problema alimentado con corrente monofásica. Esta metodoloxía ofrece a alternativa de crear un método computacional máis barato capaz de explotar as simetrías de certos fornos. A técnica está inspirada nas ideas exploradas en Halvorsen et al. (2016) no contexto de corrente continua.

A continuación resúmense os contidos estudados en cada capítulo así como as conclusións obtidas nos estudos máis relevantes.

O Capítulo 1 describe o problema industrial que motivou o estudo levado a cabo na tese. O Capítulo 2 presenta unha revisión da literatura relacionada co comportamento electromagnético de fornos trifásicos para coñecer o estado de arte neste campo así como para definir os principais desafíos na tese. As referencias agrupáronse de acordo aos obxectivos dos modelos: un primeiro bloque de referencias adicadas ao estudo completo do forno, un segundo grupo centrado no estudo dos electrodos e das partes que o rodean e un último bloque con referencias que recollen estudos experimentais e datos dos materiais.

O Capítulo 3 describe os modelos matemáticos que permiten estudar os campos electromagnéticos nos SAFs. Estes fornos son alimentados con corrente eléctrica alterna a baixa frecuencia polo que se poden estudar mediante o coñecido modelo de correntes inducidas ou *eddy currents* caracterizado por despreciar as correntes de desprazamento. O modelo descríbese en termos do vector potencial magnético e do potencial escalar eléctrico que é opción empregada por Comsol Multiphysics®e introdúcense condicións de contorno axeitadas para definir as fontes de corrente. Máis concretamente, introducíronse dous modelos diferentes 2D obtidos a partir do modelo 3D: un modelo con correntes no plano (*in plane*) e outro con correntes perpendiculares ao plano (*out of plane*). O modelo 2D *in plane* inclúe no dominio computacional dous dos tres electrodos e poden atoparse referencias de estudos similares en fornos SAFs en contextos multifísicos K. T. Karalis et al. (2016). Nesta tese, este modelo emprégase tanto para estudos en corrente alterna como en corrente continua. Por outra banda, os modelos 2D *out of plane* son útiles para modelar a parte superior do forno onde se pode asumir que a corrente é perpendicular á sección e se poden incluír os revestimentos e a carcasa de aceiro; este modelo é axeitado para analizar o efecto de proximidade entre os tres electrodos e os efectos inductivos na carcasa e revestimento.

O Capítulo 4 presenta os resultados obtidos na simulación de fornos de produción de FeMn empregando os modelos descritos (3D e 2D) así como estudos non

USC UNIVERSIDADE DE SANTIAGO DE COMPOSTELA

dimensionais. Aplícanse así os modelos estudados no capítulo previo para analizar distintos fenómenos electromagnéticos no forno, que se poden resumir en dous bloques:

a) **Efectos de indución no fogar do forno**. Estudáronse os efectos inductivos no interior de fornos de arco somerxido onde se combinan moi bos conductores (metal, electrodos), con conductores moderados (escoria, leito de coque) e materiais moi pouco conductores (carga, revestimento illante). Aplicouse un modelo 2D reducido tanto mediante análise non dimensional como mediante simulación numérica para analizar o impacto da xeometría e os materiais nos campos electromagnéticos e poder explicar deste xeito, os efectos indutivos entre as diferentes rexións. Por outra banda, os modelos 2D tamén se empregaron para o comparar o uso de modelos AC xenuínos con modelos aproximados DC tendo en conta diferentes aproximacións para o leito de coque.

   En relación con estes puntos, concluíuse que analizando a ecuación que determina o campo eléctrico nun condutor rectangular, a distribución da corrente eléctrica no condutor está determinada por dous tipos de números non dimensionais, relacionados co aspecto xeométrico e coa razón entre lonxitude/espesor e a respectiva profundidade de pel. Isto aplicouse a un modelo de forno 2D e validouse mediante simulacións numéricas. A análise de ecuacións non dimensionais con supostos naturais para os valores dos parámetros, viuse que era suficiente para amosar que as propiedades do leito de coque (condutividade, altura e anchura efectivas) son importantes para as condicións eléctricas do forno e, por tanto, importantes para o funcionamento do forno. Por outra banda, cando a corrente flúe entre dous bos condutores a través dun material menos condutor, as solucións de AC e DC son similares. Con todo, se hai correntes paralelas en materiais adxacentes de diferente condutividade, os efectos indutivos alterarán a distribución de AC. Se hai unha corrente considerable no material menos condutor, os modelos de AC e DC difiren, e a diferenza aumenta co incremento da condutividade. Observáronse algunhas diferenzas entre os modelos 2D e 3D que indican que os modelos 2D de corrente no plano non substituirían completamente ás simulacións 3D completas, pero a súa simplicidade e o comportamento cualitativo poden axudar a comprender a sensibilidade a distintos parámetros físicos e xeométricos.

b) **Análise do impacto de deseños estruturais alternativos no aforro enerxético e no desgaste do material no revestimento e na carcasa de aceiro**. As correntes no interior da carcasa de aceiro, flúen en tres grandes bucles, verticalmente detrás de cada eléctrodo e pechándose horizontalmente entre os electrodos. Isto provoca unha disipación importante de calor na carcasa (perda de potencia) e a consecuente necesidade de refrixeración activa por auga. Se esta situación persiste durante un período de tempo prolongado, o aceiro pode adelgazar e deteriorarse debido ao dano oxidativo. No peor dos casos, o aceiro pode gretarse

USC UNIVERSIDADE DE SANTIAGO DE COMPOSTELA

ou perforarse, co consecuente risco de fuga incontrolada de gas, redución da eficacia do proceso, paradas de produción non desexadas para reparacións e, potencialmente, unha redución da vida útil do forno. Por iso, empregando modelos 2D (out-of-plane) e modelos 3D, estudáronse as correntes inducidas no aceiro da carcasa así como nos materiais condutores do revestimento de fornos de produción de FeMn. En particular, investigouse o efecto de cambios estruturais no revestimento e na carcasa dende o punto de vista da potencia disipada nas distintas partes de cara a unha produción máis sostible.

As simulacións amosaron grandes correntes verticais detrás de cada electrodo. Observouse ademais que se a carcasa de aceiro se secciona con ocos electricamente illantes, se formarían fortes correntes opostas a ambos os dous lados dos ocos, o que provocaría unha maior perda de calor e un maior risco de puntos quentes daniños. Por outra banda, viuse que as correntes inducidas na carcasa de aceiro modifícanse mediante un revestimento condutor da electricidade. O revestimento ten un efecto de apantallamiento que reduce as correntes na carcasa de aceiro. Por tanto, a modificación da xeometría do revestimento condutor pode contribuír a deseñar fornos cunha menor disipación de enerxía non desexada. Isto reduciría a perda de calor, a necesidade de auga de refrixeración así como o risco de danos no aceiro estrutural.

O Capítulo 5 céntrase na construción e na aplicación dun modelo analítico 1D que permite estudar o comportamento electromagnético nun sistema formado por distintas capas de materiais. A solución constrúese considerando dous tipos de condicións de contorno: proporcionando o valor do campo eléctrico nunha determinada posición ou ben a corrente total atravesando o conxunto de condutores. As solucións analíticas empregáronse para distintos propósitos: para analizar efectos indutivos en condutores adxacentes, para calcular a distribución de corrente a través de múltiples capas, e para comparar modelos de corrente alterna e corrente continua. Os estudos permitiron concluír que a distribución nunha soa capa de material gobérnase pola relación entre a profundidade da pel do material e o espesor da capa. Ademais, os materiais circundantes teñen unha influencia significativa, determinada polas condicións nas interfaces entre materiais para os campos eléctrico e magnético. A comparación da distribución do campo eléctrico obtida a partir do modelo 1D cun modelo 2D resolto numericamente demostrou que o modelo 1D proporciona unha boa estimación da solución 2D, especialmente cando se aplica a diferentes rexións de SAFs. Así pois, os mecanismos físicos implicados son descritos adecuadamente polo modelo 1D. Por outra banda, analizouse o comportamento da solución cando unha capa (moderadamente) condutora está cerca dunha capa moi condutora e explotáronse os resultados para determinar propiedades relevantes para a potencia disipada nas distintas partes. Concluíuse que o modelo 1D se revela como unha ferramenta útil, doada de empregar e versátil, para abordar aplicacións onde a corrente se pode considerar unidimensional.

USC UNIVERSIDADE DE SANTIAGO DE COMPOSTELA

Publicáronse dous artigos en revistas indexadas no JCR. O primeiro está baseado no estudo do fogar do forno mediante modelos 2D *in plane* e mediante análise non dimensional. O segundo artigo está centrado no estudo de correntes inducidas no revestimento e na carcasa de aceiro dos fornos incluíndo resultados obtidos cun modelo 2D out of plane e cun modelo 3D. Actualmente, estase finalizando a redacción dun terceiro traballo, relacionado co modelo analítico 1D:

- M. Fromreide, D. Gómez, S.A. Halvorsen, E. Herland, P. Salgado. (2021). *Reduced 2D/1D mathematical models for analysing inductive effects in submerged arc furnaces*. Applied Mathematical Modelling, vol. 98, pp. 59-70. ISSN: 0307-904X. doi:10.1016/j.apm.2021.04.034
- M. Fromreide, D. Gómez, S.A. Halvorsen, E. Herland, P. Salgado. (2023) *Induced currents in the lining and steel shell of submerged arc furnaces*. Journal of Sustainable Metallurgy. Vol. 9. pp. 375-385. doi:10.1007/s40831-022-00625-6

Como continuación do proxecto ElMet, iniciouse un novo proxecto de colaboración titulado *Electrical Conditions in Submerged Arc Furnaces - Identification and Improvement* (SAFECI). No proxecto SAFECI participan varios socios industriais. Os resultados e conclusións do proxecto ElMet, incluídos os modelos desenvolvidos nesta tese, investigaranse máis a fondo e utilizaranse como valiosas ferramentas para a industria. Seguir investigando os efectos indutivos nos fornos de FeMn e noutros fornos, con máis estudos de casos de simulacións 3D completas, será unha continuación natural dos estudos realizados con simulacións 2D e modelos analíticos. Será interesante observar se o comportamento das correntes a través do leito de coque segue sendo coherente nas simulacións 3D, como se demostrou nas simulacións 2D e se deduciu analiticamente na análise 1D, en función das propiedades do leito de coque. Esta investigación proporcionaría, entre outras cousas, información sobre a aplicabilidade do uso de modelos de corrente continua como aproximacións a modelos completos de corrente alterna

USC UNIVERSIDADE DE SANTIAGO DE COMPOSTELA

Bibliography

AC/DC Module User's Guide. (2022). *COMSOL Multiphysics® V 6.1. COMSOL AB, Stockholm, Sweden.*

Alonso-Rodríguez, A. (2011). Formulation via vector potentials of eddy-current problems with voltage or current excitation. *Communications in Applied and Industrial Mathematics*, *2*(1), e–369, 20.

Alonso-Rodríguez, A., & Valli, A. (2010). *Eddy current approximation of Maxwell equations* (Vol. 4). Springer-Verlag Italia, Milan. (Theory, algorithms and applications) doi: 10.1007/978-88-470-1506-7

Amrouche, C., Bernardi, C., Dauge, M., & Girault, V. (1998). Vector potentials in three-dimensional non-smooth domains. *Mathematical Methods in the Applied Sciences*, *21*(9), 823–864. doi: https://doi.org/10.1002/(SICI)1099-1476(199806)21:9<823::AID-MMA976>3.0.CO;2-B

Barcza, N. A., Koursaris, A., See, J. B., & Gericke, W. A. (1979). The 'Dig Out' of a 75 MVA High-carbon Ferromanganese Electric Smelting Furnace. In *37th Electric Furnace Conference, Detroit, USA, AIME* (pp. 19–33).

Bøckmann, O. C. (1971). *Patent: Arrangement for measuring the crater voltages in a three-phase electric furnace with electrode arranged in delta* (No. 3919/71). Norway.

Bermúdez, A., Bullón, J., & Pena, F. (1998). A finite element method for the thermoelectrical modelling of electrodes. *Communications in Numerical Methods in Engineering*, *14*(6), 581–593. doi: https://doi.org/10.1002/(SICI)1099-0887(199806)14:6<581::AID-CNM175>3.0.CO;2-S

Bermúdez, A., Bullón, J., Pena, F., & Salgado, P. (2003). A numerical method for transient simulation of metallurgical compound electrodes. *Finite Elements in Analysis and Design*, *39*(4), 283–299. doi: https://doi.org/10.1016/S0168-874X(02)00069-0

Bermúdez, A., Gómez, D., & Salgado, P. (2014). *Mathematical Models and Numerical Simulation in Electromagnetism*. Springer International Publishing Switzerland. doi: 10.1007/978-3-319-02949-8

Bermúdez, A., López-Rodríguez, B., Rodríguez, R., & Salgado, P. (2013). An eddy current problem in terms of a time-primitive of the electric field with non-

USC UNIVERSIDADE DE SANTIAGO DE COMPOSTELA

local source conditions. *ESAIM: Mathematical Modelling and Numerical Analysis - Modélisation Mathématique et Analyse Numérique*, *47*(3), 875–902. doi: 10.1051/m2an/2013065

Bermúdez, A., Muñiz, M. C., Pena, F., & Bullón, J. (1999). Numerical computation of the electromagnetic field in the electrodes of a three-phase arc furnace. *International Journal for Numerical Methods in Engineering*, *46*(5), 649–658. doi: https://doi.org/10.1002/(SICI)1097-0207(19991020)46:5<649::AID-NME664>3.0.CO;2-C

Bermúdez, A., Rodríguez, R., & Salgado, P. (2005). FEM for 3D eddy current problems in bounded domains subject to realistic boundary conditions. An application to metallurgical electrodes. *Archives of Computational Methods in Engineering*, *12*(1), 67-114.

Beukes, J. P., Roos, H., Shoko, L., van Zyl, P. G., Neomagus, H. W. J. P., Strydom, C. A., & Dawson, N. F. (2013). The use of thermomechanical analysis to characterise Søderberg electrode paste raw materials. *Minerals Engineering*, *46-47*, 167–176. doi: https://doi.org/10.1016/j.mineng.2013.04.016

Bezuidenhout, J. J., Eksteen, J. J., & Bradshaw, S. M. (2009). Computational fluid dynamic modelling of an electric furnace used in the smelting of PGM containing concentrates. *Minerals Engineering*, *22*(11), 995–1006. doi: https://doi.org/10.1016/j.mineng.2009.03.009

Böchmann, O., & Olsen, L. (1968). Skin and proximity effects in electrodes of large smelting furnaces. In *6th International Congress of Electroheat, Brighton, UK.*

Bossavit, A. (1985). Two dual formulations of the 3D eddy currents problem. *COMPEL - The international journal for computation and mathematics in electrical and electronic engineering*, *4*(2), 103–116. doi: 10.1108/eb010005

Bossavit, A. (1998). *Computational Electromagnetism: Variational Formulations, Complementarity, Edge Elements*. Academic Press. Retrieved from https://books.google.es/books?id=zN0eAQAAIAAJ

Bossavit, A. (1999). Eddy currents in dimension 2: Voltage drops. In *Proceedings ISTET'99* (Vol. 99, pp. 103–107). University Otto-von-Guericke, Magdeburg, Germany.

Bullón, J., Lage, M., Bermúdez, A., & Pena, F. (1998). The new compound electrode: current situation and thermoelectric studies. In *INFACON VIII: Eighth International Ferroalloys Congress, Beijing, China* (Vol. 8, pp. 389–393).

Choudhary, M., & Szekely, J. (1980). The modeling of pool profiles, temperature profiles and velocity fields in ESR systems. *Metallurgical Transactions B*, *11*(3), 439–453. doi: 10.1007/BF02676888

USC UNIVERSIDADE DE SANTIAGO DE COMPOSTELA

Coetsee, T. (2020). A review of ore smelting in high carbon ferromanganese production. *Mineral Processing and Extractive Metallurgy Review*, *41*(4), 255–278. doi: 10.1080/08827508.2019.1634566

Cui, H., Li, T., Bai, C. G., Tan, M., & Zhu, Y. L. (2023). Numerical simulation of coupling multi-physical field in electrical arc furnace for smelting titanium slag. *Journal of Iron and Steel Research International*. doi: https://doi.org/10.1007/s42243-023-00949-x

Darmana, D., Olsen, J. E., Tang, K., & Ringdalen, E. (2012). Modelling Concept For Submerged Arc Furnaces. In *Ninth International Conference on CFD in the Minerals and Process Industries.*

Davidsen, J. (2010). Reaction mechanisms in the silicomanganese process. *Project work, Department of Material Science and Engineering, Faculty of Natural Science and Technology, Norwegian University of Science and Technology*.

De Gersem, H., Hameyer, K., & Weiland, T. (2004). Field–circuit coupled models in electromagnetic simulation. *Journal of Computational and Applied Mathematics*, *168*(1), 125–133. doi: https://doi.org/10.1016/j.cam.2003.05.008

Deng, H. W., Zhao, Y. J., Liang, C. J., Jiang, W. S., & Ning, Y. M. (2009). Effective skin depth for multilayer coated conductor. *Progress In Electromagnetics Research M*, *9*, 1–8.

Dhainaut, M. (2004). Simulation of the electric field in a submerged arc furnace. In *Proceedings of the Tenth International Ferroalloy Congress* (pp. 605–613).

Dilawari, A. H., & Szekely, J. (1977). A mathematical model of slag and metal flow in the ESR Process. *Metallurgical Transactions B*, *8*(1), 227–236. doi: 10.1007/BF02657651

Dilawari, A. H., & Szekely, J. (1978). Heat transfer and fluid flow phenomena in electroslag refining. *Metallurgical Transactions B*, *9*(1), 77–87. doi: 10.1007/BF02822674

Dunski, V. (1962). Répartition du courant dans les électrodes d'un four triphasé à arcs en régimes équilibré et déséquilibré. *Elektrowärme*, *20*(10), 503–511.

Eidem, P. A. (2008). *Electrical Resistivity of Coke Beds* (PhD Thesis, Norwegian University of Science and Technology). doi: https://ntnuopen.ntnu.no/ntnu-xmlui/bitstream/handle/11250/248765/132857_FULLTEXT01.pdf?sequence=1

Eidem, P. A., Runde, M., Tangstad, M., Bakken, J. A., Zhou, Z. Y., & Yu, A. B. (2009). Effect of Contact Resistance on Bulk Resistivity of Dry Coke Beds. *Metallurgical and Materials Transactions B*, *40*(3), 388–396. doi: 10.1007/s11663-009-9235-1

USC UNIVERSIDADE DE SANTIAGO DE COMPOSTELA

Eidem, P. A., Tangstad, M., & Bakken, J. A. (2007). Measurement of Material Resistivity and Contact Resistance of Metallurgical Coke. In *INFACON XI: Eleventh International Ferroalloy Conference, Dehli, India* (pp. 561–571).

Eidem, P. A., Tangstad, M., & Bakken, J. A. (2008). Determination of Electrical Resistivity of Dry Coke Beds. *Metallurgical and Materials Transactions B*, *39*(1), 7–15. doi: 10.1007/s11663-007-9105-7

Eidem, P. A., Tangstad, M., Bakken, J. A., & Ishak, R. (2010). Influence of Coke Particle Size on The Electrical Resistivity of Coke Beds. In *INFACON XII: Twelfth International Ferroalloys Congress, Helsinki, Finland* (pp. 6–9).

Emanuel, A., & Doepken, H. C. (1974). Calculation of losses in steel enclosures of three phase bus or cables. *IEEE Transactions on Power Apparatus and Systems*, *PAS-93*(6), 1758–1767. doi: 10.1109/TPAS.1974.293827

Emson, C., & Simkin, J. (1983). An optimal method for 3-D eddy currents. *IEEE Transactions on Magnetics*, *19*(6), 2450–2452. doi: 10.1109/TMAG.1983.1062910

Fawzi, T., Ahmed, M., & Burke, P. (1985). On the use of the impedance boundary conditions in eddy current problems. *IEEE Transactions on Magnetics*, *21*(5), 1835–1840. doi: 10.1109/TMAG.1985.1063920

FerroAlloys. (2013). *Handbook of Ferroalloys: Theory and Technology* (M. Gasik, Ed.). Elsevier Ltd.

Fromreide, M., Gómez, D., Halvorsen, S. A., Herland, E. V., & Salgado, P. (2021). Reduced 2D/1D mathematical models for analyzing inductive effects in submerged arc furnaces. *Applied Mathematical Modelling*, *98*, 59–70. doi: https://doi.org/10.1016/j.apm.2021.04.034

Fromreide, M., Halvorsen, S. A., Sparta, M., Risinggård, V. K., Salgado, P., Gómez, D., & Herland, E. V. (2021). Effects of Alternating Currents in the Hearth of Submerged Arc Furnaces. In *INFACON XVI: Sixteenth International Ferro-Alloys Congress* (*virtual*).

Glastonbury, R. I. and Beukes, J. P. and van Zyl, P. G. and Tangstad, M. and Ringdalen, E. and Dall, D. and Steenkamp, J. D. and Mushwana, M. (2021). Characterisation of a real-world Søderberg electrode. *Metals*, *11*(1). doi: https://doi.org/10.3390/met11010005

Griffiths, D. J. (2017). *Introduction to Electrodynamics* (4th ed.). Cambridge University Press. doi: 10.1017/9781108333511

Gunnewiek, L., Oshinowo, L., Plikas, T., & Haywood, R. (2004). The Application of Numerical Modelling to the Design of Electric Furnaces. In *INFACON X: Tenth International Ferroalloys Congress,Cape Town, South Africa* (pp. 555–564).

USC UNIVERSIDADE DE SANTIAGO DE COMPOSTELA

Halvorsen, S. A., Olsen, H. A. H., & Fromreide, M. (2016). An Efficient Simulation Method for Current and Power distribution in 3-Phase Electrical Smelting Furnaces. *IFAC-PapersOnLine*, *49*(20), 167–172. doi: https://doi.org/10.1016/j.ifacol.2016.10.115

Halvorsen, S. A., Sparta, M., Risinggård, V. K., & Fromreide, M. (2021). Electrical conditions in 3-phase submerged arc furnaces: learning from the ElMet project. In *INFACON XVI: Sixteenth International Ferro-Alloys Congress (virtual)*. doi: 10.2139/ssrn.3926712

Hannesson, T. (2016). *The Si process DRAWINGS*. doi: https://www.elkem.is/globalassets/iceland/si-process.pdf

Harris, C. R., Millman, K. J., van der Walt, S. J., Gommers, R., Virtanen, P., Cournapeau, D., ... Oliphant, T. E. (2020). Array programming with NumPy. *Nature*, *585*(7825), 357–362. doi: 10.1038/s41586-020-2649-2

Herland, E. V., Sparta, M., & Halvorsen, S. A. (2018). 3D models of proximity effects in large FeSi and FeMn furnaces. *Journal of the Southern African Institute of Mining and Metallurgy*, *118*, 606–618. doi: 10.17159/2411-9717/2018/v118n6a8

Herland, E. V., Sparta, M., & Halvorsen, S. A. (2019). Skin and Proximity Effects in Electrodes and Furnace Shells. *Metallurgical and Materials Transactions B*, *50*(6), 2884–2897. doi: 10.1007/s11663-019-01651-8

Hot, E., Haznadar, Z., & Majer, I. (1980). Improvement of Electrode Systems in Electric Reduction Furnaces and a Non-Conventional Model for Current Density Measurement. In *9th International Congress of the UIE, Cannes, France.*

Hunter, J. D. (2007). Matplotlib: A 2D graphics environment. *Computing in Science & Engineering*, *9*(3), 90–95. doi: 10.1109/MCSE.2007.55

Ingason, H. T., & Jonsson, M. T. (1996). The geometrical effect on the thermal stresses of a self-baked carbon electrode. *Scandinavian Journal of Metallurgy*, *25*(2), 59–64.

Innvaer, R., Vatland, A., & Olsen, L. (1985). *Operational parameters for Soderberg electrodes from calculations, measurements, and plant experience*. Retrieved from https://books.google.es/books?id=YIkFjwEACAAJ

Innvær, R., Fidje, K., & Sira, T. (1987). 3-Dimensional calculations on smelting electrodes. *Modeling, Identification and Control*, *8*(2), 103–115. doi: 10.4173/mic.1987.2.3

Kadkhodabeigi, M., Ravary, B., & Hjertenes, D. O. (2015). Modeling of off-gas and particles flow under roof of a closed submerged arc furnace. In *INFACON XIV: Fourteenth International Ferroalloys Congress, Kyiv, Ukraine* (pp. 598–608).

Kameari, A. (1989). Three Dimensional Eddy Current Calculation Using Edge Elements for Magnetic Vector Potential. In K. Miya (Ed.), *Applied electromagnetics*

USC UNIVERSIDADE DE SANTIAGO DE COMPOSTELA

in materials (pp. 225–236). Pergamon. doi: https://doi.org/10.1016/B978-0-08-037191-7.50024-9

Kameari, A. (1990). Calculation of transient 3D eddy current using edge-elements. *IEEE Transactions on Magnetics*, *26*(2), 466–469. doi: 10.1109/20.106354

Kamilova, A. A. (2021). *Modelling and analysis of paste flow in high performance Søderberg electrodes* (Doctoral dissertation). doi: https://www.maths.ox.ac.uk/study-here/postgraduate-study/industrially-focused-mathematical-modelling-epsrc-cdt/infomm-resear-32

Karalis, K., Karkalos, N., Antipas, G. S. E., & Xenidis, A. (2017). Pragmatic analysis of the electric submerged arc furnace continuum. *Royal Society Open Science*, *4*(9), 170313. doi: 10.1098/rsos.170313

Karalis, K. T., Karalis, N., Karkalos, N., Ntallis, N., Antipas, G. S. E., & Xenidis, A. (2021). Three-dimensional computational fluid dynamics analysis of an electric submerged arc furnace. *Scientific Reports*, *11*(1). doi: 10.1038/s41598-021-96085-1

Karalis, K. T., Karkalos, N., Cheimarios, N., Antipas, G. S. E., Xenidis, A., & Boudouvis, A. G. (2016). A CFD analysis of slag properties, electrode shape and immersion depth effects on electric submerged arc furnace heating in ferronickel processing. *Applied Mathematical Modelling*, *40*(21), 9052–9066. doi: https://doi.org/10.1016/j.apm.2016.05.045

Kawasaki, K., Inami, M., & Ishikawa, T. (1981). Theoretical considerations on eddy current losses in non-magnetic and magnetic pipes for power transmission systems. *IEEE Transactions on Power Apparatus and Systems*, *PAS-100*(2), 474–484. doi: 10.1109/TPAS.1981.316904

Kero, I. T., Eidem, P. A., Ma, Y., Indresand, H., Aarhaug, T. A., & Grådahl, S. (2019). Airborne emissions from Mn ferroalloy production. *JOM*, *71*(1), 349–365. doi: 10.1007/s11837-018-3165-9

Larsen, B., Feldborg, H., & Halvorsen, S. A. (2013). Minimizing thermal stress during shutdown of Søderberg electrodes. In *INFACON XIII: Thirteenth International Ferroalloys Congress, Almaty, Kazakhstan* (pp. 453–466).

Larsen, H. L. (2006). Current Distribution in the Electrodes of Industrial Three-phase Electric Smelting Furnaces. *In Proceedings of the 2006 Nordic Comsol Conference, Copenhagen Denmark*.

Luckins, E. K. (2021). *Mathematical modelling of electrical, thermal, and chemical processes occurring within a silicon furnace* (Doctoral dissertation). doi: https://ora.ox.ac.uk/objects/uuid:ca50df39-3887-438c-8f54-1221c81cd92d/files/dkd17ct22d

Luckins, E. K., Oliver, J. M., Please, C. P., Sloman, B. M., Valderhaug, A. M., & Van Gorder, R. A. (2022). Modelling alternating current effects in a submerged arc

USC UNIVERSIDADE DE SANTIAGO DE COMPOSTELA

furnace. *IMA Journal of Applied Mathematics*, *87*(3), 492–520. doi: 10.1093/imamat/hxac012

Luckins, E. K., Oliver, J. M., Please, C. P., Sloman, B. M., & Van Gorder, R. A. (2022). Homogenised model for the electrical current distribution within a submerged arc furnace for silicon production. *European Journal of Applied Mathematics*, *33*(5), 828–-863. doi: 10.1017/S0956792521000243

Lupi, S. (2017). *Fundamentals of Electroheat. Electrical Technologies for Process Heating*. Springer Link. doi: https://doi.org/10.1007/978-3-319-46015-4

Madias, J. (2011). A review of the production of Ferromanganese in blast furnace. In *AISTech Proceedings 2011* (Vol. 1, pp. 401–412).

McDougall, I. (2007). Finite element modelling of electric currents in AC submerged arc furnaces.. Retrieved from http://hdl.handle.net/10204/962

McDougall, I., Smith, C. F. R., Olmstead, B., & Gericke, W. A. (2004). A Finite Element Model of a Søderberg Electrode With an Application in Casing Design. In *INFACON X: Tenth International Ferroalloys Congress,Cape Town, South Africa* (pp. 575–584).

Meunier, G. (Ed.). (2008). *The Finite Element Method for Electromagnetic Modeling* (1st ed.). ISTE.

Meyjes, R., Venter, J., & Van Rooyen, U. (2010). Advanced Modelling and Baking of Electrodes. In *INFACON XII: Twelfth International Ferroalloys Congress, Helsinki, Finland* (pp. 779–788).

Mintek. (n.d.). *Enhanced Minstral System.* Retrieved from https://www.mintek.co.za/2001/09/29/enhanced-minstral-system/ (Last access 15/05/2023)

Miyauchi, Y., Mochida, M., & Fuchi, Y. (2001). High thermal property of manganese ore in production of high carbon ferromanganese. In *INFACON IX: Ninth International Ferroalloys Congress, Quebec City, Canada* (pp. 236–243).

Olsen, S. E., & Tangstad, M. (2004). Silicomanganese Production - Process Understanding. In *INFACON X: Tenth International Ferroalloys Congress, Cape Town, South Africa* (pp. 231–238).

Olsen, S. E., Tangstad, M., & Lindstad, T. (2007). *Production of Manganese Ferroalloys*. Tapir Academic Press.

Rauf Hurman, E. (2014). *Chapter 1.10 - Production of Ferroalloys* (S. Seetharaman, Ed.). Elsevier. doi: https://doi.org/10.1016/B978-0-08-096988-6.00005-5

Ringdalen, E., & Eilertsen, J. (2001). Excavation of a 54 MVA HC-ferrochromium furnace. In *INFACON IX: Ninth International Congress on Ferroalloys, Quebec City, Canada* (pp. 166–173).

USC UNIVERSIDADE DE SANTIAGO DE COMPOSTELA

Ringdalen, E., & Ksiazek, M. (2018). Excavation of a SiMn-Furnace. *Furnace Tapping*.

Roberts, L., Nordgård-Hansen, E., Mikkelsen, ., Halvorsen, S. A., & Van Gorder, R. A. (2017). A heat and mass transfer study of carbon paste baking. *International Communications in Heat and Mass Transfer*, *88*, 9-19. doi: https://doi.org/10.1016/j.icheatmasstransfer.2017.07.025

Rooney, C. M. (2019). *Homogenisation of the electrothermal behaviour of granular material* (Doctoral dissertation, University of Oxford). doi: https://ora.ox.ac.uk/objects/uuid:b1ffd234-c9e3-4a22-bde2-d9aac3e4f7e1/files/ma474eb5ac2a3bb9d0382014dfc43b122

Rooney, C. M., Please, C. P., & Howison, S. D. (2021). Homogenisation applied to thermal radiation in porous media. *European Journal of Applied Mathematics*, *32*(5), 784–805.

Ryff, P. F. (1981). Eddy current losses in cylindrical arc furnace shells. *IEEE Transactions on Industry Applications*, *IA-17*(3), 329–333. doi: 10.1109/TIA.1981.4503948

Schlanbusch, R., Halvorsen, S. A., Shinkevich, S., & Gómez, D. (2014). Electrical scale-up of metallurgical processes. In *Proceedings of the 2014 COMSOL Conference, Cambridge, UK* (pp. 7–31).

Scorretti, R. (2021). Coupling of External Electric Circuits with Computational Domains. *J*, *4*(4), 865–880. doi: 10.3390/j4040059

Sheng, Y. Y., Irons, G. A., & Tisdale, D. G. (1998, Feb). Transport phenomena in electric smelting of nickel matte: Part II. Mathematical modeling. *Metallurgical and Materials Transactions B*, *29*(1), 85–94. doi: 10.1007/s11663-998-0010-5

Skjeldestad, A. (2019). *Electrode paste behavior in Søderberg electrodes in ferroalloy production* (Doctoral dissertation). doi: http://hdl.handle.net/11250/2643618

Skjeldestad, A., Tangstad, M., Lindstad, L., & Larsen, B. (2015). Temperature profiles in Søderberg electrodes. In *INFACON XIV: Fourteenth International Ferroalloys Congress, Kyiv, Ukraine* (pp. 327–337).

Sloman, B. M., Please, C. P., Van Gorder, R. A., Valderhaug, A. M., & Birkeland, H., R. G.and Wegge. (2017). A heat and mass transfer model of a silicon pilot furnace. *Metallurgical and Materials Transactions B*, *48*(5), 2664–2676. doi: 10.1007/s11663-017-1052-3

Sparta, M., Fromreide, M., Risinggård, V. K., & Halvorsen, S. A. (2022). Electrical conditions in submerged arc furnaces: A web-based simulator. In *Proceedings of the Silicon for the Chemical and Solar Industry XVI*. doi: 10.2139/ssrn.4118651

USC UNIVERSIDADE DE SANTIAGO DE COMPOSTELA

Sparta, M., Risinggård, V. K., Einarsrud, K. E., & Halvorsen, S. A. (2021). An Overall Furnace Model for the Silicomanganese Process. *JOM*, *73*(9), 2672–2681. doi: 10.1007/s11837-021-04791-y

Sparta, M., Stråbø, K., Halvorsen, S. A., Herland, E. V., & Martens, H. (2021). Metamodeling of the electrical conditions in submerged arc furnaces. *Metallurgical and Materials Transactions B*, *52*(3), 1267–1278. doi: 10.1007/s11663-021-02089-7

Sparta, M., Varagnolo, D., Martens, H., & Halvorsen, S. A. (2021). Metamodeling of the electrical conditions in submerged arc furnaces. In *INFACON XVI: Sixteenth International Ferro-Alloys Congress (virtual)*. doi: 10.2139/ssrn.3926715

Steenkamp, J. D., Gous, J. P., Grote, W., Cromarty, R., & Gous, H. J. (2018). Process Zones Observed in a 48 MVA Submerged Arc Furnace Producing Silicomanganese According to the Ore-Based Process. In B. R. Davis et al. (Eds.), *Extraction 2018* (pp. 639–651). Springer International Publishing.

Tesfahunegn, Y. A., Magnusson, T., Tangstad, M., & Saevarsdottir, G. (2018a). Dynamic Current Distribution in the Electrodes of Submerged Arc Furnace Using Scalar and Vector Potentials. In Y. Shi et al. (Eds.), *Computational Science – ICCS 2018* (pp. 518–527). Springer International Publishing.

Tesfahunegn, Y. A., Magnusson, T., Tangstad, M., & Saevarsdottir, G. (2018b). Effect of electrode shape on the current distribution in submerged arc furnaces for silicon production - A modelling approach. *Journal of the Southern African Institute of Mining and Metallurgy*, *118*, 595–600.

Tesfahunegn, Y. A., Magnusson, T., Tangstad, M., & Saevarsdottir, G. (2018c). The Effect of Pitch Circle Diameter of Electrodes on Current Distributions in Submerged Arc Furnace. In *2018 IEEE MTT-S International Conference on Numerical Electromagnetic and Multiphysics Modeling and Optimization (NEMO)* (pp. 1–4). doi: 10.1109/NEMO.2018.8503177

Tesfahunegn, Y. A., Magnusson, T., Tangstad, M., & Saevarsdottir, G. (2019). Dynamic Current and Power Distributions in a Submerged Arc Furnace. In G. Lambotte, J. Lee, A. Allanore, & S. Wagstaff (Eds.), *Materials Processing Fundamentals 2019* (pp. 3–14). Springer International Publishing.

Tesfahunegn, Y. A., Magnusson, T., Tangstad, M., & Saevarsdottir, G. (2020). Comparative Study of AC and DC Solvers Based on Current and Power Distributions in a Submerged Arc Furnace. *Metallurgical and Materials Transactions B*, *51*(2), 510–518. doi: 10.1007/s11663-020-01794-z

Tesfahunegn, Y. A., Saevarsdottir, G., Magnusson, T., & Tangstad, M. (2018). The Effect of Frequency on Current Distributions Inside Submerged Arc Furnace. In *2018 IEEE MTT-S International Conference on Numerical Electromagnetic and*

USC UNIVERSIDADE DE SANTIAGO DE COMPOSTELA

Multiphysics Modeling and Optimization (NEMO) (pp. 1–4). doi: 10.1109/NEMO.2018.8503083

Touzani, R., & Rappaz, J. (2014). *Mathematical Models for Eddy Currents and Magnetostatics, With Selected Applications*. Springer Link. doi: 10.1007/978-94-007-0202-8

Van Gorder, R. A., Kamilova, A., Birkeland, R. G., & Krause, A. L. (2021). Locating the baking isotherm in a Søderberg electrode: analysis of a moving thermistor model. *SIAM Journal on Applied Mathematics*, *81*(4), 1691–1716. doi: 10.1137/20M1314276

Van Rossum, G., & Drake, F. L. (2009). *Python 3 Reference Manual*. Scotts Valley, CA: CreateSpace. doi: 10.5555/1593511

Westly, J. (1974). Resistance and heat distribution in a submerged-arc furnace. In *INFACON I: First International Ferroalloys Congress, Johannesburg, South Africa* (pp. 121–127).

White, J. F., Rigas, K., Andersson, S. P., & Glaser, B. (2020). Thermal properties of Söderberg electrode materials. *Metallurgical and Materials Transactions B*, *51*(5), 1928–1932. doi: 10.1007/s11663-020-01890-0

Yoneka, S., Harada, K., Kojima, K., & Nakagawa, K. (1980). *Considerations of Electric Furnace Dimension and Dynamic Operation Bas on Research of Reduction Burden in a Model Furnace.* Retrieved from https://www.pyrometallurgy.co.za/InfaconII/386-Yoneka.pdf

Yu, Y., Li, B., Qi, F., Liu, Z., & Liu, S. (2021). Numerical Study on Transient Smelting Process for Manganese-Silicon Production in a Submerged Arc Furnace. In *Proceedings of the 16th International Ferro-Alloys Congress (INFACON XVI)*. doi: 10.2139/ssrn.3926232

Yu, Y., Li, B., Yun, C., Qi, F., & Liu, Z. (2021). Modeling on reduction reaction of metal oxides for submerged arc furnace in ferrochrome pellets smelting process. *Metallurgical and Materials Transactions B*, *52*(6), 3907–3919. doi: 10.1007/s11663-021-02304-5

Yuferev, S., & Ida, N. (2005). Time domain surface impedance concept for low frequency electromagnetic problems—Part I: Derivation of high order surface impedance boundary conditions in the time domain. *IEE Proceedings - Science, Measurement and Technology*, *152*, 175–185(10).

Zhaozhao, Y., Z., J., Yanbin, Y., Haitao, M., L., H., & Xingxing, W. (2022). Effect of steel rod embedded in electrode on continuous consumption of graphite by using numerical simulation. *Ironmaking & Steelmaking*, *0*, 1–12. doi: 10.1080/03019233.2022.2135810

USC UNIVERSIDADE DE SANTIAGO DE COMPOSTELA

Nomenclature

Abbreviations

1D	One dimensional
2D	Two dimensional
3D	Three dimensional
AC	Alternating current
DC	Direct current
SAF	Submerged arc furnace
FeMn	Ferromanganese
FeSi	Ferrosilicon
SiMn	Siliconmanganese
FeNi	Ferronickel
FeCo	Ferrocobalt

Greek symbols

α	The complex number $1 + i$
Γ	Boundary of a 3D domain
$\hat{\Gamma}$	Boundary of a 2D domain
δ	Material skin depth
ε_0	Electric permittivity of vacuum
θ	Phase shift
μ_0	Magnetic permeability of vacuum
μ	Magnetic permeability of material
μ_r	Relative magnetic permeability
ρ_V	Volumetric charge density
σ	Electrical conductivity
Ω	Three dimensional computational domain
$\hat{\Omega}$	Two dimensional computational domain
ω	Angular frequency
λ	wavelength

USC
UNIVERSIDADE DE SANTIAGO DE COMPOSTELA

Latin symbols

$\mathbf{A}$	Magnetic vector potential
$\boldsymbol{\mathcal{B}}$	Magnetic flux Density (time dependent)
$\mathbf{B}$	Magnetic flux Density (time harmonic)
$\boldsymbol{\mathcal{D}}$	Electric displacement field (time dependent)
$\mathbf{D}$	Electric displacement field (time harmonic)
D	Furnace diameter (simple model)
D_F	Furnace diameter
D_E	Electrode diameter
d	Electrode distance (center-center)
$\boldsymbol{\mathcal{E}}$	Electric field (time dependent)
$\mathbf{E}$	Electric field (time harmonic)
E_0	Characteristic field value
f	Frequency
$\boldsymbol{\mathcal{H}}$	Magnetic field Intensity (time dependent)
$\mathbf{H}$	Magnetic field Intensity (time harmonic)
H_C	Thickness of carbon lining (bottom)
H_{Ch}	Thickness of charge layer
$H_{Ch,400}$	Thickness of charge, 400°C
$H_{Ch,800}$	Thickness of charge, 800°C
$H_{Ch,1200}$	Thickness of charge, 1200°C
H_{Co}	Height of coke bed
H_E	Height of electrode
H_{EM}	Distance between electrode tip and metal alloy
H_M	Thickness of metal alloy
H_O	Thickness of oxide lining (bottom)
I	Current intensity
I_{tot}	Total current
i	Imaginary unit
$\boldsymbol{\mathcal{J}}$	Current density (time dependent)
$\mathbf{J}$	Current density (time harmonic)
L_E	Electrode distance (edge-edge)
$\mathbf{n}$	Unit normal vector
p	Electric active power density
P	Electric active power
R_{Co}	Radius of coke bed
t	Time unit
T	Thickness
T_C	Thickness of carbon lining (sides)
T_O	Thickness of oxide lining (sides)
T_{St}	Thickness of steel shell
V	Electric scalar potential

USC UNIVERSIDADE DE SANTIAGO DE COMPOSTELA

W	Width
$\mathbf{x}$	Vector of spatial coordinates
Z_ω	Intrinsic wave impedance

USC
UNIVERSIDADE DE SANTIAGO DE COMPOSTELA

USC
UNIVERSIDADE
DE SANTIAGO
DE COMPOSTELA

USC
UNIVERSIDADE
DE SANTIAGO
DE COMPOSTELA

Submerged Arc Furnaces (SAFs) are large electric arc furnaces used primarily in the production of ferromanganese (FeMn) and other ferroalloys. Smelting processes run at high temperatures and power is normally supplied by intensive three-phase alternating current (AC). Measurements of internal conditions are difficult or impossible to obtain and several process variations are not properly understood.

The project “Electrical Conditions and their Process Interactions in High Temperature Metallurgical Reactors (ElMet)” has applied mathematical modelling to increase this knowledge. The project has involved close collaboration between NORCE Norwegian Research Centre, the companies Elkem and Eramet Norway, the Norwegian University of Science and Technology and the Universities of Oxford and Santiago de Compostela, the latter through the Technological Institute for Industrial Mathematics (now integrated in CITMAga).

This thesis has been developed in the framework of ElMet. It has focused on studying reduced dimensional models using both analytical and numerical methods. More real furnace simulations have been carried out in 2D and 3D. New fundamental knowledge on AC inductive effects has been acquired by analysing comparatively simple 1D and 2D models. The models have been applied to different regions of smelting furnaces. Among others, good insights have been obtained on induced currents in the furnace steel shell and carbon lining.